Instabilités dans les systèmes spatialement périodiques : application aux instabilités secondaires et aux surfaces complexes.

Antoine Jouin

▶ **To cite this version:**

Antoine Jouin. Instabilités dans les systèmes spatialement périodiques : application aux instabilités secondaires et aux surfaces complexes.. Mécanique des fluides [physics.class-ph]. HESAM Université; Politecnico di Bari, 2023. Français. NNT : 2023HESAE020 . tel-04125853

HAL Id: tel-04125853
https://pastel.hal.science/tel-04125853

Submitted on 12 Jun 2023

HAL is a multi-disciplinary open access archive for the deposit and dissemination of scientific research documents, whether they are published or not. The documents may come from teaching and research institutions in France or abroad, or from public or private research centers.

L'archive ouverte pluridisciplinaire **HAL**, est destinée au dépôt et à la diffusion de documents scientifiques de niveau recherche, publiés ou non, émanant des établissements d'enseignement et de recherche français ou étrangers, des laboratoires publics ou privés.

HESAM UNIVERSITÉ

Politecnico di Bari

Arts et Métiers Sciences et Technologies

ÉCOLE DOCTORALE SCIENCES ET MÉTIERS DE L'INGÉNIEUR
[Laboratoire Dynfluid - Campus de Paris]

THÈSE

présentée par : **Antoine JOUIN**
soutenue le : **6 mars 2023**

pour obtenir le grade de : **Docteur d'HESAM Université**

préparée à : **École Nationale Supérieure d'Arts et Métiers**
Spécialité : **Mécanique des fluides**

Instabilities in spatially periodic systems: application to secondary instabilities and complex surfaces

THÈSE dirigée par :
[M. ROBINET Jean-Christophe]

et co-dirigée par :
[Mme CHERUBINI Stefania]

Jury

M. Nicolas MAZELLIER	Professor, Univ. of Orléans	Président
M. Shervin BAGHERI	Professor, KTH	Rapporteur
M. Ricardo GARCÍA-MAYORAL	Professor, Univ. of Cambridge	Rapporteur
M. Jan O. PRALITS	Assistant Professor, Univ. di Genova	Examinateur
Mme Taraneh SAYADI	Researcher, CNRS Sorbonne Univ.	Examinatrice
M. Jean-Christophe ROBINET	Professor, ENSAM Paris	Directeur
Mme Stefania CHERUBINI	Associate Professor, Politecnico di Bari	Co-directrice

THÈSE

Remerciements

En tout premier lieu, j'aimerais remercier mes encadrants Jean-Christophe Robinet et Stefania Cherubini pour la très grande liberté qu'ils m'ont accordée durant cette thèse. Merci Jean-Christophe d'avoir accepté de me prendre en stage (puis en master, puis en thèse) il y a quelques années et de m'avoir fait connaître la mécanique des fluides. Merci encore pour les longues discussions et les précieux conseils. Merci Stefania pour ton dynamisme incroyable et tes (nombreux) coups de main sur l'écriture et la rédaction de la thèse qui m'ont vraiment bien aidé. Votre implication a clairement permis la réussite de cette thèse.

Je tiens à remercier les membres de mon jury qui ont accepté de relire et de juger mon travail. Merci au professeur Nicolas Mazellier pour avoir apporté un point de vue expérimental sur le sujet et d'avoir accepté le rôle de président du jury. J'aimerais remercier ensuite les professeurs Shervin Bagheri et Ricardo García-Mayoral d'avoir accepté la charge de rapporteur de ce manuscrit et pour leurs commentaires précis et pertinents sur le manuscrit. Merci également aux professeurs Taraneh Sayadi et Jan Pralits d'avoir accepté de faire partie du jury et pour leurs très bonnes questions durant la soutenance.

Que seraient ces trois années de doctorat sans les rencontres que j'ai pu faire, et notamment les membres du laboratoire DynFluid. Parmi eux, j'aimerais remercier mes amis et collègues doctorants avec qui j'ai passé tant de bons moments. D'abord, les vieux briscards italiens qui m'ont montré les ficelles du métier: Leonardo, Aldo, Cosimo et Francesco. Ensuite la team des BG -Max, Camille et Enza- qui a su me soutenir durant ces trois années. Enfin, je tiens aussi à remercier ceux qui sont arrivés après moi -Matteus, Soufiane, Ricardo, Ismaïl, Alessandro et Ozgür- et à qui je souhaite le meilleur. Je ne me permettrais pas non plus d'oublier le représentant des doctorants, vice-président du labo et organisateur en chef des activités festives Aurélien. Enfin, le plus grand de tous les napolitains, merci à toi Gabriele pour tous les bons moments passés ensemble.

Je terminerais en remerciant ma famille qui m'a aidé pendant toutes ces années. Au final, si je fais de la mécanique des fluides, c'est sûrement grâce à Papy et à ses problèmes de baignoire qui fuient. Enfin, merci à toi Alice pour être restée à mes côtés pendant tout ce temps.

A toutes et tous, vous avez toute ma gratitude.

Résumé

Le présent manuscrit de thèse propose une étude des instabilités dans des écoulements spatialement périodiques. Deux types de périodicité, correspondant à des systèmes physiques sensiblement différents, peuvent être distinguées. Le premier type de périodicité, le plus simple, est géométrique et résulte de la répétition d'un motif ou d'un obstacle qui forcerait spatialement et périodiquement l'écoulement. Un exemple serait l'écoulement au-dessus d'une surface rugueuse ou superhydrophobe. La périodicité pourrait également être générée par une modulation de l'écoulement causée par l'émergence d'une structure cohérente via une instabilité primaire comme c'est le cas pour des stries dans une couche limite. Un cadre permettant la réalisation des analyses de stabilité modale et non-modale d'un système spatialement périodique est proposé. Il est basé sur la théorie de Bloch et des matrices circulantes, couplée à un problème de stabilité bidimensionnel. Un premier cas, qui sert également de validation de la méthode, porte sur la stabilité secondaire d'une couche limite tridimensionnelle. La stabilité secondaire de stries dans une couche limite laminaire est également examinée. Dans ce cas, les analyses non-modales mettent en exergue l'apparition d'un nouveau mécanisme potentiellement responsable de la transition vers la turbulence. Une compétition entre le mécanisme d'Orr et celui de génération des stries conduit également à l'apparition d'un régime de verrouillage de phase. La seconde partie de la thèse porte sur la stabilité d'un écoulement dans un canal dont une des parois est une surface complexe, soit rugueuse ou superhydrophobe. Dans un premier temps, les rugosités sont prises en compte via une technique d'homogénéisation, qui vient approximer l'effet des rugosités par une condition aux limites équivalentes. Une simulation est réalisée et met en évidence la présence de structures similaires à celles trouvées lors de l'analyse de la couche limite tridimensionnelle. La stabilité de ces structures est alors analysée sous cette nouvelle lumière. La transition vers la turbulence étant dependante de la technique d'homogénéisation, elle est ensuite étudiée avec la rugosité dans toute sa complexité. Là encore, les analyses non-modales montrent l'appartition de

phénomènes de résonance entre le mécanisme de génération des stries et le forcage lié à la rugosité. Ces deux mêmes mécanismes sont également à l'origine d'un régime en verrouillage de phase pour des rugosités avec une grande périodicité. Une dernière partie vient étendre l'analyse précédente aux surfaces superhydrophobes en considérant une dynamique de paroi.

Mots clés : stabilité, ondes de Bloch, verrouillage de phase, couche limite, rugosités, superhydrophobe

Abstract

This thesis manuscript proposes a study of instabilities in spatially periodic flows. Two types of periodicity, corresponding to significantly different physical systems, can be distinguished. The first type of periodicity, the simplest, is geometric and results from the spatial repetition of a pattern or an obstacle that periodically deforms the flow. An example is the flow above a rough or superhydrophobic surface. The periodicity could also be generated by a modulation of the flow caused by the emergence of a coherent structure via a primary instability as in the case of streaks in a boundary layer. A framework allowing modal and non-modal stability analyses of spatially periodic systems is proposed. It is based on the Bloch theory and circulating matrices, and it is coupled with a two-dimensional stability problem. A first case, which also serves as validation of the method, concerns the secondary stability of a three-dimensional boundary layer characterized by steady cross-flow vortices. The secondary stability of a streaky flow in a laminar boundary layer is also examined. In this case, the non-modal analyses highlight the appearance of a new mechanism potentially responsible for the transition to turbulence. A competition between the Orr mechanism and that allowing the generation of streaks also leads to the appearance of a frustration regime. The second part of the thesis deals with the stability of a flow in a channel where one of the walls is a complex surface, either rough or superhydrophobic. First, the roughnesses are taken into account via a homogenization technique, which approximates the effect of the roughnesses by an equivalent boundary condition. A direct numerical simulation is carried out and highlights the presence of structures similar to those found during the analysis of the three-dimensional boundary layer. The stability of these structures is then analysed under this new light. Then, the case of the flow over a rough wall is considered, taking into account the geometrical complexity of the roughness. Here again, the non-modal analyses show the appearance of resonance phenomena between the mechanism of generation of the streaks and the forcing linked to the roughness. These two mechanisms are also at the origin of a phase-locked regime for roughnesses

with a large periodicity. The last part of the thesis extends the previous analysis to superhydrophobic surfaces, taking into account the gas-liquid interface dynamics.

Keywords : instabilities, Bloch waves, boundary layer, streaks, rough and superhydrophobic surfaces

Contents

List of Tables

List of Figures

Chapter 1

Introduction

Contents

Stability of fluid flows and the consequent onset of turbulence are definitely interesting topics. From jet engines to clouds on Jupiter, fluids and their instabilities are ubiquitous. Thus, a better understanding of the mechanisms underlying the turbulent transition would prove beneficial for a vast number of applications. At first glance, the concept of laminar-turbulent transition is quite straightforward: as some threshold is crossed, the flow evolves from a well-ordered, laminar state to a chaotic, turbulent state. Despite the apparent simplicity of the previous claim, several difficulties may arise. The thresholds that would determine with certainty the stability of given flows have been sought since the early work of Reynolds (1883) and have been the subject of considerable research. Despite the subsequent development of stability theory (Helmholtz, 1868; Rayleigh, 1879), no satisfactory answer to the question could be given. Even worse, the existence of such a threshold is questionable as recent work showed the simultaneous coexistence of both laminar and turbulent states was possible under very specific conditions (Tuckerman *et al.*, 2020; Parente *et al.*, 2022).

A second problematic aspect of the transition lies in the fact that there is no single route to turbulence. Essentially, due to the highly dissipative nature of the turbulent state, transition must be triggered by injecting energy in the system, thus driving it out of its thermodynamic equilibrium. In

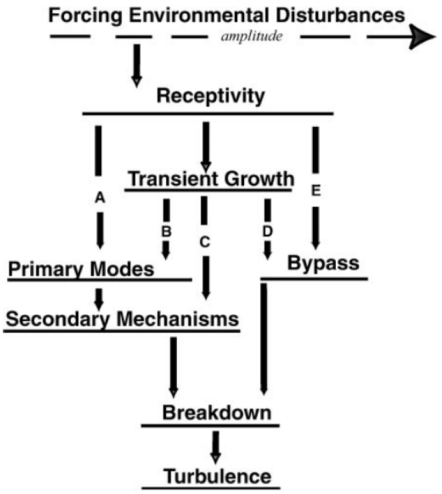

Figure 1.1: Classification of possible transition scenarii. From Morkovin (1969).

such a state, one of the most striking feature is the emergence of self-organising processes capable of generating complex spatial patterns (Cross & Hohenberg, 1993) and explaining, to some extent, why transition exhibits a seemingly infinite wealth of flow patterns of ever increasing complexity.

1.1 Transition and pattern formation

A phenomenological (and not-so-naïve) approach to modelling the laminar-turbulent transition would consider it as a progressive superposition of flow patterns: from the laminar flow stems a first instability, generating the first flow pattern. This pattern would deform the mean flow, leading to a second instability, and producing another pattern. This occurs until the flow reaches a memoryless turbulent state. Mathematically, these new flow structures can be traced by monitoring changes (*bifurcations*) in the topology of the phase space. This concept was initially proposed by Landau & Lifshitz (1959) who also introduced a distinction between *supercritical* and *subcritical* transitions. The phenomenological difference between supercritical and subcritical transitions is relatively simple but quite problematic. Subcritical transition happens when the parameter governing the stability of the flow is below the threshold value obtained with linear stability theory. In other words, transition happens when, according to the stability theory, there is no linear instability triggering it. A much deeper understanding can be obtained by considering phase-space dynamics. In the supercritical case, transition can be seen as continuous in the phase space as the flow progresses through an ordered

sequence of bifurcations (Landau & Lifshitz, 1959). At first, it was supposed that when supercritical transition occurs, turbulent dynamics could be decomposed into a superposition of quasi-periodic functions. This last point was later invalidated due to non-linear effects and correction of Landau's theory led to the establishment of the Ruelle-Takens route to turbulence (Ruelle & Takens, 1971). In the case of subcritical transition, on the contrary, the bifurcation is discontinuous in the phase space. The flow should be seen as a bistable system with both laminar and fully-developed turbulent states being linearly stable. Possible stability exchanges between the two states result in a hysteresis dynamics, appearing through the presence of an intermittent regime (Barkley, 2016).

For the sake of clarity, these two ideas will be illustrated by an example. Consider the transition to turbulence of a fluid of viscosity ν and with velocity U_∞ flowing over an infinite flat plate. Initially, the laminar flow near the wall is characterised by a special lengthscale δ and can be approximated by a hyperbolic tangent velocity profile, commonly called a Blasius profile. The application of stability theory to this profile yields a stability criterion based on the Reynolds number $Re_c = U_\infty \delta/\nu \approx 520$. Below it, no linear instability should be able to destabilise the flow while above, some waves may experience exponential growth.

↪ **Supercritical transition**

The stability analysis indicates that two-dimensional Tollmien-Schlichting (TS) waves (Tollmien, 1930; Schlichting, 1933) may become unstable. The development of these waves breaks the streamwise continuous symmetry of the velocity profile (but not the spanwise one). The stability analysis also provides a threshold, based on the Reynolds number $Re_c = U_\infty \delta/\nu \approx 520$. Below it, no instability should be able to destabilise the flow while above, the amplitude of the TS waves grows exponentially until a critical value is reached. At this stage, secondary instabilities arise (Herbert, 1983, 1988), breaking the spanwise invariance. Non-linear effects also become important as they redistribute energy, eventually causing the distortion of the base flow. The transition is then characterised by increasingly complex coherent structures: the symmetry breaking generates three-dimensional oblique waves, which in turn produce so-called Λ-shaped vortices, due to their herringbone shape. Of interest is the fact that the Λ-vortices may appear side-by-side (K-type transition) or in a staggered fashion (H-type transition). This leads to the formation of hairpin structures which end up breaking down. From the initial streamwise modulation of the TS wave to the eventually staggered pattern of Λ-vortices, the

importance of spatial patterns in the transition is quite clear. Numerous numerical simulations of this type of scenario have been realised and can be found, for example, in the early works of Kleiser & Zang (1991) or in the more recent work by Sayadi *et al.* (2013).

↪ **Subcritical transition**

The subcritical transition is in sharp contrast with the previously described chain of events. Initially, no TS waves can be observed (actually, their observation arrived significantly after their theoretical prediction, see Klebanoff *et al.* (1962)), giving a strong indication on the presence of other mechanisms capable of triggering transition. Of interest is the fact that some external disturbances (free-stream turbulence, wall roughness...) appear to be strongly amplified by the boundary layer. Mechanisms behind this energy amplification can be studied through receptivity analyses (Kerschen, 1989; Goldstein & Hultgren, 1989). Instead of TS waves, these mechanisms generate streamwise elongated coherent structures called streaks, *bypassing* exponential instabilities. Streaks break the spanwise symmetry and induce a spanwise modulation of the streamwise velocity of the flow. Due to the spanwise velocity gradient, secondary instabilities may develop, ultimately leading to a localised breakdown to turbulence and to the formation of a small turbulent region called a spot (Emmons, 1951). Laminar and turbulent regions compete with each other and, in general, turbulence ends up contaminating the entire flow (a rather interesting exception being the turbulent bands found in Tuckerman *et al.* (2020) where the two states were found to coexist without contamination). Turbulent spots are separated from the laminar regions by fronts and may expand or collapse at a finite growth rate, depending on the local environment of the spot (Barkley, 2016). More details and visualisations of the transition can be found in the works of Schlatter *et al.* (2008) (oriented on the secondary stability of streaks) or Wu *et al.* (2017) (for a focus on turbulent spots). An overview of this transition is given in the review of Zaki (2013).

1.2 From patterns to instabilities

Pattern formation is not limited to the laminar-turbulent transition and is observed in a large number of systems and physical fields such as the development of living organisms via morphogenesis (Turing, 1952), reaction-diffusion models of chemical reactions (Prigogine & Nicolis, 1985) or optics (Lugiato & Lefever, 1987). In all cases, behind the arising of patterns lies the concept of instabilities

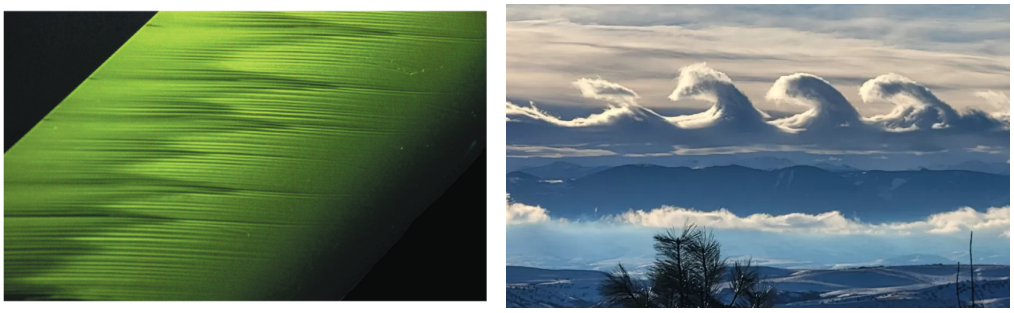

Figure 1.2: Examples of flow patterns resulting from primary instabilities. Left: cross-flow vortices in the transition over a swept plate. Flow is from left to right and darker shades indicate the presence of turbulence. From Serpieri & Kotsonis (2016). Right: Clouds acting as a tracer of Kelvin-Helmholtz waves.

and a clear link can be established between the first pattern appearing during the transition and unstable modes found from stability analysis (see for example Gallaire & Brun (2017)). In the context of fluid dynamics, the number of observable patterns is quite large. Among these primary instabilities, one can find cross-flow vortices in swept flows (Mack, 1984), gravity waves in stratified flows (Chandrasekhar, 1955), Kelvin-Helmholtz waves (Kelvin, 1871), creases on a deformable substrate (Li *et al.*, 2012), Taylor-Couette rolls (Coles, 1965). These structures are likely to further destabilise and continue the transition process. However, the primary stability analysis does not yield any information neither on these subsequent steps, nor on the eventual development of localised disturbances. A rather straightforward (albeit slightly naïve) solution to this shortcoming would reconsider a stability problem where the base flow is now constituted as the superposition of a laminar base flow and a primary instability. This is the idea behind the concept of secondary instabilities, presented in the seminal works of Orszag & Patera (1983) and Herbert (1983, 1985) for two-dimensional TS waves in wall-bounded flows. Several remarks can be made: the primary instability breaks the continuous symmetry of the laminar base flow and turns it into a discrete translational symmetry (characterised by the pattern's wavelength), yielding a more complex stability problem. Some difficulties may also arise from non-linear terms, not taken into account in the secondary base flow and which may cause the deformation of the primary pattern. Ultimately, secondary stability theory was successfully applied to most of the examples of primary instabilities previously given: streaks in boundary-layer (Liu *et al.*, 2008), cross-flow vortices in swept flows (Fischer & Dallmann, 1991; Bonfigli & Kloker, 2007), Kelvin-Helmholtz waves (Smyth, 2003), leading to breakthroughs in the identification of the underlying mechanisms of transition to turbulence.

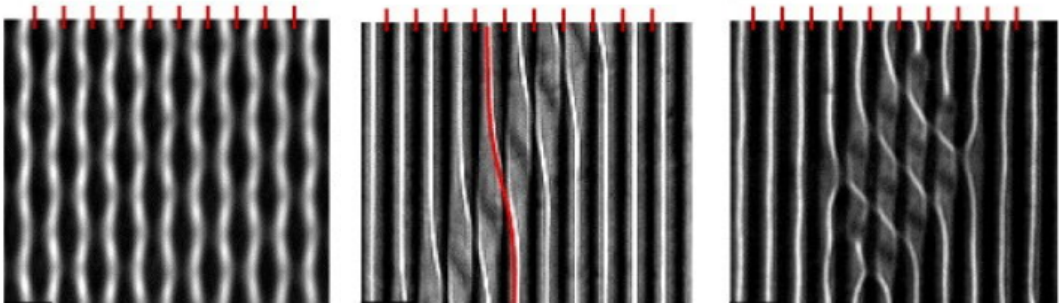

Figure 1.3: Rayleigh-Bénard convection rolls over a heated rough surface. The rough surface induces a forcing, causing the instability of the convection rolls. Depending on the riblet periodicity, the rolls exhibit a varicose instability (left) or a commensurate-incommensurate bifurcation leads to the appearance of localised dynamical structures (defects), either in the form of a travelling band (middle) or a cluster (right). Roughness positions are denoted by the red dashes. From Weiss *et al.* (2012).

1.3 Spatial forcings, wavenumber locking and frustration

Secondary stability analysis can be seen in a different light: the modulation induced by the primary pattern may be considered as a spatially periodic forcing of the laminar base flow. Quite surprisingly, systems with a spatially periodic forcing have received less attention than their temporal counterpart (see for example the review of Davis (1976)), despite exhibiting a number of interesting phenomena. Some of these are illustrated in figure 1.3 in the case of Kelvin-Helmholtz convection rolls forced by a rough surface. The key parameter governing the instability appears to be the ratio of the rolls' "natural" wavelength and the roughness wavelength. Depending on this quantity, the rolls may exhibit varicose oscillations or defects either in the form of a travelling band, either in the form of a cluster. The reader may notice some similarity between these patterns and structures observed in a bypass transition scenario such as varicose secondary instability of streaks (Schlatter *et al.*, 2008), turbulent bands (Tuckerman *et al.*, 2020) or spots (Zaki, 2013). Starting with the latter, these defects arise from a commensurate-incommensurate bifurcation (Coullet, 1986) of the system: a large-scale phase dynamics give rise to dissipative solitons, either stationary ("bands") or propagating ("spots") (Coullet *et al.*, 1985). The propagating solitons are associated with the external breaking of the Galilean invariance of the problem (Coullet & Huerre, 1986). In the case of the varicose instability, the forced system is adjusting the wavelength of the rolls to a rational fraction of the forcing wavelength associated with the rough surface if the mismatch between the two wavelengths is small enough. This phenomenon is called wavenumber locking and is the spatial analogue of the usual frequency locking with a twist as

spatially forced extended systems have the freedom to respond in two or three spatial dimensions, even if the spatial forcing is one-dimensional (Manor *et al.*, 2008). It has been identified in a large number of systems and domain of physics such as nematic liquid crystals (Lowe & Gollub, 1985), reaction-diffusion models (Lin *et al.*, 2000, 2004), synthetic exotic materials (Chalker *et al.*, 1992) or trapped ions (Kim *et al.*, 2010). In the domain of fluid mechanics, the phenomenon appears in Rayleigh-Bénard convection. It has been investigated initially in the work of Schmitz & Zimmermann (1996) and reexamined in full detail in the studies of Hossain & Floryan (2013, 2014, 2015, 2022). Experiments in the works of Freund *et al.* (2011) and Weiss *et al.* (2012, 2014) considered convection rolls spatially forced with a rough surface and shed some light on the wealth of (eventually localised) secondary patterns caused by the forcing. In their work, Floryan & Inasawa (2021) considered convection rolls forced simultaneously by a rough surface and a spatially periodic modulation of the temperature of the heated bottom plate. They demonstrated the existence of a pattern interaction effect: the combined effect of the two forcings yielded more complex secondary patterns than in the case of the two forcings taken separately.

A spatially forced system may also exhibit "frustration", defined in Nixon *et al.* (2013) (for a network of coupled lasers) as the inability of an ordered system to find a unique ground state. To give some context, in such a system, finding the ground state requires the minimisation of an interaction energy, depending on the coupling between the lasers. The resulting optimisation problem may be degenerate, yielding the frustration. Frustration is also observed in certain synthetic exotic materials (Chalker *et al.*, 1992) and trapped ions (Kim *et al.*, 2010). To the author's knowledge, this mechanism has not been observed nor investigated in fluid dynamics but still could be relevant as non-modal stability analyses (Schmid, 2007) relies on the resolution of an optimisation problem. Eventually, all these phenomena results from a competition between different wavelengths (Zimmermann *et al.*, 1993) either internal (and determined by instability mechanisms) or external (as for forcings). Interestingly, as less as three different wavelengths (Rucklidge *et al.*, 2012) may be enough to ensure spatiotemporal chaos through three-wave interactions, as in the temporal case (Cumming & Linsay, 1988).

1.4 Towards a better understanding of complex surfaces

As seen previously, rough surfaces have already been used in the Rayleigh-Bénard convection case (Schmitz & Zimmermann, 1996; Weiss *et al.*, 2014) to induce pattern formation as they constitute a

reliable form of spatial forcing. In this case, the periodicity of the system becomes geometric as it arises from the repetition of the fixed roughness shape. On their own, complex surfaces have already been well investigated as they present drag-reducing properties (see Bechert *et al.* (1997) for an example or the review of Jiménez (2004) for a more global view), very interesting from an engineering point of view

↪ **Experimental investigations and drag-reducing mechanisms**

For rough surfaces, drag-increasing properties were initially observed for turbulent pipe flows in the seminal works of Nikuradse (1933) and Colebrook & White (1937). These experiments allowed the identification of an optimal riblet spacing (Bechert *et al.*, 1997), maximising the drag reduction. The mechanisms at play, explaining these properties, have been mostly elucidated, but some aspects remain controversial. For small riblet spacing, flow in the grooves is dominated by viscous effects while coherent structures responsible for most of the drag are lifted on top of the riblets. Thus, only a fraction of a wall is seen by the flow, leading to the expected drag reduction. The drag reduction itself can be efficiently quantified through the determination of "protrusion heights" (Luchini *et al.*, 1991), characterising the riblets. Far from the optimal spacing, the performance of the rough surface starts to degrade as the viscous flow assumption starts to break down (García-Mayoral & Jiménez, 2011*a*,*b*). The origin of this failure is not totally clear and appears to depend on several factors. Initially, Goldstein & Tuan (1998) believed the decrease in drag reduction was due to the generation of secondary vortices near the tip of the riblets, thus creating extra dissipation. In their work, García-Mayoral & Jiménez (2011*b*) showed the existence of a spanwise invariant, Kelvin-Helmholtz related coherent structure that may be responsible for the drag increase. Chavarin & Luhar (2020) managed to retrieve these structures through a resolvent mean flow analysis. Later, Endrikat *et al.* (2021) studied numerically the onset of these Kelvin-Helmholtz rollers for various roughness shapes and found they arose in a limited number of configurations. The key parameters identified were the groove cross-section area and the momentum absorption at the tip of the riblets.

Another notable example of complex surfaces with drag-reducing properties is that of superhydrophobic and the closely related liquid-infused surfaces. Considering a rough surface, a gas or a liquid may remain trapped in the grooves (Lee & Kim, 2011), forming a superhydrophobic surface. In the case of a trapped liquid (of different viscosity), the surface is said to be liquid-infused (Ville-

gas *et al.*, 2019). In this configuration, the flow over such a surface only sees a fraction of the solid rough surface and slips on the lubricant interfaces, leading once again to drag reduction. However, this Cassie-Baxter state (Cassie & Baxter, 1944), in which the lubricant remains trapped, may not be durable as the interface between the two species becomes unstable (Zhang *et al.*, 2015; Gose *et al.*, 2018) and leads to the depletion of the superhydrophobic layer (the *wetting* transition). Due to their complexity, the drag-reducing effect of superhydrophobic surfaces could be quantified experimentally only rather recently first in laminar (Ou *et al.*, 2004; Ou & Rothstein, 2005; Byun *et al.*, 2008; Schäffel *et al.*, 2016) and then turbulent (Daniello *et al.*, 2009; Woolford *et al.*, 2009) configurations. Two failure mechanisms could be observed and identified: the development of capillary pressure waves, highly detrimental to the interface stability (Seo *et al.*, 2015; Seo & Mani, 2018) and mass diffusion of the trapped gas (Ling *et al.*, 2017). In an effort to overcome the previous shortcomings, liquid-infused surfaces were considered as they are less sensible to the failure mechanisms identified in their superhydrophobic counterpart (Wong *et al.*, 2011). Experiments demonstrating their drag-reduction potential were carried (Van Buren & Smits, 2017; Fu *et al.*, 2019). However, capillary waves were still observed and led to large interface deformations which appeared to induce a roughness effect degrading the drag reduction Sundin *et al.* (2021). A new shear-driven failure mechanism, leading to the progressive drainage of the grooves, could also be identified (Wexler *et al.*, 2015).

↪ **Complex surface modelling and stability analysis**

As previously stated, the drag-reducing properties of rough and superhydrophobic (SH) surfaces are of great interest from an engineering point of view. Unfortunately, due to their complexity (and notably the scale difference between the macroscopic flow and the microscopic roughnesses/SH patches), it is notoriously difficult to simulate numerically the flow over them. One of the approaches that has been proven effective is the use of homogenised boundary conditions (Luchini *et al.*, 1991). The idea is rather simple: the complex surface is reduced to a virtual plane on which are imposed boundary conditions mimicking the effects of the surface on the overlying flow. A common choice of boundary conditions are partial-slip Robin boundary conditions imposed on the tangential velocity components:

$$u = L_x \frac{\partial u}{\partial y}, \qquad v = 0 \qquad w = L_z \frac{\partial w}{\partial y}$$

where L_x and L_z are the streamwise and spanwise slip lengths corresponding to the complex surface. Such a set of boundary conditions was found to correctly predict drag-reducing properties for both

laminar (Choi *et al.*, 2003; Ou *et al.*, 2004) and turbulent regimes (see Abderrahaman-Elena *et al.* (2019); Ibrahim *et al.* (2021) for rough surfaces and Zhang *et al.* (2016); Seo & Mani (2016) for the SH case).

Still, several difficulties arise: first and foremost, the slip lengths appearing in the boundary conditions, must be determined in such a way that they correspond to a real, physically relevant configuration of the complex surface. The Navier type of the boundary conditions also causes some trouble. Take, for example, the case of an anisotropic surface as considered in the works of Stroock *et al.* (2002); Aghdam & Ricco (2016) or Pralits *et al.* (2017), that is a pattern, say riblets or SH patches, oriented at an angle θ with the direction of the flow. In a small region near the wall, the flow will follow the orientation of the riblets, thus creating a small spanwise component of velocity. With the usual Navier slip boundary conditions, this shear misalignment near the riblets will be missed. Also problematic, Gómez-de Segura & García-Mayoral (2020) showed that the development of Kelvin-Helmholtz rollers was linked to the apparition of a transpiration (a non-zero normal velocity gradient) at the virtual interface, once again not possible with the Navier boundary conditions. Ultimately, these shortcomings were progressively resolved through the consideration of more complex boundary conditions. First, tensorial slip boundary conditions (Kamrin *et al.*, 2010; Luchini, 2013) were used, replacing the slip lengths by slip tensors. Later, through a multiple scale analysis, Bottaro (2019); Zampogna *et al.* (2019); Bottaro & Naqvi (2020) and Lācis *et al.* (2020) established the homogenised boundary conditions at the virtual interface for second and higher orders and demonstrated the existence of transpiration as a second-order effect. Coefficients appearing in these expansions, can be found through the resolution of a forced Stokes problem over the roughness geometry.

Finally, and of interest for this thesis, homogenised boundary conditions do not appear to be suitable to study the laminar-turbulent transition. Indeed, early stability analyses considering the roughness in its full complexity (Luchini & Trombetta, 1995; Ehrenstein, 1996) exhibited a destabilising effect of the riblets on the flow stability while homogenised boundary conditions tend to stabilise it (Picella *et al.*, 2019; Xiong & Tao, 2020). This result was further confirmed by the group of Floryan which considered a large number of roughness shapes (Floryan, 1997*a*, 2007; Mohammadi & Floryan, 2013; Moradi & Floryan, 2014; Mohammadi *et al.*, 2015). Regarding SH surfaces, results on the transition to turbulence are more scarce, mostly due to two difficulties that need to be tackled: moving interfaces and the triple point (that is the contact point between the solid, liquid and gas phases),

whose dynamics remains an open question (de Gennes, 1985). Still, stability of the flow over a SH wall was studied through an homogenised approach in the works of Min & Kim (2005) and Pralits *et al.* (2017). In the case of geometrically complex (not homogenised) boundary conditions, flow stability was investigated numerically either through direct numerical simulation in the work of Picella *et al.* (2020), either through the resolution of a two-dimensional stability problem in Yu *et al.* (2016) and Tomlinson & Papageorgiou (2022) (albeit with no moving interfaces).

1.5 Research objectives and organisation of the manuscript

The present work is intended to shed some light on some interesting phenomena that may arise in spatially periodic systems. To this end, an alternative to the usual Floquet analysis is proposed in §2. In chapter §3, the framework is applied to secondary instabilities. It is first tested to cross-flow vortices and directly compared to a Floquet analysis. The second application is boundary layer streaks with an emphasis on the non-modal stability analysis. A case study of the flow transition over an anisotropic complex surface modelled with homogenised boundary conditions and based on the case from Pralits *et al.* (2017) is proposed in chapter §4. Two laminar-turbulent transition scenarii, corresponding to the two family of modes identified in the stability analysis, are investigated through direct numerical simulations via Nek5000. In chapter §5, flow stability over rough and superhydrophobic surfaces is investigated without the use of homogenised boundary conditions. Regarding SH surfaces, the idea is to extend the work of Picella *et al.* (2020) by considering the stability analysis of the flow over such surfaces. Finally, conclusions and perspectives are drawn in §6. More information on the numerical methods used throughout this work can be found in the appendices A and B.

Chapter 2

Hydrodynamic stability

Contents

In this section, several notions necessary to the study of fluid flows and laminar-to-turbulent transition will be presented. The core of this section will be dedicated to the theory of hydrodynamic instabilities which, as its name implies, aims at understanding the onset of turbulence in fluid flows. An overview of the theory and its numerous underlying concepts will be provided. The classic linear stability framework will be described together with the more recent non-modal tools such as transient growth or resolvent analyses. Considering a Newtonian and incompressible fluid with viscosity ν, the flow is governed by the Navier-Stokes equations (Navier, 1822):

$$\begin{cases} \dfrac{\partial \mathbf{U}}{\partial t} + \mathbf{U} \cdot \nabla \mathbf{U} = -\nabla P + \dfrac{1}{Re} \nabla^2 \mathbf{U} \\ \nabla \cdot \mathbf{U} = 0 \end{cases} \tag{2.1}$$

where $\mathbf{U}(\mathbf{x}, t)$ is the velocity vector and $P(\mathbf{x}, t)$ the pressure field. The Reynolds number $Re = Uh/\nu$ where U and h are respectively a characteristic velocity and length scale of the flow, is also

introduced. The first equation represents the conservation of momentum while the second enforces the incompressibility constraint.

2.1 Instability framework

The theoretical and numerical study of hydrodynamic instabilities are inherently linked to the concept of base flow and to the spectral properties of the associated linearised Navier-Stokes operator. Usually, the base flow is the laminar state from which transition to turbulence departs. Mathematically, it can be considered as a fixed point (in the case of a stationary solution) or a limit cycle (for periodic solutions) of the Navier-Stokes equations. Next, to investigate the stability of this base flow, say $\mathbf{Q}_0$, a perturbation $\mathbf{q}_1 = [u_1, v_1, w_1, p_1]^T$ is added to the system, such that $\mathbf{q} = \mathbf{Q}_0 + \mathbf{q}_1$. Assuming $\mathbf{q}_1$ is infinitesimal, the system (2.1) can be approximated by its first-order expansion around $\mathbf{Q}_0$, yielding the following linearised system:

$$\mathbf{B}\frac{\partial \mathbf{q}_1}{\partial t} = \mathbf{A}\mathbf{q}_1 \tag{2.2}$$

where $\mathbf{A}$ is the Jacobian of the system and $\mathbf{B} = \mathrm{diag}(1, 1, 1, 0)$. The composition of the Jacobian may vary greatly depending on the complexity of the base flow and the stability framework considered. To illustrate this point, a few general examples will be given in the next sections.

Starting from an initial perturbation $\mathbf{q}_1(0)$, the previous system (2.2) can be solved explicitly after being projected on a divergence-free space:

$$\mathbf{q}_1(T) = e^{\mathbf{A}T}\mathbf{q}_1(0) \tag{2.3}$$

The operator $\mathbf{M}(T) = e^{\mathbf{A}T}$ is often called the *exponential propagator* of the linearised system. As we will see in the next sections, the propagator plays a major role in both modal and non-modal stability analyses for periodic systems (either time- or spatially periodic).

2.1.1 Local stability analysis

The first step in understanding the instabilities that may arise is to investigate the transition to turbulence through local stability theory. For simplicity, it may be assumed that the wavelength of

the instability mechanism is small compared to the spatial scale characterising the flow development in the streamwise direction. Such an assumption is called the parallel flow hypothesis and yields to considering a simple one-dimensional base flows of the form $\mathbf{Q}_0 = [U_0(y), 0, W_0(y)]^T$. Poiseuille and Couette flows are canonical examples of strictly parallel base flows. Quasi-parallel base flows, where the (slow) streamwise evolution of the flow is neglected, also fall into this category. Examples of this type include the Blasius boundary layer or the wake flow. The base flow may also include a spanwise component W_0. The case of a swept wing, modelled with a Falkner-Skan-Cooke profile, will be of special interest in the context of this thesis. Both components only depend on the wall-normal coordinate, hence corresponding to a one-dimensional base flow. Introducing the previous base flow into the linearised Navier Stokes equations greatly reduces their complexity and yields:

$$\begin{cases} \dfrac{\partial u_1}{\partial t} = -v_1\dfrac{\partial U_0}{\partial y} - U_0\dfrac{\partial u_1}{\partial x} - W_0\dfrac{\partial w_1}{\partial z} - \dfrac{\partial p_1}{\partial x} + \dfrac{1}{Re}\nabla^2 u_1 \\ \dfrac{\partial v_1}{\partial t} = -U_0\dfrac{\partial v_1}{\partial x} - W_0\dfrac{\partial v_1}{\partial z} - \dfrac{\partial p_1}{\partial y} + \dfrac{1}{Re}\nabla^2 v_1 \\ \dfrac{\partial w_1}{\partial t} = -v_1\dfrac{\partial W_0}{\partial y} - U_0\dfrac{\partial w_1}{\partial x} - W_0\dfrac{\partial w_1}{\partial z} - \dfrac{\partial p_1}{\partial z} + \dfrac{1}{Re}\nabla^2 w_1 \\ \dfrac{\partial u_1}{\partial x} + \dfrac{\partial v_1}{\partial y} + \dfrac{\partial w_1}{\partial z} = 0 \end{cases} \tag{2.4}$$

The resulting system is homogeneous in both the streamwise and spanwise directions x and z and also in time. It can be further simplified by considering the perturbation as a superposition of propagating waves. This is usually denoted as a *normal mode expansion* and is mathematically equivalent to a separation of variables. Thus, the infinitesimal disturbance $\mathbf{q}_1 = [\mathbf{u}_1, p_1]^T$ takes the following form:

$$\mathbf{q}_1(x,y,z,t) = \int_{L_\omega}\int_{F_\alpha}\int_{F_\beta} \hat{\mathbf{q}}_1(y) e^{i\alpha x} e^{i\beta z} e^{-i\omega t} d\alpha d\beta d\omega + c.c. \tag{2.5}$$

where $c.c$ denotes the complex conjugate, α and β are respectively the streamwise and spanwise wavenumbers and ω a

$$\begin{cases} -i\omega\hat{u}_1 = -\hat{v}_1\dfrac{\partial U_0}{\partial y} - i\alpha U_0\hat{u}_1 - i\beta W_0\hat{u}_1 - i\alpha\hat{p}_1 + \dfrac{1}{Re}\nabla_\alpha^2\hat{u}_1 \\ -i\omega\hat{v}_1 = -i\alpha U_0\hat{v}_1 - i\beta W_0\hat{v}_1 - \dfrac{\partial\hat{p}_1}{\partial y} + \dfrac{1}{Re}\nabla_\alpha^2\hat{v}_1 \\ -i\omega\hat{w}_1 = -\hat{v}_1\dfrac{\partial W_0}{\partial y} - i\alpha U_0\hat{w}_1 - i\beta W_0\hat{w}_1 - i\beta\hat{p}_1 + \dfrac{1}{Re}\nabla_\alpha^2\hat{w}_1 \\ i\alpha\hat{u}_1 + \dfrac{\partial\hat{v}_1}{\partial y} + i\beta\hat{w}_1 = 0 \end{cases} \tag{2.6}$$

where $\nabla^2_\alpha \bullet = \left(\partial^2/\partial y^2 - \alpha^2 - \beta^2\right) \bullet$. The previous system can be recast into the more compact form 2.2, with the Jacobian of the system $\mathbf{A}$ such as:

$$\mathbf{A} = \begin{pmatrix} -i\alpha U_0 - i\beta W_0 + \dfrac{1}{Re}\nabla^2_\alpha & -\dfrac{\partial U_0}{\partial y} & 0 & -i\alpha \\ 0 & -i\alpha U_0 - i\beta W_0 + \dfrac{1}{Re}\nabla^2_\alpha & 0 & -\dfrac{\partial}{\partial y} \\ 0 & -\dfrac{\partial W_0}{\partial y} & -i\alpha U_0 - i\beta W_0 + \dfrac{1}{Re}\nabla^2_\alpha & -i\beta \\ i\alpha & \dfrac{\partial}{\partial y} & i\beta & 0 \end{pmatrix} \tag{2.7}$$

The system (2.6) falls into the framework of *local stability theory* and has been the subject of a large number of studies, both theoretical and numerical. Several type of analyses have emerged in order to investigate the properties of the system:

- Temporal stability analysis: $\alpha, \beta \in \mathbb{R}$, $\omega \in \mathbb{C}$. The temporal growth of a spatially periodic perturbation is investigated. This will be the formulation employed throughout this thesis.
- Spatial stability analysis: $\alpha, \beta \in \mathbb{C}$, $\omega \in \mathbb{R}$. This is also known as the signalling problem: the flow is excited by a time-harmonic localised forcing and the response to this forcing is investigated.
- Spatio-temporal analysis: $\alpha, \beta \in \mathbb{C}$, $\omega \in \mathbb{C}$. The flow response to a spatially and temporally localised impulse is investigated.

The two first analyses can be considered as different points of view of the same problem. The works of Michalke (1964, 1965) illustrates quite well these different methods in the case of a mixing layer while more recent developments can be found in the books of Schmid (2001) or Drazin & Reid (2004).

2.1.2 Short time dynamics and transient growth

Unfortunately, linear stability by itself is not sufficient to assess if the flow will transition. Consider the case of a plane Poiseuille flow: the base flow is strictly parallel and one-dimensional. The base flow has no spanwise component indicating the Squire's theorem is valid and the most unstable mode, for a fixed Reynolds number Re, is two-dimensional *i.e.* $\beta = 0$. In this context, Orszag (1971*a*)

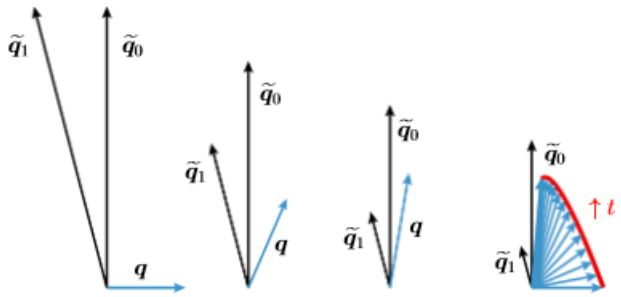

Figure 2.1: Illustration of the transient growth mechanism. Consider a non-normal system with two eigenvectors $\tilde{\mathbf{q}}_0$ and $\tilde{\mathbf{q}}_1$ and the vector $\tilde{\mathbf{q}}$ resulting from their difference. Since the system is non-normal, the eigenvectors $\tilde{\mathbf{q}}_0$ and $\tilde{\mathbf{q}}_1$ are not orthogonal. These eigenvectors are associated with negative eigenvalues, meaning that their magnitude will decrease with time without changing their direction. In the last sketch on the right, summarises the vector evolution over the course of time. From Schmid (2007).

determined the critical Reynolds number as $Re_c \approx 5772$. And yet, transition to turbulence have been observed for Reynolds numbers as low as $Re \approx 1000$ (Manneville, 2015). Initially, this discrepancy was ascribed to nonlinear effects neglected in traditional stability analysis. Nevertheless, nonlinear terms are conservative terms that deploy energy in all length scales of the flow through linear mechanisms (Henningson, 1996). This can be observed in the Orr-Reynolds energy equation (Schmid, 2001): the growth rate of a finite-amplitude disturbance can, at each instant of its evolution, be found from an infinitesimal disturbance with an identical shape. Thus, perturbation transient growth can only be explained by linear mechanisms not detected by the asymptotic approach of modal stability analysis.

The framework for computing transient energy growth was introduced in Farrell (1988), and shed some light on the strong transient effects occurring in the shear flows of Couette and Poiseuille. Later, Trefethen *et al.* (1993) and Schmid (2001) established a connection between transient effects and the non-normality of the Jacobian. The idea behind is rather simple and is illustrated in figure 2.1: the non-normality of the Jacobian implies the non-orthogonality of the eigenvectors, which may lead to a huge energy growth despite the eigenvalues having negative growth rate.

Thus, a non-modal analysis avoids the assumption of an exponential time-dependence $e^{-i\omega t}$ and, instead, reframes the stability problem into an optimisation one. Mathematically, we can define a time-dependent quantity of interest $G(T)$ to be optimised. In the present configuration, $G(T)$ will

describe the amplification of the kinetic energy of a disturbance after a time T:

$$G(t) = \max_{\mathbf{q_1(0)}} \frac{E(\mathbf{q}_1(T))}{E(\mathbf{q}_1(0))} = ||\exp(\mathbf{A}T)||_E^2 \tag{2.8}$$

where $E(\mathbf{q}_1(t)) = ||\mathbf{q}_1||_E = \int_V |\mathbf{u}_1^2| dV$ is the kinetic energy of the perturbation. Other quantities of interest, such as enstrophy or viscous dissipation, could be considered, depending on the case. Introducing the singular eigenvalue decomposition (SVD) of the exponential propagator $\mathbf{M}(T) = e^{\mathbf{A}T} = \mathbf{U}\mathbf{\Sigma}\mathbf{V}^H$, the gain $G(T)$ is given by the principal singular value $G(t) = \sigma_1^2$. The initial optimal perturbation $\mathbf{q}_{opt}(0)$ yielding the maximum gain and its response $\mathbf{q}_{opt}(T)$ at time T correspond respectively to the right and left singular eigenvectors associated with σ_1.

In parallel shear flows, two mechanisms responsible for the transient growth of the kinetic energy could be identified: the *lift-up effect* (Ellingsen & Palm, 1975) and the *Orr mechanism* (Orr, 1907*b*). The lift-up mechanism, originally identified in wall bounded shear flows (Landahl, 1975, 1980), is associated with pairs of counter-rotating streamwise vortices which lift up fluid of low momentum in high velocity regions and reciprocally move down high momentum fluid towards lower velocity regions, thus generating streamwise aligned layers of streamwise velocity perturbations, generally known as streamwise velocity streaks. The Orr mechanism (Orr, 1907*b*), prominent in shear layer flows, relies on the two-dimensional deformation of vortical structures by the mean flow. Structures which are initially aligned against the direction of the flow tend to realign themselves with it and, in doing so, generate transient growth through the concentration of vorticity. This effect is especially important in shear layer flows (Barkley *et al.*, 2008; Blackburn *et al.*, 2008; Cantwell *et al.*, 2010). More information on the concept of transient growth can be found in the review of Schmid (2007) while an up-to-date view on the two mechanisms can be found in the works of Brandt (2014) for the lift-up effect and Jiao *et al.* (2021) for the Orr mechanism.

2.1.3 Receptivity, optimal forcing and resolvent analysis

Until now, the concepts we introduced, either modal or non-modal, dealt with the evolution in time of a perturbation. But nothing has been said on the mechanisms that generate these perturbations. This question may be partially answered through a receptivity analysis. The receptivity framework, similar to the one for transient growth, will be quickly described in the following. The reader is referred to the reviews of Schmid (2007) and Jovanović (2021) for full detail. Consider the linear

system (2.2) which is now forced by an harmonic forcing $\mathbf{f}_1 = \hat{\mathbf{f}}_1 e^{i\omega t}$. We are interested in the forcing which yields the maximum response in the flow. As previously, mathematically, an optimal quantity to be optimised can be defined as:

$$H(\omega) = \max_{\mathbf{f_1}} \frac{E(\mathbf{q}_1)}{E(\mathbf{f}_1)} = ||(i\omega\mathbf{I} - \mathbf{A})^{-1}||_E^2, \tag{2.9}$$

which is called the resolvent operator, that can be decomposed via an SVD. Energy amplification between a forcing and its response in the flow is dictated by the largest singular value while optimal forcings and responses correspond respectively to the left and right singular eigenvectors associated with the largest singular value. The receptivity framework is quite versatile as the forcing $\mathbf{f}_1$ may represent any type of external body forces or perturbations. For example, in boundary layers, transition may arise from acoustic disturbances, free-stream perturbations or isolated roughnesses among many other possible disturbances. However, the flow will respond differently to each type of perturbation, eventually causing different routes to transition. These matters have been discussed in depth in the reviews of Kerschen (1989) and Saric *et al.* (2002). More recent applications of the framework considered complex spatially evolving base flows as in the work of Sipp *et al.* (2010) and made the link with the previous concepts of local/global stability analysis (Bagheri *et al.*, 2009). Eventually, for turbulent flows, a receptivity analysis based on a mean flow (Beneddine *et al.*, 2016) and with the forcing $\mathbf{f}_1$ used as a proxy for nonlinear terms of the (turbulent) Navier-Stokes equations may shed some light on the mechanisms sustaining turbulence (McKeon & Sharma, 2010*a*) or on large-scale noise-generating coherent structures (Lesshafft *et al.*, 2019).

2.2 Two-dimensional local stability analysis

So far, we have assumed a one-dimensional base flow of the form $\mathbf{Q_0} = [U_0(y), 0, W_0(y)]^T$. It is possible to extend these concepts to two-dimensional base flows evolving, for example, in the wall-normal and spanwise directions. The base flow now takes the following form $\mathbf{Q_0} = [U_0(y,z), 0, W_0(y,z)]^T$. The linearised Navier-Stokes equation now takes the following form:

$$\begin{cases} \dfrac{\partial u}{\partial t} = -v\dfrac{\partial U_0}{\partial y} - w\dfrac{\partial U_0}{\partial z} - U_0\dfrac{\partial u}{\partial x} - W_0\dfrac{\partial u}{\partial z} - \dfrac{\partial p}{\partial x} + \dfrac{1}{Re}\nabla^2 u \\ \dfrac{\partial v}{\partial t} = -U_0\dfrac{\partial v}{\partial x} - W_0\dfrac{\partial v}{\partial z} - \dfrac{\partial p}{\partial y} + \dfrac{1}{Re}\nabla^2 v \\ \dfrac{\partial w}{\partial t} = -v\dfrac{\partial W_0}{\partial y} - w\dfrac{\partial W_0}{\partial z} - U_0\dfrac{\partial w}{\partial x} - W_0\dfrac{\partial w}{\partial z} - \dfrac{\partial p}{\partial z} + \dfrac{1}{Re}\nabla^2 w \\ \dfrac{\partial u}{\partial x} + \dfrac{\partial v}{\partial y} + \dfrac{\partial w}{\partial z} = 0 \end{cases} \tag{2.10}$$

As these equations are no longer homogeneous in the spanwise direction and the modal expansion is adapted in consequence:

$$\mathbf{q}(x,y,z,t) = \int_{L_\omega}\int_{\alpha} \hat{\mathbf{q}}(y,z)e^{i\alpha x - i\omega t}d\alpha d\omega + c.c \tag{2.11}$$

Introducing this normal mode expansion into the linearised equation (2.10) gives:

$$\begin{cases} -i\omega\hat{u} = -\hat{v}\dfrac{\partial U_0}{\partial y} - \hat{w}\dfrac{\partial U_0}{\partial z} - i\alpha U_0\hat{u} - W_0\dfrac{\partial \hat{u}}{\partial z} - i\alpha\hat{p} + \dfrac{1}{Re}\nabla_\alpha^2\hat{u} \\ -i\omega\hat{v} = -i\alpha U_0\hat{v} - W_0\dfrac{\partial \hat{v}}{\partial z} - \dfrac{\partial \hat{p}}{\partial y} + \dfrac{1}{Re}\nabla_\alpha^2\hat{v} \\ -i\omega\hat{w} = -\hat{v}\dfrac{\partial W_0}{\partial y} - \hat{w}\dfrac{\partial W_0}{\partial z} - i\alpha U_0\hat{w} - W_0\dfrac{\partial \hat{w}}{\partial z} - \dfrac{\partial \hat{p}}{\partial z} + \dfrac{1}{Re}\nabla_\alpha^2\hat{w} \\ i\alpha\hat{u} + \dfrac{\partial \hat{v}}{\partial y} + \dfrac{\partial \hat{w}}{\partial z} = 0 \end{cases} \tag{2.12}$$

where $\nabla_\alpha^2 \bullet = \left(\partial^2/\partial y^2 + \partial^2/\partial z^2 - \alpha^2\right)\bullet$. Both temporal and spatial stability can be investigated. In the case of temporal stability, which is the framework used throughout this thesis, the system can be recast into a linear generalised eigenvalue problem of the form:

$$-i\omega\mathbf{B}\hat{\mathbf{q}} = \mathbf{A}\hat{\mathbf{q}} \tag{2.13}$$

where $\mathbf{B} = \mathrm{diag}(1,1,1,0)$ and $\mathbf{A}$ the Jacobian of the system given by:

$$\mathbf{A} = \begin{pmatrix} -i\alpha U_0 - W_0\dfrac{\partial}{\partial z} + \dfrac{1}{Re}\nabla_\alpha^2 & -\dfrac{\partial U_0}{\partial y} & -\dfrac{\partial U_0}{\partial z} & -i\alpha \\ 0 & -i\alpha U_0 - W_0\dfrac{\partial}{\partial z} + \dfrac{1}{Re}\nabla_\alpha^2 & 0 & -\dfrac{\partial}{\partial y} \\ 0 & -\dfrac{\partial W_0}{\partial y} & -i\alpha U_0 - W_0\dfrac{\partial}{\partial z} - \dfrac{\partial W_0}{\partial z} + \dfrac{1}{Re}\nabla_\alpha^2 & -\dfrac{\partial}{\partial z} \\ i\alpha & \dfrac{\partial}{\partial y} & \dfrac{\partial}{\partial z} & 0 \end{pmatrix} \tag{2.14}$$

As for the local 1D stability analysis, the linear asymptotic stability of the base flow $\mathbf{Q}_0$ is dictated by the sign of the real part of $-i\omega$: if it is positive, the perturbation will grow exponentially in time and the base flow $\mathbf{Q}_0$ is asymptotically unstable and conversely, if it is negative, the perturbation will decay exponentially in time and the base flow $\mathbf{Q}_0$ is asymptotically stable.

This type of stability analysis may somehow be related to the biglobal instability framework of Theofilis (2003). However, an important distinction lies in the fact that the two spatial directions of the eigenvectors are orthogonal to the direction of advection, which remains homogeneous. The parallel flow assumption is still used and no streamwise evolution of the base flow can be taken into account.

2.3 Linear instability of n-periodic systems

2.3.1 Floquet theory

A very useful tool for the study of periodic systems is the Floquet theory (Floquet, 1883). It will be quickly described in its most common formulation, that is for time-periodic systems. Its spatial formulation, which is used throughout this thesis, is detailed right after. For a general review on the theory and its concepts, the reader is referred to the book of Kuchment (1993). Applications to fluid mechanics can be found, for example, in the works of Barkley & Henderson (1996) and Rolandi (2021) for the temporal framework and in the book of Schmid (2001) for its spatial counterpart.

↪ *Temporal framework*

Suppose we are interested in the stability of a system described by its T-periodic Jacobian $\mathbf{A}$, in the following general form:

$$\mathbf{B}\frac{\partial \mathbf{q}_1}{\partial t} = \mathbf{A}\mathbf{q}_1 \tag{2.15}$$

with $\mathbf{B} = \mathrm{diag}[1, 1, 1, 0]$. Floquet analysis relates the study of the stability of a limit cycle to that of a fixed point through the so-called Poincaré map. The stability of the system can be deduced by looking at the evolution of the points of the Poincaré map. Introducing the Floquet transition matrix $\phi(0, T)$ that relates the state of the system at time $t = 0$ and $t = T$, we have:

$$\mathbf{q}_1(T) = \phi(0,T)\mathbf{q}_1(0) \tag{2.16}$$

On the other hand, 2.15 can be solved to yield $\mathbf{q}_1(t) = e^{At}\mathbf{q}_1(0)$. The eigenvalues ω of the exponential propagator matrix $\mathbf{M} = e^{\mathbf{A}t}$ and the eigenvalues μ of the Floquet transition matrix $\phi(0,T)$, also called the Floquet multipliers, are thus related through the following expression:

$$\mu = e^{\omega T} \tag{2.17}$$

Ultimately, stability can be obtained from the sign of the real part of ω or from the modulus of μ: if $\omega_r \leq 0$ or $|\mu| > 1$, the system is unstable and conversely. Of importance also is the way the characteristic multipliers will cross the unit circle. Several cases, yielding different bifurcations of the limit cycle and summarised in figure 2.2, can be considered:

- when $\mu = +1$, the limit cycle presents a saddle-node bifurcation and a new stable periodic orbit emerges with the same periodicity of the original orbit.
- when $\mu = -1$, the system presents a period doubling bifurcation: the new orbit has twice the periodicity of the original orbit.
- when $\mu \neq \pm 1$, a new frequency ω_i appears. The new periodic orbit can be then visualised as lying on a torus with periodicity $2\pi/\omega_i$. This bifurcation is called Secondary Hopf bifurcation or Neimark–Sacker bifurcation.

↪ *Spatial framework*

Consider now that the system 2.15 is spatially periodic in the spanwise direction with wavelength L_z and a corresponding wavenumber $\beta_0 = 2\pi/L_z$. The perturbation $\mathbf{q}_1$ can be expanded in so-called Bloch waves, which take the following form:

$$\mathbf{q}_1(x,y,z,t) = \hat{\mathbf{q}}_2(y,z)e^{\gamma z}e^{\sigma t}e^{i\alpha x} \tag{2.18}$$

where $\gamma = \gamma_r + i\gamma_i$ is the Bloch exponent, $\sigma = \sigma_r + i\sigma_i$ is the circular frequency and $\hat{\mathbf{q}}_2(y,z)$ is a periodic function with period $2\pi/\beta_0$. This expression can be further developed by Fourier transforming $\hat{\mathbf{q}}_2(y,z)$ and one can obtain:

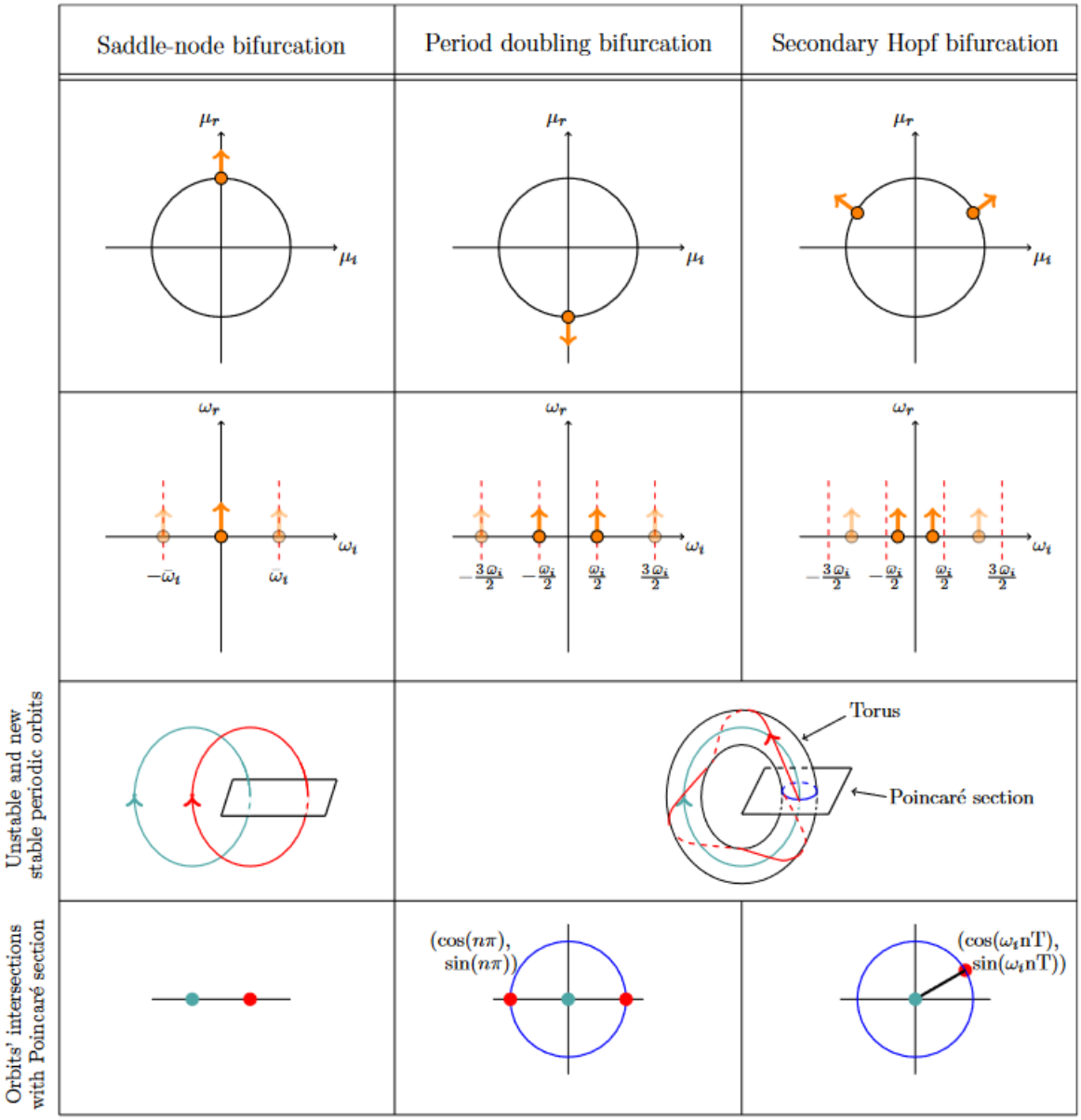

Figure 2.2: Bifurcations of a periodic limit cycle through the Floquet multipliers μ (first row) and eigenvalues of the Jacobian matrix ω (second row). Visualization of the unstable periodic solution represented in green with the resulting stable one in red (third row) and the asymptotic intersections of trajectories with the Poincaré section (fourth row), $n \in \mathbb{N}$. From Rolandi (2021).

$$\mathbf{q}_2(x, y, z, t) = e^{\gamma z} e^{\sigma t} e^{i\alpha x} \sum_m \tilde{\mathbf{q}}_2^m(y) e^{im\beta_0 z} \tag{2.19}$$

As per the local stability analysis, a framework, whether spatial or temporal, must be chosen to

clear the ambiguity and close the equations. More precisely, σ_r and γ_r are associated respectively with the growth of the perturbations in time and space.

It can also be seen that γ and $\gamma \pm in\beta_0$ yield the same eigenvalues for any positive integer n. Thus, investigation of the imaginary part of the Floquet exponent γ_i can be restricted to the range $-\beta_0/2 < \gamma_i \leq \beta_0/2$. Introducing the detuning factor $\epsilon = \gamma_i/\beta_0$, three :

- fundamental modes corresponding to $\epsilon = 0$,

$$\mathbf{q}_2(x, y, z, t) = e^{\sigma t} e^{i\alpha x} \sum_m \tilde{\mathbf{q}}_2^m(y) e^{im\beta_0 z} \tag{2.20}$$

- subharmonic modes corresponding to $\epsilon = 1/2$,

$$\mathbf{q}_2(x, y, z, t) = e^{\sigma t} e^{i\alpha x} \sum_m \tilde{\mathbf{q}}_2^m(y) e^{i(m+\frac{1}{2})\beta_0 z} \tag{2.21}$$

- detuned modes corresponding to $0 < \epsilon \leq 1/2$,

$$\mathbf{q}_2(x, y, z, t) = e^{\sigma t} e^{i\alpha x} \sum_m \tilde{\mathbf{q}}_2^m(y) e^{i(m+\epsilon)\beta_0 z} \tag{2.22}$$

The spatial Floquet theory behaves in a similar way than its temporal counterpart: in the case of a fundamental instability, the spatial period of the secondary modes is equal to the spatial period of the primary instability, as in the case of a saddle-node bifurcation. The subharmonic instability is twice the one of the primary, indicating a period doubling bifurcation. Other spatial periods for the secondary modes can be reached through variation of the detuning factor ϵ. Physically, detuned modes can only exist as the superposition of two complex conjugate modes with opposite detuning as for a secondary Hopf bifurcation. Concepts of non modal analysis and local/global instabilities can also be defined for spatially periodic systems. Transient growth can be easily found for periodic base flows by replacing the Jacobian matrix with a monodromy matrix (Schmid, 2007) while the ideas behind the local/global distinction were extended to spatially periodic configurations in the work of Brevdo *et al.* (1996); Brevdo & Bridges (1997). Originally, the spatial Floquet framework was applied to very simple, mostly theoretical flows (Beaumont, 1981; Gotoh *et al.*, 1983). Later, through the works of (Herbert, 1983, 1985), it became an indispensable tool in the study of secondary instabilities.

2.3.2 Circulant matrices and Bloch wave formalism

The Bloch wave formalism which will be developed in the following originates from the field of solid-state physics and the work of Brillouin (1953). It was used notably to solve the Schrodinger equation in a periodic potential, as a model for the propagation of waves in a crystal lattice. The framework was later used to study the vibration in rotationally periodic assembly of bladed discs (Ewins, 1973). For a recent review on the theory in the context of vibrational analysis, the reader is referred to Olson *et al.* (2014). In the context of fluid mechanics, this formalism was introduced in the work of Schmid *et al.* (2017) in which it was applied to the stability of a system of n turbine blades. It was later applied to investigate the stability in configurations as diverse as three-dimensional transonic buffet (Paladini *et al.*, 2019), annular combustors (Murthy *et al.*, 2019) and rough hypersonic boundary layer (Margaritis *et al.*, 2022).

Mathematically, the disturbance equations can be recast under the following form:

$$\frac{\partial}{\partial t}\begin{pmatrix} \mathbf{q}_2^0 \\ \mathbf{q}_2^1 \\ \vdots \\ \mathbf{q}_2^{n-1} \end{pmatrix} = \underbrace{\begin{pmatrix} \mathbf{A}_0 & \mathbf{A}_1 & \dots & \mathbf{A}_{n-1} \\ \mathbf{A}_{n-1} & \mathbf{A}_0 & \dots & \mathbf{A}_{n-2} \\ \vdots & \vdots & & \vdots \\ \mathbf{A}_1 & \mathbf{A}_2 & \dots & \mathbf{A}_0 \end{pmatrix}}_{\mathbf{A}} \underbrace{\begin{pmatrix} \mathbf{q}_2^0 \\ \mathbf{q}_2^1 \\ \vdots \\ \mathbf{q}_2^{n-1} \end{pmatrix}}_{\mathbf{q}_2} \tag{2.23}$$

with $\mathbf{A}'$ the Jacobian associated to the full stability problem, which is composed of the matrices $\mathbf{A}_0$ and $\mathbf{A}_j$ (for $j = 1, ..., n-1$) describing respectively the dynamics in a sub-unit and the coupling interactions between sub-units. The secondary disturbance state vector in the j^{th} sub-unit is denoted as $\mathbf{q}_2^j$. The Jacobian matrix $\mathbf{A}$ is block-circulant due to the specific n-periodic nature of the system and can become block-diagonal through the similarity transformation:

$$\mathbf{P}^H \mathbf{A}' \mathbf{P} = \text{diag}(\hat{\mathbf{A}}_0, \hat{\mathbf{A}}_1, ..., \hat{\mathbf{A}}_{n-1}) \equiv \hat{\mathbf{A}} \tag{2.24}$$

The transfer matrix $\mathbf{P}$ can be found analytically as:

$$\mathbf{P} = \mathbf{J} \otimes \mathbf{I} \tag{2.25}$$

with $\mathbf{J}$ a matrix such as $\mathbf{J}_{j+1,k+1} = \rho_j^k/\sqrt{n}$ for $j, k = 1, ..., n-1$ and $\rho_j = \exp(2i\pi j/n)$ the n^{th} roots of unity. The symbol $\otimes$ denotes the usual Kronecker product and $\mathbf{I}$ the identity matrix. With

this transformation, the linear stability problem has been reduced to the study of n smaller sub-systems characterised by the matrices $\hat{\mathbf{A}}_j$. Hence, the full spectrum of the matrix $\mathbf{A}$ can be found merging the n spectra of $\hat{\mathbf{A}}_j$ for $j = 1, ..., n-1$. Similarly, provided $\mathbf{v}_j$ is an eigenvector of $\hat{\mathbf{A}}_j$, the eigenfunctions of the full system can be retrieved and take the form $[\mathbf{v}_j, \rho_j \mathbf{v}_j, \rho_j^2 \mathbf{v}_j, ..., \rho_j^{n-1} \mathbf{v}_j]^T$ for $j = 1, ..., n-1$. Due to their specific structure, it can be shown that eigenvectors are linearly independent. The demonstration can be found in Schmid *et al.* (2017) and is reproduced here for the sake of completeness. We want to calculate the scalar product of two eigenvectors $\mathbf{q}_j$ and $\mathbf{q}_k$ associated respectively with the roots-of-unity ρ_j and ρ_k. Introducing $\mathbf{v}_j$ and $\mathbf{v}_k$ the eigenvectors of $\hat{\mathbf{A}}_j$ and $\hat{\mathbf{A}}_k$, we have:

$$\mathbf{q}_j \mathbf{Q} \mathbf{q}_k = \begin{pmatrix} \mathbf{v}_j \\ \rho_j \mathbf{v}_j \\ \vdots \\ \rho_j^{n-1} \mathbf{v}_j \end{pmatrix}^H \begin{pmatrix} \mathbf{Q}_0 & & & \\ & \mathbf{Q}_0 & & \\ & & \ddots & \\ & & & \mathbf{Q}_0 \end{pmatrix} \begin{pmatrix} \mathbf{v}_k \\ \rho_k \mathbf{v}_k \\ \vdots \\ \rho_k^{n-1} \mathbf{v}_k \end{pmatrix}^H \tag{2.26}$$

$$= (1 + \xi + \ldots + \xi^{n-1}) \mathbf{v}_j^H \mathbf{Q}_0 \mathbf{v}_k \tag{2.27}$$

$$= \frac{1 - \xi^n}{1 - \xi} \mathbf{v}_j^H \mathbf{Q}_0 \mathbf{v}_k \tag{2.28}$$

where $\xi = \rho_j^* \rho_k = e^{2\pi i (k-j)/n}$, $\mathbf{Q}_0$ is the weight matrix on a sub-unit and $\mathbf{Q} = \mathrm{diag}(\mathbf{Q}_0, \ldots, \mathbf{Q}_0)$ is the weight matrix of the full system. Observing that $\xi^n = 1$ for $j \neq k$, the last expression in 2.28 is equal to zero which concludes the demonstration.

Physically, the argument θ_j of the root-of-unity ρ_j acts as a phase shift between the different sub-units: the farther it is from 0 (or 2π), the more desynchronised the collective mode is. Thus, the eigenfunction $\mathbf{v}_j$, after each sub-unit, is phase shifted by $\theta_j = \arg(\rho_j) = 2\pi j/n$, meaning that after $n_j = 2\pi/\theta_j = n/j$ sub-units, the cumulative phase shift will exceed 2π, giving an estimate of the effective fundamental period of the eigenfunction of the full system. Associated with this number of coupled sub-units, the fundamental wavenumber of the mode can be retrieved and is equal to $\beta_{eff} = n\beta_0/j$. The equivalence with the Floquet analysis and the detuning factor ϵ can be precised. After Fourier expanding the base flow, it can be found (see Schmid (2001) for example) that the secondary disturbance has the following modal expansion:

$$\mathbf{q}_2(x, y, z, t) = e^{\sigma t} e^{i\alpha x} \sum_m \hat{\mathbf{q}}_m(y) e^{i(m+\epsilon)\beta_0 z} \tag{2.29}$$

The fundamental wavenumber ($m = 0$) of the resulting mode is $\epsilon_j \beta_0$ which gives, after equating with the one found for an eigenmode with root-of-unity ρ_j, $\epsilon_j = 1/n_j = j/n$. Reintroducing the expression of the detuning factor into the Floquet modal expansion yields for $j = 1, ..., N-1$:

$$\mathbf{q}_2^j(x,y,z,t) = e^{\sigma t} e^{i\alpha x} e^{ij\frac{\beta_0}{n}z} \sum_m \hat{\mathbf{q}}_m(y) e^{im\beta_0 z} \tag{2.30}$$

$$= e^{\sigma t} e^{i\alpha x} e^{ij\frac{\beta_0}{n}z} \tilde{\mathbf{q}}(y,z) \tag{2.31}$$

$$= e^{ik_j z} \tilde{\mathbf{q}}_2(x,y,z,t) \tag{2.32}$$

where $k_j = \epsilon_j \beta_0 = j\beta_0/n$ is the Bloch wavenumber and $\tilde{\mathbf{q}}_2(x,y,z,t)$ is a $2\pi/\beta_0$-periodic function. Thus, the Bloch theorem for the system with the n sub-units is retrieved.

In the case of nearest-neighbour coupling, rather common in many applications, the Jacobian $\mathbf{A}'$ reduces to a block-tridiagonal matrix. Only a three-unit system $\mathbf{A}_0, \mathbf{A}_1, \mathbf{A}_2$ needs to be discretized and processed, significantly reducing the complexity and computational cost of the method. Both temporal and spatial approaches for the stability problem can be considered.

Ultimately, transient growth and resolvent analyses (Schmid, 2007) can also be realised within the same framework. Note that transient effects may arise from the superposition of modal solutions within a single sub-unit, or as the superposition of modal solutions from all sub-units. The latter is especially interesting as it may involve cross-unit dynamics. Thus, introducing an harmonic forcing of the form $\mathbf{f} = \hat{\mathbf{f}} e^{i\omega t}$, the system (2.2) takes the following form:

$$\mathbf{B}\frac{\partial \mathbf{q}_1}{\partial t} = \mathbf{A}\mathbf{q}_1 + \mathbf{f} \tag{2.33}$$

with $\mathbf{B} = \mathrm{diag}[1,1,1,0]$. As previously defined, the maximum amplification $G(t)$ and optimal frequency response $H(\omega)$ are then given by:

$$G(t) = \max_{\mathbf{q_1(0)}} \frac{E(\mathbf{q}_1(t))}{E(\mathbf{q}_1(0))} = ||\exp(\mathbf{A}t)||_E^2, \quad H(\omega) = \max_{\mathbf{f}} \frac{E(\mathbf{q}_1(t))}{E(\mathbf{f})} = ||(i\omega\mathbf{I} - \mathbf{A})^{-1}||_E^2 \tag{2.34}$$

where $E(\mathbf{q}_1(t)) = ||\mathbf{q}_1||_E = \int_V |\mathbf{u}_1^2| dV$ is the kinetic energy of the perturbation. As previously stated, other quantities of interest could also be considered. Numerically, the norm is defined through the imposition of a weight matrix $\mathbf{Q}_0$, identical for each sub-system.

Besides amplification curves, 'optimal' perturbation $\mathbf{u}_{\text{opt}}$ and forcing $\mathbf{f}_{\text{opt}}$ yielding respectively the maximum energy growth and maximum response at a target time T can also be obtained (Luchini, 2000; Schmid, 2007). These disturbances can be retrieved through a singular value decomposition (Schmid & Brandt, 2014; Schmid *et al.*, 2017) defined as follows:

$$\mathbf{U}_j \Sigma_j \mathbf{V}_j^H = \text{SVD}[\mathbf{F_0} f(\hat{\mathbf{A}}_j) \mathbf{F_0}^{-1}] \tag{2.35}$$

where f is defined as $f(\mathbf{A}) = \exp(\mathbf{A}t)$ for the optimal perturbation and as $f(\mathbf{A}) = (i\omega\mathbf{I} - \mathbf{A})^{-1}$ for the optimal forcing. As per the linear stability eigenfunctions, principal left and right singular vectors, representing optimal perturbation (or forcing depending on f) at initial and target times, take the following form:

$$\mathbf{u}_{\text{opt}}(0) = \begin{pmatrix} \mathbf{u}_j \\ \rho_j \mathbf{u}_j \\ \rho_j^2 \mathbf{u}_j \\ \vdots \\ \rho_j^{n-1} \mathbf{u}_j \end{pmatrix}, \qquad \mathbf{u}_{\text{opt}}^H(T) = \begin{pmatrix} \mathbf{v}_j^H \\ \rho_j \mathbf{v}_j^H \\ \rho_j^2 \mathbf{v}_j^H \\ \vdots \\ \rho_j^{n-1} \mathbf{v}_j^H \end{pmatrix} \tag{2.36}$$

where ρ_j is the root-of-unity yielding the largest singular value. As for the linear stability analysis, optimal perturbations and forcings can be now obtained for the whole system by calculating the singular value decomposition associated with the n smaller sub-systems. Further information on the spectral methods or their use in the Bloch-wave formalism can be found in Appendix A.

Chapter 3

Secondary instabilities: application to cross flow vortices and boundary layer streaks

Contents

3.1 Problem formulation

The idea in this section will be to adapt the framework described in chapter 2 to the study of secondary instabilities. Thus, let us consider a general, time-evolving system of the form:

$$\frac{\partial \mathbf{Q}}{\partial t} = \mathbf{F}(\mathbf{x}, t; \mathbf{Q}) \tag{3.1}$$

where $\mathbf{Q}$ is the state vector, $\mathbf{F}$ a non-linear operator and $\mathbf{x} = (x, y, z)$ is the spatial coordinates vector. The flow is decomposed into a base flow $\mathbf{Q}_0\,(y)$, assumed to be locally parallel, and a small primary disturbance $\mathbf{q_1}(\mathbf{x}, t)$, such that $\mathbf{Q}(\mathbf{x}, t) = \mathbf{Q}_0(y) + \mathbf{q_1}(\mathbf{x}, t)$. Substituting the previous decomposition

into Eq.(3.1) and neglecting nonlinear terms results in the following system for the perturbation:

$$\frac{\partial \mathbf{q}_1}{\partial t} = \mathbf{A}\mathbf{q}_1 \tag{3.2}$$

with $\mathbf{A}$ the Jacobian of the system. Assuming normal modes of the form

$$\mathbf{q}_1(\mathbf{x}, t) = \tilde{\mathbf{q}}_1(y) \exp\left[i(\alpha x + \beta z - \omega t)\right],$$

modal and non modal stability analysis can be performed, identifying specific waves of interest, with wavenumbers (α, β) and frequency ω.

From there, following Herbert (1985), the secondary base flow $\mathbf{Q}_1$ is defined as the superposition of the primary disturbance of interest $\mathbf{q}_1$, with amplitude A, and the primary base flow $\mathbf{Q}_0$, such that $\mathbf{Q}_1(\mathbf{x}, t) = \mathbf{Q}_0(y) + A\mathbf{q}_1(\mathbf{x}, t)$. If necessary, we also introduce a new Galilean coordinate system (x_v, y, z_v) normal to the wave vector $\mathbf{k} = (\alpha, \beta)^T$ of the primary disturbance moving with phase speed $c = \omega_i/||\mathbf{k}||$ in the z_v-direction. The passage from one coordinate system to the other can be performed through the following Squire transform: $x_v(t) = \beta/||\mathbf{k}||x - \alpha/||\mathbf{k}||z$ and $z_v(t) = \alpha/||\mathbf{k}||x + \beta/||\mathbf{k}||z - ct$. In this new frame, the secondary base flow $\mathbf{Q}_1(y, z_v)$ is stationary, streamwise independent and $2\pi/||\mathbf{k}||$-periodic in the spanwise direction z_v. In the wave-oriented reference frame, the flow is decomposed into the secondary base flow $\mathbf{Q}_1(y, z_v)$ and a small secondary perturbation $\mathbf{q}_2(x_v, y, z_v, t)$ such as $\mathbf{Q}(x_v, y, z_v, t) = \mathbf{Q}_1(y, z_v) + \mathbf{q}_2(x_v, y, z_v, t)$. This formulation requires the shape assumption to be valid. Potentially, the base flow for secondary stability analysis can be retrieved by other means, such as parabolised stability equations or direct extraction from a numerical simulation. The key point is to guarantee the spatial periodicity of the secondary base flow on the sub-units. Modal secondary perturbations are assumed:

$$\mathbf{q}_2(x_v, y, z_v, t) = \tilde{\mathbf{q}}_2(y, z_v) e^{i\alpha_v x_v} e^{\sigma t}$$

with α_v and σ being respectively the streamwise wavenumber and the circular frequency. In the classical theory of secondary stability, Floquet analysis would be applied on the secondary base flow $\mathbf{Q}_1$. Instead, we want to take advantage of the periodicity induced by the primary flow structures to apply the Bloch wave framework. Thus, consider a fluid system composed of the repetition in the spanwise direction z_v of the secondary base flow $\mathbf{Q}_1$ over n sub-units of length $2\pi/||\mathbf{k}||$. The Navier-Stokes equations are then linearised around the $2\pi/||\mathbf{k}||$-periodic base flow $\mathbf{Q}_1(y, z_v)$. The ansatz for the secondary disturbance is introduced, yielding a two-dimensional local stability problem with $2\pi/||\mathbf{k}||$-periodic coefficients which can be found in section 2.2.

3.2 Linear stability of cross-flow vortices

This first application of the described framework is dedicated to cross-flow vortices in a swept boundary layer. This case has been the subject of a number of studies (Fischer & Dallmann, 1991; Wassermann & Kloker, 2002, 2003; Bonfigli & Kloker, 2007; Serpieri & Kotsonis, 2016), and the mechanisms underlying the secondary instabilities are now rather well understood. The flow can be modelled in a simple way through a Falkner-Skan-Cooke boundary layer on which is superimposed the most unstable primary perturbation. This has already been realised in the work of Fischer & Dallmann (1991) where a spatial Floquet analysis was used to study the secondary instability. From this analysis, the existence of a detuned mode was demonstrated, which was later found to be related to *type-III* modes (Malik *et al.*, 1994). Recently, this configuration was reconsidered experimentally in the work of Serpieri & Kotsonis (2016); Serpieri (2018). POD decomposition retrieved the *type-III* mode found with the Floquet analysis, but also shed some light on a more energetic, low-frequency mode which appeared to be missed by secondary instability analysis. Thus, the idea of this section is to compare the Bloch waves framework with the Floquet analysis of Fischer & Dallmann (1991), check if the original detuned *type-III* mode is retrieved and find if the POD mode found by Serpieri (2018) is captured with the adopted framework. All the stability results hereafter are obtained using a temporal approach ($\omega, \sigma \in \mathbb{C}$). The secondary stability problem is tackled considering the nearest-neighbour coupling assumption.

3.2.1 Primary stability analysis

In the following, we consider the incompressible flow over an infinite swept flat plate with an imposed negative pressure gradient (i.e. decreasing pressure in the chordwise direction). The laminar base flow $\mathbf{Q}_0 = [U_0(y), 0, W_0(y)]^T$ is modelled with a Falkner-Skan-Cook profile (Falkner & Skan, 1931; Cooke, 1950). Precisely, introducing f and g such that $U_0(y) = f'(y)\cos\theta$ and $W_0(y) = g(y)\sin\theta$, we have:

$$(2-\beta_H)f''' + ff'' + \beta_H\left[1-(f')^2\right] = 0 \tag{3.3}$$

$$(2-\beta_H)g'' + fg' = 0, \tag{3.4}$$

where the Hartree dimensionless pressure-gradient parameter (β_H), the local sweep angle and the local Reynolds number are set respectively to $\beta_H = 0.630$, $\theta = 46.9°$ and $Re_\delta = 826$. These parameters

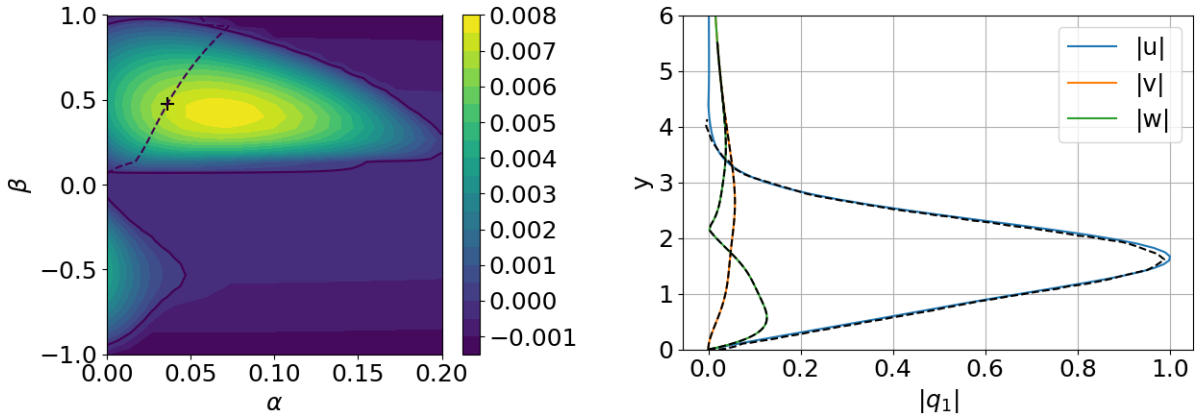

Figure 3.1: Left: Neutral curve of the swept boundary layer for $Re_\delta = 826$. The dashed line corresponds to stationary disturbances, i.e., $\omega_i = 0$. Right: Absolute value of the eigenfunctions for $Re_\delta = 826$, $\alpha = 0.0361$ and $\beta = 0.4774$ ($\Psi = \arctan(\beta/\alpha) = 89.9^o$). The dashed lines are extracted from Fischer & Dallmann (1991).

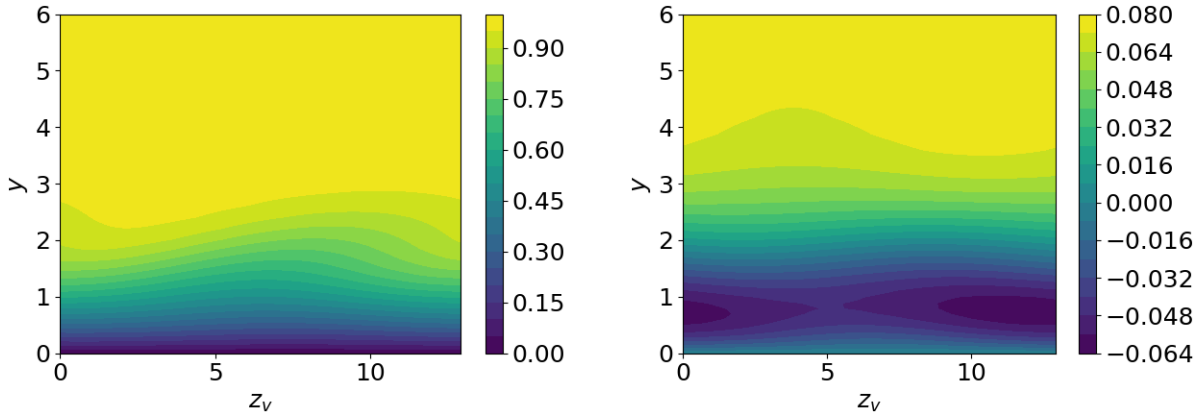

Figure 3.2: Secondary base flow $U_1(y, z_v)$ (left) and $W_1(y, z_v)$ (right) in the wave-oriented reference frame, for one sub-unit. The wall-normal component V_1 is non-zero but is one order of magnitude smaller than W_1, thus it is not shown.

are taken directly from Fischer & Dallmann (1991), and set to fit qualitatively experimental results from Müller (1990). Assuming wave-like solutions for the disturbances, modal stability analysis is performed for this configuration. Stationary disturbances maximising the temporal growth rate with respect to the streamwise and spanwise wavenumbers α and β are sought. Figure 3.1 exhibits the neutral curve of the primary instability. Since Squire's theorem is not valid for three-dimensional flows (see Pralits *et al.* (2017) for an example), the $\beta < 0$ plane was also investigated for the sake of completeness. The maximum growth rate for stationary disturbances is reached for $(\alpha, \beta) = (0.0361, 0.4774)$. The eigenfunctions of this mode are displayed in figure 3.1 (right). A second instability region appears as well, albeit with lower growth rates and no stationary disturbances. The agreement with the results found in Fischer & Dallmann (1991) is excellent.

3.2.2 Secondary stability of cross-flow vortices

3.2.2.1 Comparison with Floquet theory and flow physics

Secondary stability of the flow is investigated using the framework described in §2.3.2. The secondary base blow is defined as $\mathbf{Q}_1(y, z_v) = \mathbf{Q}_0(y) + A\mathbf{q}_1(y, z_v)$ with $\mathbf{q}_1$ the disturbance with wavevector $\mathbf{k} = (0.0361, 0.4774)^T$ in the original reference frame. The amplitude A is set as $A = 0.0789$ (Fischer & Dallmann, 1991). The resulting base flow on one sub-unit and in the wave-oriented reference frame is shown in figure 5.3. Qualitative validity of the shape assumption in this particular case is shown through comparison with experiments in Fischer & Dallmann (1991). Regarding the saturation amplitude, in a similar configuration, White & Saric (2005) found a saturation amplitude of 19% for a subcritical transition. This has been retrieved in the more recent work of Serpieri & Kotsonis (2016) where, at worst, a N-factor of 3 was found, corresponding to a saturation amplitude of 20%. Returning to the study of White & Saric (2005), in the case where the generated primary cross-flow vortices were supercritical, their amplitude only grew by a few percent before reaching saturation, in agreement with the chosen amplitude.

Secondary growth rate for the full system as a function of the streamwise wavelength is displayed in figure 3.3. Two modes appear to compete: the maximum growth rate $\sigma_r = 0.0068$ is reached for $\alpha_v = 0.087$ while streamwise independent perturbations ($\alpha_v = 0$) also display strong amplification with $\sigma_r = 0.0065$. A direct comparison can be made with figure 8 from Fischer & Dallmann (1991), where Floquet analysis (on one sub-unit) is conducted for both harmonic modes and resonant modes

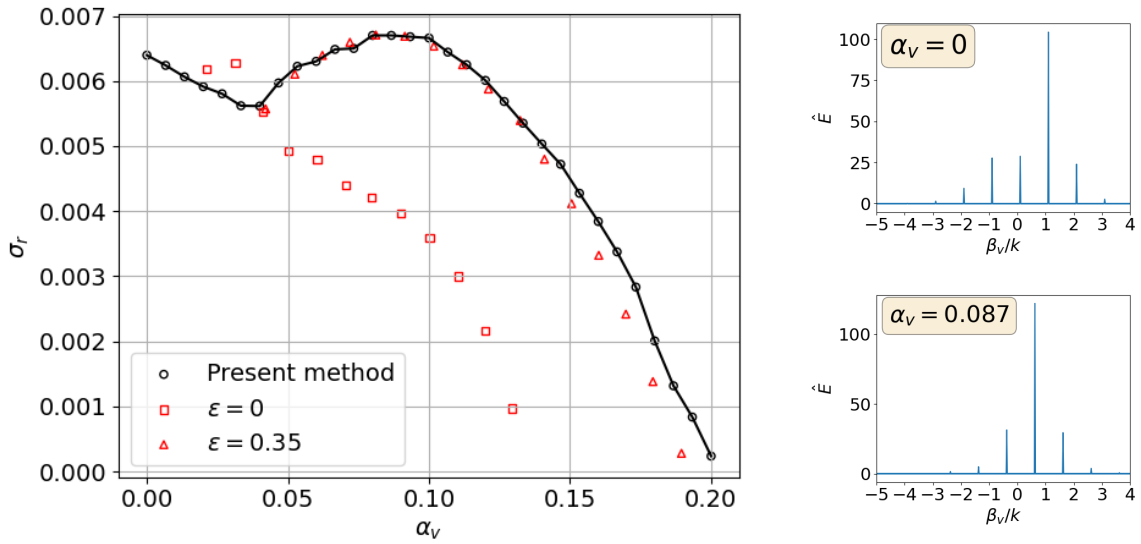

Figure 3.3: Left: evolution of the secondary growth rate σ_r (black circles) as a function of the streamwise wavenumber α_v. A comparison is made with figure 8 of Fischer & Dallmann (1991) (red symbols). ϵ corresponds to the detuning factor of the Floquet analysis (Fischer & Dallmann, 1991). Right: Spatial Fourier spectra of the energy of the most unstable mode for $\alpha_v = 0$ (top) and $\alpha_v = 0.087$ (bottom).

with a detuning factor $\epsilon = 0.35$, where $\epsilon = \gamma_i/||\mathbf{k}||$ and γ_i is the imaginary part of the Floquet exponent γ. Maximum growth rates are obtained for $\alpha_v = 0.03$ and $\alpha_v = 0.087$, respectively. The agreement with the $\epsilon = 0.35$ curve is good although some discrepancies are observed for the growth rates of harmonic modes. The Floquet analysis seems to overestimate the secondary growth rate in the range where small wavenumber modes are predominant.

The nature of the instabilities obtained in the new framework can be inferred inspecting the spatial Fourier energy spectra of the most unstable modes. These Fourier spectra, realised for the cases with $\alpha_v = 0$ and $\alpha_v = 0.087$, are shown in the right part of figure 3.3. The detuning factor can be identified, from the spectra, as $\epsilon = 1 - \beta_v^0/\|\mathbf{k}\|$ with β_v^0 the wavenumber of the Fourier fundamental mode. Thus, the maximum at $\alpha_v = 0.087$ is associated to a detuned mode with $\epsilon = 0.35$, in agreement with Fischer & Dallmann (1991). For $\alpha_v = 0$, all the frequencies are almost multiples of $\|\mathbf{k}\|$, indicating a quasi-fundamental ($\epsilon = 0.08$) nature of the instability. It is also worth noticing the larger number of modes required to accurately describe the instability. The secondary perturbation is truly multi-modal with important coupling effects between sub-units. Notice that Fischer & Dallmann (1991) missed this secondary mode, since the associated value of ϵ is very low, but still not zero.

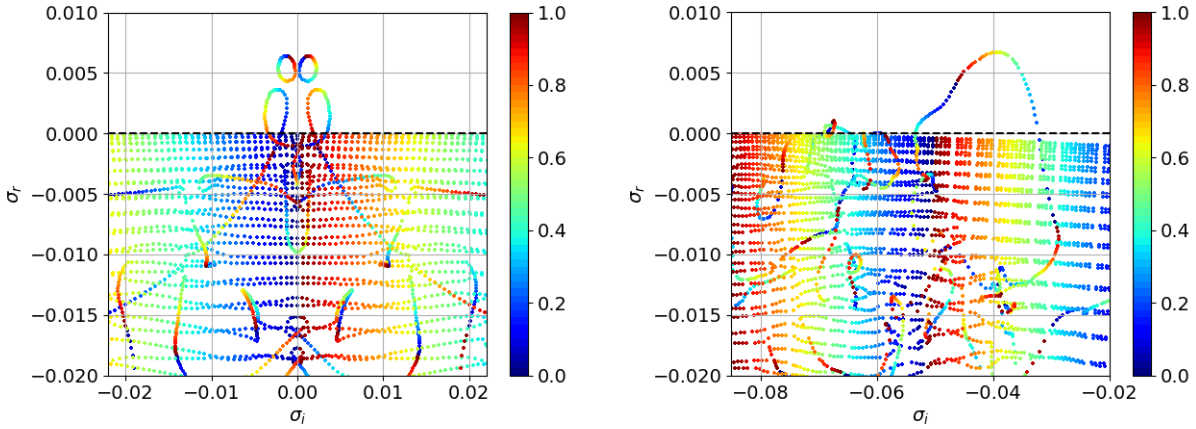

Figure 3.4: Full spectra of the secondary stability problem for $Re_\delta = 826$, $A = 0.0789$, $n = 50$ and for $\alpha_v = 0$ (left) and $\alpha_v = 0.087$ (right). The full spectrum is constructed merging the n spectra of the sub-systems. The eigenvalues have been coloured by the argument of their respective root of unity: $z \in [0, 1]$ such as $\rho = \exp(2i\pi z)$. The dashed line corresponds to the $\sigma_r = 0$ line.

The spectra for the system composed of $n = 50$ sub-units and for $\alpha_v = 0$ and $\alpha_v = 0.087$ are displayed in figure 3.12. A high number of sub-units corresponds to a (very) large system and allows a wide range of admissible spanwise wavenumbers. This explains the appearance of many branches within the spectra. The higher the number of sub-units, the more continuous these branches will be. Quasi-horizontal branches represent convective Squire modes and do not play a role in the asymptotic stability as they are always stable. The eigenvalues are coloured with the argument of their corresponding root-of-unity ρ_j. Brighter colours indicate important phase shift between sub-units and, thus, strong desynchronisation of the perturbation. For $\alpha_v = 0$, as expected, the spectrum is symmetric about the $\sigma_i = 0$ axis. Two unstable branches are found: the most unstable one loops on itself. The second remains open ended. The maximum growth rate is reached for $\rho_4 = 0.87 + 0.48j$, corresponding to a phase shift $\theta = 29^o$ between the sub-units and indicating limited desynchronisation. The spectrum for $\alpha_v = 0.087$ is quite different. Two unstable branches are also observed. The first is marginally stable, and reaches a maximum growth rate for synchronised modes. The second is much more unstable and reaches a maximum for $\rho_{31} = -0.73 - 0.68j$, equivalent to a phase shift $\theta = -137^o$ and causing strong desynchronisation.

Ultimately, the most unstable modes are reconstructed for $\alpha_v = 0$ and $\alpha_v = 0.087$. Figure 3.5 displays the streamwise component of the disturbance velocity in the full domain while figure 3.6 exhibits the cross-flow velocities for a group of three sub-units. The streamwise velocity disturbance

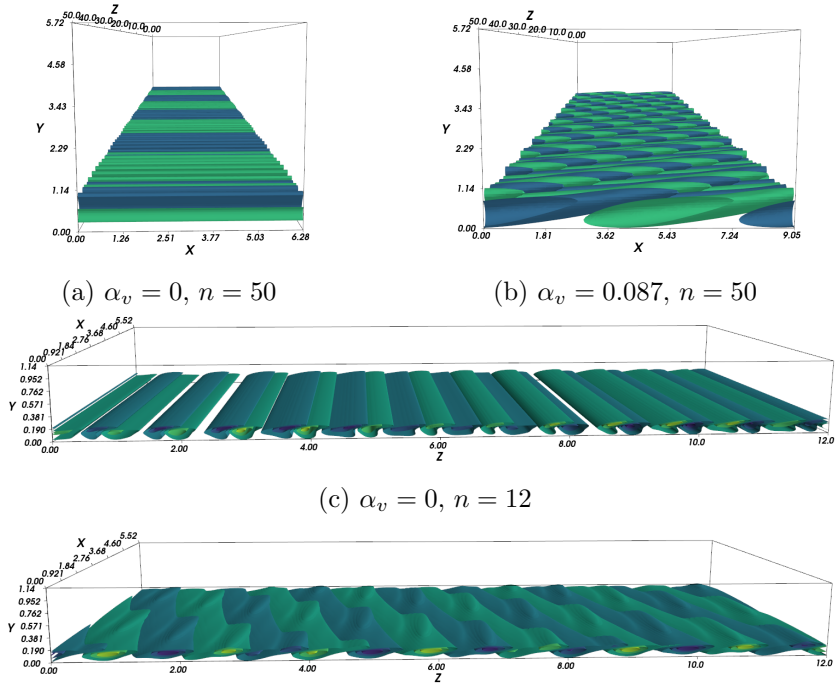

(a) $\alpha_v = 0$, $n = 50$

(b) $\alpha_v = 0.087$, $n = 50$

(c) $\alpha_v = 0$, $n = 12$

(d) $\alpha_v = 0.087$, $n = 12$

Figure 3.5: Three dimensional views of the streamwise velocity perturbation of the most unstable mode for different streamwise wavenumber α_v and number of visualised sub-units n. Notice the large wavelength instability for $\alpha_v = 0$.

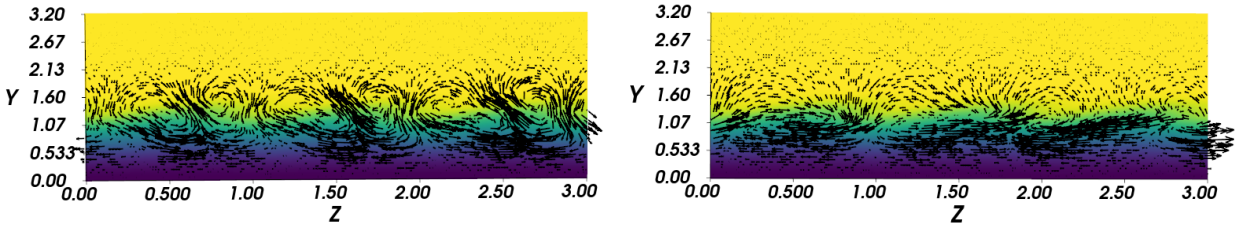

Figure 3.6: Vectors: cross-flow velocity in the plane (y, z_v) for a group of three sub-units, with $\alpha_v = 0$ (left) and $\alpha_v = 0.087$ (right). The contour plot represents the streamwise component of the secondary base flow. The flow in the z direction goes from left to right.

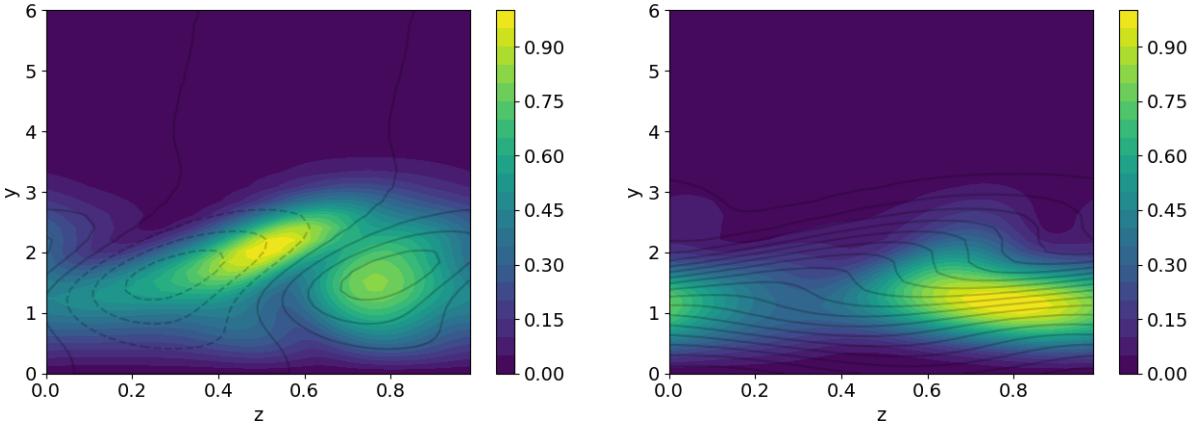

Figure 3.7: Absolute value of the streamwise component of the eigenfunction for $\alpha_v = 0$ (left) and $\alpha_v = 0.087$ (right). The solid contours depict the spanwise and wall-normal velocity gradients of the secondary base flow, respectively.

is one order of magnitude higher than the cross-flow components. The position of the maxima of the streamwise disturbance slightly varies across the sub-units, although it is approximately located on the upwelling of the wave pattern of the secondary base flow. A collective behaviour can be observed in both modes: for $\alpha_v = 0$, approximately twelve sub-units are involved in large-wavelength oscillations; whereas a staggered pattern, characteristic of subharmonic instabilities, is observed for $\alpha_v = 0.087$.

The cross-flow dynamics, displayed in figure 3.6 on a group of three sub-units, is less sensitive to collective behaviour, likely due to the smaller magnitude of the components. The streamwise-independent mode displays counter-rotating vortices. The left vortex seems to be constituted of the merger of two smaller co-rotating vortices. For $\alpha_v = 0.087$, the vortical structures are sensibly different. The vortices seem to arise from the roll-up of a shear layer. This might have been anticipated, since it has been shown that secondary instability of swept flows can be related to Kelvin-Helmholtz instabilities (Wassermann & Kloker, 2002). Furthermore, these secondary vortices are located on the edge of the boundary layer, in a region associated with strong wall-normal and spanwise shear layers. Ultimately, it appears that two distinct collective mechanisms are at play. The first is linked to streak instabilities, which push high-velocity fluid downwards near the walls while low-velocity fluid from the near-wall region is ejected higher in the boundary layer. The second instability mechanism is Kelvin-Helmholtz related, and generates secondary vortices through the roll-up of the shear layer located at the edge of the boundary layer.

In an effort to assess more precisely the instability nature of these two modes, a comparison can be made with the experimental work of Serpieri & Kotsonis (2016); Serpieri (2018) in which a POD decomposition of the laminar-turbulent transition on a swept wing was realised. The most energetic POD mode appeared to be streamwise-independent, with a shape similar to that found in the present analysis. Furthermore, it was characterized by a very low frequency in the $[1\text{Hz}, 20\text{Hz}]$ range, in agreement with the frequency $f = 4$ Hz found here for the $\alpha_v = 0$ mode. However, no modulation of the mode has been observed as the POD was realised for only one cross-flow vortex. Figure 3.7 depicts the absolute value of the streamwise component of the disturbance. For $\alpha_v = 0.087$, the concentration of the streamwise velocity disturbance in the bottom part of the cross-flow vortices is reminiscent of a *type-III* instability (Serpieri, 2018). The frequency $f = 154$ Hz obtained for this mode is smaller than the frequency range 350 Hz $\leq f \leq$ 550 Hz found by Serpieri (2018) but still in good agreement with the frequency $f = 145$ Hz found by Fischer & Dallmann (1991). This type of mode is traditionally associated with interactions between primary stationary and travelling modes. The $\alpha_v = 0$ mode is quite interesting: the streamwise component of the perturbation is located on the upwelling of the cross-flow vortex which is characteristic of a *type-I* instability. The mode is also strongly correlated with the spanwise gradient of the base flow, as for *type-I* modes. However, these are usually associated with non-zero streamwise wavenumber and higher frequencies.

3.2.2.2 Exceptional points and resonances

In order to assess more precisely the nature of the $\alpha_v = 0$ mode, the amplitude A of the primary disturbance was varied. Figure 3.8 displays the evolution of the spectrum of the $\alpha_v = 0$ mode for different amplitudes. When $A \to 0$, characteristics of the primary instability are retrieved: the primary growth rate is reached for stationary cross-flow vortices. However, this mode results from the merging of two spatial branches, forming an exceptional point (Kato, 1995). Exceptional points are spectral singularities in the parameter space of a system in which two or more eigenvalues, and their corresponding eigenvectors, simultaneously coalesce, yielding a degeneracy of the eigenvalue (Heiss, 2012). The eigenvalues need to stem from two different spatial branches. Formally, this degeneracy may be understood as a resonance giving rise to an algebraic growth. Besides a few early works (Gustavsson & Hultgren, 1980; Gustavsson, 1981, 1986), the study of these resonances remained limited, likely due to the development of transient growth analysis. Only recently, these special points received once

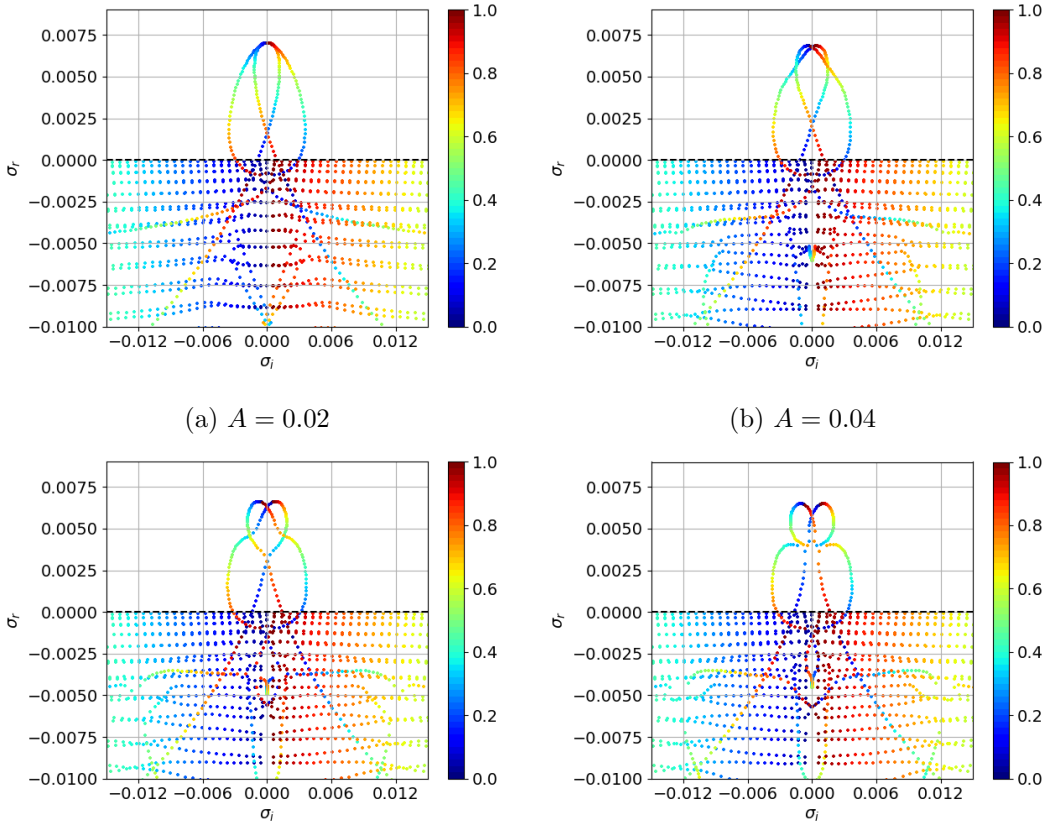

(a) $A = 0.02$ (b) $A = 0.04$

(c) $A = 0.06$ (d) $A = 0.07$

Figure 3.8: Spectra of the secondary stability problem for $Re_\delta = 826$, $A = 0.0789$, $n = 50$, $\alpha_v = 0$ and for variable amplitudes A. The dashed line corresponds to the $\sigma_r = 0$ line.

again some interest as they were investigated in a pulsatile Poiseuille flow in the work of Kern *et al.* (2021, 2022). In the present case, the exceptional point indicates the presence of interactions between cross-flow vortices with different spanwise wavenumbers. When the amplitude is increased, the outer branch is deformed, leading to the formation of two other exceptional points associated to interactions between travelling disturbances with opposite spanwise wavenumbers. For $A = 0.07$, a change in the topology of the spectrum can be observed: the two spatial branches break up, then reconnect in a different configuration, forming the loops observed in the spectrum of figure 3.12. This evolution of the spectrum tends to indicate a change in the nature of the modes, and indicates the presence of a proper secondary instability. On the contrary, carrying out the same analysis for the $\alpha_v = 0.087$ mode as in figure 3.9, only a continuous deformation of the unstable branch can be observed. This is in agreement with the findings of Malik *et al.* (1994) who argued, using an NPSE approach, that the

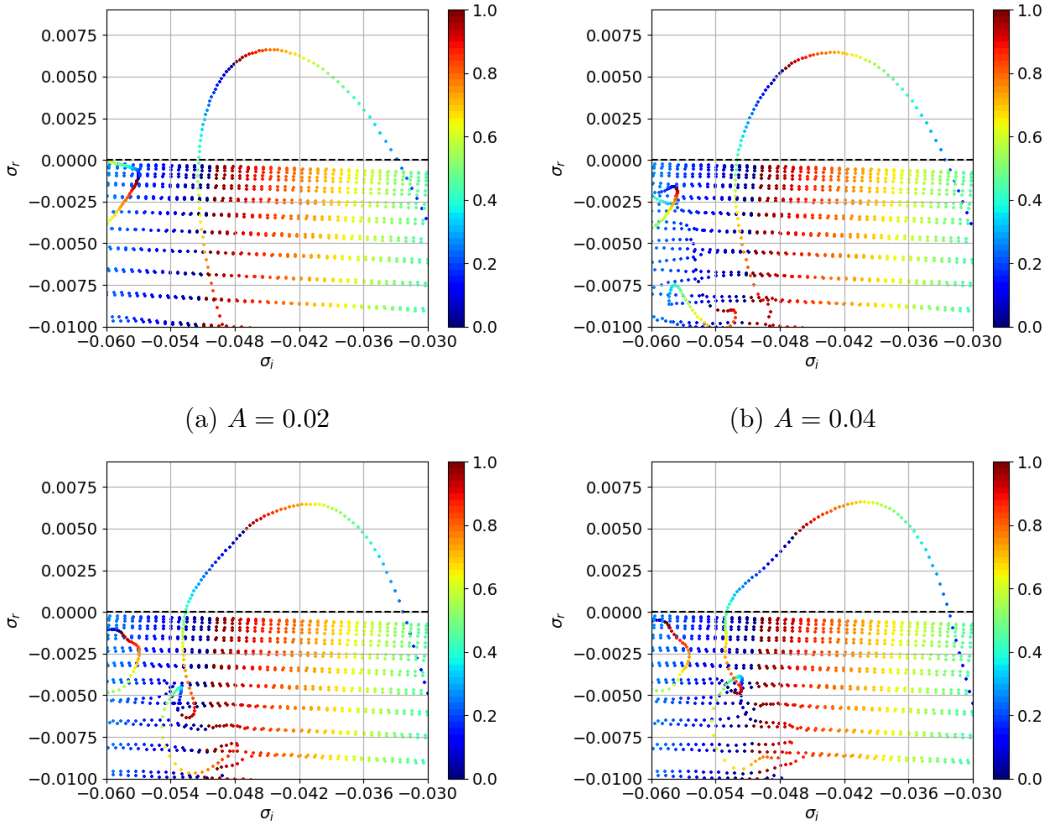

(a) $A = 0.02$ (b) $A = 0.04$

(c) $A = 0.06$ (d) $A = 0.07$

Figure 3.9: Same as figure 3.8 for the $\alpha_v = 0.087$ mode.

modulation is simply a result of the nonlinear interaction of the stationary and travelling disturbances that becomes more pronounced as the amplitude A is increased.

3.3 Linear stability of a streaky boundary layer

In an effort to further demonstrate the relevance of the framework for the study of secondary instabilities, a second case is considered: optimal streaks in a boundary layer. This configuration is especially interesting due to the ubiquitous nature of the streaks in the bypass transition to turbulence. Accordingly, the asymptotic secondary instability of the streaks have been quite thoroughly investigated numerically, albeit with different degrees of accuracy: seminal results in the inviscid case were obtained by Hall & Horseman (1991) and Andersson *et al.* (2001). The viscous problem was considered in analyses of Ustinov (2002); Liu *et al.* (2008). Mean flows taken from DNS and taking

distortion into account, were considered in the works of Cos (2004) and Hack & Zaki (2014). Cos (2004) were also the first to identify the potential of streaks for delaying the transition to turbulence and to flow control in general. The stabilising effect of the streaks was also observed on oblique waves in Bagheri & Hanifi (2007). Bypass transition has also been investigated through the use of models as the one proposed and developed in the works of Zaki & Durbin (2005, 2006) and Vaughan & Zaki (2011), based on mode interactions.

Experimentally, secondary stability of streaks has also been extensively looked into: Asai *et al.* (2002); Konishi & Asai (2004) described streak generation and secondary instabilities in a controlled environment (no free-stream turbulence, imposed frequencies) while Tani & Komoda (1962); Brandt *et al.* (2004); Schlatter *et al.* (2008) focused on the later stages and the breakdown to turbulence. On special aspects of the transition, Fransson *et al.* (2005) investigated experimentally the stabilising effect of the streaks and Balamurugan & Mandal (2017) considered the role of localisation of the secondary perturbations in the breakdown to turbulence. Results on the non-modal aspects of the transition of streaks in a boundary layer are much more scarce: transient growth was studied experimentally by Fransson *et al.* (2004) and numerically by Hoepffner *et al.* (2005). Receptivity of a boundary layer has attracted quite a lot of attention (see for examples the review of Kerschen (1989), Goldstein & Hultgren (1989) and Saric *et al.* (2002)), and yet, on a streaky boundary layer, only the work of Zhang *et al.* (2018) can be found. For a review on the different works on the different stages of bypass transition, the reader is referred to the review of Zaki (2013).

3.3.1 Governing equations, optimal streaks and secondary base flow

The flow of incompressible fluid over a flat plate is considered. All velocities are scaled using the free-stream velocity U_∞ and the pressure with ρU_∞^2 where ρ is the fluid density. The length scale is defined as $\delta = (L\nu/U_\infty)^{1/2}$, with ν the kinematic viscosity and L the distance to leading edge. Two Reynolds number can be defined: one based on the displacement thickness $Re_\delta = U_\infty \delta/\nu$ and the other based on the distance from the leading edge $Re_L = U_\infty L/\nu$, and it is easily found that $Re_L = Re_\delta^2$.

As per usual, the secondary base flow can be obtained either through direct superposition of the Blasius profile and the optimal streaks or by obtaining a saturated mean flow through simulation of the flow. Both methods are considered in Andersson *et al.* (2001). For the latter, an optimal spatial perturbation at initial time was used as input close to the leading edge and its downstream

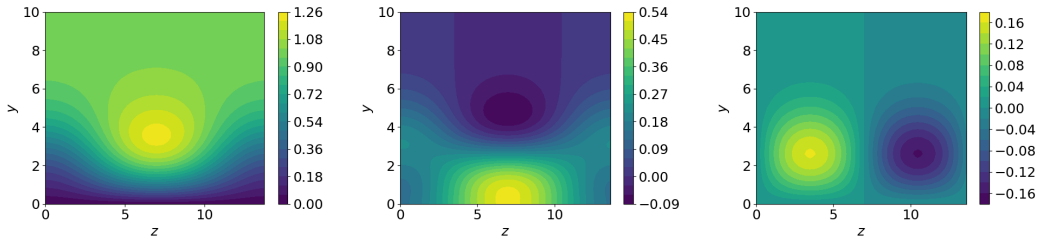

(a) U_0 (b) $\partial_y U_0$ (c) $\partial_z U_0$

Figure 3.10: Secondary base flow $U(y, z)$ and its wall-normal and spanwise gradients for $A = 0.25$

nonlinear development was monitored for different upstream amplitudes of the input disturbance. These computations are carried out for streaks with wavenumber $\beta_0 = 0.45$, which corresponds to linearly optimally growing streaks at the streamwise position $x = 1$ (with the scaling adopted in Andersson *et al.* (1999)). Ultimately, the amplitude of the primary disturbance could be defined in the following way:

$$A(x) = \frac{1}{2}\left[\max_{y,z}\Big(U(x,y,z) - U_B(x,z)\Big) - \min_{y,z}\Big(U(x,y,z) - U_B(x,y)\Big)\right] \tag{3.5}$$

where $U(x, y, z)$ is the total streamwise velocity of the flow with the streaks and $U_B(x, y)$ the Blasius profile. The nonlinear mean flow is then extracted at the position $x = 2$ where $A \approx 0.36$. Some significant differences can be found between the two secondary base flows, indicating that the shape assumption does not perfectly hold. In the present case, the first approach will be used.

3.3.2 Linear instability and amplitude thresholds

Linear instability of a streaky boundary layer is investigated within the framework previously described. The amplitude A of the primary disturbance is varied in order to assess the effects of developing streaks on the transition. Neutral curves in the (α, A) plane for the secondary stability are displayed in figure 3.11. Only fundamental and subharmonic modes are considered as detuned modes do not seem to play an important role in the asymptotic stability of the flow.

A first glimpse of the instability mechanisms can be obtained by looking at the spectra of figure 3.12. First notice that, in all cases, only half of the spatial branches is visible. This is expected as the eigenvalues associated with roots-of-unity ρ_j and ρ_{n-j} are equal due to the symmetry in the coupling of the sub-units. For small amplitude, the spectrum of a two-dimensional stability problem of the

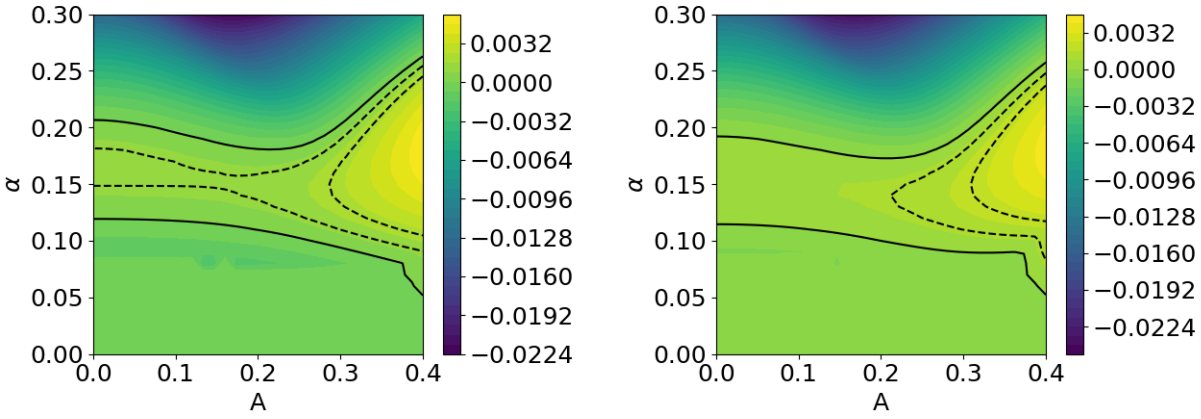

Figure 3.11: Neutral curves of the secondary instability of streaks in the (α, A) plane for fundamental (left) and subharmonic (right) modes. Black line denotes $\sigma_i = 0$ while dashed lines represent $\sigma_i = 10^{-3}, 2 \cdot 10^{-3}$

Blasius flow can be retrieved. The spatial branch associated with TS waves can easily be identified. When the amplitude is increased, the TS branch breaks into multiple, smaller branches, indicating topological changes of the modes. However, unlike the previous case, no exceptional points can be seen, limiting the possibility of (linear) resonances. Ultimately, two spatial branches appear relevant as they become unstable.

The most unstable branch, which stems from the tip of the original TS branch, displays very little evolution when the amplitude is increased. The frequency is almost identical to the TS wave frequency while the growth rate slightly increases only for large amplitudes. On the contrary, modes of the second spatial branch, initially having large negative growth rates due to their position in the middle of the TS branch, appear to be strongly destabilised by the presence of streaks. This destabilisation comes with a shift to higher frequencies.

Eigenfunctions of the most unstable modes of these two spatial branches, denoted in the following FS (fundamental symmetric) and SS (subharmonic symmetric), can be seen in figures 3.13 and 3.14. In both cases, the streamwise component of the velocity disturbance is stronger than its cross-flow counterparts. The FS mode results from the continuous deformation of the initial 2D TS wave (for $A = 0$) into the flow structure observed in figure 3.13 (for $A = 0.35$). The mode has a characteristic M-shaped structure (Ustinov, 2002; Cos, 2004), yielding a doubly-peaked wall-normal velocity distribution, which has been observed in the experiments of Tani & Komoda (1962) and Kachanov &

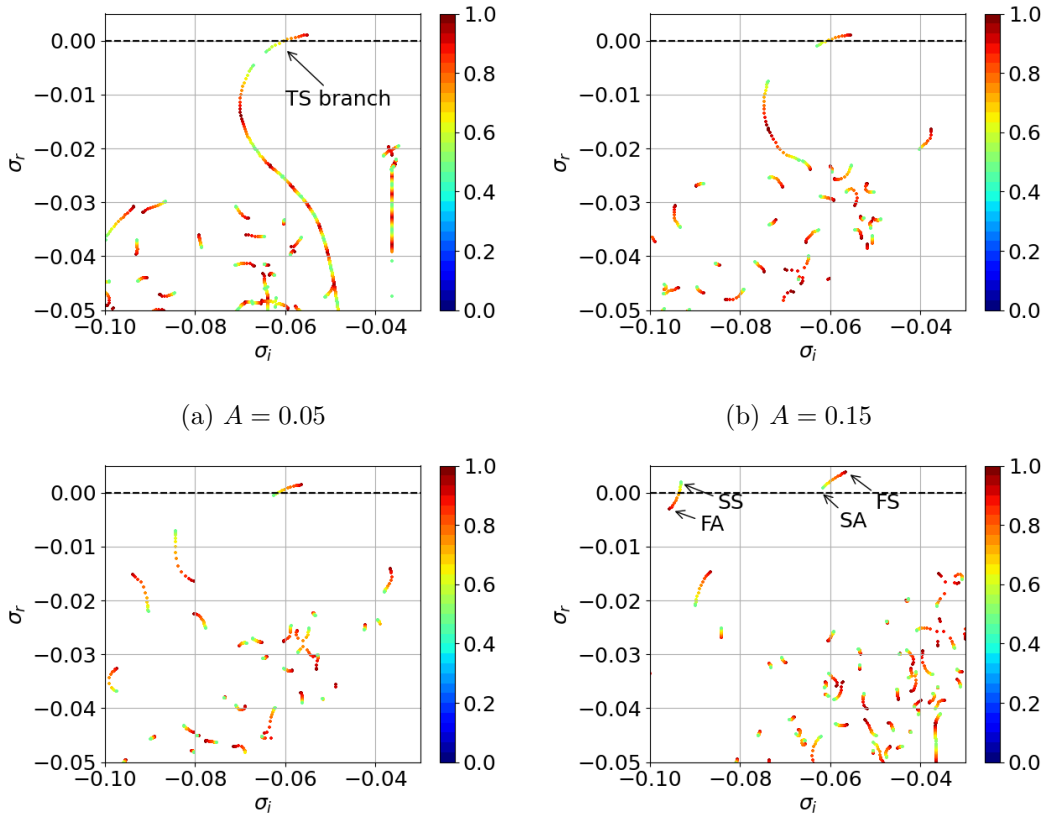

(a) $A = 0.05$ (b) $A = 0.15$

(c) $A = 0.25$ (d) $A = 0.35$

Figure 3.12: Close-up of the TS branch of the spectra for $Re_\delta = 430$, $\alpha = 0.15$ and for different amplitudes. FS: fundamental symmetric. SA: subharmonic antisymmetric. SS: subharmonic symmetric. FA: fundamental antisymmetric. Eigenvalues are coloured corresponding to the argument of their respective root-of-unity. Dashed line corresponds to $\sigma_r = 0$.

Tararykin (1987). The SS (subharmonic symmetric) mode has a rather different structure. Notice also the rather large number (≈ 15) of Fourier modes necessary to retrieve accurately this subharmonic mode. The FS and SS modes also appear to be respectively related to the *inner* and *outer* modes found in the works of Vaughan & Zaki (2011) and Zaki (2013).

For all the amplitudes considered, the most unstable modes are found to be varicose, in disagreement with the results of Andersson *et al.* (2001) who found sinuous modes to be the dominating instabilities. These discrepancies may be explained by a combination of several factors. Among them, viscosity is likely to promote the development of the near-wall, varicose instabilities through the enhancement of the wall-normal velocity gradients. Distortion of the base flow due to non-linearities

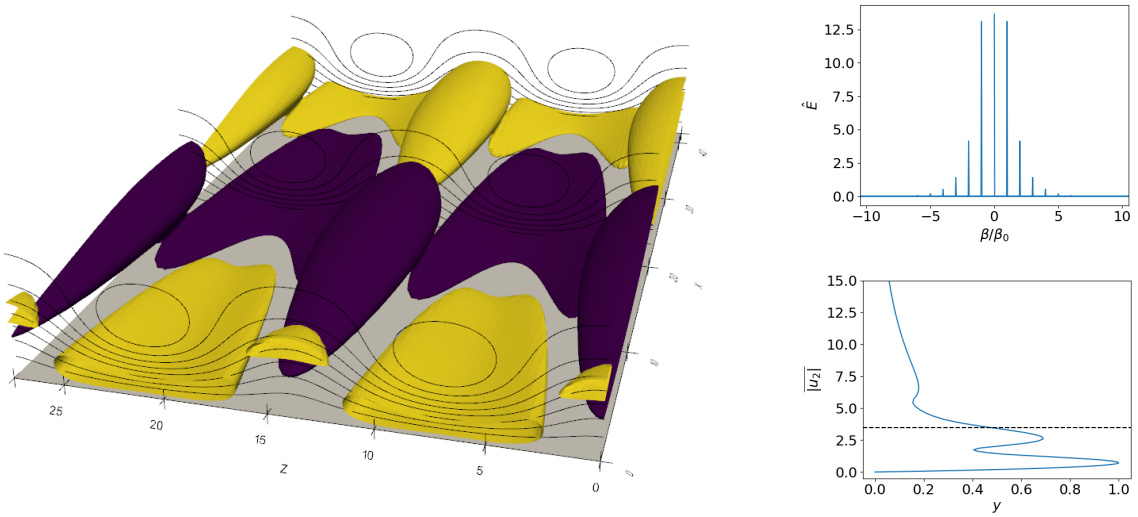

Figure 3.13: Eigenfunction of the most unstable fundamental varicose mode (FS) for $Re_\delta = 430$, $\alpha = 0.15$ and $A = 0.35$. Left: three-dimensional view of the streamwise component of the disturbance. Contours of the secondary base flow are represented in black. Right top: spatial Fourier spectrum of the kinetic energy of the disturbance. Right bottom: Wall-normal profile of the absolute value of the streamwise velocity perturbation. The absolute value has been averaged in the spanwise direction. Dotted line indicate the location of the maximum of the primary disturbance.

may also play a role as it generates stronger spanwise velocity gradients in the mean flow, and thus promoting the development of sinuous instabilities. Ultimately, note that all these symmetry considerations should be viewed cautiously since detuned modes were also found to be unstable even for small amplitudes.

The neutral curves associated with these two modes are displayed in figure 3.11 and can be compared to the ones in the work of Andersson *et al.* (2001). In general, viscosity strongly dampens the growth rate of the secondary instability: it is one order of magnitude inferior to the one found in Andersson *et al.* (2001) but in agreement with Cos (2004). Noticeably, instabilities with zero or small streamwise wavenumbers are now stable even for large amplitude of the streaks. Still linked to viscosity effects, the primary instability of the Blasius boundary layer can be retrieved. Indeed, as the amplitude A tends to zero, the problem reduces to the two-dimensional stability analysis of the Blasius boundary layer. For the fundamental mode, the agreement between the range of unstable streamwise wavenumbers at $A = 0$ and the primary instability is perfect. On the other hand, primary subharmonic perturbations are slightly less unstable due to Squire's theorem. Besides these viscosity

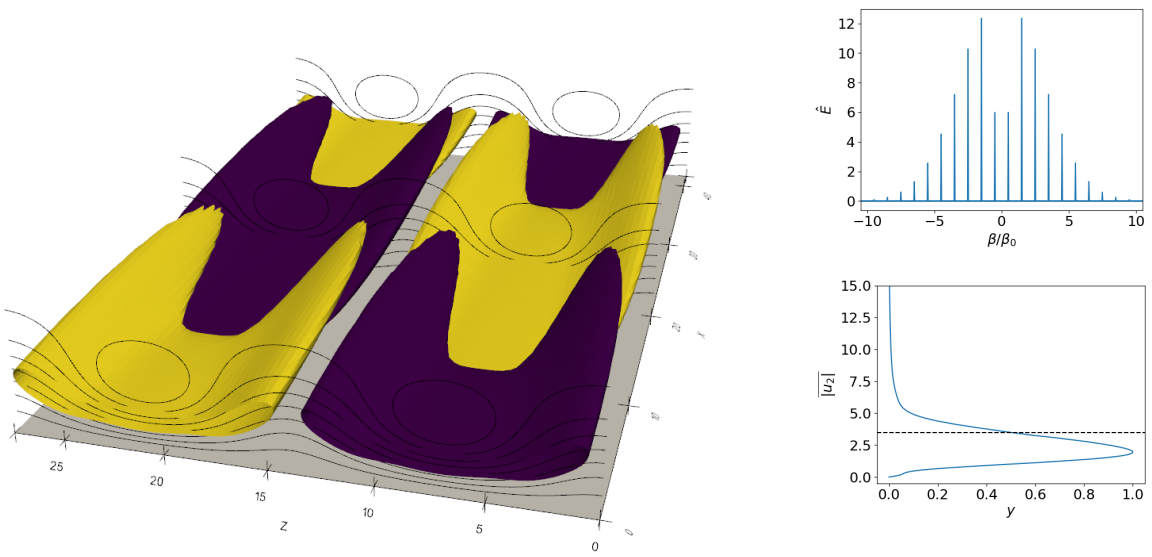

Figure 3.14: Same as figure 3.13 but for the second most unstable mode (SS).

effects, it appears the unstable region can be further divided into two zones with separate instability mechanism. In the case of a small or moderate amplitude, the TS waves are stabilised by the presence of the streaks. This stabilising effect of the streaks on the TS instability is well known and has been been used as a passive method to control and delay the laminar-turbulent transition (Cos, 2004; Fransson *et al.*, 2005; Bagheri & Hanifi, 2007). The second region, for high amplitude A, is characterised by larger growth rates, corresponding to the development of a Kelvin-Helmholtz related instability (Andersson *et al.*, 1999). Amplitude threshold between the two regions can be estimated to be respectively $A \approx 0.27$ and $A \approx 0.3$ for fundamental and subharmonic modes, in agreement with the literature.

3.3.3 Transient growth

In the regions where the streaks are stable or even slightly unstable, transient growth is likely to play a significant role in the transition process. This possibility is suggested in the experimental works of Lundell & Alfredsson (2003) and Fransson *et al.* (2004). Numerically, secondary transient growth

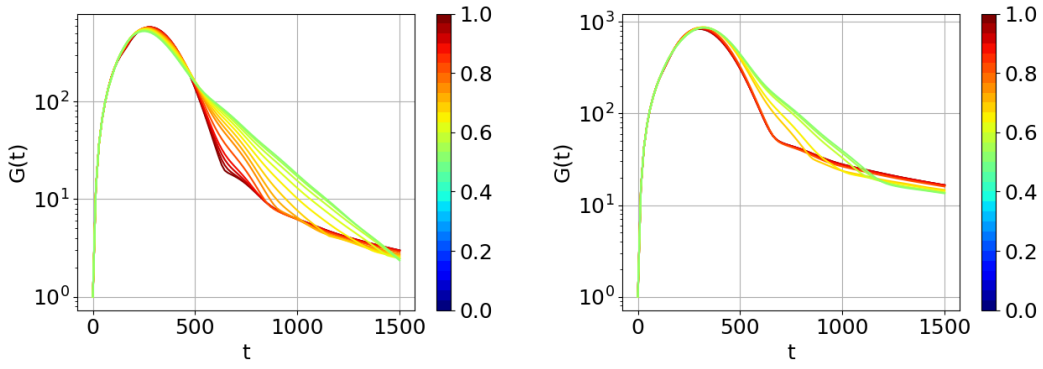

(a) $A = 0.05$

(b) $A = 0.15$

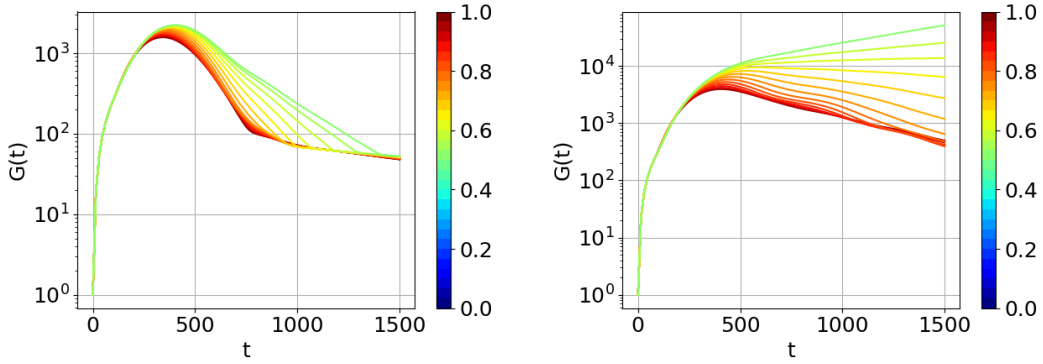

(c) $A = 0.25$

(d) $A = 0.35$

Figure 3.15: Energy amplification $G(t)$ for $Re_\delta = 430$, $\alpha = 0.05$ and for different amplitudes.

of streaks has already been investigated in the work of Hoepffner *et al.* (2005) for a boundary layer and in Cossu *et al.* (2007) in the case of a channel flow. In both cases, only fundamental perturbations were considered. The aim of this section is to complete and extend this analysis to detuned and subharmonic disturbances via the n-periodic framework.

3.3.3.1 Gain, optimal disturbances and amplitude effects

The effects on the optimal gain and perturbations of varying the amplitude of the streaks is investigated for $\alpha = 0.05$. This choice of wavenumber results from a compromise between the willingness to investigate the small-wavenumber region, which is linearly stable and associated to large transient growth (Hoepffner *et al.*, 2005) and the fact that small wavenumbers implies large wavelengths for which the parallel assumption may eventually become erroneous. Also note that small wavenum-

bers are associated with large optimal times (Hoepffner *et al.*, 2005), quickly yielding a prohibitive computational cost. The Reynolds number considered is still $Re_\delta = 430$.

The maximum energy growth $G(t)$ has been obtained for different values of the streak amplitude A and is displayed in figure 3.15. As per the eigenvalues, the gain curves are coloured correspondingly to their respective root-of-unity and, physically, are associated with disturbances with different detuning factors.

Starting with large amplitudes, for $A = 0.25$, a subharmonic mechanism appears to dominate clearly. The system becomes linearly unstable to both detuned and subharmonic perturbations for $A = 0.35$. The maximum gain G_{max} has the same order of magnitude than the ones found in Hoepffner *et al.* (2005) and scales with the square of the amplitude $G_{max} \propto A^2$. The optimal perturbation associated with the subharmonic varicose mechanism is displayed in figure 3.16. Flow structures exhibit a rotation from upstream to downstream tilting, due to the Orr mechanism (Orr, 1907*b*; Butler & Farrell, 1992*b*). This non-modal growth mechanism is the only present in the case of spanwise independent perturbations in a shear flow and describes short term inviscid instabilities due to the tilting of initial disturbances into the direction of the mean shear. Notice also the strong similarity between the optimal perturbation at the optimal time (figure 3.16 (c)) and the SS mode (figure 3.14) found in the linear stability analysis, making it difficult to assess from experimental results whether the streak breakdown is triggered by an exponential instability or by a non-modal mechanism (Hoepffner *et al.*, 2005). Still, the optimal disturbance has been compared with experimental profiles obtained in the work of Fransson *et al.* (2004) and, as it can be seen in figure 3.17, showed a qualitative agreement between the two. Initially, the disturbance is characterised by the presence of strong vortices located on top of the low-velocity streaks. A smaller, secondary vortex, is observed below. At the optimal time, zones of high and low-velocity regions can be visualized below the high-velocity streaks, where the wall-normal velocity gradient of the base flow is maximal. Cross-flow velocity components are one order of magnitude higher than the streamwise component of velocity at the initial time. While at the optimal time the streamwise component dominates the other two components, similarly to what has been observed for the unstable modes. Thus, it seems that the mechanism responsible for transient growth is still related, to some extent, to the lift-up effect (Brandt, 2014): energy is extracted from the secondary base flow by the cross-flow components of the initial perturbation and is redistributed towards the streamwise component of the disturbance, leading to the apparition of elongated coherent

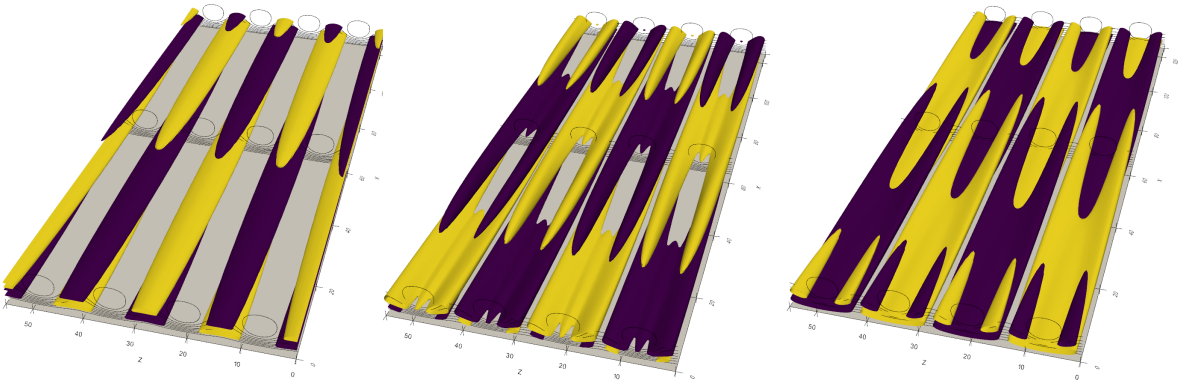

(a) $v_{opt}(0)$ (b) $w_{opt}(0)$ (c) $u_{opt}(T_{opt})$

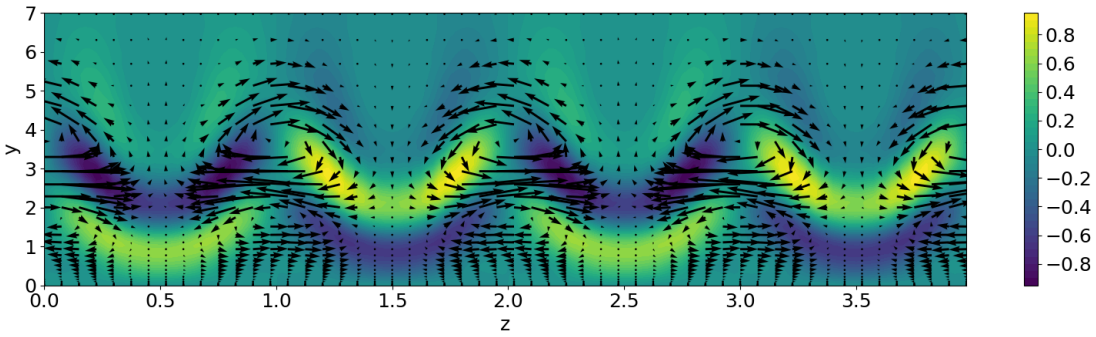

(d)

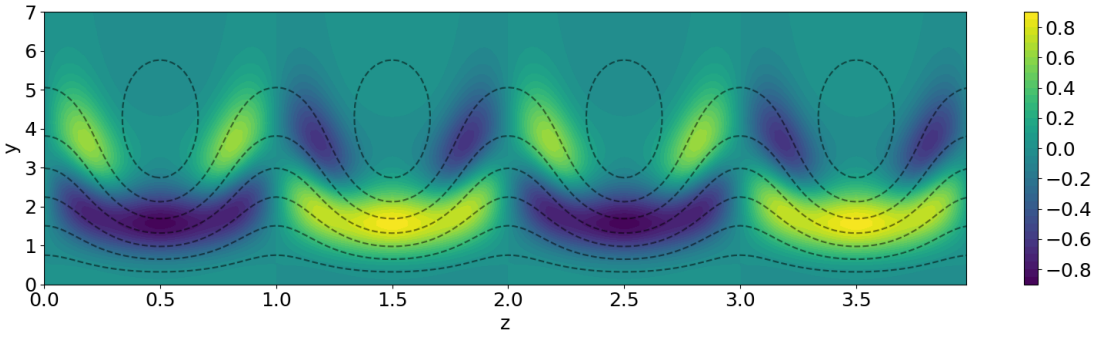

(e)

Figure 3.16: (a) to (c): three-dimensional representation of the subharmonic varicose optimal perturbation for $Re_\delta = 430$, $\alpha = 0.05$ and $A = 0.25$. (d) Contour plot of the optimal disturbance at the initial time. Quiver plot corresponds to the cross-flow dynamics $(v-w)$ at the initial time. (e) Contour plot of the streamwise component of the disturbance at the optimal time $T_{opt} = 400$. Dotted lines denotes isocontours of the secondary base flow U_0. Contours and quiver plots have been extracted at the streamwise position $x = \pi/\alpha$.

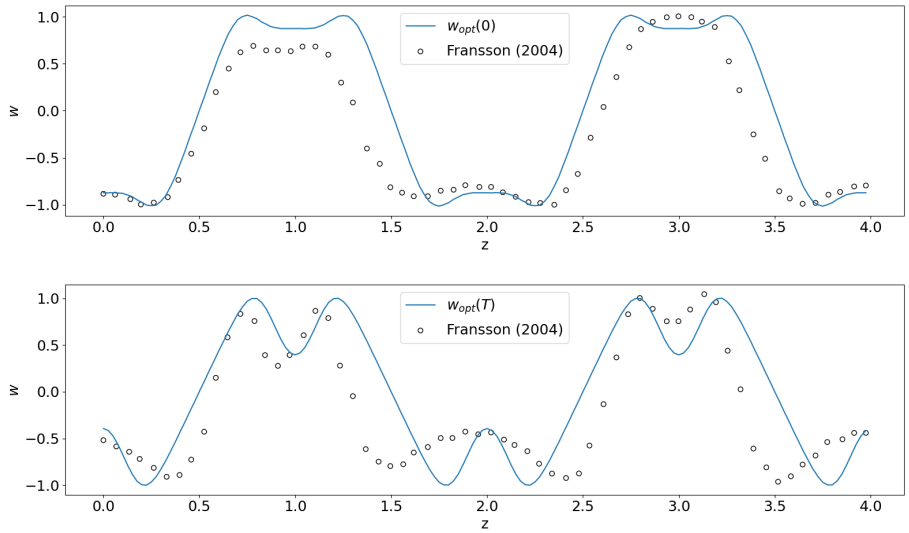

Figure 3.17: Comparison between the spanwise component of the optimal disturbance found for $A = 0.25$ and the experimental profiles retrieved from Fransson *et al.* (2004). All the profiles are taken at the wall-normal position corresponding to the disturbance peak. Top: disturbance at the initial time is compared with an experimental profile obtained at a position $x = 100$ mm. Bottom: disturbance at the optimal time is compared with an experimental profile obtained at a position $x = 70$ mm.

structures at the optimal time. Physically, the mechanism also appears quite similar: fluid in the low-velocity streak is pushed towards the high-velocity streaks while the high-velocity streak is sent towards lower-velocity regions near the wall. Ultimately, elongated coherent structures are created below the high-speed velocity streak in the near-wall region, and yielding large wall-normal velocity gradients, either between the wall and the structure or between the structure and the high-velocity streak.

For small and moderate amplitudes, the amplification curves associated with different roots-of-unity are almost superposed, so that there are n optimal perturbations instead than a single one. Thus, it can be inferred that the principal singular value of the full system is approximately degenerate with multiplicity n. The corresponding eigenfunctions form a vector subspace of dimension n and a basis of this subspace can be defined by the n optimal perturbations themselves since they are linearly independent (see 2.3.2 and Schmid *et al.* (2017) for the demonstration). Note that this is not a just a trivial effect of the symmetry: optimal perturbations have different periodicities and spatial structures as it can be seen in figure 3.18. For detuning factors close to zero, optimal perturbations present a rather usual streaky structure. On the contrary, disturbances with detuning factors close to one-half

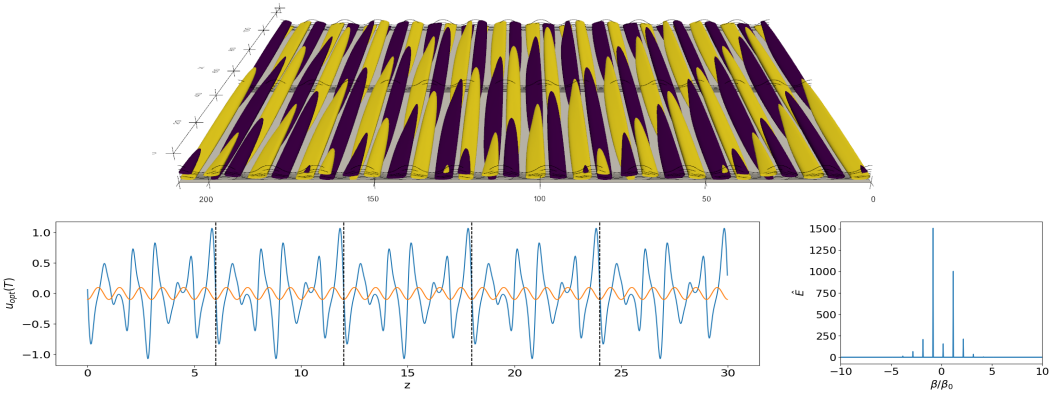

(a) ρ_5

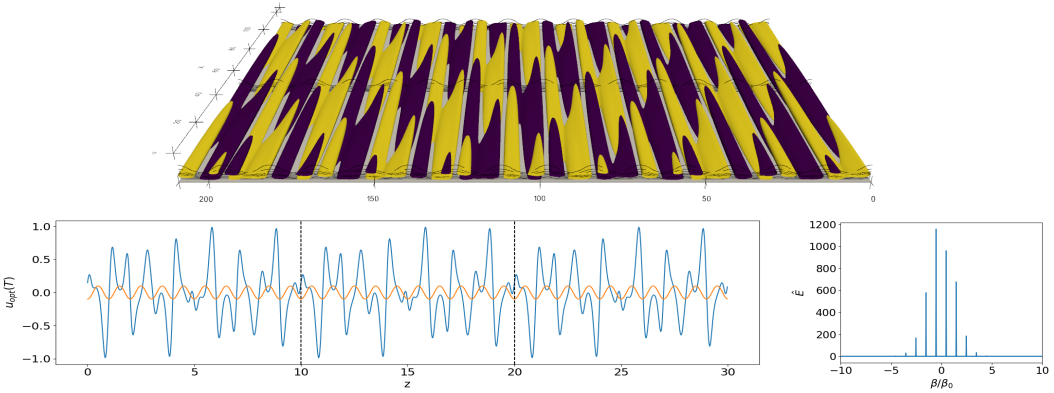

(b) ρ_9

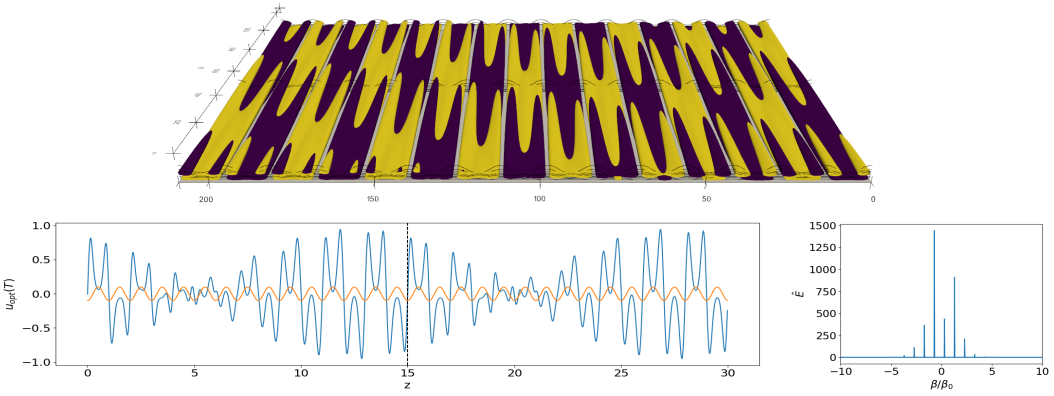

(c) ρ_{14}

Figure 3.18: Examples of optimal perturbation for $Re_\delta = 430$, $\alpha = 0.05$, $A = 0.15$ and different roots-of-unity. Left: Profile of the streamwise component of velocity at the optimal time T_{opt}. Wall-normal position is taken to be the maximum of the primary disturbance. Dotted lines indicate the periodicity of the disturbances. Right: three dimensional view of the streamwise component of velocity at the optimal time T_{opt}. All these optimal disturbances share the same amplification curves, including maximum gain and optimal times.

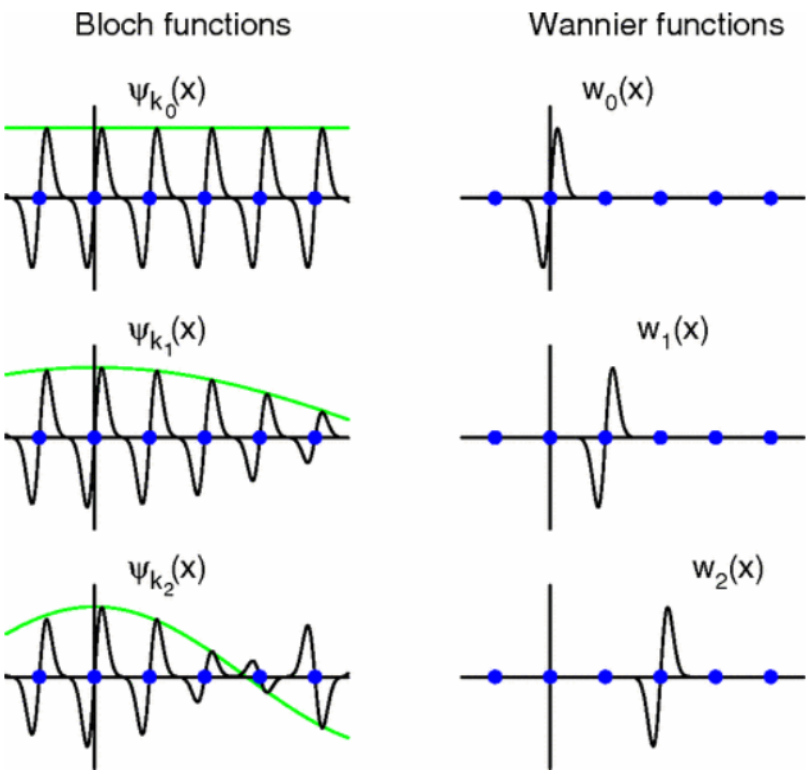

Figure 3.19: Sketch of localisation of Bloch waves through the use of Wannier functions. From Marzari *et al.* (2012).

tend towards the previously described optimal structures, found for large streak amplitudes. The shape of the optimal perturbation as a function of the root-of-unity varies continuously. For detuning factors very close to zero or one-half (usually ρ_1 and ρ_{14}), a beating phenomenon, resulting from the interaction between the modes β_0 and $\beta_0 + \epsilon$, appears, as it can be seen in figure 3.18 (c).

3.3.3.2 Frustration, optimal localised perturbations and spot formation

An interesting insight from the field of condensed matter is the concept of "frustration" (see Nixon *et al.* (2013) for example). The idea is quite simple: the systems considered (crystal lattices, networks of couple lasers, metamaterials...) usually organise in such a way that they have the lowest possible energy, as for instance a liquid drop arranges its shape for minimising its surface energy. However, competing spatial wavelengths prevent this, leading to a degeneracy of the eigenvalue and resulting in the inability of the system to find a unique ground state (hence the frustration). In fluid mechanics, the concept has been observed recently in Rayleigh-Bénard convection forced by a rough surface (Schmitz

& Zimmermann, 1996; Hossain & Floryan, 2022) and may also be related to the "pattern interaction effect" found by Floryan & Inasawa (2021). There seems to be a strong similarity with the present situation: we seek to maximise the kinetic energy of the perturbation, but this optimisation yields a degeneracy of the largest singular value giving us n possible optimal perturbations instead of just one. In our case, the competing effects are linked to the two fundamental mechanisms in shear flows: the lift-up effect and the Orr mechanism. This is further suggested by the fact that if $\alpha = 0$, frustration disappears as streamwise independent modes alone do not allow the existence of the Orr mechanism.

↪ **Wannier functions**

In the case of a degenerate system, its final state results from a superposition of the degenerate orthogonal eigenfunctions. For Bloch waves, such a superposition is usually known as a Wannier function (Wannier, 1937, 1962) and takes the following form :

$$\mathbf{q}_W^{\mathbf{Z}}(x,y,z,t) = \frac{1}{\sqrt{n}} \sum_{l=0}^{n-1} e^{-i\mathbf{k_1}\cdot\mathbf{Z}} \mathbf{q}_2^l(x,y,z,t), \qquad j = 0, ..., n-1 \tag{3.6}$$

where $\mathbf{k}_1$ is the Bloch wavevector, $\mathbf{Z}$ is a vector between any two points of the "lattice" and $\mathbf{q}_2^l$ are the Bloch eigenfunctions or, in this case, optimal perturbations. In our case, the "lattice" is just a simple line, meaning that $\mathbf{Z} = 2\pi/\beta_0 k\mathbf{z}$ and $\mathbf{k_l} = \epsilon_l \beta_0 \mathbf{z} = \beta_0 l/n\mathbf{z}$ with $k, l \in [0, n-1]$. The Wannier functions now read:

$$\mathbf{q}_W^j(x,y,z,t) = \frac{1}{\sqrt{n}} \sum_{l=0}^{n-1} e^{-i2\pi l/n} \mathbf{q}_2^l(x,y,z,t) \tag{3.7}$$

$$= \frac{1}{\sqrt{n}} \sum_{l=0}^{n-1} \rho_{n-l} \mathbf{q}_2^l(x,y,z,t), \qquad j = 0, ..., n-1 \tag{3.8}$$

Analytical properties of these functions were described in Kohn (1959) and the most important are given in the following for the sake of clarity. Since the Wannier functions $\mathbf{q}_W^j$ are orthogonal, their set form a basis of the perturbation space. The inverse transformation also exists: a Bloch eigenfunction could be retrieved from the superposition of the Wannier functions. Due to the detuning factor, which acts as a (constant) phase shift between sub-units, the superposition of the Bloch waves generates interferences, either constructive or destructive and leads to the localisation of the Wannier functions. This is worth noticing since mode localisation is usually obtained when transient growth is computed

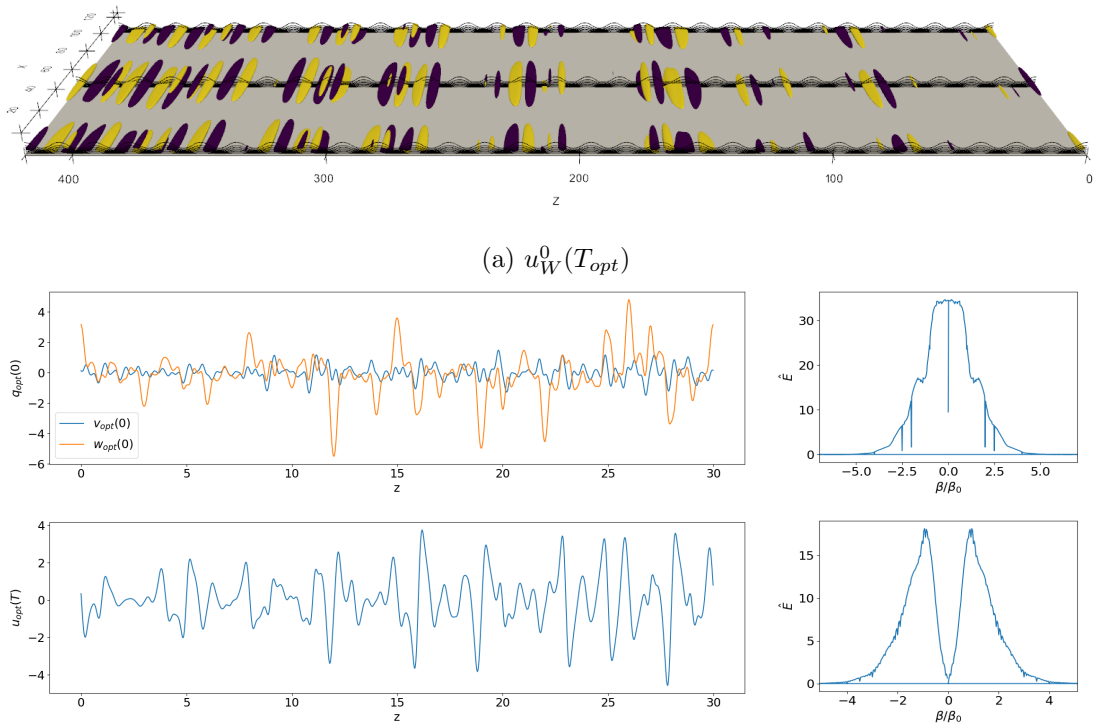

(a) $u_W^0(T_{opt})$

Figure 3.20: (a): Three-dimensional representation of the streamwise velocity of several Wannier modes at the optimat time T_{opt}. Left bottom part: disturbances profiles taken at the wall-normal position where the maximum of w_W^j is reached. Right bottom part: spatial Fourier spectra for the spanwise velocity disturbance w_W^j at the initial time (top) and the streamwise velocity disturbance u_W^j at the optimal time (bottom).

in a fully nonlinear framework (Cherubini *et al.*, 2010; Pringle & Kerswell, 2010; Monokrousos *et al.*, 2011). It also seems possible to generate a set of Wannier modes yielding maximum localisation of the modes through optimisation of a phase shift in the Bloch disturbances (Mostofi *et al.*, 2008; Marzari *et al.*, 2012). Ultimately, and most importantly, the Wannier functions, through linearity, are also optimal perturbations.

The Wannier mode for $A = 0.15$ and $\alpha = 0.05$ is displayed in figure 3.20. Since the optimal disturbances are orthogonal to one another (see 2 or Schmid & Brandt (2014)), the optimal perturbation at time T_{opt} can also be retrieved. As expected, both look "localised" in the spanwise direction in the sense that some streaks may experience a strong disturbance while some others none. The periodicity of the full system is still retained, but the perturbation inside the system exhibits a very complex, quasi-chaotic behaviour. Dynamics tend to be dictated by the spanwise component of the disturbance velocity as its large variations at the initial time appear associated with strong streamwise velocity

gradients at the optimal time T_{opt}, as shown in the left bottom frames of figure 3.20. The right bottom frames show the related Fourier spectra of these perturbations. Initially, the energy is equally distributed between the different Bloch modes, yielding a continuous spectrum. At the optimal time T_{opt}, the spectrum appears much more peaked, reaching a maximum for detuned modes ($\beta_{opt} = 1.13$) with $\epsilon = 0.13$ and indicating the presence of a selection mechanism for the spatial wavelength.

$\hookrightarrow$ **Analogy with the Rayleigh-Bénard convection and conjectures on spot formation**

The point of this small section is to develop some ideas deemed interesting and based on what could be obserbed previously. For now, these are just hypotheses but will be the subject of some work in the future.

Let's start by considering the Rayleigh-Bénard convection. Primary instability leads to the development of convection rolls with a given optimal spatial wavelength. Note that this instability is purely modal (zero non-normality) due to the absence of any flow initially. In several articles (Schmitz & Zimmermann, 1996; Hossain & Floryan, 2022), the rolls are then forced by the presence of a rough surface, resulting in the wavelength competition necessary for a system to exhibit frustration. From this forcing, the rolls experience either a secondary instability (for example, subharmonic in the case of Weiss *et al.* (2012)) or the development of localised dynamical structures (defects), either in travelling bands or in clusters (see the introduction or Weiss *et al.* (2012) for pictures). Secondary instability could be investigated through a Floquet analysis (Hossain & Floryan, 2013) but not the defects. Instead, their formation appeared linked to a commensurate-incommensurate bifurcation (Coullet, 1986), and has been studied via monitoring the amplitude of the rolls with equations determined through a weakly nonlinear analysis (Coullet *et al.*, 1985; Coullet & Huerre, 1986). Since the amplitude of the rolls appears critical for this phenomenon to occur, then transient growth (which had yet to be discovered at the time of publication of these articles) may be the right framework to study the instability. Non-normality would arise from the flow generated by the primary convection rolls and the localised dynamical structures would be optimal perturbations. Nonlinearities must also play a role but it remains unclear to what extent (see the discussion by Waleffe (1995) and the response from Henningson (1996)).

Going back to the streaks in the boundary layer, late stages of the bypass transition are characterised by the formation of localised regions of turbulence, called spots (Balamurugan & Mandal,

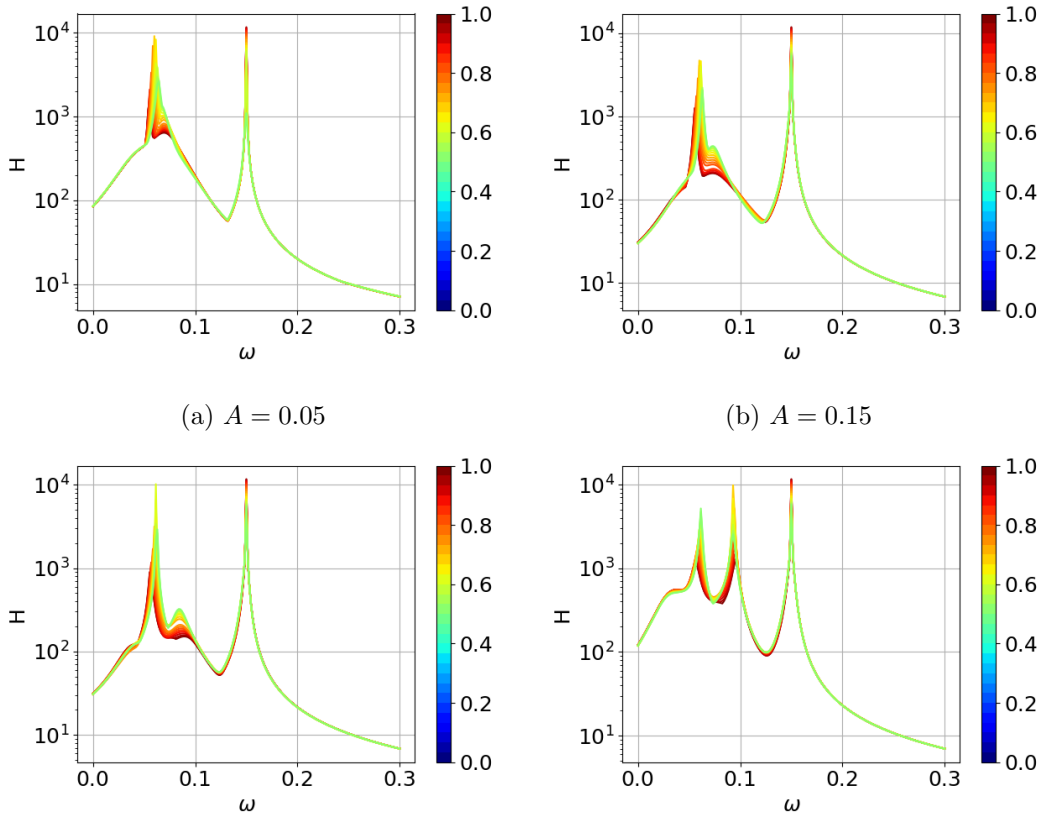

(a) $A = 0.05$ (b) $A = 0.15$

(c) $A = 0.25$ (d) $A = 0.35$

Figure 3.21: Resolvent norm for $Re_\delta = 430$, $\alpha = 0.15$ and for different amplitudes.

2017; Wu *et al.*, 2017). These structures bear some resemblance with the cluster of localised dynamical structures observed in forced Rayleigh-Bénard convection. Similarly, the streaks in a boundary layer were found to exhibit frustration just as for the forced Rayleigh-Bénard convection. Thus, following the same logic, spots may result from localised optimal perturbations of the streaks in the boundary layer as the one that was found with the Wannier functions.

3.3.4 Resolvent analysis of a streaky boundary layer

In bypass transition, there is a sharp difference between the disturbance environment in the free stream and interior of the boundary layer. The two regions interact through receptivity mechanisms: streaks may be interpreted as the boundary layer response to the broadband forcing of the free stream Zaki (2013). Even in later stages of the transition, free stream perturbations appear to keep playing

an important role. In the works of Zaki & Durbin (2005, 2006) and Schlatter *et al.* (2008), it was found that the bypass transition could be modelled quite accurately by considering the superposition of two free-stream modes of different frequencies as an initial condition. Physically, the low-frequency mode is responsible for the generation of streaks while the high-frequency mode triggers secondary instability upon the streaky flow.

The previous results are completed by a resolvent analysis for $Re_\delta = 430$ and $\alpha = 0.15$. Resolvent curves associated with different amplitudes are displayed in figure 3.21. For small amplitudes, two main pseudo-resonances can be observed for $\omega = 0.15$ and $\omega = 0.06$. As in the local framework, the former is associated with free-stream disturbances while the second corresponds to structures linked to transient growth. The largest response is obtained for $\omega = 0.15$. For $A = 0.35$, a third pseudo-resonance can be seen for $\omega = 0.09$ and is associated with a detuned mode (ρ_9). Unlike what has been shown previously, the maximum response is reached with a subharmonic mode.

Optimal forcings and their responses of the three pseudo-resonances at $A = 0.35$ are shown in figures 3.22 and 3.23. In this second figure, the optimal responses have superimposed on the secondary base flow to illustrate what kind of deformation the response will induce. This is purely for visualisation purposes. Three mechanisms can be identified: the first, and the one with the strongest response, is associated to fundamental free-stream disturbances. This can be seen in the top row of figure 3.22: the optimal forcing is located strictly in the free-stream region. It is characterised mainly by a strong spanwise component of the disturbance velocity and the presence of small vortices at the top of the low-velocity streaks. The response to this forcing appears in the region in between low- and high-velocity streaks (see the top row of figure 3.23) and leads to the deformation of the top part of the high-velocity streaks, intertwining it with the adjacent low-velocity streak. The pseudo-resonance at $\omega = 0.06$ reaches a maximum for a subharmonic mode while the other at $\omega = 0.09$ is associated to a detuned mode (ρ_9) coupling 10 sub-units. Both forcings are located on the low-velocity streaks and appear related to transient growth and lift-up: their strong cross-flow dynamics redistribute high-momentum fluid towards low-velocity regions and conversely. For $\omega = 0.06$ (see the middle row of figure 3.23), this redistribution takes place between two adjacent low-velocity streaks: the fluid in the low-velocity streak is pushed towards an adjacent one through the near-wall region below the high-velocity streaks. Such a forcing, in the close vicinity of the wall, may be the result of wall-related disturbances, as isolated roughness or wall oscillations and generates oscillations of the bottom part

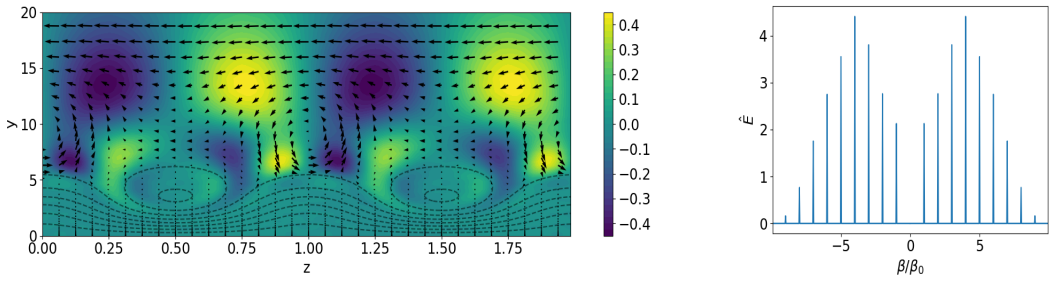

(a) $\omega_{opt} = 0.15$, ρ_0

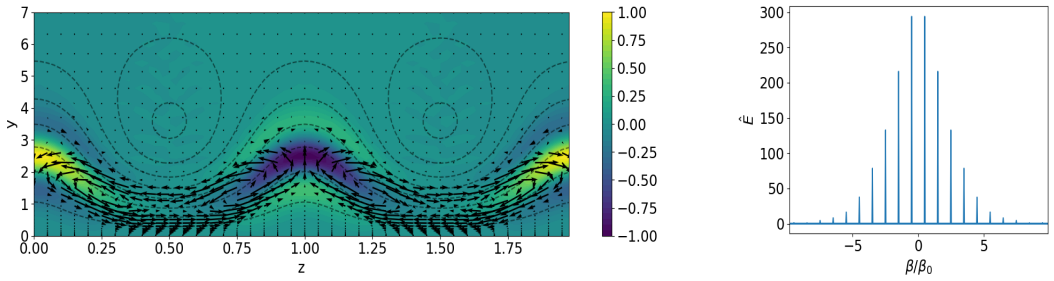

(b) $\omega_{opt} = 0.06$, ρ_{15}

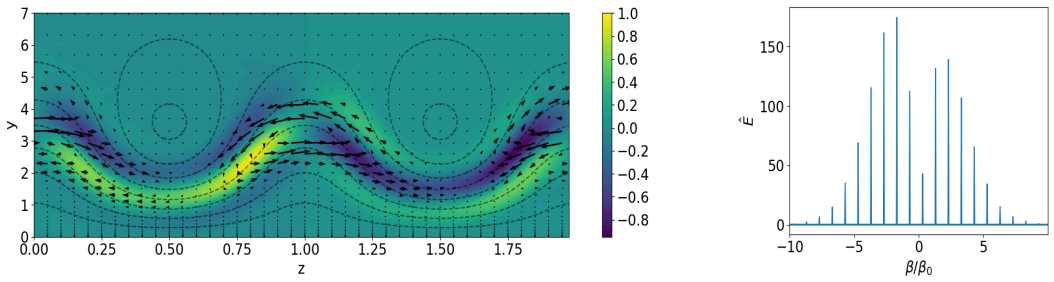

(c) $\omega_{opt} = 0.09$, ρ_9

Figure 3.22: Left: Coloured contours of the streamwise component of the optimal forcings for $Re_\delta = 430$, $\alpha = 0.15$, $A = 0.35$, for the three pseudo-resonant frequencies. Quiver plot denotes the cross-flow dynamics $(v - w)$ and dotetd lines the isocontours of the secondary base flow U_0. Right: Spatial Fourier spectrum of the kinetic energy of the disturbances.

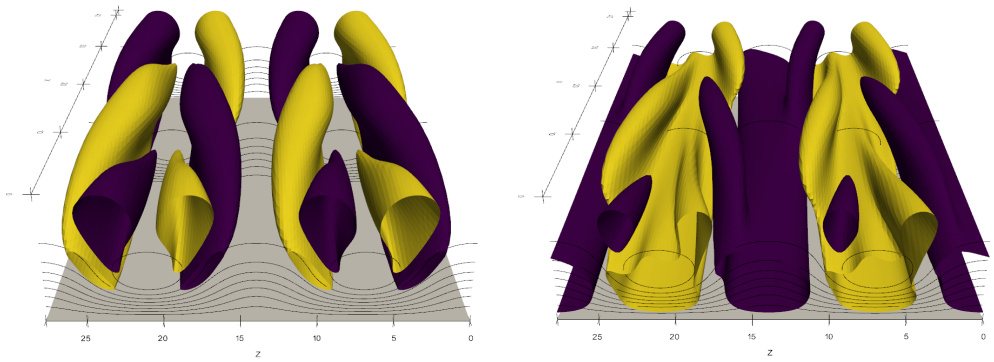

(a) $\omega_{opt} = 0.15$, ρ_0

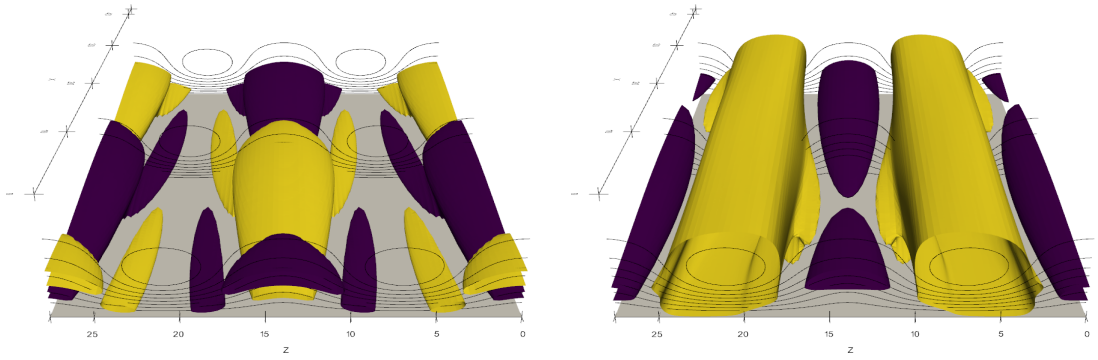

(b) $\omega_{opt} = 0.06$, ρ_{15}

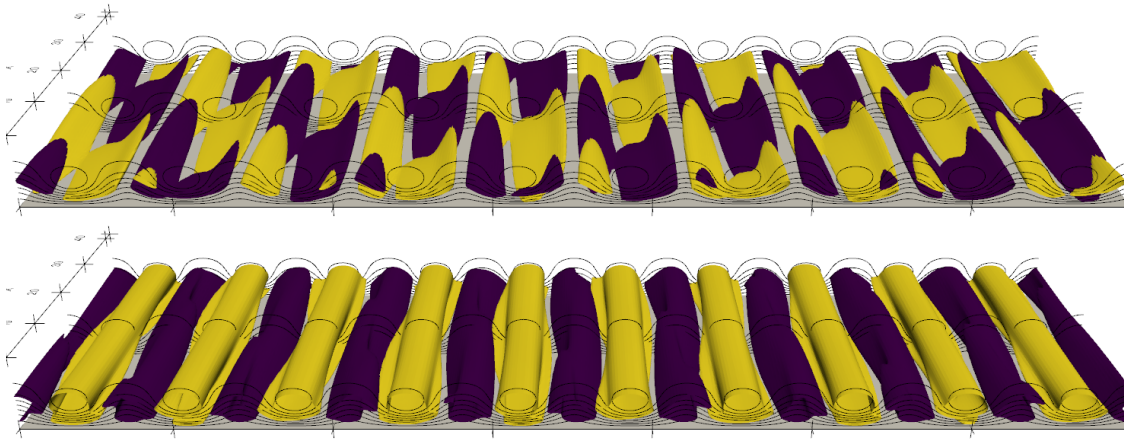

(c) $\omega_{opt} = 0.09$, ρ_9

Figure 3.23: Streamiwse component of the optimal response for $Re_\delta = 430$, $\alpha = 0.15$ and $A = 0.35$ and the different pseudo-resonances. The left/top figures is the optimal response by itself. The right/bottom figures are a superposition of the previous response and the secondary base flow. This superposition is made with an arbitrary coefficient and is done only for visualisation purposes and to identify which regions of the streaks will deform first.

of the high-velocity streaks. Ultimately, for $\omega = 0.09$ (see the bottom rows of figure 3.23), the forcing appears to be contained in the upper part of a single low-velocity streak. In turn, this causes a large-scale oscillation of the bottom part of the high-velocity streaks and of the top part of the low-velocity streaks, quite similarly to the meandering of the streaks that can be seen in Wu *et al.* (2017) for example. Notice also the strong similarity of the cross-flow dynamics between the optimal forcing ω and the optimal initial perturbations found previously (see figure 3.16).

Chapter 4

Stability of the flow over homogenised superhydrophobic surfaces: roughness anisotropy and cross-flow effects

Contents

4.1 Problem formulation

The flow of an incompressible Newtonian fluid in a channel of height $2h$ with superhydrophobic (SH) walls is considered. The reference frame is chosen as (x, y, z), with x being the streamwise direction, y the wall normal and z the spanwise direction. Following Picella *et al.* (2019); Picella (2019), we introducing the reference velocity $U_r = 3U_a/2$, with U_a being the average of the base flow velocity $U_a = 1/2h \int U dy$ and the kinematic viscosity of the fluid ν, the Reynolds number is defined as $Re = U_r h/\nu$. The dynamics of the flow is governed by the Navier-Stokes equations:

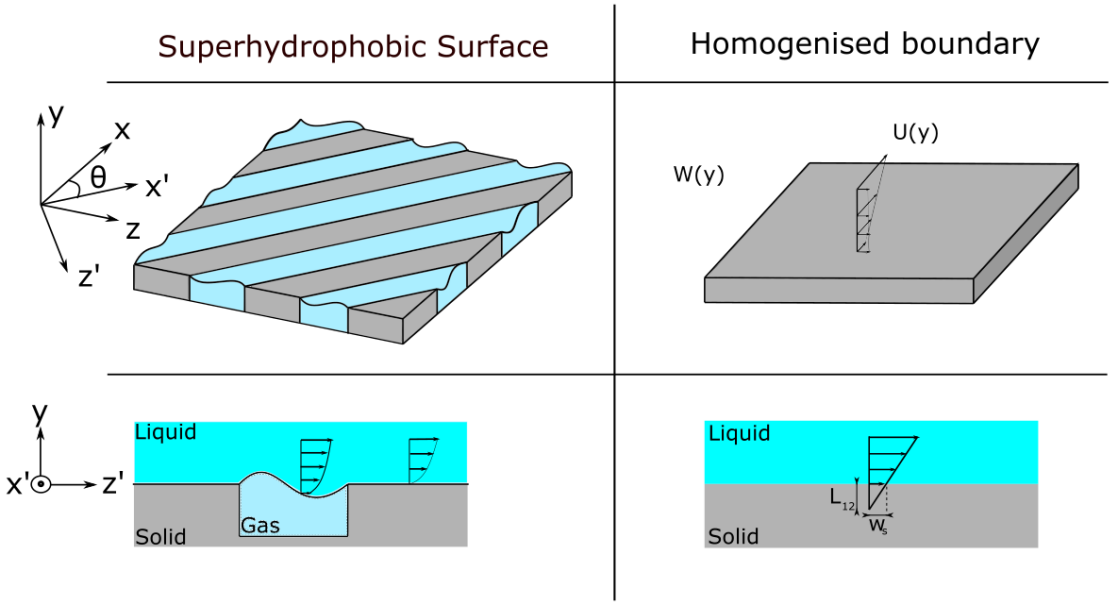

Figure 4.1: Channel flow over superhydrophobic surfaces oriented at an angle θ with respect to the streamwise direction. The superhydrophobic surface depicted in the left is homogenised and reduces to an anisotropic boundary condition.

$$\frac{\partial \mathbf{U}}{\partial t} = -(\mathbf{U}\cdot\nabla)\mathbf{U} - \nabla p + \frac{1}{Re}\nabla^2\mathbf{U} \tag{4.1}$$

$$\nabla\cdot\mathbf{U} = 0, \tag{4.2}$$

where $\mathbf{U} = (U, V, W)^T$ is the velocity vector and p is the pressure. The flow is periodic in the streamwise and spanwise directions, and different domain sizes will be considered, as detailed in section 4.3. The walls of the channel are covered with SH riblet-like roughnesses oriented with an angle θ, defined with respect to the x direction (see figure 4.1).

For $\theta = 0^o$, the grooves are longitudinal while $\theta = 90^o$ corresponds to transverse riblets. The effect of longitudinal SH riblet-like roughnesses can be modelled using equivalent streamwise and spanwise slip lengths $\lambda_{\parallel}$ and $\lambda_{\perp}$ (Gogte *et al.*, 2005; Belyaev & Vinogradova, 2010), which lead to the homogenised boundary conditions $U = \lambda_{\parallel}\partial_y U$, $V = 0$, and $W = \lambda_{\perp}\partial_y W$. When the grooves are aligned with the mean pressure gradient, the streamwise slip length is twice the spanwise one, i.e. $\lambda_{\parallel} = 2\lambda_{\perp}$ (Philip, 1972; Asmolov & Vinogradova, 2012). Whereas, when the riblets are not aligned with the pressure gradient, the homogenised boundary conditions for the Navier-Stokes equations have a more general form:

$$\begin{bmatrix} U \\ W \end{bmatrix} = \mp \mathbf{L} \partial_y \begin{bmatrix} U \\ W \end{bmatrix}, \quad V = 0, \quad \text{at} \quad y = \pm 1 \tag{4.3}$$

where the mobility tensor $\mathbf{L}$ depends on $\lambda_{\parallel}$, $\lambda_{\perp}$ and on the rotation matrix $\mathbf{R}(\theta)$, allowing the rotation of the roughness of an angle θ (Pralits *et al.*, 2017):

$$\mathbf{L} = \mathbf{R} \begin{pmatrix} \lambda_{||} & 0 \\ 0 & \lambda_{\perp} \end{pmatrix} \mathbf{R}^T = \frac{\lambda_{\parallel}}{2} \begin{pmatrix} 1 + \cos^2\theta & \cos\theta \sin\theta \\ \cos\theta \sin\theta & 1 + \sin^2\theta. \end{pmatrix} \tag{4.4}$$

Notice that the mobility tensor can be expressed as a function of $\lambda_{\parallel}$ and θ only.
Following Pralits *et al.* (2017), we set $\lambda_{\parallel} = 0.03$ and $\theta = 45^o$ yielding $L_{11} = L_{22} = 0.0225$ and $L_{12} = L_{21} = 0.0075$. These effective slip lengths comply with the wetting-stable conditions reported by Seo *et al.* (2018). As found by Pralits *et al.* (2017), the laminar base flow takes the form $\mathbf{U}_0 = (U_0(y), 0, W_0)$, with:

$$U_0 = \frac{2L_{11} + 1 - y^2}{1 + 3L_{11}}, \qquad W_0 = \frac{2L_{12}}{1 + 3L_{11}} \tag{4.5}$$

The streamwise component of the base flow is similar to that found for a Poiseuille flow with a partially slippery wall with $\lambda_{\parallel} = \lambda_{\perp}$ (Philip, 1972; Picella *et al.*, 2019). Note that U_0 has the same mass flux as a plane Poiseuille flow with no slip. The Reynolds number remains fixed when the slip length is changed, justifying the use of U_r as the reference velocity. The presence of a spanwise base flow component, which remains constant across the wall-normal direction may seem counter-intuitive. However, being one order of magnitude smaller than the streamwise component, the spanwise one will mostly affect the near-walls regions, while having negligible effects in the centre of the channel.

4.2 Linear stability analysis

4.2.1 3D TS waves and cross-flow vortices

Linear stability of the previous base flow is investigated. Perturbation equations can be found in chapter 2. In the present configuration, Squire's theorem does not hold as shown by Pralits *et al.* (2017). Thus, stability is investigated in the full (α, β, Re) domain, for $\lambda_{\parallel} = 0.03$ and $\theta = 45^o$. For a parametric study over the influence of $\lambda_{\parallel}$ and θ on the linear stability analysis, the reader is referred to Pralits *et al.* (2017). Mainly, two main unstable zones can be identified: a patch for small values of α and $\beta \neq 0$ and a horseshoe region at small α and β closer to zero. A strong asymmetry of the neutral isosurface can be seen: perturbations are most unstable in the opposite direction of the cross-flow

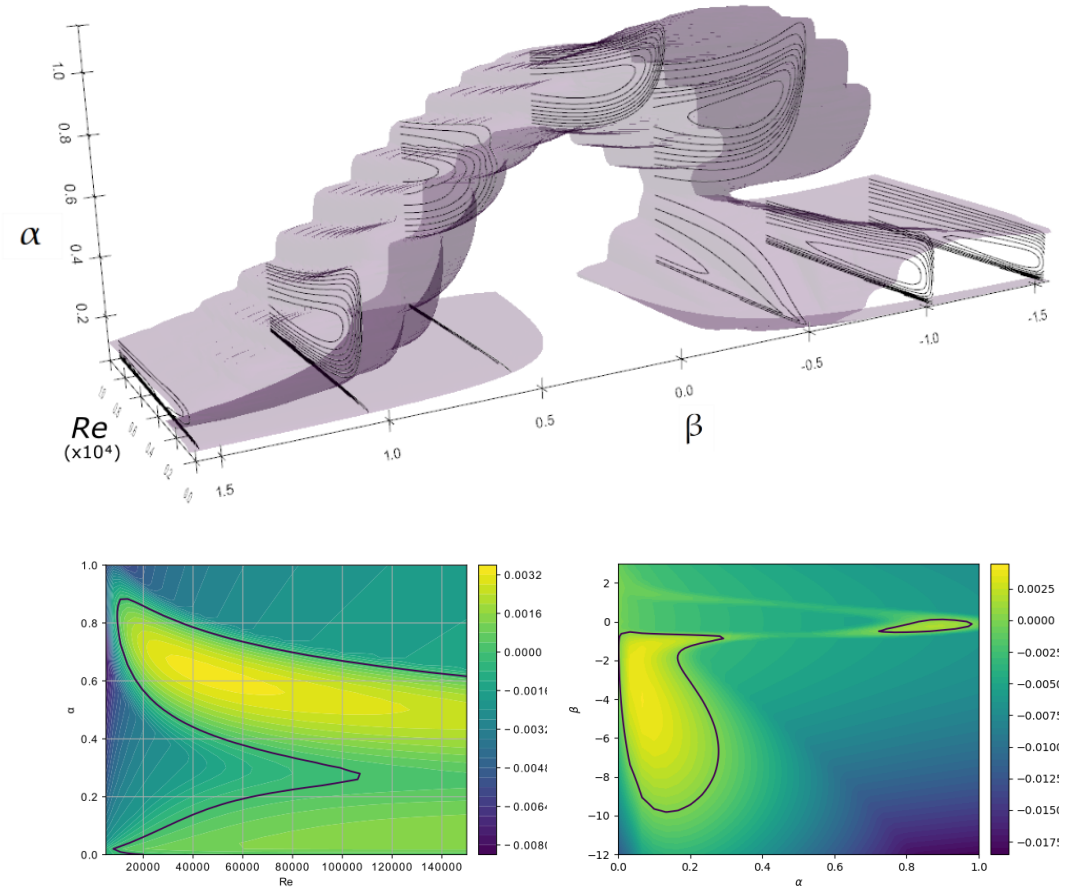

Figure 4.2: Top: Neutral surface in the $\alpha - \beta - Re$ space. Contour plots: slices of the isosurface for a few chosen β. Isocontours are only depicted in the unstable regions ($\omega_i > 0$). Bottom: Neutral curve in the $\alpha - Re$ plane for $\beta = -0.5$ (left) and in the $\alpha - \beta$ plane for $Re = 12000$ (right). Black contours correspond to the projection of the neutral isosurface in the respective planes.

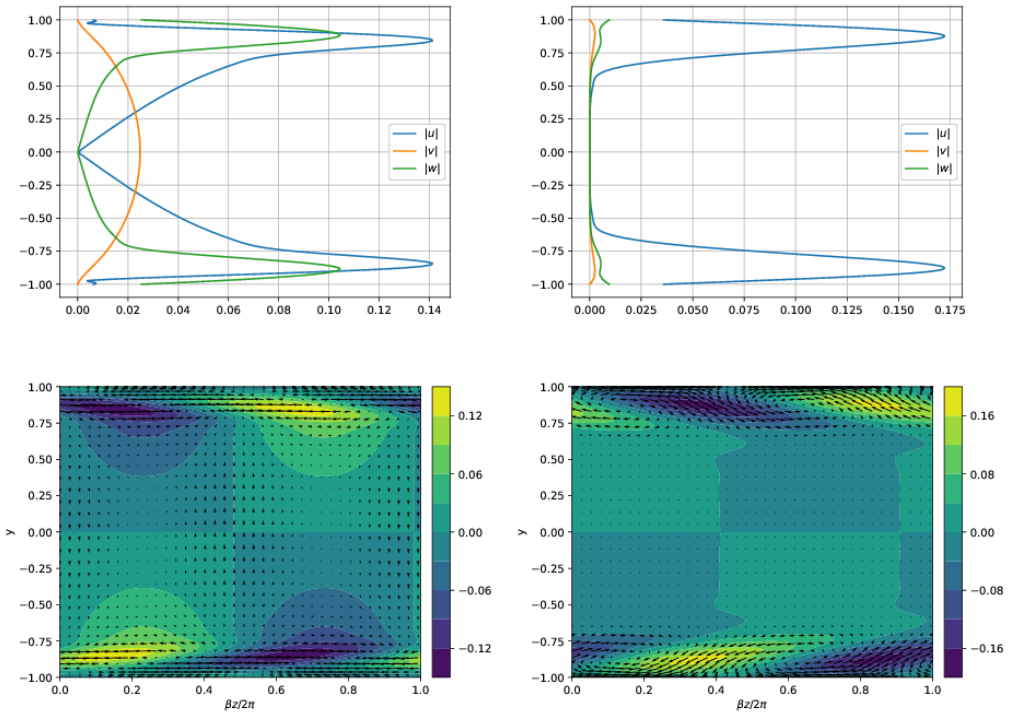

Figure 4.3: Eigenfunctions of the most unstable mode for the two identified regions of interest: for the left column, $\alpha = 0.7$, $\beta = -0.6$ and $\omega = 0.0004 - 0.1643j$ (TS wave) and for the right column, $\alpha = 0.2$, $\beta = -6$ and $\omega = 0.0033 + 0.02245j$ (CF vortices). Top row: absolute value of the disturbance velocity components. Bottom row: the contour plot represents the streamwise velocity disturbance while quiver plot shows the $v - w$ cross-flow.

base flow velocity ($\beta < 0$). This has already been noticed for swept wings (Mack, 1984). Slices of the neutral isosurface in the $\alpha - Re$ and $\alpha - \beta$ planes, showing the regions of strongest instability, are provided in the bottom of Figure 4.2.

For further insight, Figure 4.3 displays several representations of the eigenfunctions of the most unstable mode for both regions. The horseshoe instability region is reminiscent of the unstable region of both classic and homogeneous slip Poiseuille flows. The usual shape of a 3D TS-wave (Zang & Krist, 1989) is also retrieved. The second region exhibits modes with tilted counter-rotating vortices. These vortices are quasi-stationary ($\omega_i = 0.022$) and propagate almost perpendicularly to the streamwise direction ($\phi = \arctan(\beta_0/\alpha_0 \approx 88^o$). All these characteristics are reminiscent of unstable modes of swept boundary layers (Mack, 1984; Saric *et al.*, 2003; Serpieri & Kotsonis, 2016) or rotating disks flows (Lingwood, 1995) linking this region to cross-flow (CF) related instability mechanisms. This is

unusual: cross-flow instability is usually depicted as a mainly inviscid mechanism (Saric *et al.*, 2003), thus necessitating an inflection point in the spanwise velocity W_0. For a fixed Reynolds number, cross-flow related modes are more unstable than the Tollmien-Schlichting (TS) waves. The presence of this new instability region can be explained in a rather simple way. The boundary conditions (B.1) represent a system of equations for (u, w) which, assuming 1D profiles, can be solved. The solution is physically meaningful only in the close vicinity of the walls but can still provide some interesting insight on the physics in this region. Thus, for a wall at $y = 0$, the inversion of the system (B.1) yields:

$$\begin{bmatrix} u \\ w \end{bmatrix}(y) = \begin{bmatrix} U_0^+ \\ U_0^+ \end{bmatrix} \exp\left(y/L^+\right) + \begin{bmatrix} U_0^- \\ -U_0^- \end{bmatrix} \exp\left(y/L^-\right) \tag{4.6}$$

where $L^+ = L_{11} + L_{12}$, $U_0^+ = \frac{1}{2}(u_0 + w_0)$, $L^- = L_{11} - L_{12}$ and $U_0^- = \frac{1}{2}(u_0 - w_0)$, while u_0 and w_0 are the values of the u and w perturbations at the wall.

Taking advantage of the modal assumption, the normal velocity component $v(y)$ can be deduced from the continuity equation and reads:

$$v(y) = -i\left[(\alpha+\beta)U_0^+ L^+ \exp\left(y/L^+\right) + (\alpha-\beta)U_0^- L^- \exp\left(y/L^-\right)\right] \tag{4.7}$$

Recalling that the normal velocity is zero at $y = 0$, a relation linking the different parameters can be obtained:

$$\alpha = -\frac{U_0^+ L^+ - U_0^- L^-}{U_0^+ L^+ + U_0^- L^-}\beta. \tag{4.8}$$

From (4.8), two extreme cases can be distinguished: a first one in which $w_0 >> 0$ and a second one with $w_0 \approx 0$. Since L^+ and L^- are fixed parameters, the former leads to $U_0^+ L^+ >> U_0^- L^-$ and $\alpha \approx -\beta$ while the latter implies $U_0^+ L^+ \approx U_0^- L^-$ and $\beta >> \alpha$. The boundary condition appears to act as a mode selector, and these two distinct behaviours roughly correspond to the previously identified instability regions.

Despite this model, the influence of the boundary condition on these two instability mechanisms is not completely clear. Since TS waves are viscosity-induced near-wall structures, they will be affected by a decrease of the velocity gradients near the walls caused by the slip boundary conditions (Min & Kim, 2005; Picella *et al.*, 2019). However, cross-flow effects are also prominent in the vicinity of the

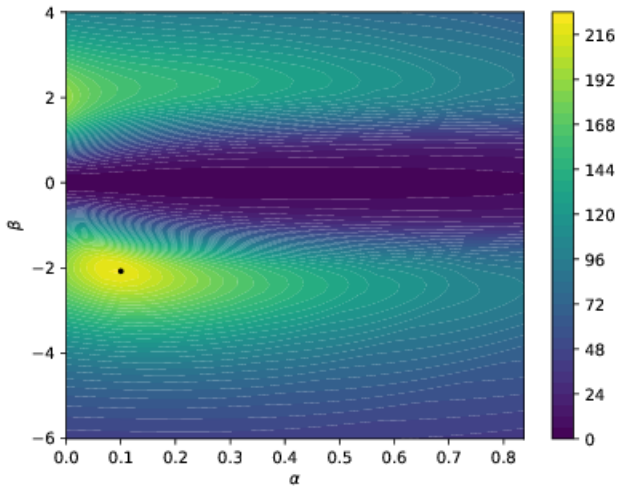

Figure 4.4: Optimal energy gain contours in the $\alpha - \beta$ plane for $Re = 1000$. The Reynolds number is chosen sufficiently low to ensure stability of the flow. The black dot corresponds to the maximum energy gain obtained for $\alpha = 0.1$ and $\beta = -2.0$.

walls and a strong influence on the evolution of the 3D TS wave is expected. Regarding cross-flow modes, they are characterised by counter-rotating vortices which, despite being rather weak, affect the stability of the flow by redistributing low-momentum flow from the near-wall regions to the centre of the channel and, conversely, re-injecting high-momentum flow near the walls (Bippes, 1999; Serpieri, 2018), potentially destabilising the flow. Once again, the intensity reduction of the velocity gradients near the walls will impact the strength of the shear layers and the redistribution mechanism, albeit it is still not clear to which extent.

4.2.2 Oblique streaks, transient growth and a modified lift-up mechanism

In subcritical conditions, non-modal mechanisms, linked to the non-normality of the Navier-Stokes equations, can induce a transient growth of the energy of small perturbations. Such a growth can be several orders of magnitude higher than the initial energy perturbation (Gustavsson, 1991; Reddy & Henningson, 1993) thus playing a crucial role in the transition to turbulence. This behaviour is typically investigated by maximising the finite-time amplification of an initial velocity perturbation $\mathbf{u}_0$ (Butler & Farrell, 1992*a*). Mathematically, the quantity to be optimised can be written as:

$$G(T) = \max_{\mathbf{u}_0} \frac{E(\mathbf{u}(T))}{E(\mathbf{u}_0)}$$

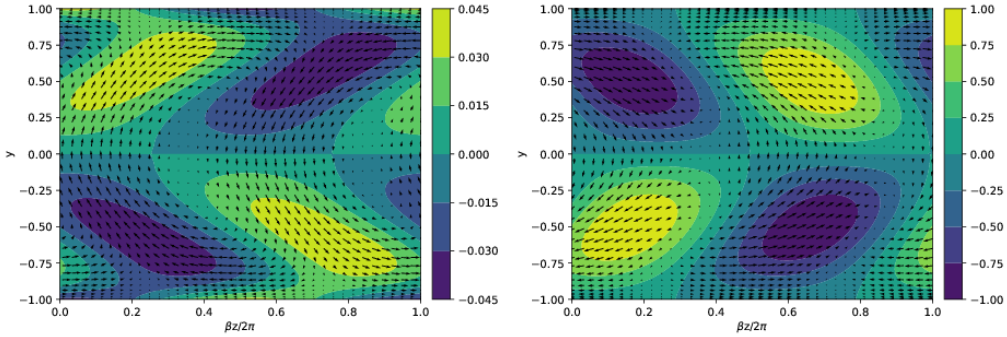

Figure 4.5: Optimal perturbation at time $t = 0$ (left) and at target time $t = T = 82$ (right). The contour plot represents the streamwise component of the perturbed velocity while the quiver plot depicts the $v - w$ cross-flow.

where $E(T)$ is the kinetic energy of a perturbation at target time T, defined as

$$E(\mathbf{u}(t)) = \frac{1}{2L_x L_z} \int_V |\mathbf{u}|^2 dV,$$

where V is the volume of the computational domain of streamwise and spanwise length L_x and L_z, respectively.

Figure 4.4 provides the optimal energy gain G in the $\alpha - \beta$ plane, which appears to be strongly affected by the presence of the wall slip. The maximum gain can be obtained for a small but non-zero α and for $\beta = -2$, differently from the channel flow with no-slip walls (Butler & Farrell, 1992*a*). Previous studies (Min & Kim, 2005; Picella *et al.*, 2019) have assessed that isotropic slip conditions have a marginal effect on transient growth. Thus, we conjecture that transient growth is mainly affected by cross-flow related effects. Notice that the region of maximum energy growth overlaps with the cross-flow instability region, hinting at the coexistence of both mechanisms. Similar results were found in the non-modal analysis conducted by Breuer & Kuraishi (1994) and Corbett & Bottaro (2001) on swept wings.

The optimal perturbation ensuring the maximum transient growth is given in Figure 4.5. The initial perturbation (left frame) consists in quasi-streamwise tilted counter-rotating vortices. The vortices are tilted in the opposite direction of the cross-flow component of the base flow and distorted by the slip conditions in the near-wall regions. The cross-flow components have an amplitude one order of magnitude higher than the streamwise component. At the optimal time, the perturbation takes the form of velocity streaks slightly tilted in the cross-flow direction. Non-modal growth is usually the

product of two mechanisms: the Orr mechanism and the lift-up effect (Brandt, 2014). Since the Orr mechanism is more efficient for short ($\mathcal{O}(10)$) time scales and high streamwise wavenumbers (Butler & Farrell, 1992*a*), in the present case the transient growth is most probably linked to the lift-up effect (Landahl, 1980). However, differently from the classical case of the channel flow with no-slip walls, in the present case the perturbation can transport both the streamwise and spanwise base flow shear, inducing changes in both the optimal perturbations and the optimal gain. Notice that the shape of this optimal perturbation resembles that of weakly nonlinear optimal perturbations computed for a channel flow by Pralits *et al.* (2015).

Ellingsen & Palm (1975) derived a model which showed algebraic growth for the amplitude of streamwise independent perturbations in time. A generalisation of this model for 3D base flows is not trivial, except for small angles for which the mechanisms remain similar. However, in the specific case of a constant spanwise component of the base flow, an extension of this model is possible and has been derived. Thus, following Ellingsen & Palm (1975) and Brandt (2014),. perturbations are assumed with the following modal form $u(y)\exp(i\beta z)$, with a streamwise invariance and a spanwise wavelength β. The linearised momentum equations yield:

$$\frac{\partial u}{\partial t} + i\beta W_0 u + vU_0' = 0 \tag{4.9}$$

$$\frac{\partial v}{\partial t} + i\beta W_0 v = 0 \tag{4.10}$$

$$\frac{\partial w}{\partial t} + i\beta W_0 w + vW_0' = 0 \tag{4.11}$$

Introducing a streamfunction ψ for the cross-stream components,

$$v = \partial_z \psi; \qquad w = -\partial_y \psi \tag{4.12}$$

it is possible to obtain an equation on $\nabla_s^2\psi$ with ∇_s^2 the two-dimensional laplacian in the $y-z$ plane:

$$\frac{\partial}{\partial t}\nabla_s^2\psi = -i\beta W_0 \nabla_s^2\psi + i\beta W_0' w + \partial_y v W_0' + vW_0'' \tag{4.13}$$

In the special case of a channel with two superhydrophobic walls, the spanwise component of the

base flow W_0 becomes constant, and Eq.(4.13) reduces to:

$$\partial_t \nabla_s^2 \psi = -i\beta W_0 \nabla_s^2 \psi \tag{4.14}$$

Now, unlike the usual lift-up effect, cross-stream components are now dependant of time: they oscillate with frequency βW_0. Since $v(t) \propto e^{-i\beta W_0 t}$ as suggested by Eq.(4.14), the linearised streamwise momentum equation can be integrated in time to obtain:

$$u(t) = u_0 \cos(\beta W_0 t) - v_0 U' t \tag{4.15}$$

While the classical algebraic growth is retrieved, a new term, due to cross-flow effects, appears. This term induces, for early times, an oscillation of frequency βW_0 of the amplitude of the streamwise velocity of the perturbation.

4.3 Direct numerical simulations

Laminar-turbulent transition to turbulence is further investigated through direct numerical simulations realised with the spectral solver solver Nek5000. For more information on the solver or on the implementation of the homogenised boundary conditions, the reader is referred to Appendix B. Two transition scenarii are considered: one initiated with a 3D TS wave having $(\alpha_0, \beta_0) = (0.7, -0.6)$, presented in section §4.4, and the other with a CF mode having $(\alpha_0, \beta_0) = (0.2, -6)$, discussed in section §4.5. This choice of wavenumbers results from a compromise between their distance to the neutral curve and the numerical cost of the simulation, since the computational domain would depend on the perturbation wavenumber. The domain sizes are respectively $[L_x, L_y, L_z] = [2\pi/\alpha_0, 2, 2\pi/\beta_0]$ and $[L_x, L_y, L_z] = [2\pi/\alpha_0, 2, 6\pi/\beta_0]$. In the CF case, a larger computational box in the spanwise direction is used to partially relax the restriction on the wavelengths of developing modes. For the CF scenario, the selected wavenumbers were also chosen not be in the region of important transient growth in an attempt to separate the different instability mechanisms. In both cases, the Reynolds number is $Re = 12000$. Both spatial (Wassermann & Kloker, 2002, 2003) and temporal (Wintergerste & Kleiser, 2000; Koch, 2002) DNS frameworks are valid and have been considered in studies of swept flows. All the numerical parameters employed in these two cases can be retrieved in table 4.1. Spectral elements in the wall-normal direction have been distributed following a Chebyshev grid to further increase the spatial resolution near the walls.

	L_x	L_y	L_z	N_x	N_y	N_z	N_p
TS case	8.9759	2	10.4720	32	24	26	8
CF case	31.4159	2	3.1415	90	32	10	8

Table 4.1: Numerical parameters for the two simulations. N_p denotes the polynomial order of the elements.

From a numerical point of view, supercritical transition can be triggered by superposing on the base flow (4.5) the most unstable wave found from the linear stability analysis, as:

$$\mathbf{U}(\mathbf{x}, t = 0) = \mathbf{U}_0(\mathbf{x}) + A\mathbf{u}(\mathbf{x})$$

where A is the amplitude of the initial perturbation which is set such as, in all the following, $E_c(t = 0) \approx 10^{-5}$. This low value for the disturbance energy density ensures a phase of linear exponential growth before nonlinear effects arise.

For further insight, several indicators are monitored through the simulation, most notably the kinetic energy density of the disturbance (as previously defined) and the friction Reynolds number, which is defined as:

$$Re_\tau = \sqrt{Re|\partial_y \overline{U}(\mathbf{x}, t)|_{\pm 1}} \tag{4.16}$$

where the overbar denotes spatial averaging on the $x - z$ plane. This quantity will brutally increase during the turbulent breakdown while remaining almost constant for both laminar and turbulent flows. In the laminar case, the friction Reynolds number can be found analytically and reads:

$$Re_\tau = \sqrt{\frac{2Re}{1 + 3L_{11}}} \approx 150$$

Transition to turbulence can also be investigated through the evolution of the spectral energy associated with Fourier modes (Zang & Krist, 1989; Schmid, 2001):

$$\hat{E}_{k_x,k_z} = \frac{1}{2}\int_{-1}^{1} |\hat{u}_{k_x,k_z}(y, t)|^2 dV \tag{4.17}$$

where $\hat{u}_{k_x,k_z}(y, t)$ is the Fourier mode of the perturbation velocity field with streamwise and spanwise wavenumbers k_x and k_z, respectively. Following the formalism of Schmid (2001), the mode

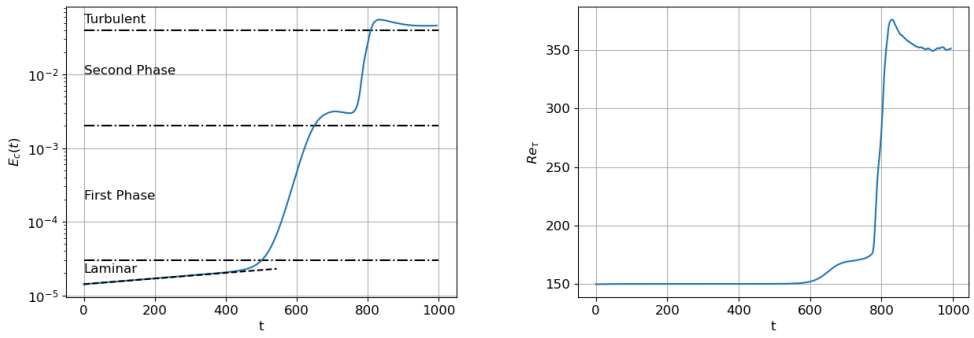

Figure 4.6: Evolution of the disturbance kinetic energy density (left) and Re_τ (right). The dashed line has a slope $2\omega_r$, where $\omega_r \approx 0.00044$ is the growth rate of the most unstable mode found by means of linear stability analysis.

denoted as (m, n) corresponds to the $(m\alpha_0, n\beta_0)$ Fourier mode. Finally, the transition scenario can also be monitored in the frequency domain through a temporal Fourier transform.

4.4 First scenario: 3D TS waves

4.4.1 Overview of the transition

The transition scenario initiated by a three-dimensional TS wave with $(\alpha_0, \beta_0) = (0.7, -0.6)$ is investigated. The time evolution of the kinetic energy evolution and friction Reynolds number are provided in figure 4.6, while figure 4.7 depicts the evolution of the spectral energy for several Fourier spatial modes. In the initial phase, the kinetic energy density displays an exponential increase, with a growth rate in perfect agreement with the linear stability analysis. Figure 4.7 shows that the Fourier mode $(1, 1)$, which is the only finite-amplitude mode present in the flow at early times, follows this evolution. Temporal Fourier analysis of this first phase of transition ($0 < t < 500$), provided in figure 4.10, exhibits a strong peak at $f = 0.024$, corresponding to the frequency of the TS wave. Figure 4.8 (top row) shows that at $t = 200$, the perturbation is still characterised by a TS wave shape.

Meanwhile, at $t \approx 100$, the mode $(0, 16)$ starts oscillating with a period $T_0 = 47$. The period of the oscillations is in good agreement with the one analytically found in 4.15, namely $2\pi/(\beta W_0) = 46.58$, hinting at the presence of the modified lift-up previously described. Notice that these oscillations can be observed only on this high wavenumber mode, while other streamwise-invariant Fourier modes such as $(0, 1)$ (see figure 4.7) does not display an initial oscillatory phase. A possible reason for this

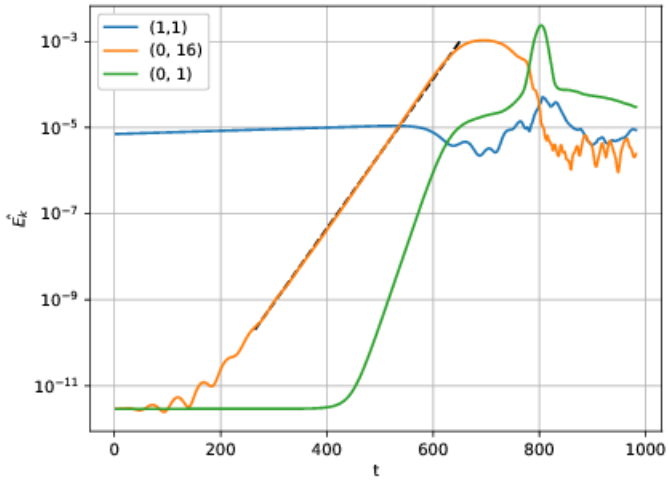

Figure 4.7: Time evolution of the Fourier modes (1,1), (0,16) and (0,1). The dashed line has a slope $2\sigma \approx 0.04$. Notice the oscillations in the early evolution of mode (0,16).

behaviour is that both the target time at which maximum transient growth is recovered, T_{opt}, and the oscillation period, T_0, are much larger for small spanwise wavenumbers. Respectively, for $(0, 16)$, it can be found that $T_{opt} = 100$ and $T_0 = 47$ while $T_{opt} = 615$ and $T_0 = 639$ for the $(0, 1)$ mode, which is a too large period to be observed during the linear phase of the perturbation evolution.

After $t \approx 280$, the $(0, 16)$ mode exhibits exponential growth, characteristic of a secondary instability. At $t \approx 520$, the $(0, 16)$ mode becomes more energetic than the primary one. At the same time, a brutal increase in the kinetic energy indicates that the first step of transition to turbulence has initiated. This translates into a change in the topology of the mode characterised by the onset of near-wall streamwise-elongated coherent structures, shown in figure 4.8 (second and third rows from the top). These streaky structures are characterized by a large spanwise wavenumber, $\beta = -9.6$, corresponding almost exactly to 16 times the fundamental spanwise wavenumber β_0 (namely, $\beta = 16\beta_0 = -9.6$). Temporal Fourier transform carried out in the time range $(0 < t < 800)$ corresponding to the first phase of transition shows the onset of low-frequency oscillations at $f = 0.007$ (see right frame of figure 4.10) which seems to be associated to such high-wavenumber spatial oscillations.

In this transition phase, energy is taken from the 3D TS wave and transferred to these oblique waves, (see figure 4.8, third and fourth rows from the top) ultimately leading to the disappearance of the TS wave. As it can be seen in figure 4.9, showing the spatio-temporal evolution of the streamwise

(left) and spanwise (right) components of the velocity, these streaky structures are not streamwise independent and are oriented with an angle $\phi = 9^o$ with respect to the streamwise direction, almost perpendicular to the initial 3D TS wave. Notice also how the first phase of the transition leads to the suppression of the spanwise velocity component, confirming the streaky nature of the structures.

At $t = 650$, the kinetic energy reaches a plateau for $E = 3 \times 10^{-3}$ as the secondary instability saturates (see figure 4.6). Ultimately, tertiary instability triggers, at $t \approx 800$, a dramatic increase in the friction Reynolds number, indicating the breakdown into a fully turbulent state. This final transition can be linked to the $(0, 1)$ mode, as suggested by its sudden growth at such time (see figure 4.7). The nature of this final instability is quite complex: it is highly nonlinear as suggested by the presence of harmonics of both primary and secondary modes, which can be observed in the right frame of figure 4.10. It also appears to be, to some extent, related to streak instability. Figure 4.9 (bottom row) depicts streaky structures which, quite interestingly, have lost their orientation and are now aligned with the streamwise direction. The streak instability can be observed at time $t \approx 700$ in the two bottom rows of figure 4.8 and in the bottom left frame of figure 4.9).

Quite notably, this transition scenario is fundamentally different from the usual transition scenario in channel flows. Indeed, supercritical transition to turbulence in channel flow is well documented in the no-slip case (Zang & Krist, 1989; Schmid, 2001): after an initial exponential growth phase, secondary instability of a subharmonic mode appears. The interaction between the TS wave and the secondary modes leads to a peak-valley structure (Herbert, 1985; Asai & Nishioka, 1989) which, in turn, results in the formation of a staggered pattern of λ-vortices. Then, λ-vortices subsequently develop into hairpin vortices that will ultimately breakdown into turbulence. In the slip case, with a homogeneous Navier slip boundary condition, Picella *et al.* (2019) have shown that a delay of the laminar-turbulent transition is possible, but the nature of the instability mechanisms remains virtually the same.

In the present case, the cross-flow component of the base flow appears to have a dramatic effect on the transition scenario. Similarly to what we have reported concerning the primary instability, this cross-flow component might originate a new secondary instability mechanism, which would be investigated in the next subsection. If these cross-flow related secondary modes have higher growth rates than the subharmonic ones leading to λ_2 vortices (Herbert, 1985), the secondary phase of transition would be dominated by cross-flow related mechanisms.

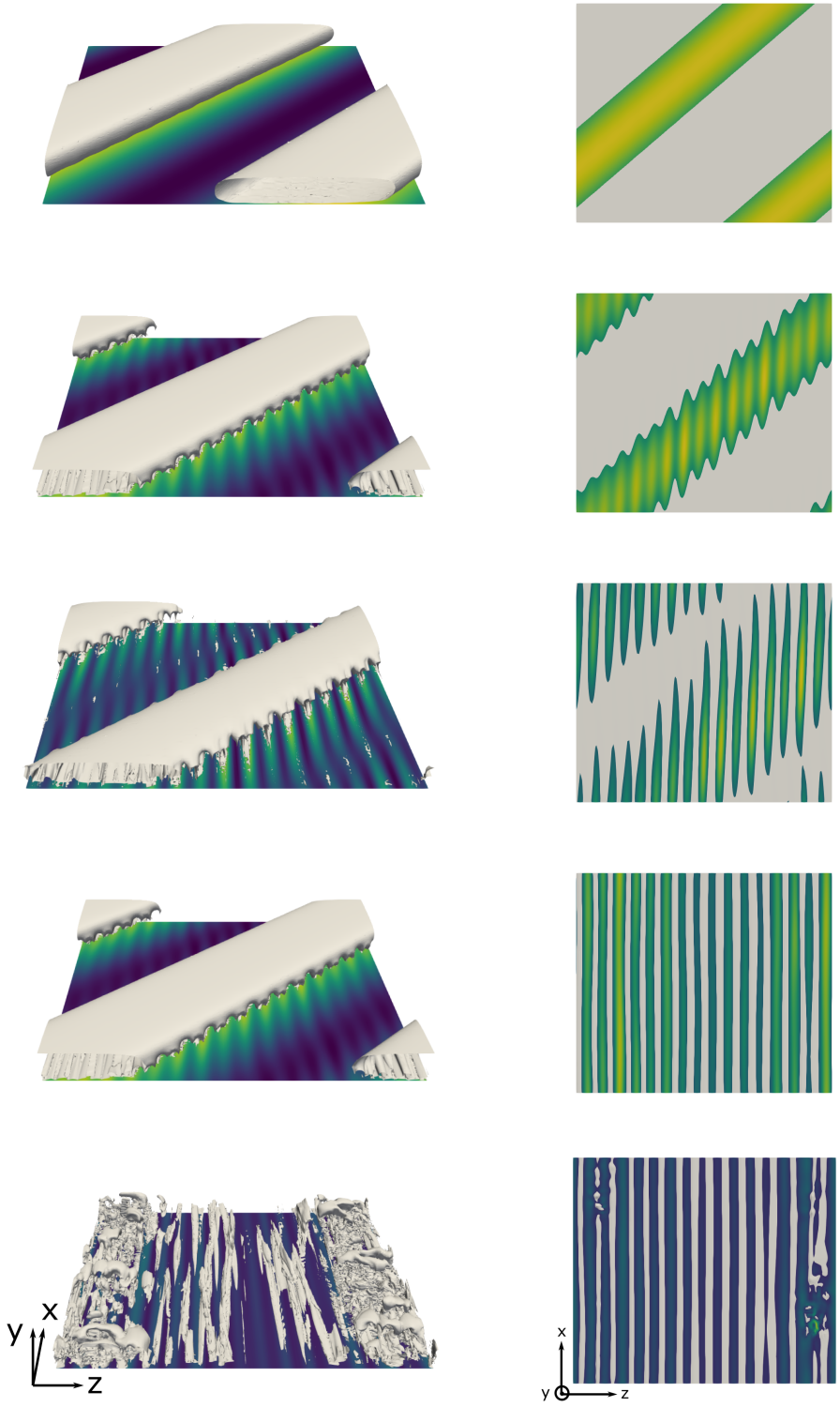

Figure 4.8: Snapshots of the flow at different time T. From top to bottom: $T = 200$, $T = 400$, $T = 600$, $T = 800$ and $T = 900$. Left: Isosurfaces of the λ_2-criterion, $\lambda_2 = -10^{-5}, -10^{-4}, 0.25$, respectively, and contours of the streamwise velocity at the wall. Right: Isosurface of the streamwise velocity ($U \approx 0.047$) and contours of u at the wall. The flow is from bottom to top, and left to right. For the sake of clarity, only half channel is shown.[105]

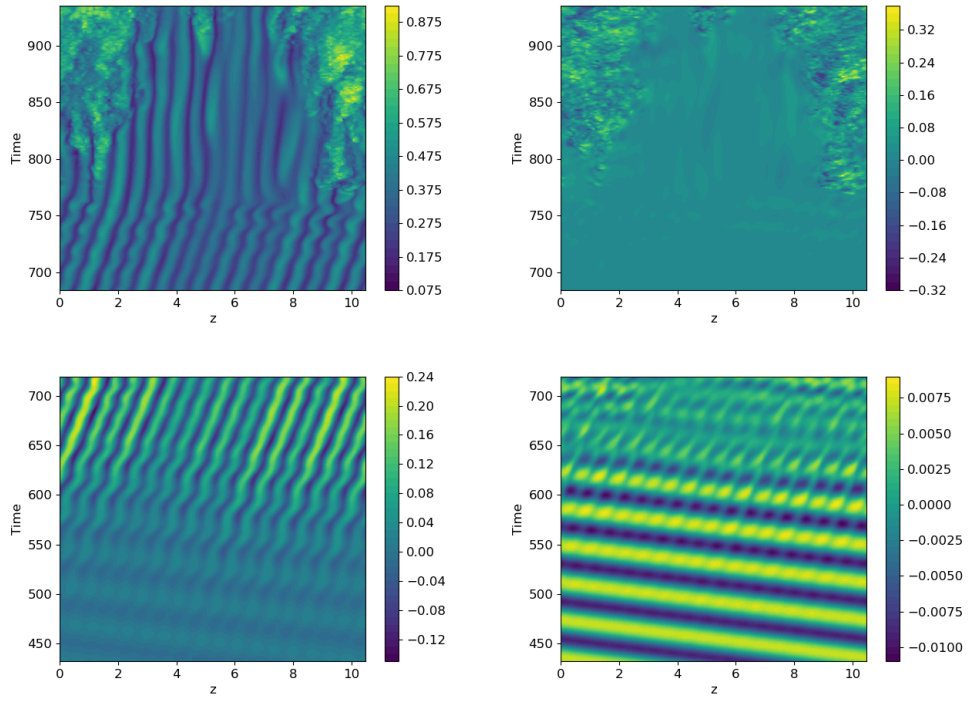

Figure 4.9: Spatio-temporal evolution of the streamwise (left column) and spanwise (right column) components of the velocity at $x = 0$ and $y = -0.85$. For visualisation purposes, the first (second) phase of the transition is depicted separately in the first (second) row.

As observed in swept flows (Serpieri, 2018), during this secondary phase, oblique waves appear and eventually, through nonlinearities, saturate. The saturated cross-flow vortices contain several strong shear layers, which can, under certain circumstances, further destabilise. The most common instability mechanism observed in such flows (Bippes, 1990, 1999) involves the shear layer at the bottom of the vortex, created from the circulation of high-speed fluid toward lower velocities region near the wall.

In the present case, the slip boundary conditions reduce the efficiency of this mechanism by lowering the wall normal velocity gradients near the walls. Instead, the flow keeps accelerating in the spanwise direction until it reaches a neighbouring vortex, thus creating stagnation points and strong shear layers in the spanwise direction. Transient growth in this region leads to the formation of streaks (Guegan *et al.*, 2007) aligned with the streamwise direction. Streak instability concludes the transition to turbulence. This scenario of transition will be corroborated in the next subsection, by means of secondary stability analysis and comparison with DNS.

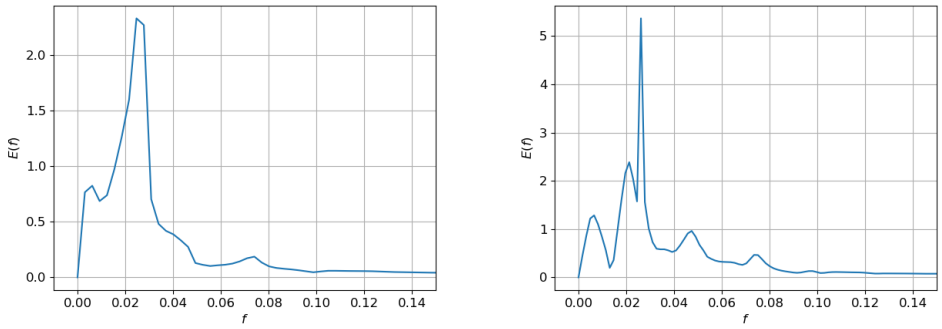

Figure 4.10: Temporal Fourier energy spectrum of transition to turbulence. The data time-series has been truncated at $t = 500$ (left) just after the onset of secondary instability and at $t = 800$ (right) before turbulence is established.

4.4.2 Floquet stability analysis

In an effort to provide a more qualitative description of the secondary phase of the transition, a secondary stability analysis, based on Floquet theory, is realised. This method has been applied to both channel flows (Herbert, 1983) and two-dimensional boundary layers (Herbert, 1985) for which it has successfully predicted the secondary instability of a 2D TS wave. An extension to three dimensional base flows was proposed and applied most notably to swept wings (Fischer & Dallmann, 1991; Janke & Balakumar, 2000; Liu *et al.*, 2008). Secondary stability equations in a velocity-vorticity formulation can be found in Fischer & Dallmann (1991). Whereas, a primitive variables formulation for 2D base flows only, can be found in Schmid (2001).

In this work, due to the three-dimensionality of the problem under consideration, we use a formulation of Floquet theory and subsequent modal expansion somewhat different (but nevertheless equivalent) from those used in these articles. In Herbert (1983) study, Squire theorem ensures a 2D initial perturbation while, for swept flows cases, an initial 3D perturbation should be considered. For this reason, Floquet theory for swept flows is usually applied in a rotated frame aligned with the 3D wave direction of propagation, thus effectively reducing the base flow to two dimensions. Precisely, the base flow for secondary stability analysis is constructed as a superposition of an unstable mode and the laminar flow profile such as:

$$\mathbf{U}_1(x, y, t) = \mathbf{U}_0(y) + A\hat{\mathbf{u}}^{TS}(y)e^{i(\alpha_0 x + \beta_0 z - \omega_0 t)} \tag{4.18}$$

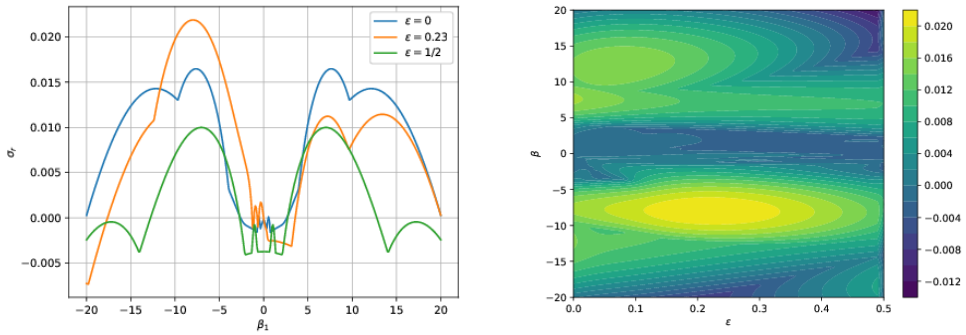

Figure 4.11: Left: Growth rate σ_r of the most unstable mode as a function of the spanwise wavenumber β_1 for $\epsilon = 0$ (fundamental), $\epsilon = 0.22$ (detuned) and $\epsilon = 1/2$ (subharmonic). Right: Contour plot of the growth rate σ_r of the most unstable mode for $\beta_1 = -9.6$ as a function of both the detuning factor ϵ and the spanwise wavenumber β_1.

with A the amplitude of the unstable 3D TS wave obtained from linear stability analysis. Considering that the TS wave moves at the velocity c_x and c_z in the x' and z' directions, respectively, the time dependence of the base flow is removed when the moving frame $(x', z') = (x - c_x t, z - c_z t)$ is considered. Linearising the Navier-Stokes equations around this new base flow in the co-moving frame leads to a system of ODEs (see chapter 2 with $2\pi/\alpha_0$-periodic and $2\pi/\beta_0$-periodic coefficients in the x- and z-directions, respectively. Thus, Floquet theorem is applied in both the streamwise and spanwise directions:

$$\mathbf{q_1}(x', y, z', t) = \tilde{\mathbf{q}}(x', y, z')e^{\gamma x'}e^{\mu z'}e^{\sigma t} \tag{4.19}$$

with $\gamma = \gamma_r + i\gamma_i$ and $\mu = \mu_r + i\mu_i$ the Floquet parameters in the streamwise and spanwise directions. Then, $\tilde{\mathbf{q}}(x', y, z')$ is Fourier transformed in both the x' and z'-directions and introducing the detuning factors $\epsilon = \sigma_i/\alpha_0$, $\delta = \mu_i/\beta_0$, the general form of the solution can be expressed as:

$$\mathbf{q_1}(x', y, z', t) = e^{\sigma t}e^{\gamma_r x'}e^{\mu_r z'} \sum_{m,n=-\infty}^{+\infty} \tilde{\mathbf{q}}_{m,n}(y)e^{i[\alpha_0(m+\epsilon)x' + \beta_0(n+\delta)z']} \tag{4.20}$$

When a numerical solution is sought, the modal expansion (4.20) needs to be truncated, usually with the lowest possible number of modes. Unfortunately, reaching the spanwise wavenumbers observed in the DNS would require a large number of modes in the z'-direction, which make the problem too computationally expensive. In order to relax this constraint, the modal expansion in the spanwise

direction is reduced to only one mode by fixing n and δ and introducing $\beta_1 = \beta_0(n+\delta)$, which represents the effective secondary spanwise wavenumber. Since $n \in \mathbb{Z}$ and $-1/2 < \delta \leq 1/2$, the quantity $n+\delta$ spans all real numbers bijectively such that every spanwise wavelength is accessible through a unique choice of n and δ.

Temporal stability is investigated, thus $\gamma_r = \mu_r = 0$ and the real part of σ indicates the growth rate of the secondary instability. Finally, the modal decomposition (4.20) reduces to:

$$\mathbf{q_1}(x', y, z', t) = e^{\sigma t} e^{i\beta_1 z'} \sum_{m=-\infty}^{+\infty} \tilde{\mathbf{q}}_m(y) e^{i\alpha_0(m+\epsilon)x'} \tag{4.21}$$

Introducing (4.21) into the linearised Navier-Stokes equations leads to an infinite set of equations which, once truncated, can be recast in an eigenvalue problem likewise the primary stability problem.

All the results given here are obtained with the lowest possible truncation that is $m = 0, 1$ in the subharmonic ($\epsilon = 1/2$) cases and $m = -1, 0, 1$ for the fundamental ($\epsilon = 0$) and detuned ($0 < \epsilon < 1/2$) modes. For the sake of clarity, the derivation of the secondary stability equations and the eigenvalue problem is fully detailed in the book of Schmid (2001). In both classic channel and boundary layer flows, the detuning factor is not relevant (Herbert, 1983, 1985): subharmonic instabilities have stronger growth rates than both fundamental and detuned modes. However, this might not be true in our case, due to the strong asymmetry induced by the spanwise component of the base flow.

The dependence of the growth rate of the most unstable mode on the detuning factor is investigated in Figure 4.11, for $Re = 12000$. A large secondary secondary growth rate can be reached for detuned modes and large spanwise wavenumbers, in the range of those recovered for the primary CF instability. The maximum secondary growth rate is $\sigma_r = 0.023$ for $\epsilon = 0.23$ and $\beta_1 = -8$. but the instability region is quite large and similar growth rates can be reached for larger β_1. Precisely, the growth rate corresponding to the spanwise wavelength observed in the DNS (namely, $\beta = -9.6$), is equal to $\sigma_r = 0.020$.

The spectrum obtained for $Re = 12000$, $\beta_1 = -9.6$, $\epsilon = 0.23$ and $A = 10^{-5}$, shown in figure 4.12, exhibits three unstable and one marginally unstable mode. All the modes share a similar structure: the $m = 0$ mode, yielding an effective streamwise wavenumber $\alpha = \epsilon\alpha_0 = 0.16$, is dominant in comparison with the $m = -1$ and $m = 1$ modes. The wavenumber in the streamwise direction is too small to be retrieved in the computational domain thus explaining, to some extent, the onset of streaky structures.

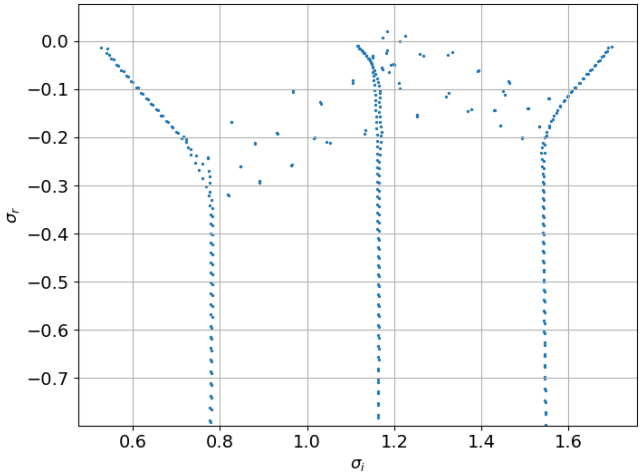

Figure 4.12: Secondary instability spectrum for $Re = 12000$, $\beta_1 = -9.6$, $A = 10^{-5}$ and $\epsilon = 0.23$. The values of the frequency and growth rate of the four most unstable modes are given in table 4.2.

	σ_r	σ_i^{TS}	σ_i^0
Mode 1	0.0205	1.1835	0.0449
Mode 2	0.0115	1.2245	0.0849
Mode 3	0.0070	1.1729	0.0349
Mode 4	0.0004	1.2118	0.0749

Table 4.2: Most unstable eigenvalues of the secondary stability analysis for $Re = 12000$, $\beta_1 = -9.6$, $\epsilon = 0.23$ and $A = 10^{-5}$. For a single mode, two frequencies, σ_i^{TS} and σ_i^0, are given: the former is the frequency of the mode in the frame moving with the TS wave while the latter corresponds to the frequency in the laboratory frame.

The eigenvalues associated to these modes are summarised in table 4.2. Considering the dominant $m = 0$ mode, frequencies in the laboratory frame are retrieved through the following equation:

$$\sigma_i^0 = \sigma_i^{TS} - \beta_1 c_z - \alpha_0 \epsilon c_x. \tag{4.22}$$

For the four most unstable modes, secondary perturbations are reconstructed based on equation (4.20). A slice of these modes in the $y - z$ plane is provided in figure 4.13, showing that they share a rather similar structure. In the spanwise direction, one can see alternated high and low streamwise-velocity patches. The streamwise velocity component is one order of magnitude higher than the cross-flow components, and is strongly localised in the region where the amplitude of the TS wave reaches a maximum. Cross-flow components form vortical structures concentrated near the walls and similar to the ones found for cross-flow instabilities. More precisely, Mode 1 consists in oblique

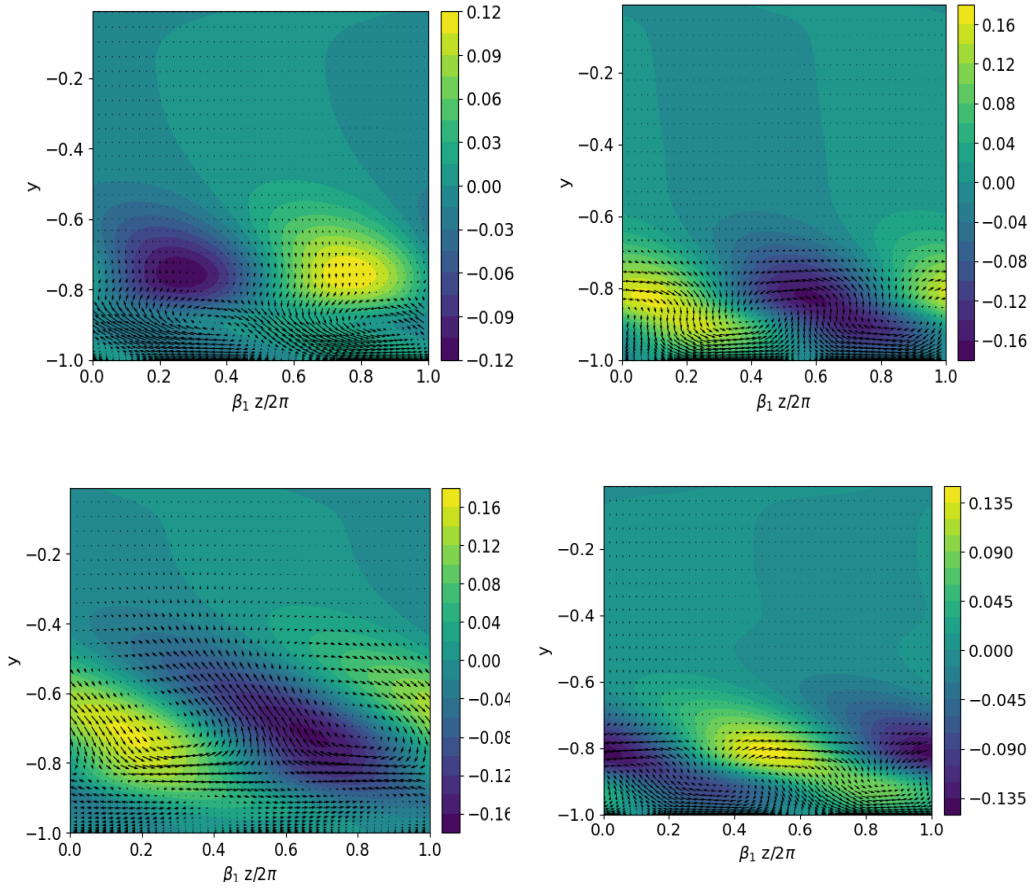

Figure 4.13: Slice at $x = L_x/2$ of the reconstructed secondary perturbations of the four most unstable modes for $Re = 12000$, $\beta_1 = -9.6$, $\epsilon = 0.23$ and $A = 10^{-5}$. From top to bottom and left to right, modes are ordered from the most unstable to the least unstable. The contour plot represents the streamwise velocity disturbance while the quiver plot shows the $v - w$ cross-flow.

vortices together with oblique streaky structures for the streamwise velocity component. Modes 2 and 4 are almost identical besides a phase shift. One can also observe a stagnation point near the wall at $z = 0.58$ for Mode 2. Mode 3 appears peculiar as its vortices sit on top of a region of low velocity. For all these modes, the vortices push high-momentum fluid towards the wall where, due to the slip boundary conditions, it is strongly accelerated in the spanwise direction. When this high-momentum flow reaches the neighbouring vortices, it is re-ejected upwards back in the flow, creating stagnation points and strong spanwise shear layers in the process.

The main features of the most unstable modes recovered by Floquet analysis are compared with those observed in the DNS in table 4.3. For the DNS, the secondary growth rate is extracted from figure 4.7 while the main temporal frequency is obtained from figure 4.10. As previously discussed,

	β_1	σ_r	σ_i^o
DNS	-9.6	0.02	0.03958
Floquet	[-6,-10]	0.02	0.0449

Table 4.3: Comparison between wavenumbers and growth rates obtained from the DNS via Fourier transform and from secondary stability analysis.

secondary stability analysis yields a range of unstable spanwise wavenumbers which includes the main wavenumber observed in the DNS. The growth rates are in perfect agreement. The small discrepancy found between the frequencies could arise from the fact that the shape assumption is likely not completely valid and the mean flow is slightly distorted during the transition. Also, only the frequency of the dominant mode $m = 0$ was considered while, formally, each mode of the Floquet expansion has its own frequency in the laboratory frame.

Finally, a comparison of the spatial structure of the secondary perturbations obtained from the DNS and some of the modes obtained by secondary stability analysis is provided in figure 4.14. Snapshots of the flow are taken at at $x = L_x/2$ and $t = 500$. The latter value is chosen for ensuring that nonlinearities have a negligible effect, while the position in the streamwise direction is the same of that used for the secondary stability analysis. Both the base flow and the initial TS wave are subtracted from the snapshot to retrieve the secondary perturbations. The snapshot is then divided into portions of size $2\pi/\beta_1$ to isolate vortical structures. The spatial structures compare rather well, although for Mode 1 (top row), one can observe that in the DNS the counter rotating vortices are located rather farther from the wall. Regarding Mode 3, its location in the wall-normal direction can be retrieved despite the size of the vortex is slightly smaller.

4.5 Second scenario: cross-flow modes

4.5.1 Overview of the transition

The second transition scenario is initiated injecting on the base flow the cross-flow unstable mode with $(\alpha_0, \beta_0) = (0.2, -6)$. The time evolution of the kinetic energy evolution and friction Reynolds number is provided in figure 4.15, while figure 4.16 depicts the evolution of the spectral energy for several Fourier spatial modes.

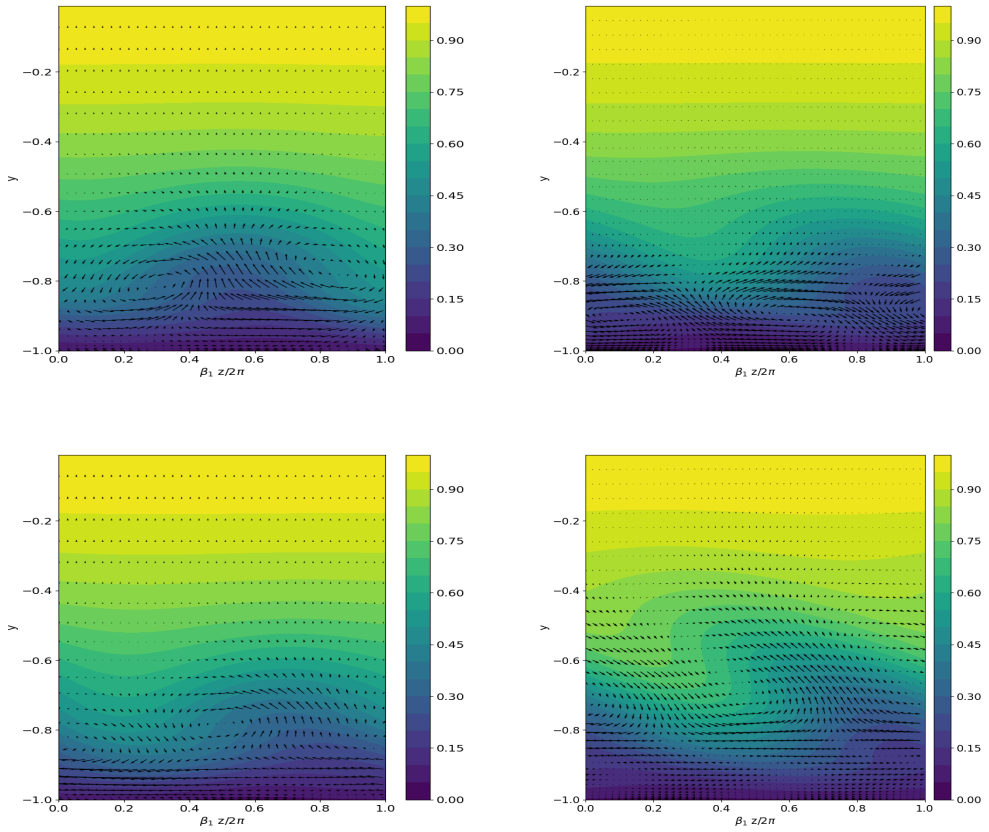

Figure 4.14: Comparison between snapshots extracted from the DNS (left column) and secondary stability modes (right column): Mode 1 (top row) and Mode 3 (bottom row). Secondary perturbations from the DNS are extracted from snapshots taken at $t = 500$, by subtracting the base flow and the primary disturbance. The contour plot represents the total streamwise velocity disturbance while the quiver plot shows the $v - w$ cross-flow.

At first, exponential growth of the disturbance kinetic energy is observed in figure 4.15. Notice that the slope of the curve corresponds to twice the growth rate $\omega_r = 0.0033$ retrieved from linear stability analysis. After $t = 600$, the kinetic energy starts saturating at $E \approx 1.8 \times 10^{-3}$. This saturation most likely arises from stabilising nonlinear effects and is also observed in a CF induced transition for swept flows. As shown in the first snapshot of figure 4.17, besides slight deformations near the walls due to the boundary conditions, the shape of the quasi-stationary ($\omega_i = 0.0225$) cross-flow vortices does not evolve much during this phase.

In the meantime, it can be seen from figure 4.16 that the mode $(2, 0)$ also experiences strong energy growth. Since the mode is linearly stable and is not expected to undergo strong transient growth, only

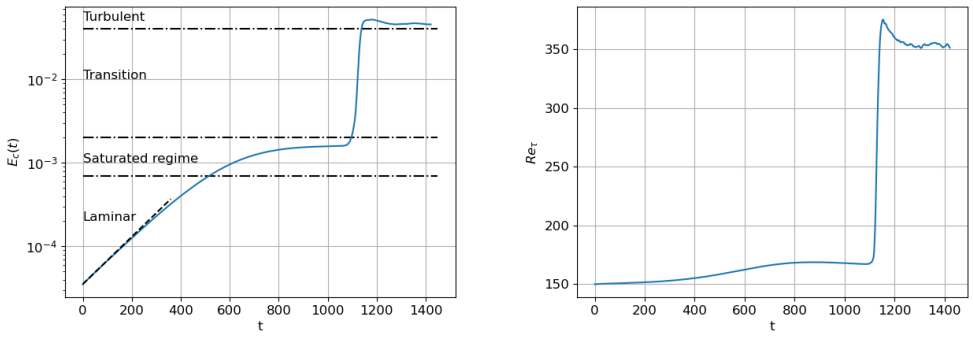

Figure 4.15: Evolution of the disturbance kinetic energy density (left) and Re_τ (right) for the CF transition scenario. The dashed line has a slope $2\omega_r$ where $\omega_r \approx 0.003267$ is the growth rate of the most unstable perturbation found with the linear stability analysis.

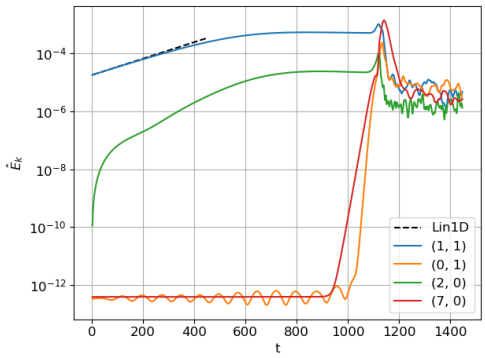

Figure 4.16: Time evolution of the Fourier modes $(1,1)$, $(2,0)$, $(7,0)$ and $(0,1)$ for the CF transition scenario. The dashed line corresponds to the exponential primary growth rate.

non-linear mechanisms could explain this growth. Nonlinear forcing of the mode $(2,0)$ by the initial perturbation is possible as it can be observed in an oblique waves transition scenario for a boundary layer (Schmid & Brandt, 2014). Usually, the $(2,0)$ mode is damped and not very receptive to forcing, meaning it is not relevant in the transition scenario. For 3D flows, El-Hady (1989) demonstrated that resonant wave triads play an important role in the stability due to the large number of interaction between the possible instabilities.

At $t = 1000$, the top of the vortices start oscillating in the streamwise direction (see bottom of figure 4.17). This can also be seen on the spatiotemporal plot of figure 4.18, where one can notice the much higher frequency of the secondary instability. This secondary instability can be traced back to the Fourier mode $(7,0)$ in figure 4.16. Secondary growth rate can be extracted from the slope of its

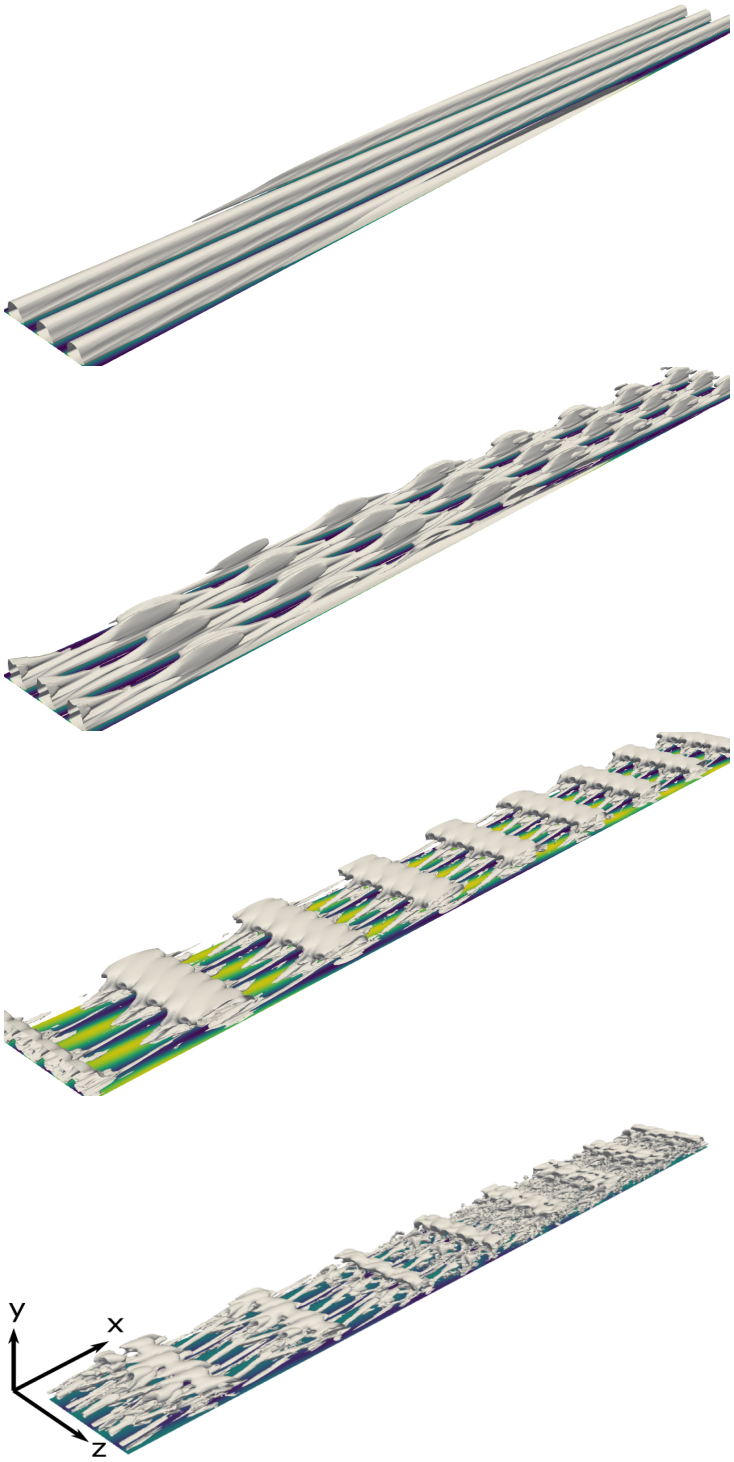

Figure 4.17: Snapshots of the flow at $T = 900$, $T = 1000$, $T = 1050$, $T = 1060$, and $T = 1080$ (from top to bottom). Isosurfaces of the λ_2-criterion, $\lambda_2 = -10^{-5}, -10^{-4}, 0.25$, respectively, and contours of the streamwise velocity at the wall. The flow is from bottom to top, and left to right. For the sake of clarity, only half the channel is shown.

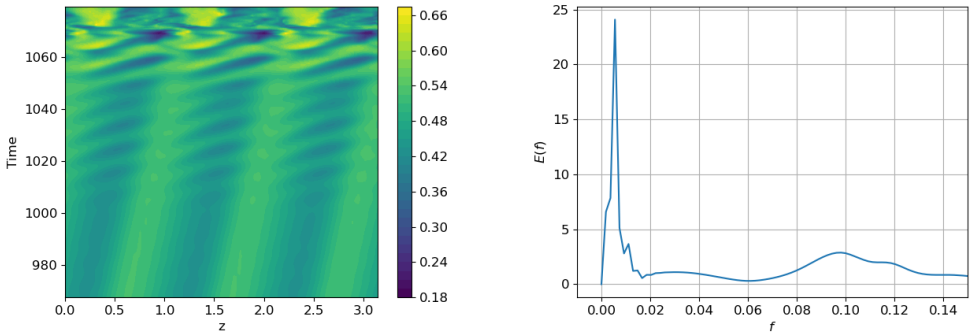

Figure 4.18: Left: Spatio-temporal evolution of the streamwise (left column) and spanwise (right column) components of the velocity at $x = 0$ and $y = -0.85$. Right: Energy temporal spectrum of the transition to turbulence.

time evolution and is equal to $\sigma_r \approx 0.084$. The frequency associated to secondary instability can be obtained from the Fourier spectrum of figure 4.18 and is equal to $\sigma_i \approx 0.095$.

At $t \approx 1050$, spanwise independent coherent structures appear as shown in figure 4.19. These structures appear on top of the cross-flow vortices and seem to be tilted. The bottom snapshot of figure 4.19 is particularly interesting: on top of the wave-like pattern of the initial disturbance, secondary vortices can be observed. These also appear in the near-wall region between two CF vortices. These vortices are most likely a consequence of the slip boundary conditions: as the fluid is accelerated in the spanwise direction near the walls, strong spanwise shear layers, which are susceptible to further destabilise, are created. Energy is transferred from the CF vortices to the secondary perturbation. Distortion of the base flow, in both streamwise and spanwise directions, is also highly likely.

The remaining part of the laminar-turbulent transition is rather complex as several instability mechanisms get intertwined. In the fourth snapshot of figure 4.17, streaks can be seen developing in the near wall region, causing the energy growth of the $(0, 1)$ Fourier mode in figure 4.16. In figure 4.19, the vortices previously described have combined to form vortex quadrupoles which create strong recirculation in the flow. Ultimately, the breakdown to turbulence seems to be related to the displacement of high-velocity fluid in the upper part of the channel (fourth snapshot of figure 4.19) towards lower-velocity regions near the wall (last snapshot of figure 4.19). In the vicinity of these regions turbulent wedges originate (see figure 4.18) which quickly propagate to the whole channel.

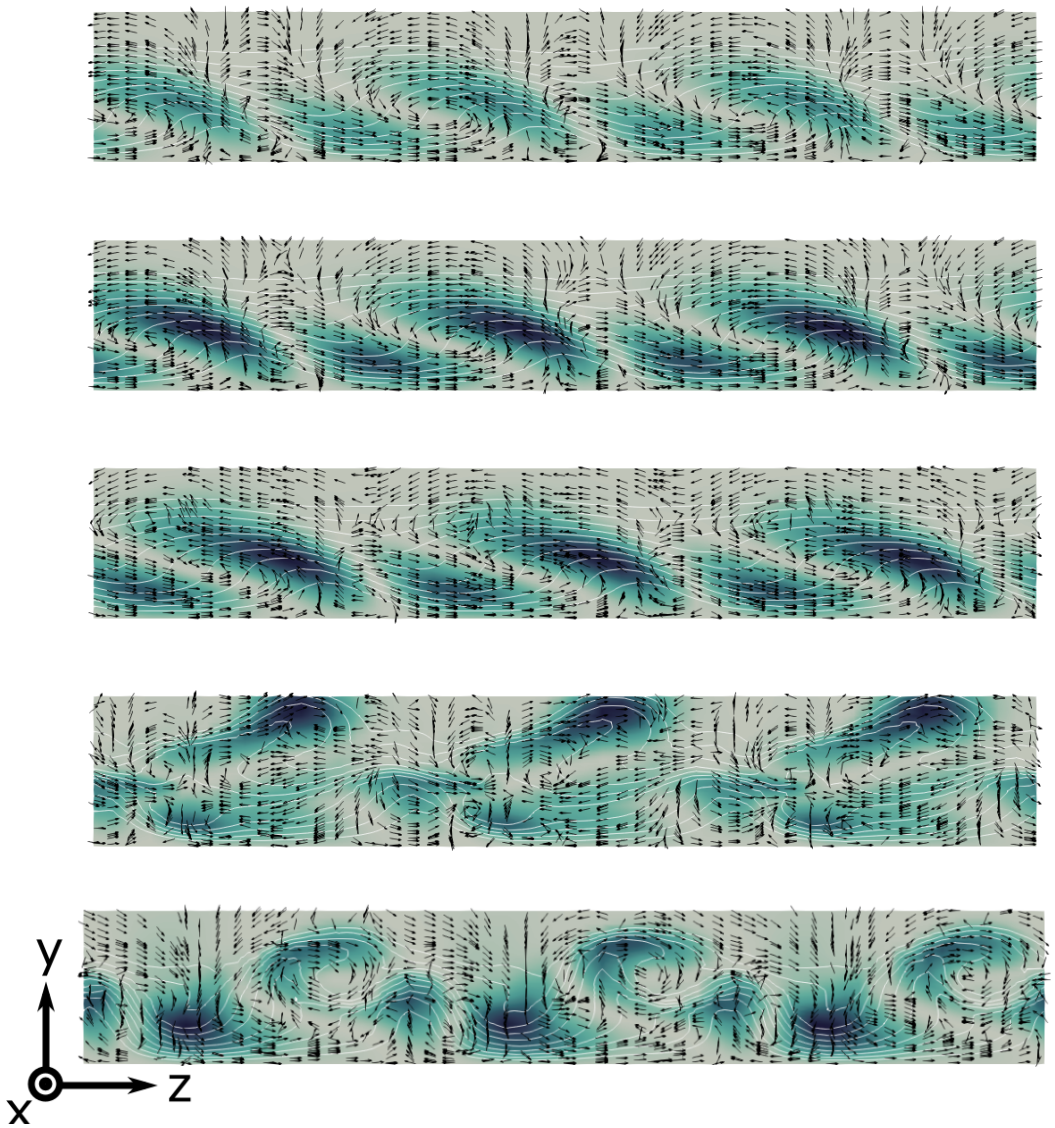

Figure 4.19: Cross-flow dynamics at different time T. From top to bottom: $T = 900$, $T = 1000$, $T = 1050$, $T = 1060$ and $T = 1080$. Slice is taken at the streamwise position $x_s = 15.71$ and only $y \in [-1, -0.7]$ is represented. Isocontours of the λ_2-criterion $[-1{\times}10^{-4} \longleftrightarrow -1{\times}10^{-2}]$. Contour plot of the u-component of the disturbance velocity. Quiver plot depicts the $(v-w)$ crossflow of the perturbation. White contours represent the magnitude of the velocity $[-5 \times 10^{-2}, -3 \times 10^{-1}; -5 \times 10^{-2}]$.

4.5.2 Revisiting the secondary stability analysis of cross-flow vortices

Due to the presence of several strong shear layers, the primary cross-flow vortices are highly likely to further destabilise. The observation of the transition scenario also strongly hints at the presence of modal secondary instability mechanisms once saturation took place. In the case of swept flows, secondary instability of cross flow vortices has been the subject of numerous efforts (see Saric *et al.* (2003) for a review) albeit, to the author's knowledge, always in the case of boundary flows and with no-slip boundary conditions. A short introduction to secondary instability of cross flow vortices is produced in the following, based on the work of Serpieri (2018).

To get a good understanding of the secondary instability of cross flow vortices, one of the key contribution is the work of Malik *et al.* (1999) who classified the secondary modes into two main families. Precisely, *type-I* unstable modes are linked to the velocity gradient of the streamwise component of the velocity in the spanwise direction, while *type-II* modes originate from gradients in the wall-normal direction. *Type-I* modes are located in the outer part of the primary vortices while *type-II* are situated on top of them. *Type-II* also tend to have a higher frequency than *type-I* modes. A third type was identified in studies by Fischer & Dallmann (1991) and Janke & Balakumar (2000) through Floquet analysis of the cross-flow vortices. This low-frequency *type-III* mode is linked to nonlinear interactions between stationary and travelling primary modes. These three families of modes have been also experimentally retrieved by Kawakami *et al.* (1999) and White & Saric (2005). Later, using DNS, Wassermann & Kloker (2002, 2003) showed that co-rotating helicoidal structures superimposed on the upwelling region of the primary vortices were characteristics of the *type-I* mode. These structures would be convected downwards if the unsteady forcing was switched off, thus confirming the convective nature of the secondary instability as already suggested by Kawakami *et al.* (1999) and Koch (2002).

Bonfigli & Kloker (2007) also studied the development of the secondary instabilities of cross-flow vortices through the combined use of a spatial DNS and Secondary Linear Stability Theory (SLST) based on Floquet theory applied on a saturated primary flow (Malik *et al.*, 1994; Janke & Balakumar, 2000; Koch *et al.*, 2000; Koch, 2002). Growth rates and structures of the *type-I* and *type-III* modes were retrieved and good agreement was shown between the two techniques. SLST predicted the instability of *type-II* modes but these were not observed in the DNS. In the particular case of travelling vortices, *type-III* modes were not reported as unstable, which was expected since this mode arises from the

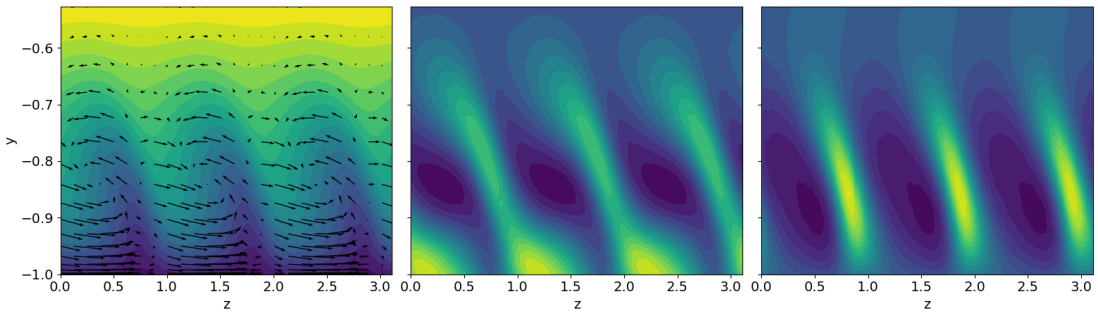

Figure 4.20: Base flow for the secondary stability analysis. The snapshot is extracted from the DNS at time $t \approx 900$, position $x_{SLST} = 15.71$ and is shown in the vortex-oriented reference frame. Left: contour plot of the velocity component U. Quiver plot of the cross-flow perturbation $(v - w)$. Constant spanwise W_0 has been substracted from w in order to observe the vortical structures. Middle: wall-normal gradient of the streamwise component of velocity $\partial_y u_v^0$. Right: spanwise gradient of the streamwise component of velocity $\partial_{z_v} u_v^0$.

generation of spanwise modulation induced by the stationary primary vortices. Another key conclusion of this study is the nature of the mechanism behind the secondary instability: both *type-I* and *type-II* are found to be related to Kelvin-Helmholtz instabilities. In all cases, the primary flow on which SLST is realised is paramount and its acquisition is not straightforward as nonlinearities lead to an important distortion of the base flow. The shape assumption does not hold anymore and Herbert's secondary stability theory cannot be directly applied.

The primary flow can be retrieved by using parabolised stability equations as in Malik *et al.* (1999) and Janke & Balakumar (2000), or directly extracted from a saturated DNS (Messing & Kloker, 2004; Bonfigli & Kloker, 2007). Recently, Groot *et al.* (2018) based their secondary stability analysis on an experimentally acquired primary flow. In any case, the extraction process is quite complex and several issues arise. In swept boundary layers, the orientation of the vortex axis of the cross-flow vortices evolves with the streamwise direction. Consequently, secondary linear stability depends on the position $x = x_{SLST}$ where the primary flow is extracted. This is not the case in our configuration, as a consequence of the choice of a temporal DNS.

As in Bonfigli & Kloker (2007) and several others, we introduce a vortex-oriented system (x_v, y, z_v) aligned with the vortex axis of the primary disturbance and moving with it. In this frame, the primary flow $\mathbf{Q}_v^0(y, z_v)$ is streamwise independent and periodic in the spanwise direction. In the framework of

Floquet theory, it is Fourier expanded in the spanwise direction and takes the following modal form:

$$\mathbf{Q}_v^0(y, z_v) = \sum_{n=-\infty}^{+\infty} \hat{\mathbf{q}}_{v,n}^0(y) e^{in\beta_v z_v} \tag{4.23}$$

with $\beta_v = \sqrt{\alpha_0^2 + \beta_0^2} \approx \beta_0$ the effective wavelength in the spanwise direction z_v. In this framework, the continuity equation reduces to:

$$\partial_y v_{v,n}^0 + in\beta_v w_{v,n}^0 = 0, \qquad \forall n, \tag{4.24}$$

directly relating the two cross-flow components of the velocity. Thus, a choice must be made between enforcing continuity and extracting both components from the DNS. Ultimately, this choice was found to have a non negligible impact on the secondary growth rates found from the SLST (Malik *et al.*, 1994; Bonfigli & Kloker, 2007).

To overcome this, here we use a two dimensional local (hence, bilocal) stability approach, as for example in (Tatsumi & Yoshimura, 1990). Several reasons motivate this choice: first and foremost, two-dimensional local stability theory encompasses Floquet stability theory. Also, as previously seen, Fourier decomposition in the spanwise direction of the primary flow leads to some difficulties with the continuity equation. In a bilocal framework, this decomposition is not necessary and these issues do not arise. To investigate the development of large-scale collective secondary instabilities, the Bloch wave formalism will also be employed and compared with results obtained from the bilocal stability problem.

For carrying out the bilocal secondary stability analysis, the flow is decomposed into the primary state $\mathbf{Q}_v^0(y, z_v)$ and a secondary perturbation $\mathbf{q}_1(x_v, y, z_v, t)$. Furthermore, the secondary perturbation can be expanded in the following way:

$$\mathbf{q}_1(x_v, y, z_v, t) = \tilde{\mathbf{q}}(y, z_v) e^{i\alpha_v x_v} e^{\sigma t} \tag{4.25}$$

where α_v and σ are complex numbers representing respectively the streamwise wavelength and the pulsation in the vortex-oriented reference frame. Both temporal (Malik *et al.*, 1999; Koch *et al.*, 2000; Wassermann & Kloker, 2002) and spatial (Janke & Balakumar, 2000; Bonfigli & Kloker, 2007) approaches have been previously considered. Koch *et al.* (2000) found a set of equations relating both frameworks through a generalisation of the Gaster transformation to 3D flows. For channel flows,

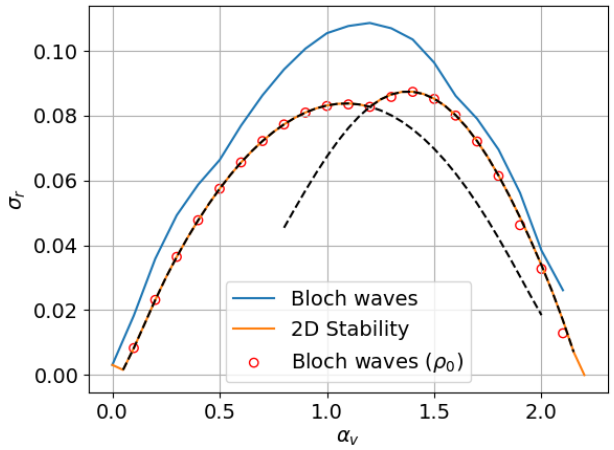

Figure 4.21: Growth rate σ_r of the secondary most unstable modes of CF vortices as a function of the effective streamwise wavenumber α_v in the vortex-oriented frame. The blue curve denotes the maximum growth obtained when all roots-of-unity are considered while red dots corresponds to the restriction to fundamental (ρ_0) modes, mathematically equivalent to the two-dimensional stability analysis with periodic boundary conditions.

a natural choice is to consider a temporal framework. As previously, Navier-Stokes are linearised around this new base flow. Stability equations for two-dimensional problems can be found for example in Loiseau (2014).

The primary flow in the vortex oriented referential is shown in figure 4.20. It was extracted from the DNS at time $t = 900$ and $x_{SLST} = 15.71$. This flow field can be compared with the flow visualisations from the experiments of Serpieri (2018) (see figure 4.14) and with the primary flow resulting from the DNS of Bonfigli & Kloker (2007) (see figure 7). The water-wave shape of the streamwise velocity component, characteristic of the cross-flow vortices, is clearly visible. However, the spatial extension of the tip of the wave is smaller than that observed for swept boundary flows, likely because the initial spanwise velocity W_0 is weaker. The instability mechanism is similar to that described in Serpieri & Kotsonis (2016): cross-flow vortices generate the circulation of low-momentum flow towards high-momentum regions higher up in the channel and conversely. In the present case, the wall-normal shear is maximum near the walls and not in the vortex core due to the slip boundary conditions. The spanwise velocity gradient reaches a maximum in the low-momentum upwelling region on the outer part of the vortex.

Stability of the secondary flow is investigated through a two-dimensional and Bloch waves frame-

	α_v	σ_r	σ_i^0
DNS	1.4	0.082	0.095
2D SLST	1.39	0.087	0.088
Bloch	1.2	0.108	0.084

Table 4.4: Comparison between secondary instability characteristics obtained from the DNS, from the most unstable mode of the secondary stability analysis and from the Bloch wave analysis.

works. In the two-dimensional stability problem, the flow stability is investigated on a single sub-unit with periodic boundary conditions imposed in the spanwise direction, which is formally equivalent to considering only fundamental secondary instabilities. On the contrary, the Bloch waves formalism can also retrieve subharmonic and detuned instabilities. The evolution of the temporal secondary amplification rates in the vortex-oriented frame as a function of the effective streamwise wavelength is shown in figure 4.21. The two frameworks give rather different results: growth rates found with the Bloch waves framework are larger, indicating the presence of detuned of secondary instabilities. The maximum $\sigma_r = 0.108$ is reached for $\alpha_v = 1.2$. Note that these instabilities are not visible in the DNS as the computational box does not allow them. Besides, as expected, a perfect agreement is found between the bilocal stability results in the DNS domain and the growth rates obtained by the Block wave formalism for fundamental modes. In this case, the maximum growth rate is equal to $\sigma_r = 0.084$ for $\alpha_v = 1.4$. Both the growth rate and the effective streamwise wavenumber are in good agreement with the ones observed in the DNS. A direct comparison between the characteristics of the secondary instability obtained from the SLST and those extracted from the DNS is provided in table 4.4.

All the results from the SLST and the Bloch wave framework are obtained in the moving vortex-oriented frame. Values of streamwise wavelengths and frequencies in the laboratory frame can be retrieved by expanding equation (4.25):

$$\sigma_i^0 = \sigma_{i,v} - \alpha_v c \tag{4.26}$$

$$\alpha_1^0 = -\frac{\alpha_v \beta_0}{k} \tag{4.27}$$

$$\beta_1^0 = \frac{\alpha_v \alpha_0}{k} \tag{4.28}$$

where $k = \sqrt{\alpha_0^2 + \beta_0^2}$ and c is the velocity of the CF vortices.

Figure 4.21 also displays a competition between two types of modes. The eigenfunctions for these

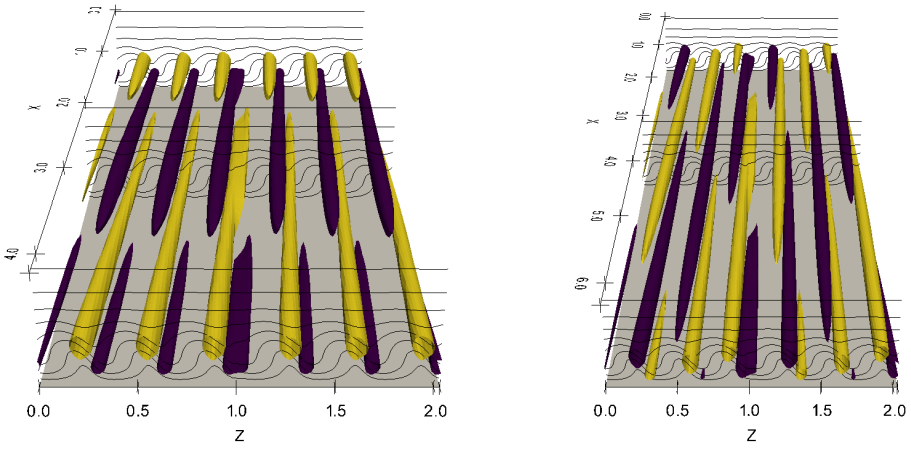

(a) $\alpha_v = 1.1$ (b) $\alpha_v = 1.4$

Figure 4.22: Left: three-dimensional streamwise velocity component for two sub-units (6 CF vortices). Contour of the secondary base flow can be seen in black.

two modes can be retrieved in figure 4.22 and are found to be almost identical. The amplitude of the streamwise perturbation is strongly localised on the upwelling of the vortex, a representative feature of *type-I* modes. Among the several unstable modes, no *type-II* nor *type-III* structures could be found. This is not unexpected: *type-III* modes require interactions with unstable stationary cross-flow vortices. *Type-II* modes stem from the instability of wall-normal velocity gradients but these are sensibly weaker than their counterparts in swept flows. This could be explained by the combined effect of the absence of an inflection point in the spanwise velocity profile W_0 and of the slip boundary conditions. The two modes have been fully reconstructed from equation (4.25) and superposed on the primary flow in figure 4.22. The difference between the two modes might result from the collective behaviour of the secondary instability. For $\alpha_v = 1.4$, the secondary perturbations are in phase on each wave-like pattern of the primary flow. Thus, a single CF vortice would have been sufficient for determining the secondary instability. On the contrary, in the $\alpha_v = 1.1$ case, a phase shift appears between the multiple iterations of the secondary perturbations, thus coupling multiple CF vortices together. Finally, as observed in the DNS, the synchronised perturbation is the most unstable.

Figure 4.21 also displays a competition between two types of modes. The eigenfunctions for these two modes can be retrieved in figure 4.22 and are found to be almost identical. The amplitude of the streamwise perturbation is strongly localised on the upwelling of the vortex, a representative feature of *type-I* modes. Among the several unstable modes, no *type-II* nor *type-III* structures could be

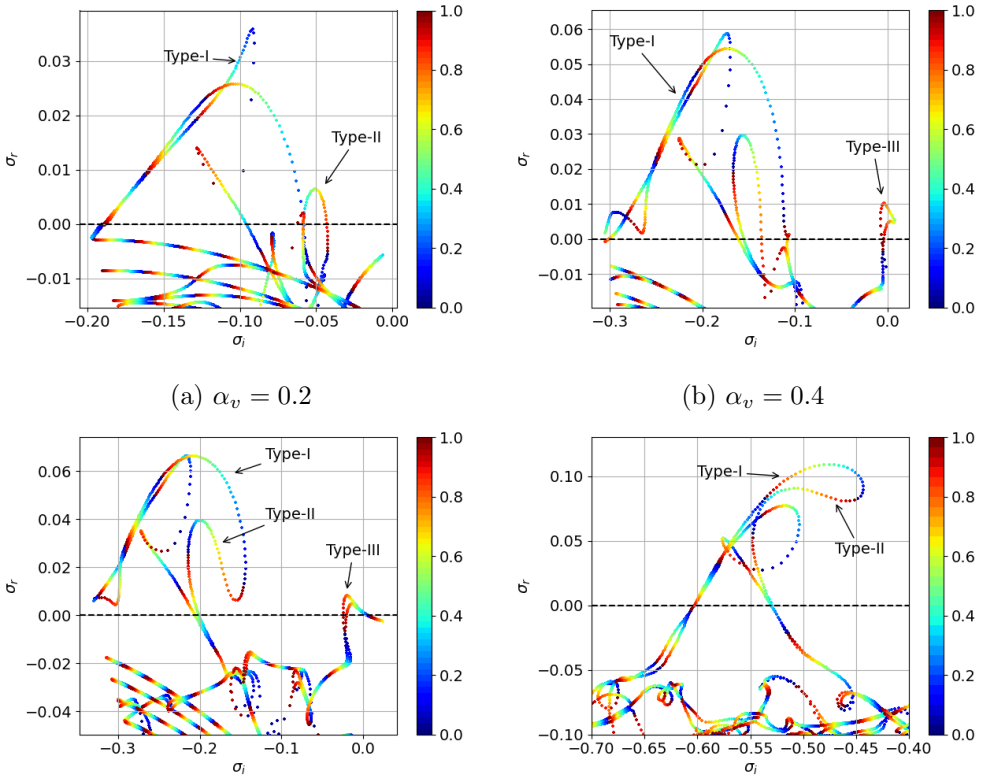

(a) $\alpha_v = 0.2$ (b) $\alpha_v = 0.4$

(c) $\alpha_v = 0.5$ (d) $\alpha_v = 1.2$

Figure 4.23: Secondary stability spectra for $Re = 12000$, $n = 50$ and several values of α_v

found. This is not unexpected: *type-III* modes require interactions with unstable stationary cross-flow vortices. *Type-II* modes stem from the instability of wall-normal velocity gradients but these are sensibly weaker than their counterparts in swept flows. This could be explained by the combined effect of the absence of an inflection point in the spanwise velocity profile W_0 and of the slip boundary conditions. The two modes have been fully reconstructed from equation (4.25) and superposed on the primary flow in figure 4.22. The difference between the two modes might result from the collective behaviour of the secondary instability. For $\alpha_v = 1.4$, the secondary perturbations are in phase on each wave-like pattern of the primary flow. Thus, a single CF vortex would have been sufficient for determining the secondary instability. On the contrary, in the $\alpha_v = 1.1$ case, a phase shift appears between the multiple iterations of the secondary perturbations, thus coupling multiple CF vortices together. Finally, as observed in the DNS, the synchronised perturbation is the most unstable.

Even though these large-scale effects cannot be retrieved from the DNS (as the computational

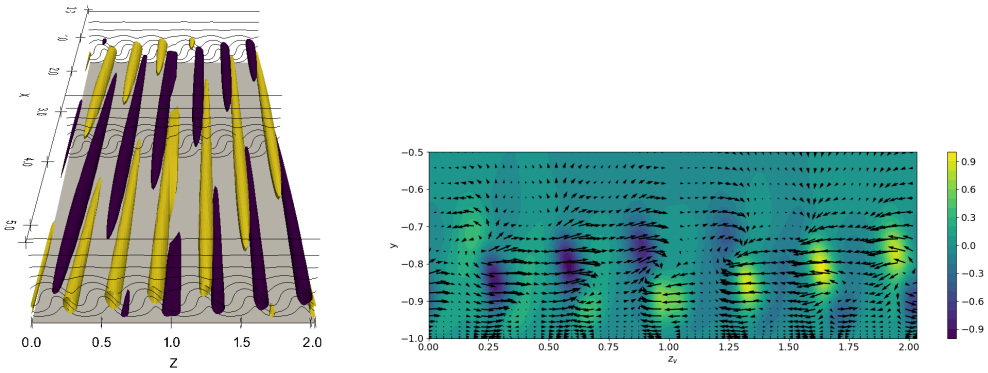

Figure 4.24: Left: 3D streamwise velocity component of the most unstable *type-I* mode. Right: contour plot of the streamwise velocity component together with a quiver plot of the cross-flow dynamics. The secondary instability is almost subharmonic, and thus approximately couples 6 CF vortices.

box is too small), they can be further investigated using the Bloch waves formalism. Spectra for several values of the streamwise wavenumber α_v are displayed in figure 4.23 and exhibit a great complexity. The different types of secondary modes previously identified can be retrieved and are indicated on the spectra. Notably, for streamwise wavenumbers larger than 0.4, the *type-I* and *type-II* instabilities, which are usually considered separately, form a unique branch. A *type-I* mode remains the most unstable for all values of α_v. The spectra are also characterised by a large number of unstable exceptional points, indicating a potential for large secondary growth. The most unstable *type-I* mode, displayed in figure 4.24 is obtained for a quasi subharmonic instability ρ_{24} in the oriented frame. Taking into account the orientation of the frame, a subharmonic instability in the laboratory frame can be retrieved. Remember however that the secondary base flow already included three CF vortices, meaning that the "subharmonic" secondary instability couples in reality six CF vortices. Notice also that, for $\alpha = 0$, the new unstable detuned mode that was previously found in a swept boundary layer could not be retrieved. It is not that surprising as it was likely linked to the inflection point in the spanwise velocity profile which is not present here since W_0 is constant.

Chapter 5

Stability of the flow over complex surfaces: roughness effects and interface dynamics

Contents

5.1 Stability of a flow over longitudinal riblets

5.1.1 Problem formulation

We consider the flow of an incompressible Newtonian fluid with viscosity ν^* in a channel of height $2h^*$ with the lower wall covered with riblets. The reference frame is chosen as $\mathbf{x}_0^* = (x_0^*, y_0^*, z_0^*)$, with x_0^*, y_0^* and z_0^* being respectively the streamwise, wall normal and spanwise directions. The dynamics

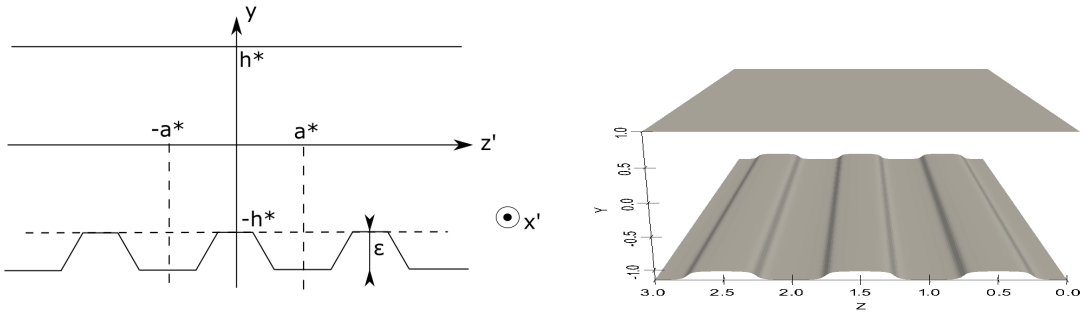

Figure 5.1: Sketch of the channel and of the riblet geometry considered. The domain is normalised in the spanwise direction.

of the flow is governed by the Navier-Stokes equations:

$$\frac{\partial \mathbf{U}^*}{\partial t^*} = -(\mathbf{U}^* \cdot \nabla)\mathbf{U}^* - \frac{1}{\rho^*}\nabla P^* + \nu^* \nabla^2 \mathbf{U}^* \tag{5.1}$$

$$\nabla \cdot \mathbf{U}^* = 0, \tag{5.2}$$

where $\bullet^*$ correspond to the dimensional variables, $\mathbf{U}^* = (U^*, V^*, W^*)^T$ is the velocity field and P^* is the pressure. No-slip boundary conditions are applied at the walls. The top wall is assumed to be smooth while streamwise invariant riblets are mounted on the bottom wall. The roughnesses are characterised by their peak height ϵ, their spanwise half-periodicity $s = a^*/h^*$ and their shape $\eta^*(z_0^*)$. In this study, trapezoidal streamwise invariant riblets with a fixed height $\epsilon^* = 0.15h^*$ will be considered. The choice of this shape is not arbitrary: in the case of a channel with two rough walls, Moradi & Floryan (2014) showed that these grooves represent an optimal choice for laminar drag reduction when both height and depth are imposed and kept equal.

The flow is characterised by the presence of two separate length scales: in the wall-normal direction y_0^*, the natural length scale is the half height of the channel h^* (taken between the centre of the channel and the tip of the riblets) while, for the spanwise direction z_0^*, it is taken to be the half-periodicity s of the riblets. Following Philip (1972) and Picella *et al.* (2019), we introduce the reference velocity $U_r^* = 3U_a^*/2$, with U_a^* being the average of the base flow velocity $U_a^* = 1/2h^* \int U^*(y^*)dy^*$. The most common choice of the centreline streamwise velocity as reference velocity is unsuitable in this case as it is dependent on the geometry of the roughness. Ultimately, the Reynolds number is defined as $Re = U_r^* h^*/\nu^*$. In the following, all the physical quantities, denoted without stars, are scaled by the channel half-height h^* and by a reference velocity U_r^*. The flow is driven by a constant pressure gradient $dP/dx = -2/Re$, resulting in a (laminar) stationary base flow $\mathbf{U}_0(\mathbf{x}_0) = [U(y_0, z_0), 0, 0]^T$,

solution of the following Stokes equation:

$$\frac{\partial^2 U}{\partial y^2} + \frac{1}{s^2}\frac{\partial^2 U}{\partial z^2} = -2, \tag{5.3}$$

together with no-slip boundary conditions at the walls, which, in the normalised physical domain, are imposed at $0 \leq z_0 \leq 1$ and $-1 + \eta(z_0) \leq y_0 \leq 1$. Periodic boundary conditions are imposed in the spanwise direction.

Irregular boundary conditions can be tackled either via a domain transformation method (Ehrenstein, 1996; Moradi & Floryan, 2013) or through an immersed boundary conditions method (Floryan & Asai, 2011; Moradi & Floryan, 2014). The latter remains limited to small amplitude riblets. Thus, a domain transform technique is employed and, following Ehrenstein (1996); Mohammadi *et al.* (2015), we introduce a new coordinate system $\mathbf{x}_1 = (x_1, y_1, z_1)$ such as:

$$x_1 = x_0, \qquad z_1 = z_0, \qquad y_1 = (1-\gamma)y_0 + \gamma, \quad \text{with} \quad \gamma = \eta(z_0)/[\eta(z_0) - 2], \tag{5.4}$$

where $\eta(z_0) = \epsilon \arctan\left(2\sin\left(\pi(z_0 - z_b)/\delta_b\right)/\pi\right.$ is defining the shape of the trapezoidal roughness. Its height is denoted by ϵ while $\delta_b = 0.4$ is a coefficient determining the slope of the roughness. By means of this domain transformation, the physical domain $\mathbf{x}_0$ is mapped into a smooth channel in the computational domain $\mathbf{x}_1$ where $0 \leq z_1 \leq 1$ and $-1 \leq y_1 \leq 1$. Relations between the derivative operators in the different coordinate systems are easily obtained from the chain rule are given :

$$\frac{\partial}{\partial y_0}\bullet = \frac{\partial}{\partial y_1}\bullet - \gamma\frac{\partial}{\partial y_1}\bullet \tag{5.5}$$

$$\frac{\partial}{\partial z_0}\bullet = \frac{\partial}{\partial z_1}\bullet + \gamma'(1-y_0)\frac{\partial}{\partial y_1}\bullet \tag{5.6}$$

In a similar fashion, second order derivatives can be obtained:

$$\frac{\partial^2}{\partial y_0^2}\bullet = \frac{\partial^2}{\partial z_1^2}\bullet + \gamma''(1-y_0)\frac{\partial}{\partial y_1}\bullet + 2\gamma'(1-y_0)\frac{\partial^2}{\partial y_1 \partial z_1}\bullet + [\gamma'(1-y_0)]^2\frac{\partial^2}{\partial y_1^2}\bullet \tag{5.7}$$

Finally, the laplacian with the new coordinates is defined as:

$$\nabla_1^2\bullet = \frac{\partial^2}{\partial y_1^2}\bullet + \frac{1}{s^2}\frac{\partial^2}{\partial z_1^2}\bullet \tag{5.8}$$

$$= (1-\gamma)^2\frac{\partial^2}{\partial y_1^2}\bullet + \frac{1}{s^2}\left[\frac{\partial^2}{\partial z_1^2} + \gamma''(1-y_0)\frac{\partial}{\partial y_1} + 2\gamma'(1-y_0)\frac{\partial^2}{\partial y_1 \partial z_1} + [\gamma'(1-y_0)]^2\frac{\partial^2}{\partial y_1^2}\right]\bullet \tag{5.9}$$

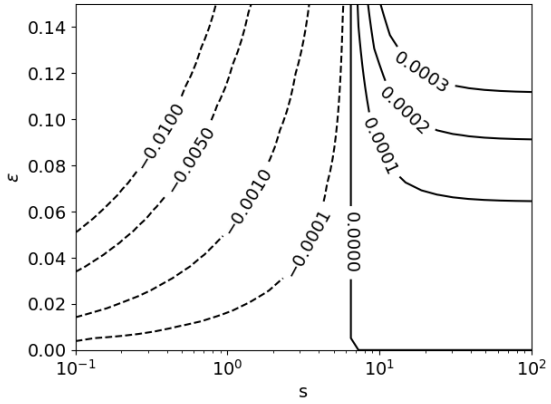

Figure 5.2: Variations of the pressure gradient correction δP as a function of the periodicity s and height ϵ. A positive pressure correction denotes drag-reducing effects and inversely.

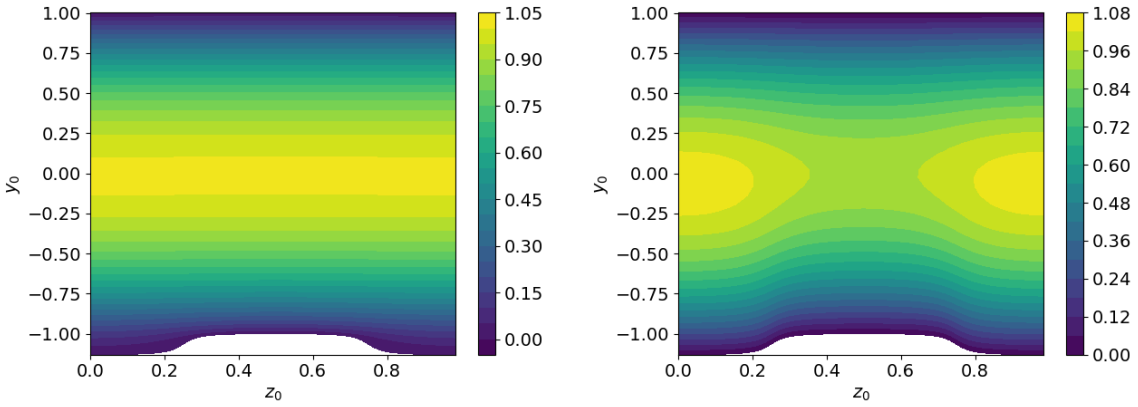

Figure 5.3: Streamwise velocity component $U(y, z)$ of the base flow for the trapezoidal roughness and for $s = 0.25$ (left) and $s = 4.5$ (right), illustrating the two types of base flows.

In the new domain, the Stokes equation (5.3) becomes $\nabla_1^2 U = -2$ where $\nabla_1^2 \bullet$ is the laplacian written in the new coordinate system, as given previously.

5.1.2 Laminar drag reduction, viscous regime and centreline velocity modulation

The presence of riblets on the channel walls induces variations of the shear-stress distribution in their neighbourhood, yielding changes in the drag generated at the wall. These changes can be quantified by comparing the pressure gradients required to obtain the same bulk velocity in a rough channel and in a smooth channel of equivalent height. Mathematically, introducing the pressure gradients ΔP_s and ΔP_r respectively corresponding to smooth and rough walls, the correction of the

pressure gradient is simply expressed as $\delta P = \Delta P_r - \Delta P_s$. The evolution of this quantity as a function of the roughness height ϵ and periodicity s is displayed in figure 5.2. This figure can be compared to its counterpart in Moradi & Floryan (2014). Note however that the half-periodicity s is considered as the abscissa instead of the riblet wavelength $\beta = \pi/s$. The critical periodicity between drag-reducing and drag-increasing effects is $s \approx 6$. This is sensibly higher than for a wavy rough wall, where it was found to be $s \approx 3.65$ (Moradi & Floryan, 2014) and can be explained likely by the large flat top of the trapezoidal roughness. Still, the drag-reduction effect can be explained as a consequence of the change of the base flow topology which can be seen in figure 5.3. In the case of small s, the flow is lifted above the tip of the riblets due to viscous friction. The region of stagnation in the grooves leads to the formation of inflection points in the velocity profile, potentially responsible of a destabilisation of the flow (Schmid & Brandt, 2014). For larger s, the presence of the riblets modulates the local centreline velocity, thus generating strong spanwise velocity gradients at the centre of the channel. In both cases, the new instability mechanisms appear inflectional and may lead to Kelvin-Helmholtz related instabilities.

5.1.3 Modal stability analysis

In a smooth channel, it is well known that two-dimensional TS waves with wavenumber $\alpha = 1.02$ become asymptotically unstable for $Re_c \geq 5772$ (Orszag, 1971*b*). This instability can be subcritically triggered even at Reynolds numbers as low as $Re_c \approx 2700$ in the case of noisy environments. It has been experimentally shown (Asa, 2006; Ho & Asai, 2018) that the classical TS transition scenario is modified in the presence of surface roughness. Precisely, Moradi & Floryan (2014) found that grooves with large periodicity tend to stabilise the flow while small-wavelength riblets destabilise it. TS-like waves, modulated in the spanwise direction by the riblets were found to be the primary source of instability. However, in the case of riblets with large periodicity, Mohammadi *et al.* (2015) uncovered a new family of unstable modes associated with small streamwise wavenumber, with a critical Reynolds number sensibly smaller than the one obtained from the TS instability. This mode was linked to an inviscid Kelvin-Helmholtz-like instability caused by the spanwise modulation of the base flow velocity in the centre of the channel.

In this work, linear stability analysis is investigated for a system composed of $n = 50$ riblets, assuming nearest-neighbour coupling. The spectra obtained for some notable cases are displayed in

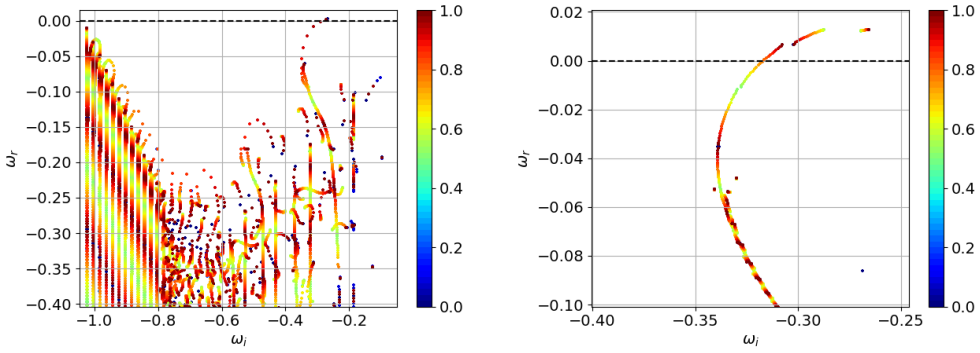

(a) $s = 0.25$, $\alpha = 1$

(b) $s = 4.5$, $\alpha = 1$, A-family close-up

(c) $s = 4.5$, $\alpha = 0.3$

(d) $s = 4.5$, $\alpha = 0.3$, P-family close-up

Figure 5.4: Spectrum for the full system composed of $n = 50$ trapezoidal riblets for $Re = 5000$ and different configurations of interest. Eigenvalues are coloured according to the normalised phase $z_j = \arg(\rho_j)/2\pi$ of their respective root-of-unity ρ_j.

figure 5.4. These are composed of the merging of $n = 50$ sub-spectra, obtained by solving the eigenvalue problems associated with the matrices $\hat{\mathbf{A}}^{(j)}$. Eventually, for systems with a sufficiently large number n of sub-systems, the spatial branches can be entirely reconstituted. The eigenvalues are coloured according to the normalised phase $z = \arg(\rho)/2\pi$ of their respective root-of-unity. Note that only half of the eigenvalues are visible as the eigenproblems associated with ρ_j and ρ_{n-j} share the same eigenvalues. This degeneracy of the eigenvalues stems from a symmetry of the three sub-unit group: the coupling between the left and centre is identical to the one between the right and centre sub-units (Schmid, 2007). Following the secondary instability framework (Herbert, 1983), the instability is said to be fundamental if $z = 0$ or $z = 1$, in the sense that it shares the same spatial periodicity as the original. Similarly, instabilities with $z = 1/2$ (that is twice the initial spatial wavelength) and $0 < z < 1/2$ (arbitrary wavelengths) are respectively said to be subharmonic and detuned.

The spectra displayed in figure 5.4 are obtained for $Re = 5000$ and $\epsilon = 0.15$ but for two different configurations, corresponding to the two types of instability of the flow over rough surfaces. The top left spectrum is computed for $\alpha = 1$ and $s = 0.25$ and exhibits a structure similar to the one found for a two-dimensional Poiseuille flow. It is composed of three main parts, usually denoted as: i) the A-branch, characterised by wall modes such as TS waves, ii) the P-branch, composed of Squire modes located in the centre of the channel and usually stable, and iii) the S-branch which represents the continuous part of the spectrum (Grosch & Salwen, 1978). In the present study, the term 'branch' in these expressions will be replaced by the word 'family' while the word 'branch' will be used to denote the ensemble of eigenmodes resulting from the variation of the root-of-unity. Note that in this configuration, a smooth Poiseuille flow of equivalent height is stable, indicating the destabilising effect of the riblets as already found in numerous studies (Ehrenstein, 1996; Moradi & Floryan, 2014; Mohammadi *et al.*, 2015).

For larger periodicities and the same value of α, as shown in the top right frame of figure 5.4, the instability still arises from the TS branch. However, in this case, it appears divided into three sub-branches (see figure 5.4(b)), two of them being fully unstable while the other only partially. The breaking of the continuity of the TS branch denotes a topological change of the spectrum and a shift in the nature of the eigenmodes constituting the sub-branches. The maximum growth rate, $\omega_r = 0.016$, is reached by two modes located on the tip of these branches. Interestingly, one of the mode is subharmonic while the other is fundamental. If the height ϵ of the roughness is reduced, the three

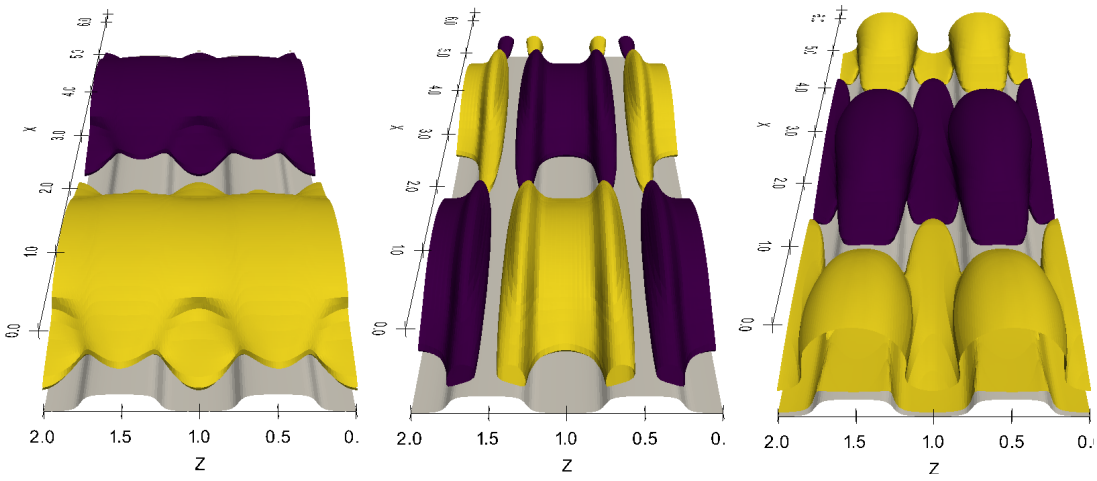

(a) $s = 0.25$ and ρ_0 (b) $s = 4.5$ and ρ_{25} (c) $s = 4.5$ and ρ_0

Figure 5.5: Three-dimensional representation of the streamwise velocity perturbation of the most unstable fundamental mode for $Re = 5000$, $\alpha = 1$ and for different configurations. Isosurfaces are taken as $u = \pm 0.75 u_{\max}$. Only half the channel is displayed for visibility.

sub-branches merge together and the most unstable mode reconnects with the classic two-dimensional TS mode.

The spectrum obtained with $s = 4.5$ and $\alpha = 0.3$ is displayed in figure 5.4(c). Several observations can be made: the instability now arises from centre Squire modes pertaining to the P-family. This is the instability mode that was discovered and investigated in the work of Mohammadi *et al.* (2015). To be accurate, the instability stems from two unstable branches: the most unstable one reaches its maximum growth rate, $\omega_r = 0.005$, for ρ_0, underlining the fundamental nature of the instability. On the contrary, for the second branch, the maximum growth rate, $\omega_r = 0.0013$, is obtained with a desynchronised mode (ρ_{12}). Also note that the P-family now looks like a succession of small Poiseuille flow spectra. For small streamwise wavenumbers, the TS branch is now marginally stable with its most unstable mode being subharmonic.

Figure 5.5 (a) depicts a three-dimensional view of the streamwise velocity component of the most unstable mode found for $Re = 5000$, $s = 0.25$ and $\alpha = 1$. The most unstable mode is reminiscent of the usual two-dimensional TS wave. In fact, the eigenfunction directly stems from the continuous deformation of a TS wave induced by the riblets, which loses its spanwise modulation when the roughness height ϵ tends towards 0. The modulation induced by the presence of the riblets, leads to

the formation of strong spanwise and wall-normal shears. Depending on the strength of the spanwise velocity gradient, the flow is likely to be further destabilised by secondary Kelvin-Helmholtz like instabilities. The concentration of momentum at the tip of the roughness has been identified by García-Mayoral & Jiménez (2011*b*); Endrikat *et al.* (2021) as a necessary condition for the development of spanwise independent structures called Kelvin-Helmholtz rollers. These structures are linked to a Kelvin-Helmholtz like instability and, despite having been originally identified in turbulent flows, may also emerge in transitional flows. The roughness also causes the appearance of a spanwise velocity component near the tip of the riblets. Despite being small, it could still play a significant role in supercritical transition scenarii where transition happens through three-dimensionalisation of the flow via secondary instabilities of the TS wave (Herbert, 1983). Figures 5.5 (b) and (c) displays a three-dimensional view of the streamwise velocity component of the most unstable modes of the two spatial branches found for $Re = 5000$, $s = 4.5$ and $\alpha = 1$. These two modes share almost the same growth rate, the fundamental mode remaining the most unstable. The competition between these two modes illustrates the effect of the centreline velocity modulation which leads to the dissociation of the TS branch into two smaller branches. The first one is characterised by a large upper part while the other remains located in the near wall region.

Finally, for $s = 4.5$ and $\alpha = 0.3$, the most unstable centre modes of the two branches are shown in figure 5.6. Streamwise and spanwise velocities are one order of magnitude higher than the wall-normal component and share the same shape: counter-rotating rolls oriented across the channel and propagating in the streamwise direction. In the fundamental case, rolls are centered at the widest channel opening while they are placed in a staggered pattern for the ρ_{12} mode. The staggered mode spans approximately 4 riblets. In both cases, instability arises from the modulation of the centreline velocity which induces strong spanwise velocity gradients in the middle of the channel. These spanwise velocity gradients are likely to destabilise the flow through inviscid, Kelvin-Helmholtz related mechanisms.

5.1.4 Streaks, parametric resonances and transient growth analysis

Transient growth plays a fundamental role in the (re)generation of turbulence through the near-wall cycle (Robinson, 1991; Jiménez & Pinelli, 1999; Brandt, 2014). The presence of riblets perturbs this cycle, since the cross-flow motion, necessary for the formation of the counter-rotating vortices, faces a greater resistance. In turn, the generated vortices are weaker than in a smooth channel flow and

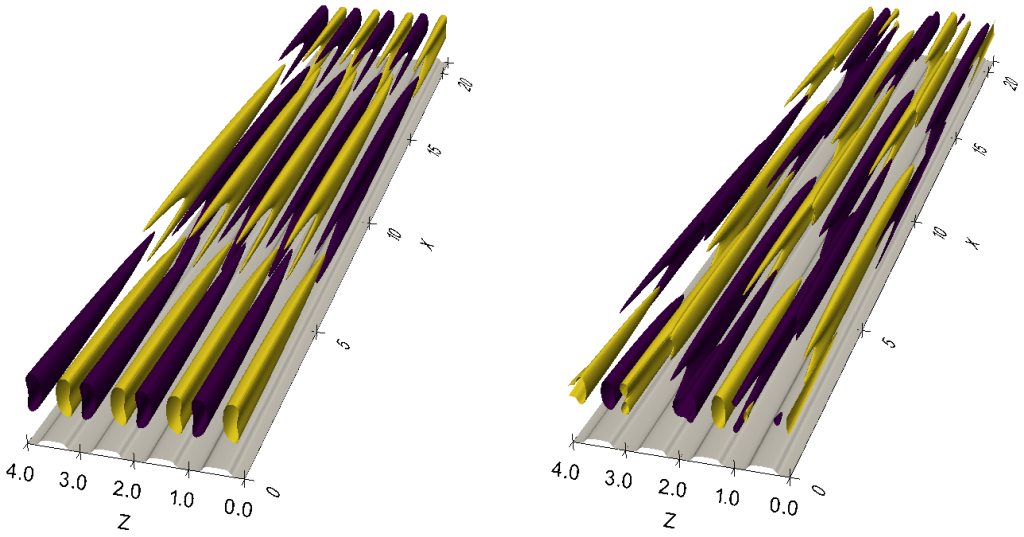

(a) ρ_0 (b) ρ_{12}

Figure 5.6: Three-dimensional representation of the streamwise velocity perturbation for $s = 4.5$, $Re = 5000$ and $\alpha = 0.3$ corresponding to centre modes. Left: fundamental mode with complex frequency $\omega = 0.0053 - 0.2971i$. Right: detuned mode with complex frequency $\omega = 0.0013 - 0.3020i$.

are located further away from the channel, eventually limiting the possibility of momentum transfer towards the streamwise velocity component of the flow (Chu & Karniadakis, 1993; Choi *et al.*, 1993; Lee & Lee, 2001). In this context, it is of interest to understand to what extent riblets influence the mechanisms behind transient growth.

Figure 5.7 displays an overview of the optimal energy amplification with respect to the periodicity. In particular, Figure 5.7 (a) represents the maximum gain as a function of the periodicity s. The other frames represent the gain G as a function of time for $Re = 5000$, $\alpha = 0$ and different periodicities s. As per the eigenvalues, the amplification curves are coloured according to their respective root-of-unity and only half of the curves are visible due to the coupling symmetry.

From figure 5.7, it is found that, besides for very small wavelengths ($s \leq 0.2$), riblets usually amplifies the strength of the near-wall cycle. A first resonance is observed for $s = \pi/4$, associated with a subharmonic disturbance. In this configuration, the riblet wavelength s is exactly half the optimal streaks wavelength. Maximum gain keeps increasing after $s = \pi/4$ until a maximum is reached for

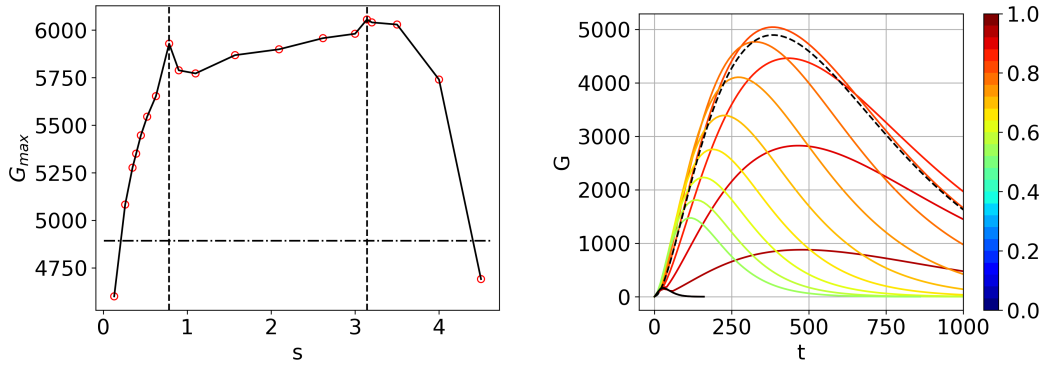

(a) $G_{max}(s)$

(b) $s = 0.25$

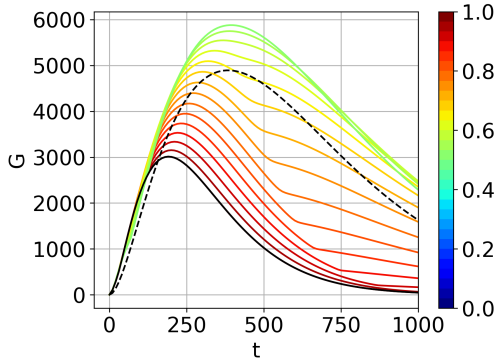

(c) $s = \pi/4$

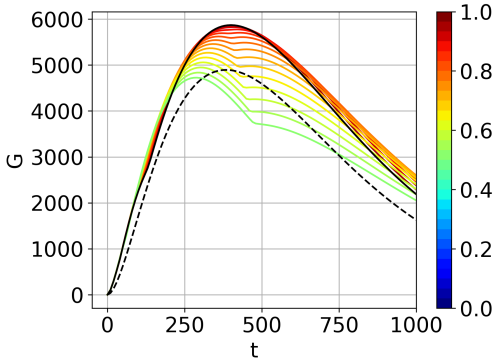

(d) $s = \pi/2$

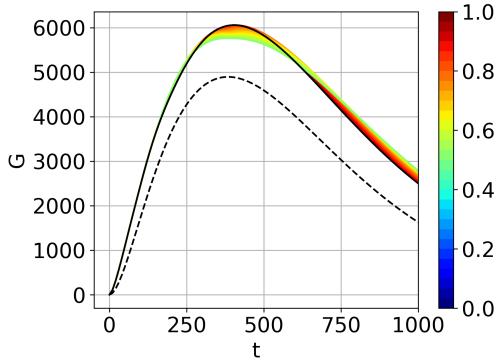

(e) $s = \pi$

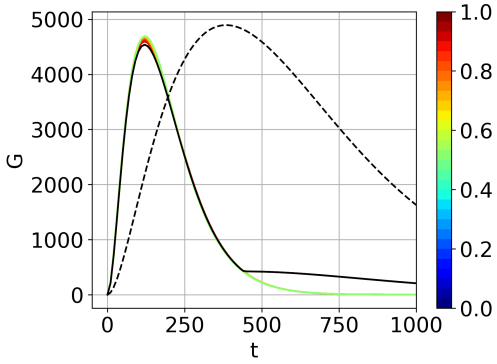

(f) $s = 4.5$

Figure 5.7: (a) Maximum gain as a function of the riblet periodicity. Vertical dotted lines indicate resonances at $s = \pi/4$ and $s = \pi$. Horizontal dotted line denotes the maximum gain in a smooth channel flow. (b) to (e) Examples of amplification curves as a function of time for $Re = 5000$, $\alpha = 0$ for several riblet periodicities, characteristic of the different regimes and resonances. For clarity, the curve associated with ρ_0, corresponding to fundamental, spanwise invariant modes is denoted in black. Dotted line represents the amplification curve for a smooth channel at $Re = 5000$, $\alpha = 0$ and $\beta = 2$, which yields the maximum optimal gain for this configuration (Schmid, 2001).

$s = \pi$. The optimal disturbance for $s = \pi$ is fundamental with the riblet wavelength s is exactly the optimal streaks wavelength. After this threshold, frustration appears and lead to both a sharp decrease in the maximum gain and smaller optimal times.

Comparing the maximum transient growth obtained for detuned modes to that with ρ_0, one can observe a difference of more than one order of magnitude. Notably, if the transient growth analysis would have been realised on a system composed of a single sub-unit, such a much weaker optimal energy gain would have been obtained. In fact, in this configuration, the size of a single sub-unit is too small to account for large-scale phenomenon such as the lift-up effect, underlining the necessity of considering a system spanning multiple sub-units. The amplification curves also appear to display a scaling with respect to the root-of-unity. This is not too surprising: each amplification curve represents an optimal perturbation whose spatial periodicity is governed by the corresponding root-of-unity. Precisely, the optimal perturbation with root-of-unity, say, ρ_j has a fundamental spanwise wavenumber equal to $\beta_j = j\pi/ns$. Ultimately, it can be found that the maximum gain scales as the square of β_j, in agreement with the scaling obtained by Gustavsson (1991) for smooth channel flow.
Notice that for $s = \pi/2$, the energy amplification is significantly enhanced by the presence of the riblets. This is probably a resonance effect as the riblet wavenumber has been chosen to be equal to the spanwise wavenumber yielding the maximum optimal gain $\beta_{opt} = \pi/s = 2$ in a smooth channel flow (Schmid & Brandt, 2014). Moreover, figure 5.7 shows that, as the riblet periodicity s is increased, the amplification curves progressively superpose themselves. This phenomenon arises from a degeneracy of the largest singular value of the exponential propagator $\exp(\mathbf{A}t)$. This is, however, not a trivial effect of the n-periodic symmetry. Mathematically, through the orthogonality of the Bloch modes, it can be demonstrated that the optimal perturbations are also orthogonal and thus form a basis of the eigenspace associated with the leading degenerate singular value. Physically, we now have n optimal perturbations corresponding to different roots-of-unity and with different wavelengths but sharing almost the same maximum gain G_{max} and optimal time T_{opt} and representing different possible and equally probable paths in phase space.

We are now focusing our attention on the form of the optimal perturbations which can be seen in figure 5.8. Cross-flow dynamics of the optimal initial disturbances for $Re = 5000$, $\alpha = 0$ and several riblet periodicity s are shown in figure 5.8. In all cases, the optimal perturbation(s) corresponds to counter-rotating vortices (CV) similar to the ones observed in a smooth channel flow (Schmid, 2001).

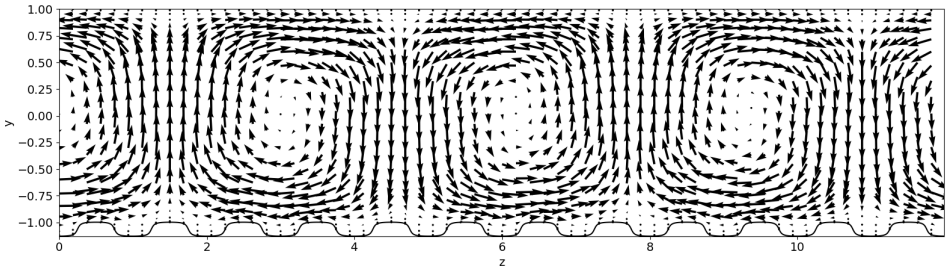

(a) $s = 0.25$

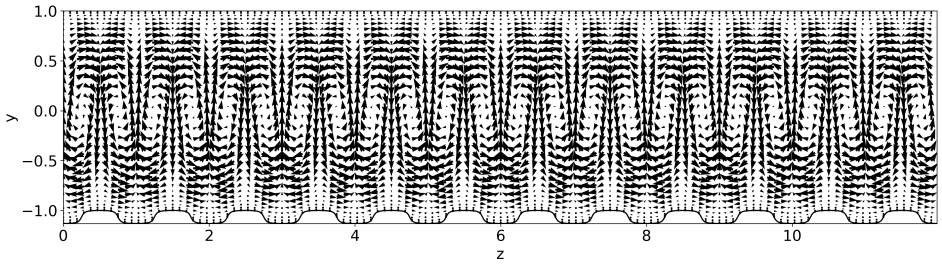

(b) $s = \pi/2$

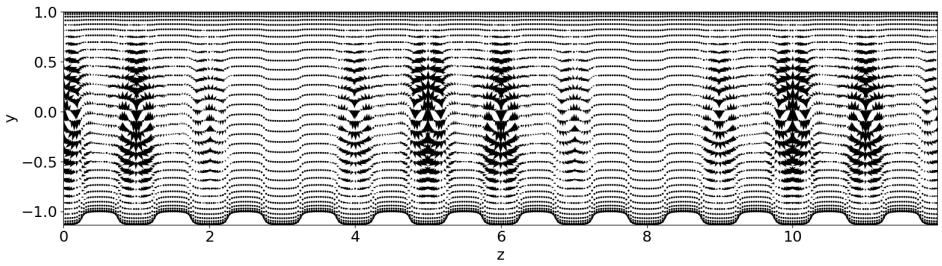

(c) $s = 4.5$

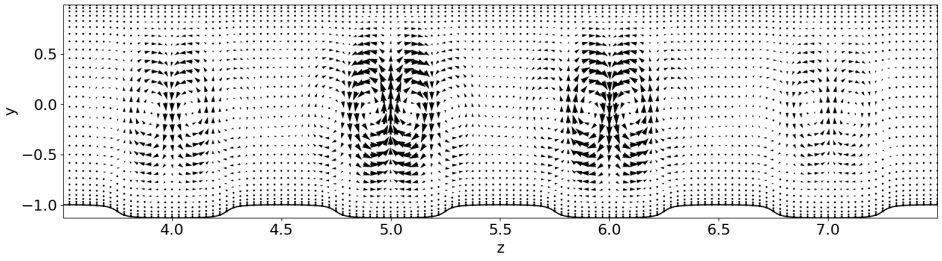

(d) $s = 4.5$, close-up of figure (c)

Figure 5.8: Cross-flow dynamics ($v - w$ vectors) of the optimal perturbation at initial time for $Re = 5000$ and $\alpha = 0$. For $s = 4.5$, the optimal perturbation is associated with root-of-unity ρ_{12} has been arbitrarily chosen between the n possible choices. Streamwise velocity disturbance is one order of magnitude weaker than the cross flow components and is not represented. The number of riblets visualised ($n = 12$) has been chosen for accommodating approximately two wavelengths of the counter-rotating optimal vortices for $s = 0.25$. Vectors are drawn every two points in the wall-normal direction and, in the spanwise direction, respectively every nine, five and two points for figures (a), (b), (c).

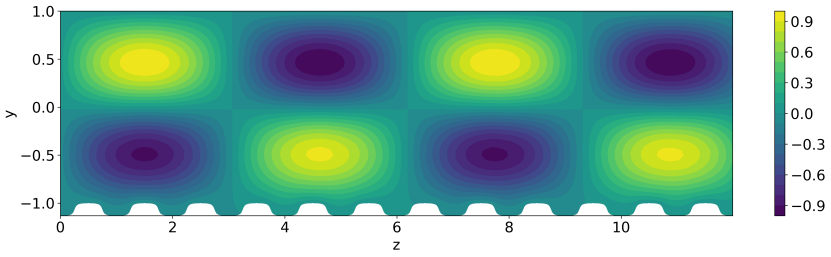

(a) $s = 0.25$

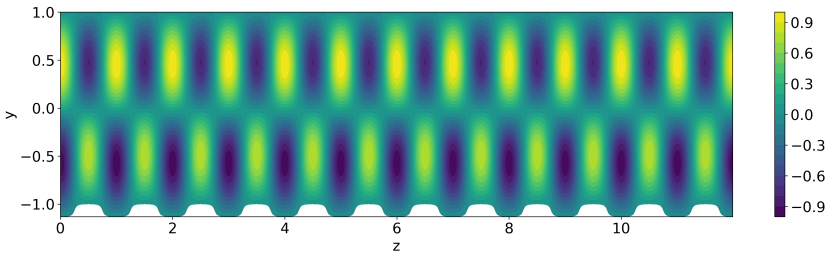

(b) $s = \pi/2$

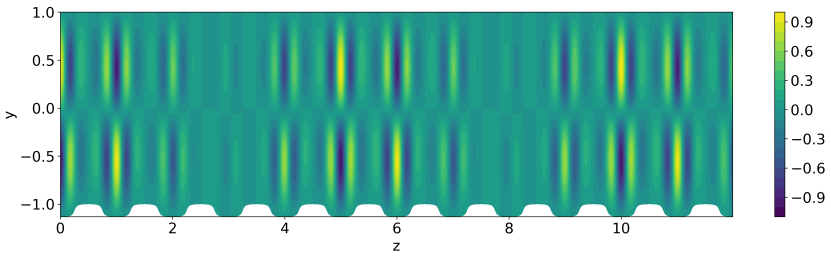

(c) $s = 4.5$

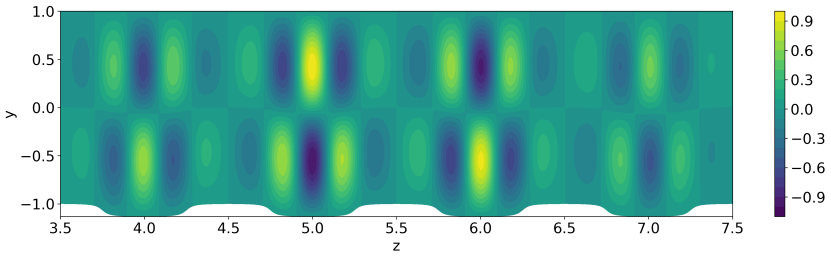

(d) $s = 4.5$, close-up of figure (c)

Figure 5.9: Streamwise velocity component of the optimal perturbation at target time T_{opt} for $Re = 5000$, $\alpha = 1$ and different periodicities s.

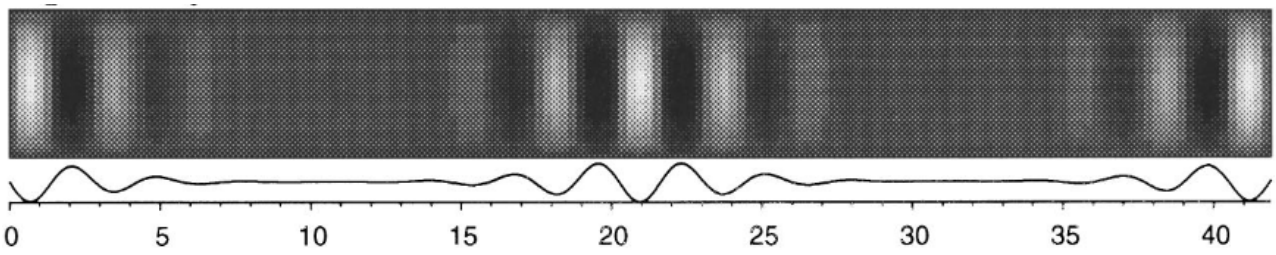

Figure 5.10: Amplitude modulation in a secondary eigenmode of forced convection rolls. Reproduced from Schmitz & Zimmermann (1996). Notice the resemblance with the modulation of the streaks' amplitude.

Streamwise velocity disturbance is one order of magnitude weaker than the cross flow components and is not represented. For $s = 0.25$, the CV span approximately six riblets, giving a spanwise wavenumber equal to $\beta = 2.09$. This is quite close to the spanwise wavenumber yielding the maximum optimal gain $\beta_{opt} = 2$ in the smooth channel, indicating a limited influence of the riblets on the flow. When the riblet periodicity is progressively increased, the wavelengths of the CV observed departs from the optimal value for the smooth channel and are closer to the riblets' own wavelength. This happens for $s = \pi/2$ where the CV exactly span one riblet.

The last case considered is obtained with $s = 4.5$. One optimal perturbation among the n possible, associated with ρ_8 is presented in figure 5.8 (c), with a close-up in (d). Other roots-of-unity are associated with different wavelength of the modulation. CV are still visible, however, they appear localised in regions with the widest channel opening and span only a third of a sub-unit. The corresponding wavenumber is $\beta = 2.11$, again quite close to β_{opt}. Differently from the two previously discussed configurations, the amplitude of the CV now appears modulated in the spanwise direction as a consequence of a beating phenomenon triggered by the superposition of two waves with incommensurable spanwise wavelengths. The optimal perturbations associated with other roots-of-unity are characterized by a similar shape, although with a different distribution of the CV as the spatial wavelengths involved in this beating phenomenon are different.

The mechanism responsible for the energy amplification, commonly called the lift-up effect (Brandt, 2014), will lead to the formation of streamwise-independent coherent structures also known as streaks. The streaks resulting from the development of the optimal disturbances presented in figure 5.8 can be seen in figure 5.9. Physically, the lift-up mechanism is characterised by a transport of the mean shear by the cross-flow velocity components to the streamwise velocity component. At target time, all the

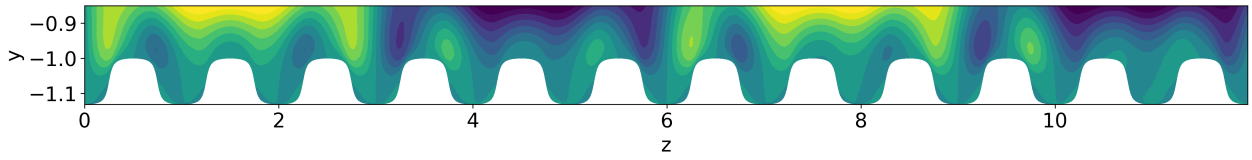

(a) $V_{opt}(0)$

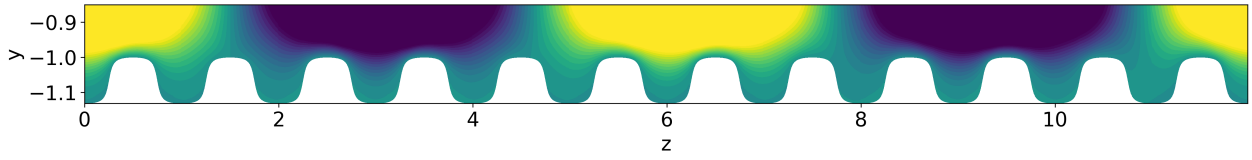

(b) $W_{opt}(0)$

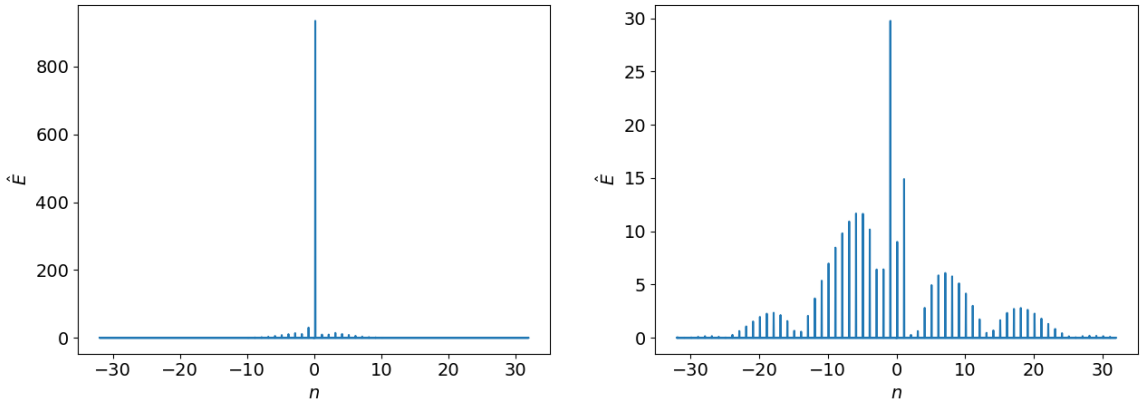

Figure 5.11: Close-up in the near-riblet region of the cross-flow dynamics ($v-w$ vectors) of the optimal perturbation at initial time for $Re = 5000$, $\alpha = 0$ and $s = 0.25$. Streamwise velocity disturbance is one order of magnitude weaker than the cross flow components and is not represented. The number of riblets visualised ($n = 12$) has been chosen for accommodating approximately two wavelengths of the counter-rotating optimal vortices. Bottom: Spatial Fourier spectra of the wall-normal velocity disturbance taken at wall-normal positions $y = 0$ (left) and $y = -.95$ (right).

optimal perturbations maintain the same spatial periodicity shown at initial time.

The non-modal behaviour of the considered flow is thus strongly affected by the periodicity of the roughness. For small s, the riblets' influence on the shape of the optimal perturbations appears limited as the initial optimal CVs are characterized by a wavelength almost corresponding to that of a smooth channel flow. The streaks are lifted above the riblets and the flow behave as in a smooth channel of smaller height. Riblets appear to have an impact limited to a buffer zone, extending approximately from the tip of the roughness to $y = -0.9$, and modifying the shape of the optimal perturbations only locally. A close-up of the region in the vicinity of the roughness for $s = 0.25$ is provided in figure 5.11 for the wall-normal and spanwise velocities at the initial time. In this region, velocities are smaller than in the bulk of the channel but still non negligible (around 10% of the maximum velocity) and exhibit a rather complex shape as shown by the spatial Fourier spectrum provided in figure 5.11(d). This also sheds some light on one small shortcoming of the ROG formulation: the assumption that the roughness shape can be accurately described by only a few leading Fourier modes is usually verified either through the convergence of the growth rate of the most unstable mode (Floryan, 2007; Moradi & Floryan, 2014) or of the maximum gain (Szumbarski & Floryan, 2006; Chavarin & Luhar, 2020). However, even when these quantities appear well converged, some regions of interest like the vicinity of the riblets may require a much larger number of modes to be accurately described. For intermediate periodicities, the CVs appear more deformed and have a wavelength departing from that recovered in the smooth channel flow. These optimal disturbances result from a competition between the natural, optimal wavenumber of the streaks and the parametric forcing due to the riblet. Resonance can be observed when the riblet wavenumber is equal to the optimal streak wavenumber or one of its subharmonics, yielding large energy amplification.

For large periodicities, riblets constrain the streaks wavelength and n possible optimal perturbations could be found, having amplitude modulated in the spanwise direction. A similar mechanism has already been described for phase-locked lasers and is denoted as geometric frustration (Nixon *et al.*, 2013). The phenomenon arise from competing mechanisms of different wavelengths which prevent the existence of a single ground state. The analogy with the present case appears quite clearly: transient growth analysis yields optimal disturbances with maximum kinetic energy at the optimal time. Competition arises between the lift-up mechanism generating CV and streaks at an optimal wavenumber $\beta_{opt} \approx 2$ and the riblets, which act as a forcing with wavenumber $\beta_f = \pi/s$. In the domain of fluid

mechanics, a similar phenomenon was observed in the study of secondary flows in Rayleigh-Bénard convection with wavy walls (Schmitz & Zimmermann, 1996). More recently, the works of Hossain & Floryan (2013, 2022) also showed the existence of a beating in the secondary pattern and its link with a wavenumber lock-in phenomenon.

5.1.5 Oblique transition, Orr mechanism and resolvent analysis

A resolvent analysis allows the identification of high-energetic flow structures in both laminar and turbulent flows through a singular value decomposition of the forcing-response transfer function, commonly called the resolvent operator (Schmid, 2007; McKeon & Sharma, 2010*b*). For a smooth channel flow, the response to a harmonic forcing is characterised by the presence of two pseudo-resonances (Schmid & Brandt, 2014): the strongest one leads to the generation of the most unstable TS wave while the other is linked to a centre Squire mode.

Resolvent curves are displayed for $Re = 5000$, $\alpha = 1$ and different periodicities in figure 5.12. For small periodicity $s = 0.12$, the two pseudo-resonances found for the smooth channel flow are retrieved. The distinction between the two mechanisms is quite clear: almost only the fundamental mode experience a pseudo-resonance for $\omega = 0.27$ while subharmonic and detuned forcings appear responsible of the excitation of the flow at larger frequencies. For these modes, the second pseudo-resonance disappears and is replaced by a plateau formed by the superposition of several amplification curves associated with different roots-of-unity. In other words, as the frequency is increased, the optimal energy amplification of the whole system remains quasi constant through an evolution of the forcings' spatial periodicity. Despite yielding responses one order of magnitude below the pseudo-resonance, these optimal forcings excite a very broad range of frequencies, making them relevant in a noise-triggered transition scenario (like the bypass transition) for which the probability to hit exactly the frequency of the pseudo-resonance is small (Chapman, 2002). The mechanism associated with these forcings is known as the Orr mechanism (Orr, 1907*a*) and shown in figure 5.13. It relies on the two-dimensional deformation of vortical structures by the mean flow. Structures which are initially aligned against the direction of the flow tend to realign themselves with it and, in doing so, generate transient growth through the concentration of vorticity (Jiao *et al.*, 2021).

For larger wavelengths s, a few observations can be made. Most importantly, the riblets induce a desynchronisation of the pseudo-resonance: the maximum gain is now reached for a detuned mode (ρ_2

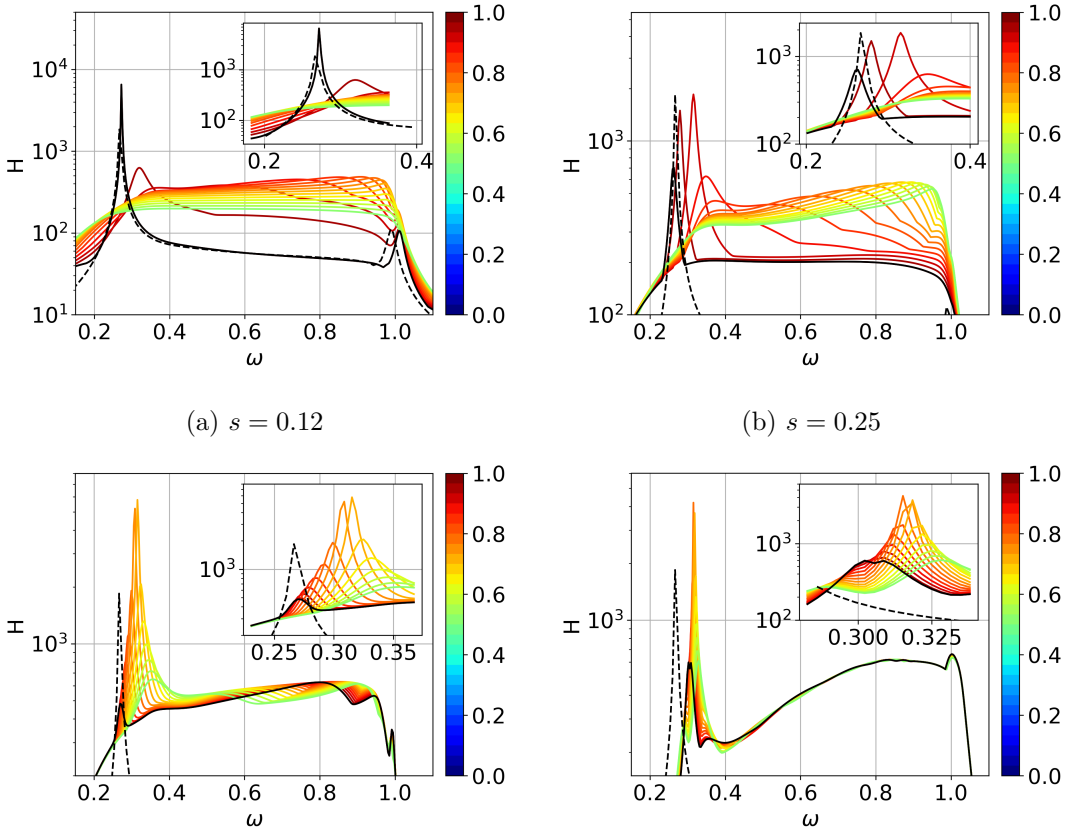

(a) $s = 0.12$ (b) $s = 0.25$

(c) $s = 1$ (d) $s = 4.5$

Figure 5.12: Resolvent norm for $Re = 5000$, $\alpha = 1$ and different riblet periodicities s. Dotted line represents the resolvent norm for a smooth channel flow with $Re = 5000$,$\alpha = 1$ and $\beta = 0$. The inset is a close-up on the first pseudo-resonance. Black curve is the curve associated with ρ_0, corresponding to fundamental, spanwise invariant modes.

for $s = 0.25$), associated with a three-dimensional optimal forcing and response, as it will be shown later. The detuning appears to increase as s is increased: maximum responses are obtained for ρ_8 ($s = 1$) and ρ_6 ($s = 4.5$). This three-dimensionalisation of the forcing and response is associated with a decrease of the maximum gain for small s, whereas it leads to an increase of the resolvent norm for intermediate and large values of s. A small shift in the pseudo-resonance optimal frequency can also be seen as it goes from $\omega_{opt} = 0.27$ to $\omega_{opt} = 0.31$ for larger periodicities. For $s = 4.5$, the amplification curves collapse, as previously observed in the transient growth analysis. Again, this superposition results from a degeneracy of the largest singular value of the resolvent operator which generates n equally amplified optimal forcing and responses. Physically, this also indicates the

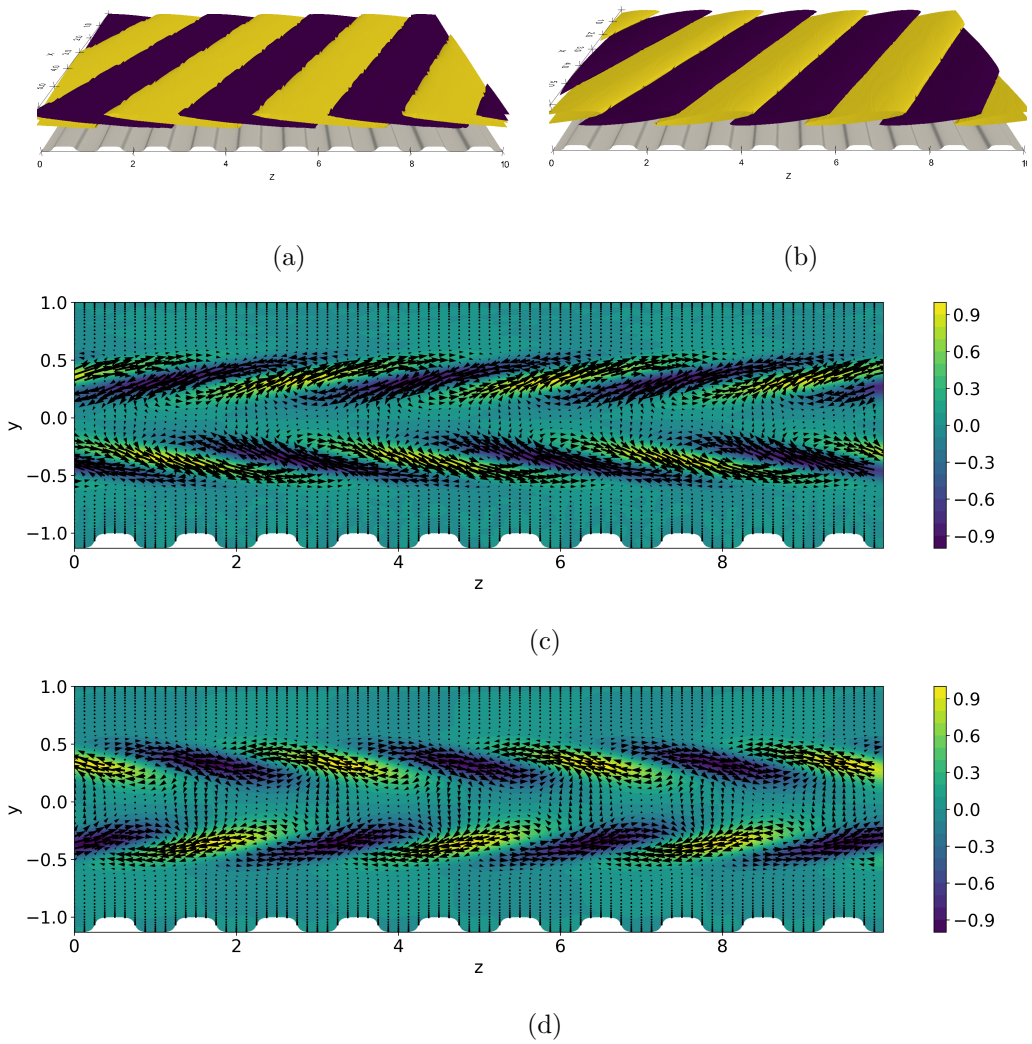

Figure 5.13: Illustration of the Orr mechanism for $s = 0.25$ and $\omega_{opt} = 0.9$. Three-dimensional view of the streamwise velocity component of the optimal forcing (a) and response (b). Only half the channel is shown. Contour plot of the streamwise velocity disturbance and quiver plot of the cross-flow dynamics for the optimal forcing (c) and response (d).

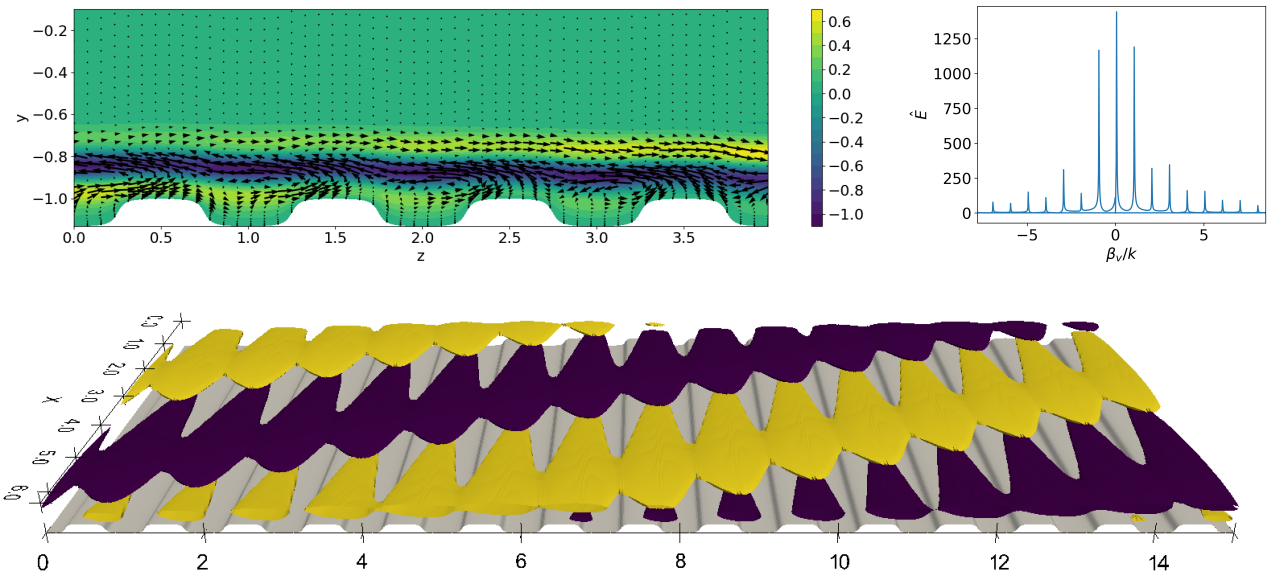

Figure 5.14: Top left: optimal forcing at initial time for a system with $Re = 5000$, $\alpha = 1$ and $s = 0.25$. Only four riblets are represented for the sake of visualisation. Corresponding root-of-unity is ρ_2. Quiver plot depicts the cross-flow dynamics (v_w). Contour plot depicts the streamwise velocity disturbance. Note the y-axis: for simplicity, only half of the channel is being shown. Bottom: three-dimensional view of the streamwise velocity component of the optimal response at the optimal frequency.

presence of a lock-in phenomenon for the forcings and their response in this range of frequency.

We now turn our attention to the optimal forcing and responses corresponding to the first pseudo-resonance. These are shown in figures 5.14, 5.15 and 5.16 for increasing values of s. The optimal forcings are three-dimensional and are characterised by strong streamwise and spanwise velocity components, while the wall-normal velocity component is one order of magnitude weaker. The optimal forcings appear as oblique waves with varying spatial wavelengths which eventually develop into deformed 3D TS waves. With this in mind, it is important to remember that detuned modes with root-of-unity ρ_j do not exist by themselves but instead form a pair with the disturbance associated with the conjugate root-of-unity $\rho_j^* = \rho_{n-j}$. The desynchronisation appears progressively: for small s the forcing couples 15 riblets and generates a three-dimensional perturbation similar to a TS wave. Structures similar to the small vortices in the top corners of the riblets were also observed numerically by Goldstein & Tuan (1998). For larger s, the influence of the riblets is stronger: the optimal forcing now only spans 5 riblets and appears to follow the shape of the roughness. The response has a strong streamwise component localised on top of the riblets. In all cases, the spanwise component takes the

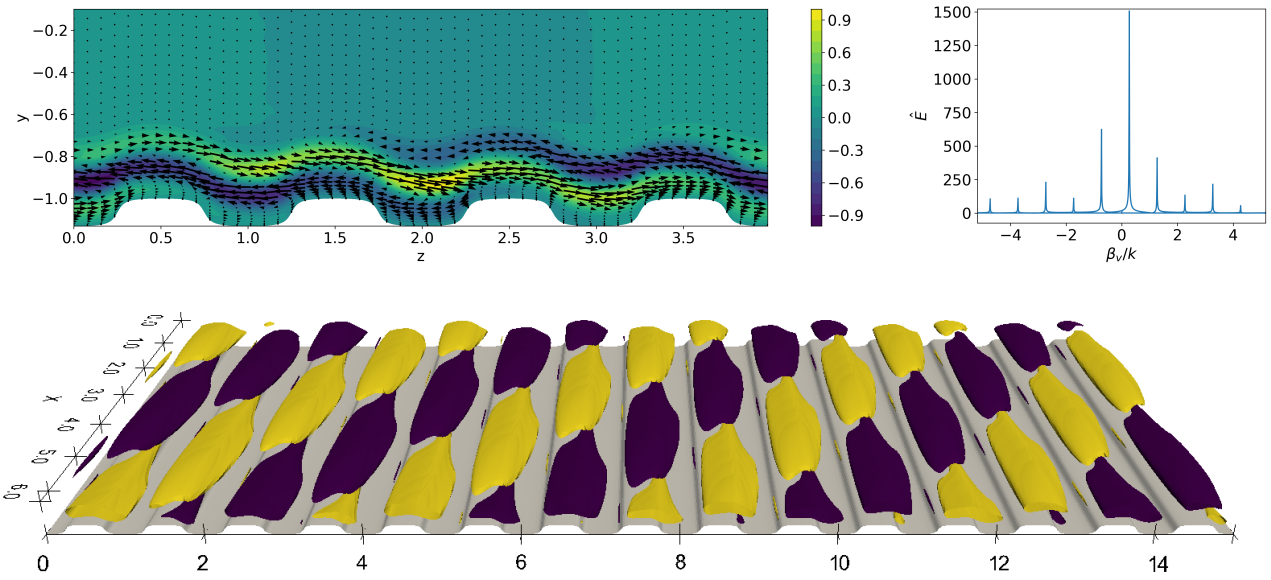

Figure 5.15: Same as figure 5.14 for $s = 1$.

form of oblique waves. Last, in the case of $s = 4.5$, the forcing wavelength becomes smaller than that of the riblets and now penetrates deeply into the grooves. For all riblet periodicities, the Orr mechanism is at play and appears through the realignment in the spanwise direction of the coherent structures. The responses are oblique waves which are likely to trigger oblique transition. In the context of controlling laminar-turbulent transition, the onset and development of oblique waves may be problematic. Indeed, because of non-linearities (Schmid & Henningson, 1992), this type of transition was found to be quicker and to require smaller initial energy than supercritical or even bypass transition (Lundbladh *et al.*, 1994; Chapman, 2002).

5.2 Stability of the flow over a superhydrophobic wall

5.2.1 Problem formulation

The influence of a superhydrophobic (SH) wall on the channel flow stability is now investigated. The grooves of the previous configuration are now fully filled with gas and the liquid is assumed in a Cassie-Baxter state. The bottom wall consists in a flat wall alternating solid patches and trapped gas pockets (Yu *et al.*, 2016; Tomlinson, 2021). As previously, the whole pattern has a half periodicity s. For simplicity, it is assumed that the solid and SH patches have the same size. No-slip boundary

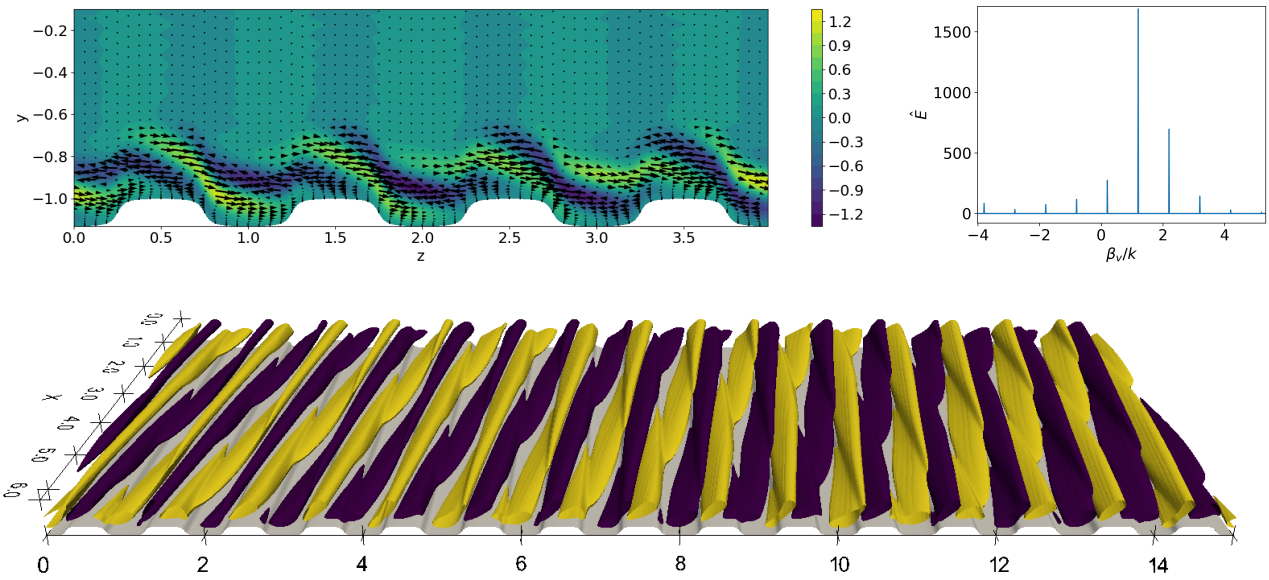

Figure 5.16: Same as figure 5.14 for $s = 4.5$.

conditions are imposed on the solid part, while a shear-free boundary condition is assumed for the gas pockets (Martell *et al.*, 2010; Park *et al.*, 2013; Jelly *et al.*, 2014; Seo & Mani, 2018).

Navier-Stokes equations still govern the flow dynamics. However, and unlike the previous stability analyses (Yu *et al.*, 2016; Tomlinson & Papageorgiou, 2022), the movement of the interface is taken into account, meaning an extra variable must be introduced, namely the interface deformation $\eta_1(x, z)$. The interface deformation is considered small and is governed by a linearised Young-Laplace equation (Seo & Mani, 2018; Picella *et al.*, 2020):

$$\nabla^2 \eta_1 = \frac{p_1}{We}, \tag{5.10}$$

where p_1 is the pressure disturbance above the interface and $We = \rho U^{*2} h^*/\gamma$ is the Weber number with ρ the density of the fluid and γ the surface tension. Note that this slightly differs from Seo & Mani (2016, 2018) in which is used a Weber number We_s based on the surface half-periodicity s instead of the flow macroscopic lengthscale. It can be easily seen that $We_s = sWe$. The interface is also assumed to be pinned to the riblets' edges (Teo & Khoo, 2008; Seo *et al.*, 2015; Seo & Mani, 2018; Picella *et al.*, 2020), and obeys the kinematic condition, yielding:

$$v(x, y = -1 + \eta_1, z, t) = \frac{\partial \eta_1}{\partial t} + u\frac{\partial \eta_1}{\partial x} + w\frac{\partial \eta_1}{\partial z}, \tag{5.11}$$

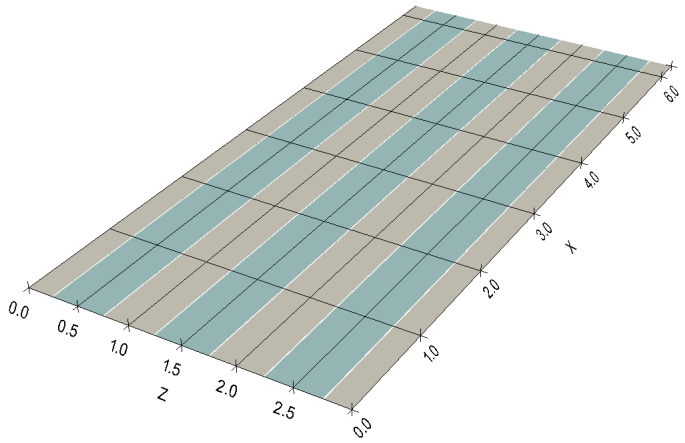

Figure 5.17: Sketch of the SH surface, composed of three sub-units. Solid surface is in grey while light blue indicates the gas interface. White lines denotes the contact lines between the three phases.

which, after Taylor expanding around $y = -1$ and linearising around the base flow $\mathbf{U}_0 = [U_0(y, z), 0, 0]^T$, gives:

$$v_1(x, y = -1, z, t) = \frac{\partial \eta_1}{\partial t} + U_0 \frac{\partial \eta_1}{\partial x}. \tag{5.12}$$

This law is imposed for the normal velocity boundary condition on the superhydrophobic patch. The validity of the linearised Young-Laplace equation is discussed in Seo & Mani (2018). Note that the configuration presented here is equivalent to the one in the stability analysis of Yu *et al.* (2016). It is also complementary to the case presented in Tomlinson & Papageorgiou (2022) where the reference lengthscale, used to non-dimensionalise the stability problem, is the "microscopic" one (the periodicity of the riblets s) while the "macroscopic" lengthscale (the height of the channel) can be varied. The present work extends these previous analyses, taking now into account the effect of the moving interface, which may have a strong effect on the flow stability, as for instance discussed in Picella *et al.* (2020)

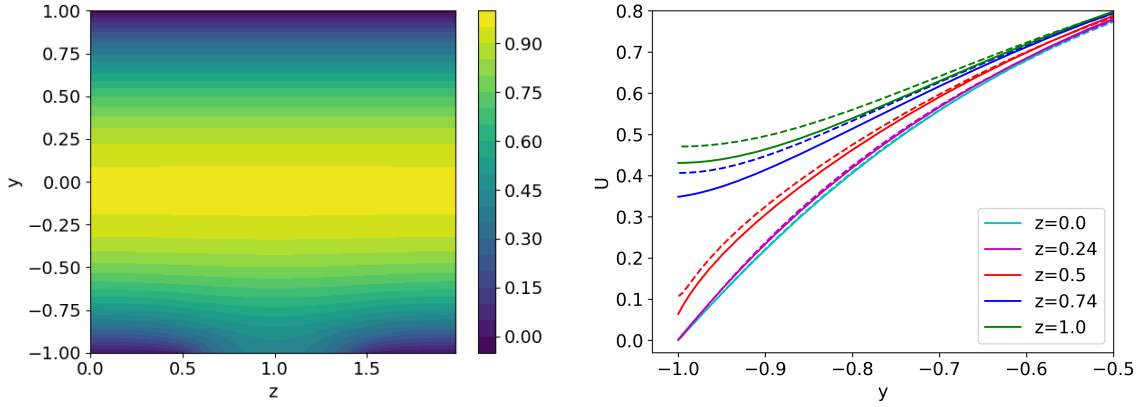

Figure 5.18: Left: base flow $U_0(y,z)$ for $s = 0.5$. No-slip boundary conditions are used on $z \in [0, 0.5]$ and $z \in [1.5, 2]$ while moving slip boundary conditions are imposed on $z \in [0.5, 1.5]$. Right: comparison between a base flow obtained with a smoothing (full lines) and without any smoothing of the discontinuity (dotted lines) at different spanwise positions.

5.2.2 Discussion on the singularity removal and laminar base flow

As for the rough surfaces, the only non-zero velocity component of the base flow $\mathbf{Q}_0$ is the streamwise velocity $U_0(y,z)$ which is solution of a Stokes equation:

$$\frac{\partial^2 U_0}{\partial y^2} + \frac{1}{s^2}\frac{\partial^2 U_0}{\partial z^2} = -2 \tag{5.13}$$

together with the mixed no-slip/slip moving boundary condition previously assumed. Interface curvature effects are neglected as they remain in general small (Ou *et al.*, 2004; Ou & Rothstein, 2005). For the interested reader, effects on the laminar flow are discussed in detail in the works of Game *et al.* (2017, 2019).

Besides, with or without interface curvature, such a boundary condition involves a stress discontinuity at the triple point which needs to be tackled in order to accurately solve the Stokes equation (and the stability problem). The simplest solution, employed all throughout the following, is to smooth out the discontinuity through the use of a continuous approximation of a step function (Kirk, 2017) of the form $H_s(z) = \frac{1}{2} + \frac{1}{\pi}\arctan(\delta_s(z - z_i))$ where z_i denotes the spanwise position of the discontinuities and δ_s is the strength of the smoothing. The resulting base flow obtained with this approach can be seen in the left part of the figure 5.18. This will definitely induce an error on the wall velocities and on the spanwise velocity gradients as it can be seen in the right part of figure 5.18. However, for now, it still remains unclear to what extent will influence the characteristics of the flow instability.

δ_s	ω_r	ω_i
0.1	0.0140	-0.4200
0.05	0.0128	-0.4385
0.01	0.0115	-0.4581
No smoothing	0.0111	-0.4549

Table 5.1: Evolution of the growth rate and frequency of the most unstable capillary mode for $Re = 5000$, $We = 12$, $\alpha = 1$ and $s = 0.5$.

Another possibility to tackle the stress discontinuity has been proposed in the work of Tomlinson & Papageorgiou (2022). The idea is to explicitly decompose the solution to the discontinuous problem (either the Stokes or the stability problem) into a regular and a singular part. In a polar coordinate system (r, θ) centred on the singularity, and after some involved algebra, the singular part can be determined at the exception of a coefficient, called the strength of the singularity. For example, for the Stokes problem, the singular term is found to be of the form $U^s = B_1^s r^{1/2} \sin(\theta/2)$, with B_s the strength of the singularity. This decomposition is then introduced in the linear stability equations yielding a stability problem where the singularity strength behaves as an extra unknown that must be determined. For more in-depth explanations of the method, the reader is referred to the PhD thesis of Tomlinson (2021) and to the works of Game *et al.* (2017, 2019). As this method allows a proper mathematical treatment of the discontinuity, it was initially preferred to the smoothing-out method. However, its generalisation to moving interfaces appeared definitely not so straightforward, and two main difficulties arise. The first is that a time-dependent interface deformation implies a time-dependant singularity strength, meaning instabilities may arise from this singular part. One may ask the physical relevance of such instabilities as, originally, the decomposition is just supposed to be a mathematical trick to remove the singularity. In a similar fashion, the interaction with the Bloch wave framework is not straightforward, since it is not clear whether the singularity strength be modulated as the other variables are. For these reasons, in this part of the work we have preferred to use a simple smoothing of the discontinuity.

5.2.3 Modified TS waves, capillary waves and modal stability analysis

The stability of the flow over a superhydrophobic wall is dependent on many parameters, that will be discussed in the following. As previously, the Reynolds number and the streamwise wavenumber

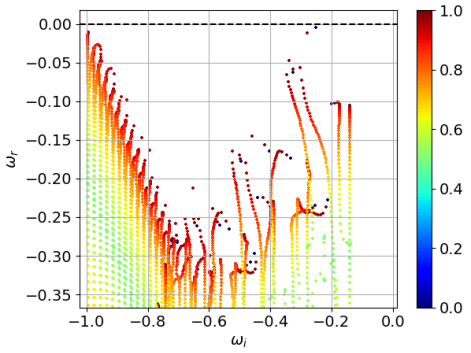

(a) $s = 0.05$

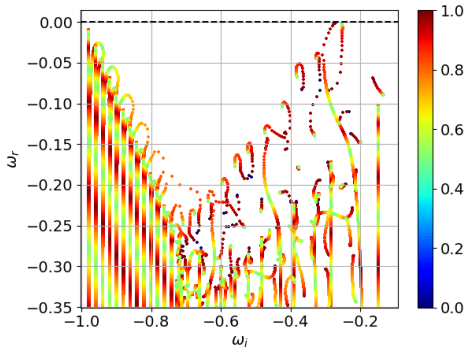

(b) $s = 0.3$

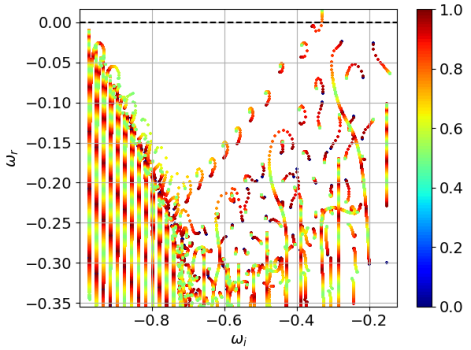

(c) $s = 0.5$

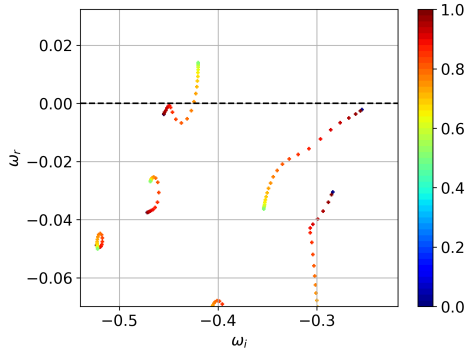

(d) $s = 0.5$, close-up on the two branches of interest

Figure 5.19: Spectra of the flow stability over a superhydrophobic wall for $Re = 5000$, $We = 12$, $\alpha = 1$, $n = 50$ and different riblet periodicities.

are fixed respectively at $Re = 5000$ and $\alpha = 1$. Concerning the Weber number, its order of magnitude can be obtained by considering a realistic operating condition, say, for example the experiment of Daniello *et al.* (2009): $\rho^* = 1000kg/m^3$, $h^* \approx 2mm$, $U_r^* \approx 1m/s$ and $\gamma^* = 0.071N/m$ giving $We \approx 12$. Mainly three pattern periodicities are considered: $s = 0.05$, $s = 0.3$ and $s = 0.5$. Basing ourselves on the semi-empirical formula from Seo *et al.* (2015) (eq. 15) and setting the solid fraction (the liquid-solid/liquid-gas area ratio of the texture pattern) ϕ_s as $\phi_s = 0.25$ (as for the present roughness), it can be found that the first case roughly corresponds to the upper admissible limit of the interface stability in the case of an overlying turbulent flow (Picella *et al.*, 2019). Thus, technically, the two others configurations can not sustain turbulent flow without experiencing the wetting transition. They still are physical and relevant as such large in the experiments of Ou *et al.* (2004); Ou & Rothstein (2005) on laminar drag reduction. In such configurations, the idea is to avoid transition to turbulence

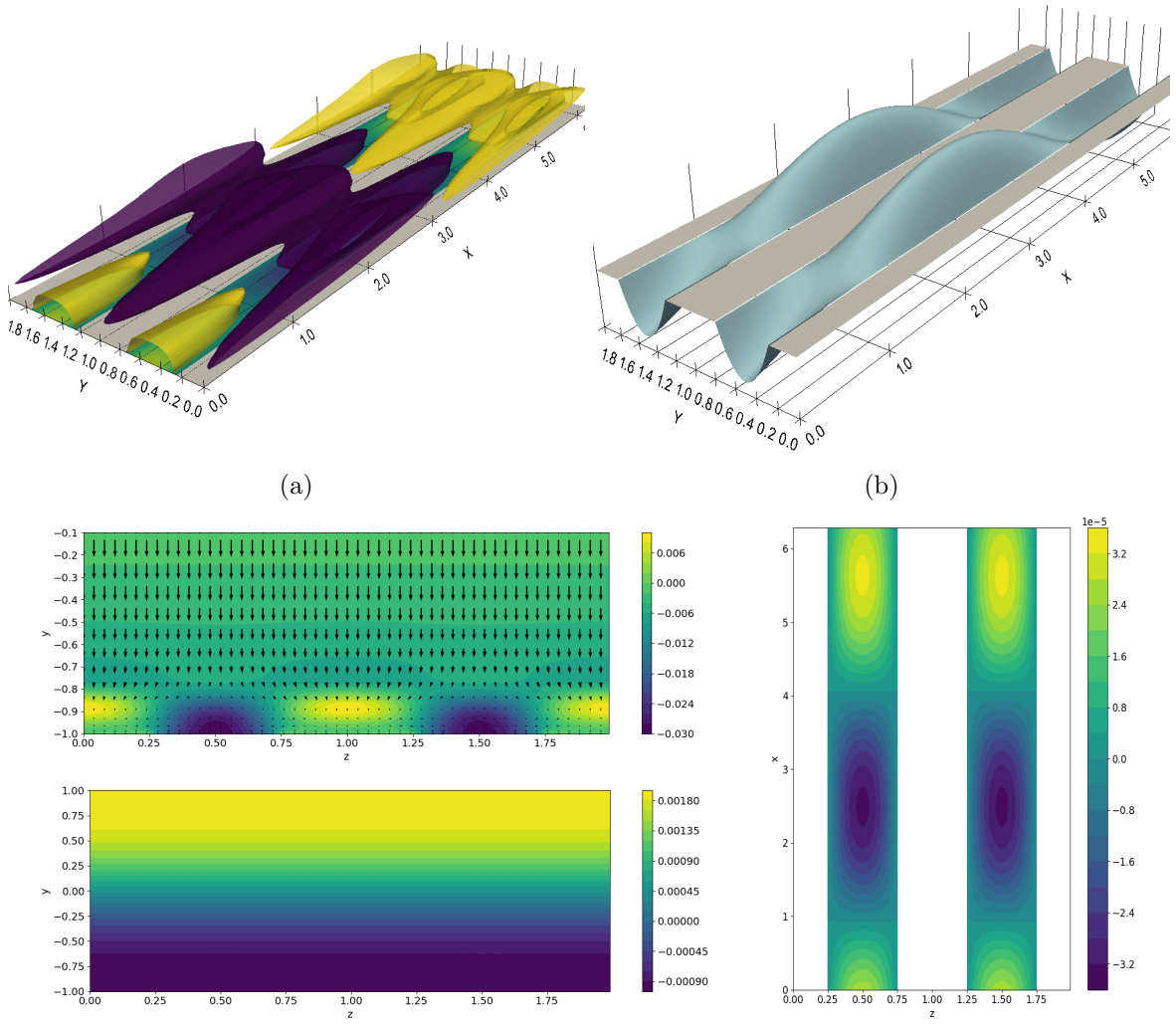

Figure 5.20: Most unstable modified TS mode for $Re = 5000$, $We = 12$, $\alpha = 1$ and $s = 0.3$. The instability is fundamental and all the figures are visualised on two sub-units. (a) Three dimensional streamwise velocity perturbation u_1. Only half the channel is shown. (b) Three-dimensional interface deformation. For visualisation purposes, the deformation has been amplified such as $\max(\eta_1) = 0.5$ (c) Top: contour plot of the streamwise velocity disturbance and quiver-plot of the cross-flow dynamics $(v - w)$ in the (y, z) plane. Bottom: contour plot of the pressure disturbance in the (y, z) plane. For these two figures, only half the channel is shown for clarity. (d) Interface deformation η_1 in the $(x - z)$ plane, without any amplification factor. The white strips are the solid parts.

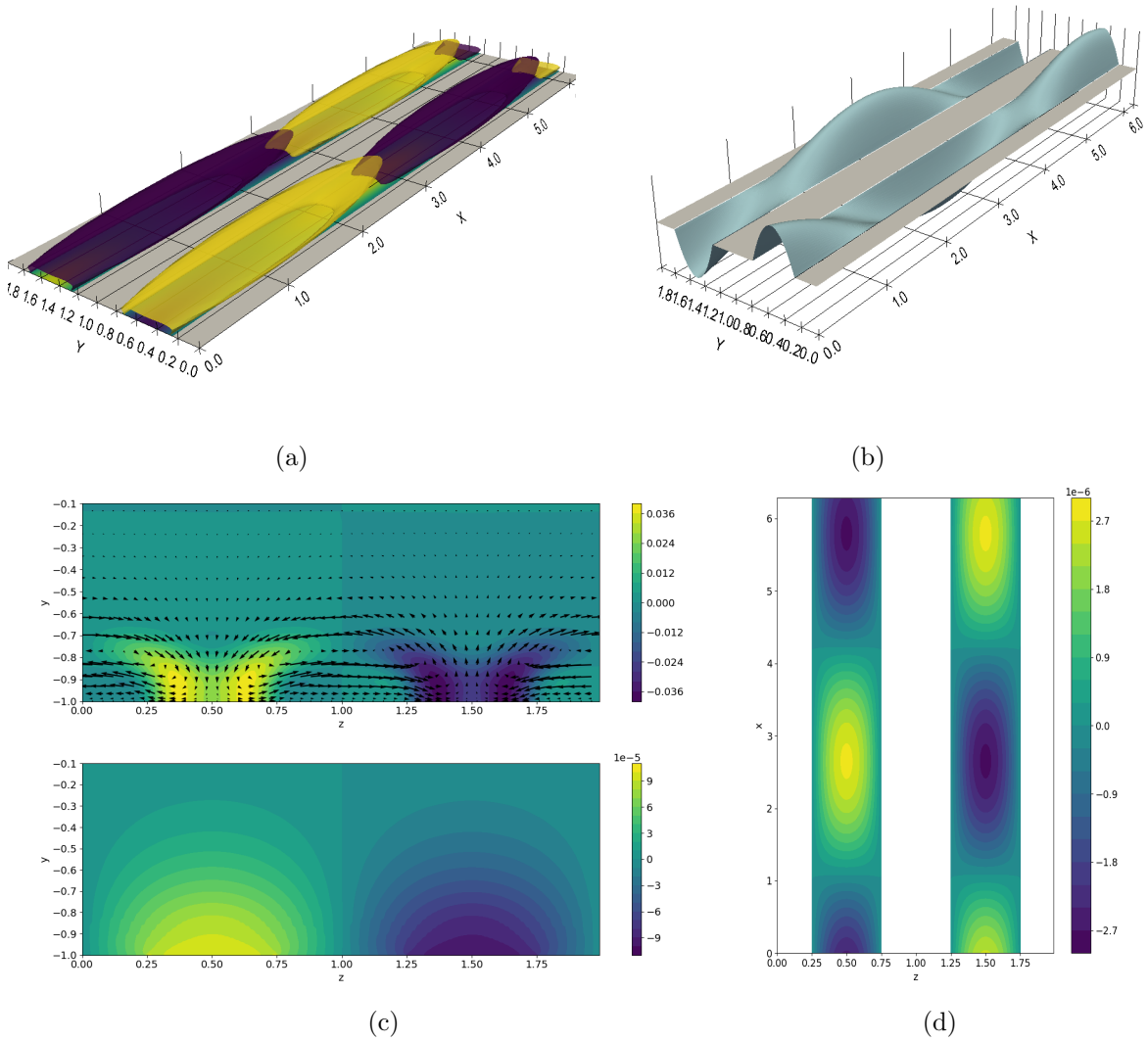

Figure 5.21: Same as figure 5.20 but for the subharmonic capillary mode.

at all cost, confirming the interest of a stability analysis. In his work, Tomlinson & Papageorgiou (2022) considered even larger periodicities but the wetting stability of the interface for such large superhydrophobic patch is rather unlikely.

Modal stability is investigated for $Re = 5000$, $We = 12$, $\alpha = 1$ and the three considered values of the periodicity s. The three spectra are displayed in figure 5.19. The most striking feature is the apparition of a new spatial branch associated with subharmonic capillary pressure waves competing with the fundamental TS branch. Besides, the surface seems to have a limited influence on the growth rate: only larger periodicities s lead to unstable growth rates. This is quite in contrast to the previous stability analyses (Yu *et al.*, 2016; Tomlinson & Papageorgiou, 2022) which found the flow to be unstable for much smaller Reynolds numbers. This indicates two possibilities: either the discontinuity smoothing on the base flow is too strong and cause a strong damping of the growth rate, either the moving interfaces have a strong stabilising effect on the flow. This first possibility is tested by investigating the growth rate of the most unstable capillary mode (allegedly more sensible to the discontinuity smoothing than the TS mode due to its interfacial nature) for $s = 0.5$, which should be the most sensible case. The results are presented in table 5.1 and, despite having an impact (up to 20% of error on the growth rate in the worst case), the influence does not appear as strong to justify the differences with the results of the previous stability analyses (Yu *et al.*, 2016; Tomlinson & Papageorgiou, 2022) not taking into account the interface motion. Also note that as the smoothing is reduced, the discontinuity gets sharper, and more points in the spanwise direction are needed. In the case of no-smoothing, to prevent the apparition of spurious oscillation, the number of points in the spanwise direction had to be doubled.

Eigenfunctions corresponding to the two families of modes are displayed for $s = 0.3$ in figures 5.20 and 5.21. The first mode, which is the most unstable for small pattern periodicity, bears a strong resemblance with a TS wave deformed by the presence of slip patches. Whereas, larger patterns tend to favour the subharmonic capillary mode, characterised by the propagation of a pressure disturbance on the interface. In this latter case, the streamwise velocity component assumes the largest values near the interface, while the cross-flow dynamics shows the development of large-scale vortices between two superhydrophobic patches. In both cases, the interface deformation is small, at the limit of the algorithm's precision but this is not too surprising: remember the interface deformation is non-dimensionalised with the channel half-height h and not the pattern wavelength s. The same

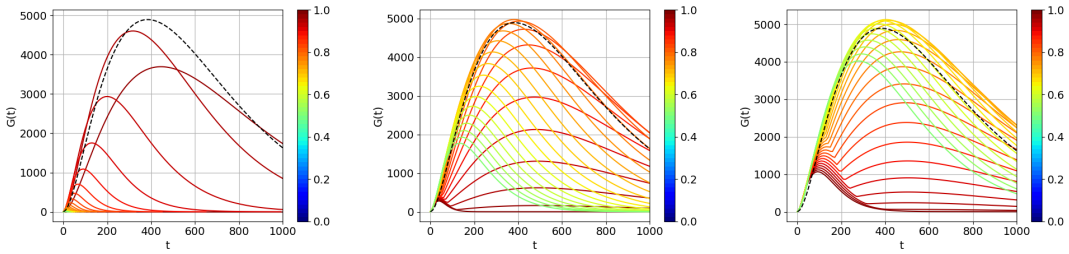

(a) $s = 0.05$ (b) $s = 0.3$ (c) $s = 0.5$

Figure 5.22: Amplification curves of the flow stability over a superhydrophobic wall for $Re = 5000$, $\alpha = 0$, $We = 12$, $n = 50$ and different riblet periodicities.

pattern periodicities were quickly investigated for the same Reynolds number but at a higher Weber number $We = 150$, corresponding to a liquid-infused surface. The mechanisms remained the same, the instability switch between the two instability types happened for slightly before $s = 0.3$, and, more importantly, interface deformations were several orders of magnitude higher. To give an order of magnitude, the interface deformation for $s = 0.5$ reached a maximum of 10^{-2}, potentially generating to the roughness effect predicted in Sundin *et al.* (2021). Regarding the shape of the interface deformation itself, since the pressure disturbance remains constant over the interface, the linearised Young-Laplace equation becomes nothing more than a Poisson equation. Interestingly (and unfortunately), it is rather well known that the solution to this type of equation is entirely determined by the boundary conditions, or, in the present case, the boundary condition assumed for the triple point. One may expect significantly different results should, for example, a dynamical contact angle condition (Legendre & Maglio, 2015) be used.

5.2.4 Streaks over a superhydrophobic wall

The influence of the superhydrophobic wall on the streaks is considered. Quite disappointingly, the superhydrophobic wall appears to have little influence on the streaks. Amplification curves are shown in figure 5.22 for$Re = 5000$, $We = 12$, $\alpha = 0$ and different periodicities. No significant changes neither in the optimal time, nor in the maximum gain can be observed, besides for small wavelengths where slightly smaller gains can be seen. The optimal perturbation associated with the maximum gain for $s = 0.3$ is displayed in 5.23. It is worth noting that the slip boundary conditions deform the bottom part of the streaks. This creates a buffer zone already mentioned for rough surfaces.

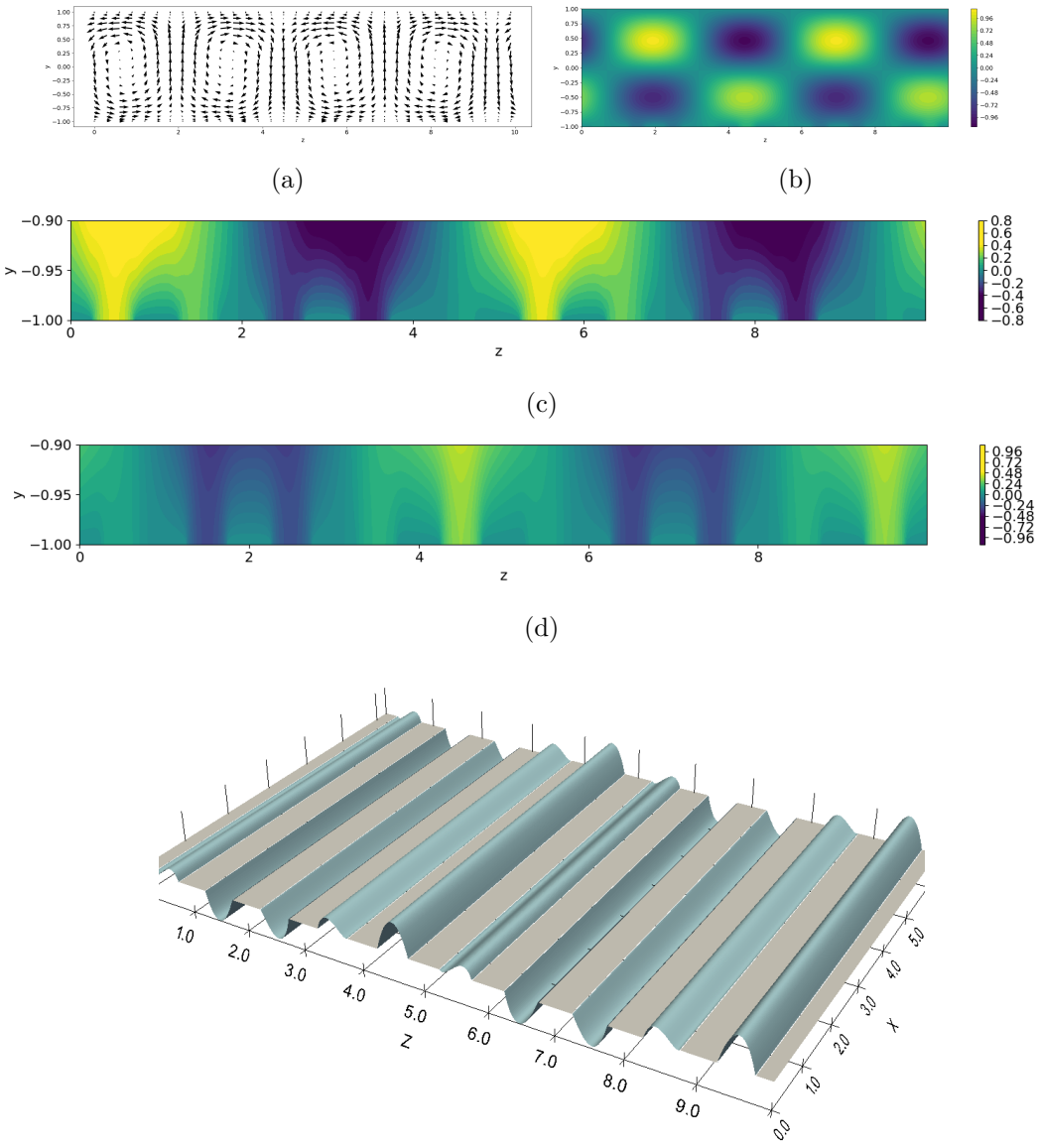

Figure 5.23: Optimal streaks for $Re = 5000$, $We = 12$, $\alpha = 0$ and $s = 0.3$. (a) (b) Perturbation at the optimal time. (c) Zoom-in on the near-wall region of the optimal perturbation at the initial time (d) Zoom-in on the near-wall region of the optimal perturbation at the optimal time. (e) Three-dimensional view of the (magnified) interface deformation.

The lack of influence of the superhydrophobic wall on the streaks is not totally unexpected, and it has been previously observed by Picella (2019). The lift-up mechanism involves an energy transfer from the cross-flow components at the initial time towards the streamwise velocity component at the optimal time. However, for counter-rotating vortices, in the near-wall region, the spanwise velocity component is dominant and, in our case, further reinforced by the slip boundary conditions at the interface. The wall-normal velocity component, dictating the interface deformation, remains small ultimately yielding small interface deformations.

Chapter 6

Conclusion and Perspectives

Contents

6.1 Overall conclusions

The aim of this thesis has been to shed some light on some of the phenomena involved during laminar-turbulent transition of spatially periodic systems. To do so, an alternative method to the usual Floquet stability has been proposed. It is based on a Bloch waves formalism, initially developed in the work of Schmid *et al.* (2017) and coupled with a local two-dimensional stability problem. Specifically, the stability problem is divided into n coupled sub-units. Through a similarity transform involving roots-of-unity, the problem is reduced to the study of the n smaller problems associated with the sub-units. Mathematically, the framework is equivalent to a Floquet analysis, which can be recovered through a quantisation of the Floquet's detuning factor. Modal stability analysis of a system with a large number of sub-units can be efficiently tackled and entire spatial branches can be retrieved. The framework also allows the computation at a reasonable cost of transient growth and resolvent analyses.

As a first test, the framework has been used to investigate secondary instability of cross-flow vortices in an idealised swept boundary layer. Such a simple case allows a direct comparison with the Floquet analysis of Fischer & Dallmann (1991). For a zero streamwise wavenumber, a previously missed instability coupling a large number of sub-units haa been observed. The frequency and modal shape

have been found coherent with a POD mode extracted from the experiments of Serpieri & Kotsonis (2016). By varying the amplitude of the cross-flow vortices exceptional points (Kato, 1995) in the spectra appeared, commonly associated with resonances (Gustavsson & Hultgren, 1980).
In an effort to further demonstrate the relevance of the method, the secondary stability of streaks in a boundary layer was also studied. For large amplitude of the streaks, a detuned forcing, yielding a collective, large-scale oscillation of the top of the low-velocity streaks can be observed in the resolvent analysis. For smaller amplitudes, the streaks exhibited frustration, resulting from the competition between the lift-up effect and the Orr mechanism. Multiple optimal perturbations could be found, each one sharing the same gain and optimal time. Ultimately, a concept from solid-state physics known as the Wannier functions, has been introduced to yield a localised optimal perturbation. From there, we proposed the idea that localised disturbances can arise from a commensurate-incommensurate bifurcation of a periodic flow, which grow due to transient growth (as the discovery of optimal localised disturbances through the Wannier functions may indicate) and cause the formation of spots.

Once the interest of the method has been established, an application to complex surfaces such as rough and superhydrophobic surfaces has been proposed. This choice is motivated by the role of complex surfaces in pattern formation and by the study of their interesting drag-reducing properties. The first approach is based on a homogenisation technique (Luchini, 2013; Bottaro & Naqvi, 2020) yielding effective boundary conditions. The validity of this type of model has been discussed in Picella (2019); Picella *et al.* (2020) for isotropic roughness and the idea of this whole chapter is to extend the analysis to anisotropic surfaces. One of the simplest way to design such a surface may be by orienting with an angle θ an initially longitudinal roughness. Notably, this leads to the apparition of a spanwise velocity component, negligible in the bulk of the flow, but definitely not in the rough wall region where it aligns the flow with the riblets. Following Pralits *et al.* (2017), local stability analysis in such a configuration has been performed and exhibits two families of unstable mode: three-dimensional TS waves and cross-flow related vortices which were previously missed. Supercritical transition scenarii corresponding to these two families of mode have been investigated through direct numerical simulation of the flow with the spectral element solver Nek5000. Homogenized effective boundary conditions had to be implemented. In both cases, cross-flow related effects appeared to play a rather fundamental role. In the scenario initiated by the cross-flow related perturbation, spanwise-independent coherent structures strongly looking like Kelvin-Helmholtz rollers (García-Mayoral &

Jiménez, 2011*b*) appeared during the late stages of the transition process and led to the turbulent breakdown. The two laminar-turbulent transition scenarios also appear to involve mostly linear, modal mechanisms. These mechanisms could be studied with the different frameworks developed for secondary instabilities, which also showcased their application to a realistic flow configuration.

Ultimately, it has been found that homogenised boundary conditions are not suitable for the study of the laminar-turbulent transition. Thus, the stability of the flow over a rough surface, taking into account its geometry, has been studied. In particular, the flow stability over longitudinal trapezoidal riblets has been considered. Since the modal stability analysis had already been investigated (Moradi & Floryan, 2014), the emphasis has been placed on the non-normal aspects. The roughness has been tackled through a coordinate transform as in the works of Ehrenstein (1996) and Floryan (1997*b*). A parametric resonance phenomenon between the streaks and the riblets' wavelengths could be observed. For very large periodicities, frustration can also be observed, leading to the modulation of the amplitude of the streaks, similar to what has been found in the case of rough Rayleigh-Bénard flows (Schmitz & Zimmermann, 1996). The last case investigated has been the flow over a superhydrophobic wall with moving boundaries. The discontinuities induced by the mixed no-slip/slip moving boundary conditions were smoothed, allowing a relatively easy numerical resolution of the stability problem at the expense of some accuracy. Two types of modes can be identified: one linked to a deformed TS wave and the other to a capillary wave. The influence of the superhydrophobic wall on the streaks also appeared limited.

6.2 Perspectives

As the reader will have likely noticed, most of the analyses provided in this work are usually limited to a few given configurations in the parameter space. This stems from both time constraints and the willingness to showcase the interest of the framework in two broadly different settings. Thus, in order to get a more global view, a good first step would be to explore more in depth the parameter space in all cases in order to clearly map where the spatial frequency lock-in or frustration arise.

The concept of frustration seems rather interesting in the study of secondary instabilities and warrants further research. The analysis could be reproduced with to yield a more localised optimal disturbance. Once it is localised enough, the disturbance may be used as an initial condition for a

DNS. Characteristics of the subsequent transition could be compared with the ones obtained with a fully non-linear optimal perturbation.

For the rough surfaces, possible developments stem from the variety of roughness shape that can be tackled. Notably, this work has highlighted the need to study more in depth anisotropic pattern as oriented simple patterns since they may involve different, cross-flow related mechanisms that could affect drag reduction. The implications of the "pattern interaction effect" found in Floryan & Inasawa (2021) would also be definitely interesting to investigate in the context of rough surfaces. This can be done by taking, for example, a roughness consisting in the superposition of two primary shapes (riblets, wave, scallops...) with slightly different amplitude and/or spatial wavelength. The modelling part of the superhydrophobic configuration could be further refined. A rather easy addition would consider the curvature of the interface in the base flow. Besides for very large superhydrophobic patches, this is not expected to yield significant differences in the described mechanisms (Tomlinson & Papageorgiou, 2022). On the contrary, the triple point and the discontinuity it generates require some extra attention. Indeed, the boundary conditions entirely dictate the interface deformation. In this work, it has been assumed fixed (in agreement with the literature). However, more complex boundary conditions involving a dynamical contact angle (Bracke *et al.*, 1989; Shikhmurzaev, 1996; Legendre & Maglio, 2015) may be imposed instead. The influence of the triple point on the flow stability could also be reduced by considering only partially filled grooves. The resulting surface would be constituted of an alternation of rough patches with a given shape and gas patches. Such a configuration would be more advantageous for the interface stability but would come at the expense of a smaller drag reduction.

In both cases, the method could be easily adapted to turbulent flows through a mean flow analysis (as presented in the work of Chavarin & Luhar (2020)) but would require the computation of a mean flow and a turbulent viscosity through a DNS.

Appendix A

Spectral collocation methods

Spectral methods emerged in the 1970's as an alternative to the finite element or differences techniques. They quickly became popular as they offer better accuracy for a smaller numerical cost than their counterparts. These methods are rapidly summarised in the following. For a full discussion, the reader is referred to Trefethen (2000).

A.1 Spectral collocation methods

All the stability problems encountered in this thesis have two directions of interest which need to be discretised: a bounded or semi-infinite wall-normal direction y and a spanwise periodic direction. For the latter, a *Fourier grid* $z_j = j/N_z, \quad j = 1, ..., N_z - 1$ appears an adequate choice as it directly enforces the periodic boundary conditions. Together with this grid, a derivative operator $\mathbf{D}^{(z)}$ can be defined as:

$$D_{ij}^{(z)} = \begin{cases} 0, & \text{if} \quad i = j \\ \frac{1}{2}(-1)^{i+j} \text{cotan}\left(\frac{z_i - z_j}{2}\right), & \text{if} \quad i \neq j, \quad i, j = 1, ..., N_z - 1 \end{cases} \tag{A.1}$$

If the same discretisation is applied in a bounded domain, discontinuities at the boundaries induce oscillations - a manifestation of the *Gibbs' phenomenon* - ultimately destroying the spectral accuracy of the solution. Thus, trigonometric polynomials are replaced with algebraic ones which, on a grid with equispaced points, is also a terrible idea as it leads to even greater oscillations. This problem is commonly known as *Runge's phenomenon* and can be overcome by clustering points near the boundaries. Such a distribution of points is commonly known as a *Chebyshev grid* and has the following form:

$$y_j = \cos(j\pi/N), \qquad j = 0, ..., N_y \tag{A.2}$$

The derivative operator associated with this grid is a matrix $\mathbf{D}^{(y)}$ of size $N_y \times N_y$ whose coefficients are given by:

$$D_{ij}^{(y)} = \begin{cases} -\frac{y_j}{2(1-y_j^2)}, & \text{if} \quad i = j \\ \frac{c_i}{c_j}\frac{(-1)^{i+j}}{y_i - y_j}, & \text{if} \quad i \neq j, \quad i,j = 1, ..., N_z - 1 \\ \frac{2N_y^2+1}{6}, & \text{if} \quad i = j = 0 \\ -\frac{2N_y^2+1}{6} & \text{if} \quad i = j = N_y \end{cases} \tag{A.3}$$

Note that in the case of a semi-infinite domain, grid points are concentrated in the near wall region through the following coordinate transformation:

$$y_j' = a\frac{1 - y_j}{b + y_j}, \tag{A.4}$$

Eventually, a Chebyshev grid could also be used to discretise the spanwise direction. However, extra care must be taken to enforce periodicity at the boundaries. Introducing $\mathbf{I}_y$ and $\mathbf{I}_z$ the identity matrices of size $N_y \times N_y$ and $N_u N_z \times N_u N_z$, derivative operators $\partial_{\mathbf{y}}$ and $\partial_{\mathbf{z}}$ can now be defined as:

$$\partial_{\mathbf{y}} = \mathbf{D}^{(y)} \otimes \mathbf{I}_z, \qquad \partial_{\mathbf{z}} = \mathbf{I}_y \otimes \mathbf{D}^{(z)} \tag{A.5}$$

where $\otimes$ is the Kronecker tensor product. Second order derivatives can be obtained in a similar fashion. In most configurations encountered throughout this work, a 64×64 grid proved to be sufficient to capture accurately the instability mechanisms. In the case of the flow over a superhydrophobic wall, the number of points in the spanwise direction had to be increased up to 100, due to the discontinuities.

A.2 Bloch waves formalism

Depending on the coupling considered, a system constituted of the repetition of N_u sub-units is discretised. If nearest-neighbour coupling is assumed, the system reduces to three interacting sub-units and $N_u = 3$. The 2D stability problem is further reduced to a one-dimensional problem through

tensor manipulations Trefethen (2000). Both the derivative operators and the stability problem have to be split into N_u^2 sub-matrices. For the derivative operators, we obtain:

$$\partial_z = \begin{pmatrix} \partial_z^0 & \partial_z^1 & \partial_z^{-1} \\ \partial_z^{-1} & \partial_z^0 & \partial_z^1 \\ \partial_z^1 & \partial_z^{-1} & \partial_z^0 \end{pmatrix}, \qquad \partial_y = \begin{pmatrix} \partial_y & 0 & 0 \\ 0 & \partial_y & 0 \\ 0 & 0 & \partial_y \end{pmatrix}, \tag{A.6}$$

Only the spanwise derivative operator inherit of the block-circulant nature as the spanwise direction is the only one periodic. Next, the stability problem is also decomposed in a similar fashion yielding the following matrices:

$$\mathbf{A}_0 = \begin{pmatrix} \mathbf{L}_0 & -\partial_y U_0 & -\partial_z U_0 & -i\alpha \\ 0 & \mathbf{L}_0 - \partial_y V_0 & -\partial_z V_0 & -\partial_y \\ 0 & -\partial_y W_0 & \mathbf{L}_0 - \partial_z W_0 & -\partial_z^0 \\ i\alpha & \partial_y & \partial_z^0 & 0 \end{pmatrix}, \quad \mathbf{A}_1 = \begin{pmatrix} \mathbf{L}_1 & 0 & 0 & 0 \\ 0 & \mathbf{L}_1 & 0 & 0 \\ 0 & 0 & \mathbf{L}_1 & -\partial_z^1 \\ 0 & 0 & \partial_z^1 & 0 \end{pmatrix}, \quad \mathbf{A}_{-1} = \begin{pmatrix} \mathbf{L}_{-1} & 0 & 0 & 0 \\ 0 & \mathbf{L}_{-1} & 0 & 0 \\ 0 & 0 & \mathbf{L}_{-1} & -\partial_z^{-1} \\ 0 & 0 & \partial_z^{-1} & 0 \end{pmatrix} \tag{A.7}$$

where

$$\begin{cases} \mathbf{L}_0 = \frac{1}{Re}\left(\partial_{yy} + \partial_{zz}^0 - \alpha^2\right) - i\alpha U_0 - V_0\partial_y - W_0\partial_z^0 \\ \mathbf{L}_1 = \frac{1}{Re}\partial_{zz}^1 - W_0\partial_z^1 \\ \mathbf{L}_{-1} = \frac{1}{Re}\partial_{zz}^{-1} - W_0\partial_z^{-1} \end{cases} \tag{A.8}$$

As previously stated, $\mathbf{A}_0$ describes the dynamics of one sub-unit while $\mathbf{A}_0$ and $\mathbf{A}_{-1}$ are coupling matrices describing interactions between the sub-units. Note that the strength of the coupling strongly depends on the magnitude of the spanwise velocity of the base flow W_0. If the flow is assumed parallel ($W_0 = 0$), the coupling only involves spanwise derivative operators and is independent of the base flow considered. In this case, it can be found that $\mathbf{A}_1 = \mathbf{A}_{-1}^H$ and the coupling is symmetric. Physically, this means the central sub-unit makes no difference between interactions with its left sub-unit and interactions with its right sub-unit. Numerically, this symmetry greatly reduces the computational cost as only half of the roots-of-unity need to be investigated.

Appendix B

Nek5000

B.1 Quick overview

The simulations presented in this work have been performed with the incompressible solver Nek5000 (Fischer *et al.*, 2008) which will be quickly presented in the following. For a good introduction, the reader is referred to the thesis of Loiseau (2014) while the full developments can be found in the books of Deville *et al.* (2002) and Canuto (1988).

In order to be solved numerically, Navier-Stokes equation are spatially discretised using spectral elements (Patera, 1984). Such a discretisation implies the resolution of the equation in their weak form and the introduction of a set of trial functions, as for standard Galerkin methods. The differences arise in the choice of the trial functions: in Nek5000, Legendre polynomials (Lee-Wing & Patera, 1990) are used as they provide the best approximation for the Sobolev norm (Deville *et al.*, 2002). Besides, to avoid spurious oscillations of the pressure, a $P_N - P_{N-2}$ formulation is adopted: velocity is discretised on a $N+1$ Gauss-Lobatto-Legendre quadrature while pressure on a $N-1$ Gauss-Legendre quadrature.

Regarding time discretisation, linear terms are solved implicitly while non-linear terms are treated explicitly, resulting in a semi-implicit scheme. Viscous terms are discretised through an implicit backward differentiation of order k while non-linear terms are tackled explicitly through extrapolation of order k ($k = 1, 2, 3$ in general). A predictor-corrector, Blair-Perot formulation is implemented to avoid the direct inversion of the projection matrix and reduce computational time.

B.2 Implementing Robin boundary conditions

The direct numerical simulations of chapter §4 require the implementation of homogenised boundary conditions mimicking the effects of the oriented superhydrophobic wall. As a reminder, these Robin-like boundary conditions take the following form:

$$\begin{bmatrix} U \\ W \end{bmatrix} = \mp \mathbf{L} \partial_y \begin{bmatrix} U \\ W \end{bmatrix}, \quad V = 0, \quad \text{at} \quad y = \pm 1 \tag{B.1}$$

where the mobility tensor $\mathbf{L}$ depends on $\lambda_{\parallel}$, $\lambda_{\perp}$ and on the rotation matrix $\mathbf{R}(\theta)$, allowing the rotation of the roughness of an angle θ (Pralits *et al.*, 2017):

$$\mathbf{L} = \mathbf{R} \begin{pmatrix} \lambda_{||} & 0 \\ 0 & \lambda_{\perp} \end{pmatrix} \mathbf{R}^T = \frac{\lambda_{\parallel}}{2} \begin{pmatrix} 1 + \cos^2\theta & \cos\theta \sin\theta \\ \cos\theta \sin\theta & 1 + \sin^2\theta. \end{pmatrix} \tag{B.2}$$

Robin boundary conditions are not originally implemented in NEK5000, and in the following we detail the procedure to include such condition. The idea is to take advantage of the SYM boundary condition, which already enforces a zero wall-normal velocity and no stress on the boundary conditions. After formulating the boundary conditions into their equivalent weak form, two extra terms, respectively corresponding to the slip contribution and an extra source term, should be added in the BCNEUSC function. For further inforamtion, the reader is referred to the thesis of Picella (2019).

Bibliography

2004 On Tollmien–Schlichting-like waves in streaky boundary layers. *European Journal of Mechanics - B/Fluids* **23** (6), 815–833.

2006 Experiments on the linear instability of flow in a wavy channel. *European Journal of Mechanics - B/Fluids* **25** (6), 971–986.

Abderrahaman-Elena, N., Fairhall, C. T. & García-Mayoral, R. 2019 Modulation of near-wall turbulence in the transitionally rough regime. *Journal of Fluid Mechanics* **865**, 1042–1071.

Aghdam, S. K. & Ricco, P. 2016 Laminar and turbulent flows over hydrophobic surfaces with shear-dependent slip length. *Physics of Fluids* **28** (3), 035109.

Andersson, P., Berggren, M. & Henningson, D. S. 1999 Optimal disturbances and bypass transition in boundary layers. *Physics of Fluids* **11** (1), 134–150.

Andersson, P., Brandt, L., Bottaro, A. & Henningson, D. S. 2001 On the breakdown of boundary layer streaks. *Journal of Fluid Mechanics* **428**, 29–60.

Asai, M., Minagawa, M. & Nishioka, M. 2002 The instability and breakdown of a near-wall low-speed streak. *Journal of Fluid Mechanics* **455**, 289–314.

Asai, M. & Nishioka, M. 1989 Origin of the peak-valley wave structure leading to wall turbulence. *Journal of Fluid Mechanics* **208**, 1–23.

Asmolov, E. S. & Vinogradova, O. I. 2012 Effective slip boundary conditions for arbitrary one-dimensional surfaces. *Journal of Fluid Mechanics* **706**, 108–117.

Bagheri, S. & Hanifi, A. 2007 The stabilizing effect of streaks on Tollmien-Schlichting and oblique waves: A parametric study. *Physics of Fluids* **19** (7), 078103.

Bagheri, S., Henningson, D. S., Hœpffner, J. & Schmid, P. J. 2009 Input-Output Analysis and Control Design Applied to a Linear Model of Spatially Developing Flows. *Applied Mechanics Reviews* **62** (2).

Balamurugan, G. & Mandal, A. C. 2017 Experiments on localized secondary instability in bypass boundary layer transition. *Journal of Fluid Mechanics* **817**, 217–263.

Barkley, D. 2016 Theoretical perspective on the route to turbulence in a pipe. *Journal of Fluid Mechanics* **803**, P1.

Barkley, D., Blackburn, H. M. & Sherwin, S. J. 2008 Direct optimal growth analysis for timesteppers. *International Journal for Numerical Methods in Fluids* **57** (9), 1435–1458.

Barkley, D. & Henderson, R. D. 1996 Three-dimensional Floquet stability analysis of the wake of a circular cylinder. *Journal of Fluid Mechanics* **322**, 215–241.

Beaumont, D. N. 1981 The stability of spatially periodic flows. *Journal of Fluid Mechanics* **108**, 461–474.

Bechert, D. W., Bruse, M., Hage, W., Van Der Hoeven, J. G. T. & Hoppe, G. 1997 Experiments on drag-reducing surfaces and their optimization with an adjustable geometry. *Journal of Fluid Mechanics* **338**, 59–87.

Belyaev, A. V. & Vinogradova, O. I. 2010 Effective slip in pressure-driven flow past super-hydrophobic stripes. *Journal of Fluid Mechanics* **652**, 489–499.

Beneddine, S., Sipp, D., Arnault, A., Dandois, J. & Lesshafft, L. 2016 Conditions for validity of mean flow stability analysis. *Journal of Fluid Mechanics* **798**, 485–504.

Bippes, H. 1990 Instability Features Appearing on Swept Wing Configurations. In *Laminar-Turbulent Transition* (ed. D. Arnal & R. Michel), pp. 419–430. Berlin, Heidelberg: Springer.

Bippes, H. 1999 Basic experiments on transition in three-dimensional boundary layers dominated by crossflow instability. *Progress in Aerospace Sciences* **35** (4), 363–412.

Blackburn, H. M., Barkley, D. & Sherwin, S. J. 2008 Convective instability and transient growth in flow over a backward-facing step. *Journal of Fluid Mechanics* **603**, 271–304.

Bonfigli, G. & Kloker, M. 2007 Secondary instability of crossflow vortices: validation of the stability theory by direct numerical simulation. *Journal of Fluid Mechanics* **583**, 229–272.

Bottaro, A. 2019 Flow over natural or engineered surfaces: an adjoint homogenization perspective. *Journal of Fluid Mechanics* **877**, P1.

Bottaro, A. & Naqvi, S. B. 2020 Effective boundary conditions at a rough wall: a high-order homogenization approach. *Meccanica* **55** (9), 1781–1800.

Bracke, M., De Voeght, F. & Joos, P. 1989 The kinetics of wetting: the dynamic contact angle. In *Trends in Colloid and Interface Science III* (ed. P. Bothorel & E. J. Dufourc), *Progress in Colloid & Polymer Science* 3, pp. 142–149.

Brandt, L. 2014 The lift-up effect: The linear mechanism behind transition and turbulence in shear flows. *European Journal of Mechanics - B/Fluids* **47**, 80–96.

Brandt, L., Schlatter, P. & Henningson, D. S. 2004 Transition in boundary layers subject to free-stream turbulence. *Journal of Fluid Mechanics* **517**, 167–198.

Breuer, K. S. & Kuraishi, T. 1994 Transient growth in two- and three-dimensional boundary layers. *Physics of Fluids* **6** (6), 1983–1993.

Brevdo, L. & Bridges, T. J. 1997 Local and global instabilities of spatially developing flows: cautionary examples. *Proceedings of the Royal Society of London. Series A: Mathematical, Physical and Engineering Sciences* **453** (1962), 1345–1364.

Brevdo, L., Bridges, T. J. & Smith, F. T. 1996 Absolute and convective instabilities of spatially periodic flows. *Philosophical Transactions of the Royal Society of London. Series A: Mathematical, Physical and Engineering Sciences* **354** (1710), 1027–1064.

Brillouin, L. 1953 *Wave Propagation in Periodic Structures: Electric Filters and Crystal Lattices*. Dover Publications.

Butler, K. M. & Farrell, B.F. 1992*a* Three-dimensional optimal perturbations in viscous shear flow. *Physics of Fluids A: Fluid Dynamics* **4** (8), 1637–1650.

Butler, K. M. & Farrell, B. F. 1992*b* Three-dimensional optimal perturbations in viscous shear flow. *Physics of Fluids A: Fluid Dynamics* **4** (8), 1637–1650.

Byun, D., Kim, J., Ko, H. S. & Park, H. C. 2008 Direct measurement of slip flows in superhydrophobic microchannels with transverse grooves. *Physics of Fluids* **20** (11), 113601.

Cantwell, C. D., Barkley, D. & Blackburn, H. M. 2010 Transient growth analysis of flow through a sudden expansion in a circular pipe. *Physics of Fluids* **22** (3), 034101, arXiv: https://doi.org/10.1063/1.3313931.

Canuto, C. 1988 *Spectral Methods*. Springer.

Cassie, A. B. D. & Baxter, S. 1944 Wettability of porous surfaces. *Transactions of the Faraday Society* **40** (0), 546–551.

Chalker, J. T., Holdsworth, P. C. W. & Shender, E. F. 1992 Hidden order in a frustrated system: Properties of the heisenberg kagomé antiferromagnet. *Phys. Rev. Lett.* **68**, 855–858.

Chandrasekhar, S. 1955 The character of the equilibrium of an incompressible heavy viscous fluid of variable density. *Mathematical Proceedings of the Cambridge Philosophical Society* **51** (1), 162–178.

Chapman, S. J. 2002 Subcritical transition in channel flows. *Journal of Fluid Mechanics* **451**, 35–97.

Chavarin, Andrew & Luhar, Mitul 2020 Resolvent Analysis for Turbulent Channel Flow with Riblets. *AIAA Journal* **58** (2), 589–599.

Cherubini, S., De Palma, P., Robinet, J.-Ch. & Bottaro, A. 2010 Rapid path to transition via nonlinear localized optimal perturbations in a boundary-layer flow. *Phys. Rev. E* **82**, 066302.

Choi, Chang-Hwan, Westin, K. Johan A. & Breuer, Kenneth S. 2003 Apparent slip flows in hydrophilic and hydrophobic microchannels. *Physics of Fluids* **15** (10), 2897–2902, publisher: American Institute of Physics.

Choi, H., Moin, P. & Kim, J. 1993 Direct numerical simulation of turbulent flow over riblets. *Journal of Fluid Mechanics* **255**, 503–539.

Chu, D. C. & Karniadakis, G. E. 1993 A direct numerical simulation of laminar and turbulent flow over riblet-mounted surfaces. *Journal of Fluid Mechanics* **250**, 1–42.

Colebrook, C. F. & White, C. M. 1937 Experiments with Fluid Friction in Roughened Pipes. *Proceedings of the Royal Society of London Series A* **161** (906), 367–381.

Coles, D. 1965 Transition in circular couette flow. *Journal of Fluid Mechanics* **21** (3), 385–425.

Cooke, JC 1950 The boundary layer of a class of infinite yawed cylinders. In *Mathematical proceedings of the Cambridge philosophical society*, , vol. 46, pp. 645–648. Cambridge University Press.

Corbett, P. & Bottaro, A. 2001 Optimal linear growth in swept boundary layers. *Journal of Fluid Mechanics* **435**, 1–23.

Cossu, C., Chevalier, M. & Henningson, D. S. 2007 Optimal secondary energy growth in a plane channel flow. *Physics of Fluids* **19** (5), 058107, arXiv: https://doi.org/10.1063/1.2736678.

Coullet, P. 1986 Commensurate-incommensurate transition in nonequilibrium systems. *Phys. Rev. Lett.* **56**, 724–727.

Coullet, P., Fauve, S. & Tirapegui, E. 1985 Large scale instability of nonlinear standing waves. *Journal de Physique Lettres* **46** (17), 787–791.

Coullet, P. & Huerre, P. 1986 Resonance and phase solitons in spatially-forced thermal convection. *Physica D: Nonlinear Phenomena* **23** (1), 27–44.

Cross, M. C. & Hohenberg, P. C. 1993 Pattern formation outside of equilibrium. *Rev. Mod. Phys.* **65**, 851–1112.

Cumming, A. & Linsay, P. S. 1988 Quasiperiodicity and Chaos in a System with Three Competing Frequencies. *Physical Review Letters* **60** (26), 2719–2722.

Daniello, R. J., Waterhouse, N. E. & Rothstein, J. P. 2009 Drag reduction in turbulent flows over superhydrophobic surfaces. *Physics of Fluids* **21** (8), 085103.

Davis, S. H. 1976 The stability of time-periodic flows. *Annual Review of Fluid Mechanics* **8** (1), 57–74.

Deville, M. O., Fischer, P. F. & Mund, E. H. 2002 *High-Order Methods for Incompressible Fluid Flow*. Cambridge.

Drazin, P. G. & Reid, W. H. 2004 *Hydrodynamic Stability*, 2nd edn. Cambridge: Cambridge University Press.

Ehrenstein, U. 1996 On the linear stability of channel flow over riblets. *Physics of Fluids* **8** (11), 3194–3196.

Ellingsen, T. & Palm, E. 1975 Stability of linear flow. *The Physics of Fluids* **18** (4), 487–488.

El-Hady, N. M. 1989 Evolution of resonant wave triads in three-dimensional boundary layers. *Physics of Fluids A: Fluid Dynamics* **1** (3), 549–563.

Emmons, H. W. 1951 The laminar-turbulent transition in a boundary layer-part i. *Journal of the Aeronautical Sciences* **18** (7), 490–498.

Endrikat, S., Modesti, D., García-Mayoral, R., Hutchins, N. & Chung, D. 2021 Influence of riblet shapes on the occurrence of Kelvin–Helmholtz rollers. *Journal of Fluid Mechanics* **913**.

Ewins, D. J. 1973 Vibration characteristics of bladed disc assemblies. *Journal of Mechanical Engineering Science* **15** (3), 165–186.

Falkner, V. M. & Skan, S. W. 1931 Lxxxv. solutions of the boundary-layer equations. *The London, Edinburgh, and Dublin Philosophical Magazine and Journal of Science* **12**, 865–6.

Farrell, B. F. 1988 Optimal excitation of perturbations in viscous shear flow. *The Physics of Fluids* **31** (8), 2093–2102.

Fischer, P. F., Lottes, J. W. & Kerkemeier, S. G. 2008 nek5000 Web page. Http://nek5000.mcs.anl.gov.

Fischer, T. M. & Dallmann, U. 1991 Primary and secondary stability analysis of a three-dimensional boundary-layer flow. *Physics of Fluids A: Fluid Dynamics* **3** (10), 2378–2391.

Floquet, G. 1883 Sur les équations différentielles linéaires à coefficients périodiques. *Annales scientifiques de l'École Normale Supérieure* **12**, 47–88.

Floryan, J. M. 1997*a* Stability of wall-bounded shear layers in the presence of simulated distributed surface roughness. *Journal of Fluid Mechanics* **335**, 29–55.

Floryan, J. M. 1997*b* Stability of wall-bounded shear layers in the presence of simulated distributed surface roughness. *Journal of Fluid Mechanics* **335**, 29–55.

Floryan, J. M. 2007 Three-dimensional instabilities of laminar flow in a rough channel and the concept of hydraulically smooth wall. *European Journal of Mechanics - B/Fluids* **26** (3), 305–329.

Floryan, J. M. & Asai, M. 2011 On the transition between distributed and isolated surface roughness and its effect on the stability of channel flow. *Physics of Fluids* **23** (10), 104101.

Floryan, J. M. & Inasawa, A. 2021 Pattern interaction effect. *Scientific Reports* **11** (1), 14573.

Fransson, J., Brandt, L., Talamelli, A. & Cossu, C. 2004 Experimental and theoretical investigation of the nonmodal growth of steady streaks in a flat plate boundary layer. *Physics of Fluids* **16**, 3627–3638.

Fransson, J. H. M., Brandt, L., Talamelli, A. & Cossu, C. 2005 Experimental study of the stabilization of Tollmien–Schlichting waves by finite amplitude streaks. *Physics of Fluids* **17** (5), 054110.

Freund, G., Pesch, W. & Zimmermann, W. 2011 Rayleigh–Bénard convection in the presence of spatial temperature modulations. *Journal of Fluid Mechanics* **673**, 318–348.

Fu, M. K., Chen, T.-H., Arnold, C. B. & Hultmark, M. 2019 Experimental investigations of liquid-infused surface robustness under turbulent flow. *Experiments in Fluids* **60** (6), 100.

Gallaire, F. & Brun, P.-T. 2017 Fluid dynamic instabilities: theory and application to pattern forming in complex media. *Philosophical Transactions of the Royal Society A: Mathematical, Physical and Engineering Sciences* **375** (2093), 20160155.

Game, S. E., Hodes, M., Keaveny, E. E. & Papageorgiou, D. T. 2017 Physical mechanisms relevant to flow resistance in textured microchannels. *Physical Review Fluids* **2** (9), 094102.

Game, S. E., Hodes, M. & Papageorgiou, D. T. 2019 Effects of slowly varying meniscus curvature on internal flows in the Cassie state. *Journal of Fluid Mechanics* **872**, 272–307.

García-Mayoral, R. & Jiménez, J. 2011*a* Drag reduction by riblets. *Philosophical Transactions of the Royal Society A: Mathematical, Physical and Engineering Sciences* **369** (1940), 1412–1427.

García-Mayoral, R. & Jiménez, J. 2011*b* Hydrodynamic stability and breakdown of the viscous regime over riblets. *Journal of Fluid Mechanics* **678**, 317–347.

de Gennes, P. G. 1985 Wetting: statics and dynamics. *Rev. Mod. Phys.* **57**, 827–863.

Gogte, S., Vorobieff, P., Truesdell, R., Mammoli, A., van Swol, F., Shah, P. & Brinker, C. J. 2005 Effective slip on textured superhydrophobic surfaces. *Physics of Fluids* **17** (5), 051701.

Goldstein, D. B. & Tuan, T.-C. 1998 Secondary flow induced by riblets. *Journal of Fluid Mechanics* **363**, 115–151.

Goldstein, M. E. & Hultgren, L. S. 1989 Boundary-layer receptivity to long-wave free-stream disturbances. *Annual Review of Fluid Mechanics* **21** (1), 137–166.

Gose, J. W., Golovin, K., Boban, M., Mabry, J. M., Tuteja, A., Perlin, M. & Ceccio, S. L. 2018 Characterization of superhydrophobic surfaces for drag reduction in turbulent flow. *Journal of Fluid Mechanics* **845**, 560–580.

Gotoh, K., Yamada, M. & Mizushima, J. 1983 The theory of stability of spatially periodic parallel flows. *Journal of Fluid Mechanics* **127**, 45–58.

Groot, K., Serpieri, J., Pinna, F. & Kotsonis, M. 2018 Secondary crossflow instability through global analysis of measured base flows. *Journal of Fluid Mechanics* **846**, 605–653.

Grosch, C. E. & Salwen, H. 1978 The continuous spectrum of the orr-sommerfeld equation. part 1. the spectrum and the eigenfunctions. *Journal of Fluid Mechanics* **87** (1), 33–54.

Guegan, A., Huerre, P. & Schmid, P. J. 2007 Optimal disturbances in swept hiemenz flow. *Journal of Fluid Mechanics* **578**, 223–232.

Gustavsson, L. H. 1981 Resonant growth of three-dimensional disturbances in plane poiseuille flow. *Journal of Fluid Mechanics* **112**, 253–264.

Gustavsson, L. H. 1986 Excitation of direct resonances in plane poiseuille flow. *Studies in Applied Mathematics* **75** (3), 227–248.

Gustavsson, L. H. 1991 Energy growth of three-dimensional disturbances in plane Poiseuille flow. *Journal of Fluid Mechanics* **224**, 241–260.

Gustavsson, L. H. & Hultgren, L. S. 1980 A resonance mechanism in plane couette flow. *Journal of Fluid Mechanics* **98** (1), 149–159.

Hack, M. J. P. & Zaki, T. A. 2014 Streak instabilities in boundary layers beneath free-stream turbulence. *Journal of Fluid Mechanics* **741**, 280–315.

Hall, P. & Horseman, N. J. 1991 The linear inviscid secondary instability of longitudinal vortex structures in boundary layers. *Journal of Fluid Mechanics* **232**, 357–375.

Heiss, W. D. 2012 The physics of exceptional points. *Journal of Physics A: Mathematical and Theoretical* **45** (44), 444016.

Helmholtz, H. von 1868 XLIII. On discontinuous movements of fluids. *The London, Edinburgh, and Dublin Philosophical Magazine and Journal of Science* **36** (244), 337–346.

Henningson, D. 1996 Comment on "Transition in shear flows. Nonlinear normality versus non-normal linearity" [Phys. Fluids 7, 3060 (1995)]. *Physics of Fluids* **8** (8), 2257–2258.

Herbert, T. 1983 Secondary instability of plane channel flow to subharmonic three-dimensional disturbances. *The Physics of Fluids* **26** (4), 871–874.

Herbert, T. 1985 Secondary Instability of Plane Shear Flows — Theory and Application. In *Laminar-Turbulent Transition*, *International Union of Theoretical and Applied Mechanics* , pp. 9–20. Berlin, Heidelberg: Springer.

Herbert, T. 1988 Secondary instability of boundary layers. *Annual Review of Fluid Mechanics* **20**, 487–526.

Ho, H.Q. & Asai, M. 2018 Experimental study on the stability of laminar flow in a channel with streamwise and oblique riblets. *Physics of Fluids* **30** (2), 024106.

Hoepffner, J., Brandt, L. & Henningson, D. S. 2005 Transient growth on boundary layer streaks **537**, 91–100.

Hossain, M.Z. & Floryan, J.M. 2022 Wavenumber lock-in and spatial parametric resonance in convection. *Journal of Fluid Mechanics* **944**, A47.

Hossain, M. Z. & Floryan, J. M. 2013 Instabilities of natural convection in a periodically heated layer. *Journal of Fluid Mechanics* **733**, 33–67.

Hossain, M. Z. & Floryan, J. M. 2014 Natural convection in a fluid layer periodically heated from above. *Phys. Rev. E* **90**, 023015.

Hossain, M. Z. & Floryan, J. M. 2015 Natural convection in a horizontal fluid layer periodically heated from above and below. *Phys. Rev. E* **92**, 023015.

Ibrahim, J. I., Gómez-de Segura, G., Chung, D. & García-Mayoral, R. 2021 The smooth-wall-like behaviour of turbulence over drag-altering surfaces: a unifying virtual-origin framework. *Journal of Fluid Mechanics* **915**, A56.

Janke, E. & Balakumar, P. 2000 On the Secondary Instability of Three-Dimensional Boundary Layers. *Theoretical and Computational Fluid Dynamics* **14** (3), 167–194.

Jelly, T. O., Jung, S. Y. & Zaki, T. A. 2014 Turbulence and skin friction modification in channel flow with streamwise-aligned superhydrophobic surface texture. *Physics of Fluids* **26** (9), 095102.

Jiao, Y., Hwang, Y. & Chernyshenko, S. I. 2021 Orr mechanism in transition of parallel shear flow. *Phys. Rev. Fluids* **6**, 023902.

Jiménez, J. 2004 Turbulent flows over rough walls. *Annual Review of Fluid Mechanics* **36** (1), 173–196.

Jiménez, J. & Pinelli, A. 1999 The autonomous cycle of near-wall turbulence. *Journal of Fluid Mechanics* **389**, 335–359.

Jovanović, Mihailo R. 2021 From bypass transition to flow control and data-driven turbulence modeling: An input–output viewpoint. *Annual Review of Fluid Mechanics* **53** (1), 311–345.

Kachanov, Iu. S. & Tararykin, O. I. 1987 An experimental study of the stability of a relaxing boundary layer. *Akademiia Nauk SSSR Sibirskoe Otdelenie Izvestiia Seriia Tekhnicheskie Nauki* pp. 9–19.

Kamrin, K., Bazant, M. Z. & Stone, H. A. 2010 Effective slip boundary conditions for arbitrary periodic surfaces: the surface mobility tensor. *Journal of Fluid Mechanics* **658**, 409–437.

Kato, T. 1995 *Perturbation Theory for Linear Operators*. New York: Springer-Verlag.

Kawakami, M., Kohama, Y. & M., Okutsu 1999 Stability characteristics of stationary crossflow vortices in three-dimensional boundary layer .

Kelvin, L. (W.T.) 1871 XLVI. Hydrokinetic solutions and observations. *The London, Edinburgh, and Dublin Philosophical Magazine and Journal of Science* **42** (281), 362–377.

Kern, J.S., Beneitez, M., Hanifi, A. & Henningson, D.S. 2021 Transient linear stability of pulsating poiseuille flow using optimally time-dependent modes. *Journal of Fluid Mechanics* **927**, A6.

Kern, J.S., Hanifi, A. & Henningson, D.S. 2022 Subharmonic eigenvalue orbits in the spectrum of pulsating poiseuille flow. *Journal of Fluid Mechanics* **945**, A11.

Kerschen, E. 1989 *Boundary layer receptivity*.

Kim, K., Chang, M.-S., Korenblit, S., Islam, R., Edwards, E. E., Freericks, J. K., Lin, G.-D., Duan, L.-M. & Monroe, C. 2010 Quantum simulation of frustrated Ising spins with trapped ions. *Nature* **465** (7298), 590–593.

Kirk, T. L. 2017 Mathematical problems on fluid flow over structured surfaces. PhD thesis, Imperial College London.

Klebanoff, P. S., Tidstrom, K. D. & Sargent, L. M. 1962 The three-dimensional nature of boundary-layer instability. *Journal of Fluid Mechanics* **12** (1), 1–34.

Kleiser, Leonhard & Zang, T. A. 1991 Numerical Simulation of Transition in Wall-Bounded Shear Flows. *Annual Review of Fluid Mechanics* **23**, 495–537.

Koch, W. 2002 On the spatio-temporal stability of primary and secondary crossflow vortices in a three-dimensional boundary layer. *Journal of Fluid Mechanics* **456** (1), 85–111.

Koch, W., P., Bertolotti F., Stolte, A. & Hein, S. 2000 Nonlinear equilibrium solutions in a three-dimensional boundary layer and their secondary instability. *Journal of Fluid Mechanics* **406** (1), 131–174.

Kohn, W. 1959 Analytic properties of bloch waves and wannier functions. *Phys. Rev.* **115**, 809–821.

Konishi, Y. & Asai, M. 2004 Experimental investigation of the instability of spanwise-periodic low-speed streaks. *Fluid Dynamics Research* **34** (5), 299–315.

Kuchment, P. A. 1993 *Floquet Theory for Partial Differential Equations*. Springer Science & Business Media.

Landahl, M. T. 1975 Wave breakdown and turbulence. *SIAM Journal on Applied Mathematics* **28** (4), 735–756.

Landahl, M. T. 1980 A note on an algebraic instability of inviscid parallel shear flows. *Journal of Fluid Mechanics* **98** (2), 243–251.

Landau, L. D. & Lifshitz, E. M. 1959 *Fluid mechanics*.

Lee, Choongyeop & Kim, Chang-Jin 2011 Underwater Restoration and Retention of Gases on Superhydrophobic Surfaces for Drag Reduction. *Physical Review Letters* **106** (1), 014502.

Lee, S.-J. & Lee, S.-H. 2001 Flow field analysis of a turbulent boundary layer over a riblet surface. *Experiments in Fluids* **30** (2), 153–166.

Lee-Wing, H. & Patera, A. T. 1990 A Legendre spectral element method for simulation of unsteady incompressible viscous free-surface flows. *Computer Methods in Applied Mechanics and Engineering* **80** (1), 355–366.

Legendre, D. & Maglio, M. 2015 Comparison between numerical models for the simulation of moving contact lines. *Computers & Fluids* **113**, 2–13.

Lesshafft, L., Semeraro, O., Jaunet, V., Cavalieri, A. V. G. & Jordan, P. 2019 Resolvent-based modeling of coherent wave packets in a turbulent jet. *Phys. Rev. Fluids* **4**, 063901.

Li, B., Cao, Y.-P., Feng, X.-Q. & Gao, H. 2012 Mechanics of morphological instabilities and surface wrinkling in soft materials: a review. *Soft Matter* **8**, 5728–5745.

Lin, A. L., Bertram, M., Martinez, K., Swinney, H. L., Ardelea, A. & Carey, G. F. 2000 Resonant phase patterns in a reaction-diffusion system. *Phys. Rev. Lett.* **84**, 4240–4243.

Lin, A. L., Hagberg, A., Meron, E. & Swinney, H. L. 2004 Resonance tongues and patterns in periodically forced reaction-diffusion systems. *Phys. Rev. E* **69**, 066217.

Ling, Hangjian, Katz, Joseph, Fu, Matthew & Hultmark, Marcus 2017 Effect of Reynolds number and saturation level on gas diffusion in and out of a superhydrophobic surface. *Physical Review Fluids* **2** (12), 124005.

Lingwood, R. J. 1995 Absolute instability of the boundary layer on a rotating disk. *Journal of Fluid Mechanics* **299**, 17–33.

Liu, Y., Zaki, T. A. & Durbin, P. A. 2008 Floquet analysis of secondary instability of boundary layers distorted by Klebanoff streaks and Tollmien–Schlichting waves. *Physics of Fluids* **20** (12), 124102.

Loiseau, J-C 2014 Dynamics and global stability analysis of three-dimensional flows. PhD thesis, ENSAM.

Lowe, M. & Gollub, J. P. 1985 Pattern selection near the onset of convection: The Eckhaus instability. *Physical Review Letters* **55** (23), 2575–2578.

Luchini, P. 2000 Reynolds-number-independent instability of the boundary layer over a flat surface: optimal perturbations. *Journal of Fluid Mechanics* **404**, 289–309.

Luchini, P. 2013 Linearized no-slip boundary conditions at a rough surface. *Journal of Fluid Mechanics* **737**, 349–367.

Luchini, P., Manzo, F. & Pozzi, A. 1991 Resistance of a grooved surface to parallel flow and cross-flow. *Journal of Fluid Mechanics* **228**, 87–109.

Luchini, P. & Trombetta, G. 1995 Effects of riblets upon flow stability. *Applied Scientific Research* **54** (4), 313–321.

Lugiato, L. A. & Lefever, R. 1987 Spatial dissipative structures in passive optical systems. *Phys. Rev. Lett.* **58**, 2209–2211.

Lundbladh, A., Henningson, D. S. & Reddy, S. C. 1994 *Threshold Amplitudes for Transition in Channel Flows*, pp. 309–318.

Lundell, F. & Alfredsson, P.H. 2003 Experiments on control of streamwise streaks. *European Journal of Mechanics - B/Fluids* **22** (3), 279–290.

Lācis, U., Sudhakar, Y., Pasche, S. & Bagheri, S. 2020 Transfer of mass and momentum at rough and porous surfaces. *Journal of Fluid Mechanics* **884**, A21.

Mack, L. M. 1984 Boundary-Layer Linear Stability Theory p. 151.

Malik, M. R., Li, F. & Chang, C.-L. 1994 Crossflow disturbances in three-dimensional boundary layers: nonlinear development, wave interaction and secondary instability. *Journal of Fluid Mechanics* **268**, 1–36.

Malik, M. R., Li, F., Choudhari, M. & Chang, C.-L. 1999 Secondary instability of crossflow vortices and swept-wing boundary-layer transition. *Journal of Fluid Mechanics* **399**, 85–115.

Manneville, P. 2015 On the transition to turbulence of wall-bounded flows in general, and plane couette flow in particular. *European Journal of Mechanics - B/Fluids* **49**, 345–362.

Manor, R., Hagberg, A. & Meron, E. 2008 Wave-number locking in spatially forced pattern-forming systems. *Europhysics Letters* **83** (1), 10005.

Margaritis, A. T., Sayadi, T., Marxen, O. & Schmid, P. J. 2022 Sensitivity of Reacting Hypersonic Boundary Layers to n-periodic Surface Roughness. In *IUTAM Laminar-Turbulent Transition*, pp. 599–612.

Martell, M. B., Rothstein, J. P. & Perot, J. B. 2010 An analysis of superhydrophobic turbulent drag reduction mechanisms using direct numerical simulation. *Physics of Fluids* **22** (6), 065102.

Marzari, N., Mostofi, A. A., Yates, J. R., Souza, I. & Vanderbilt, D. 2012 Maximally localized wannier functions: Theory and applications. *Rev. Mod. Phys.* **84**, 1419–1475.

McKeon, B. J. & Sharma, A. S. 2010*a* A critical-layer framework for turbulent pipe flow. *Journal of Fluid Mechanics* **658**, 336–382.

McKeon, B. J. & Sharma, A. S. 2010*b* A critical-layer framework for turbulent pipe flow. *Journal of Fluid Mechanics* **658**, 336–382.

Messing, R. & Kloker, M. 2004 Dns study of discrete suction in a 3-d boundary layer. In *Recent Results in Laminar-Turbulent Transition*, pp. 177–188. Berlin, Heidelberg: Springer Berlin Heidelberg.

Michalke, A. 1964 On the inviscid instability of the hyperbolic tangent velocity profile. *Journal of Fluid Mechanics* **19** (4), 543–556.

Michalke, A. 1965 On spatially growing disturbances in an inviscid shear layer. *Journal of Fluid Mechanics* **23** (3), 521–544.

Min, T. & Kim, J. 2005 Effects of hydrophobic surface on stability and transition. *Physics of Fluids* **17** (10), 108106.

Mohammadi, A. & Floryan, J. M. 2013 Groove optimization for drag reduction. *Physics of Fluids* **25** (11), 113601.

Mohammadi, A., Moradi, H. V. & Floryan, J. M. 2015 New instability mode in a grooved channel. *Journal of Fluid Mechanics* **778**, 691–720.

Monokrousos, A., Bottaro, A., Brandt, L., Di Vita, A. & Henningson, D. S. 2011 Nonequilibrium thermodynamics and the optimal path to turbulence in shear flows. *Physical Review Letters* **106** (13), 134502.

Moradi, H. V. & Floryan, J. M. 2013 Maximization of heat transfer across micro-channels. *International Journal of Heat and Mass Transfer* **66**, 517–530.

Moradi, H. V. & Floryan, J. M. 2014 Stability of flow in a channel with longitudinal grooves. *Journal of Fluid Mechanics* **757**, 613–648.

Morkovin, M. V. 1969 On the many faces of transition. In *Viscous Drag Reduction* (ed. C. Sinclair Wells), pp. 1–31. Boston, MA: Springer US.

Mostofi, A. A., Yates, J. R., Lee, Y.-S., Souza, I., Vanderbilt, D. & Marzari, N. 2008 Wannier90: A Tool for Obtaining Maximally-Localised Wannier Functions. *Computer Physics Communications* **178** (9), 685–699.

Müller, B. 1990 Experimental study of the travelling waves in a three-dimensional boundary layer. In *Laminar-Turbulent Transition* (ed. D. Arnal & R. Michel), pp. 489–498. Berlin, Heidelberg: Springer Berlin Heidelberg.

Murthy, S. R., Sayadi, T., Le Chenadec, V., Schmid, P. J. & Bodony, D. J. 2019 Analysis of degenerate mechanisms triggering finite-amplitude thermo-acoustic oscillations in annular combustors. *Journal of Fluid Mechanics* **881**, 384–419.

Navier, C.L. 1822 *Mémoire sur les lois du mouvement des fluides*.

Nikuradse, J. 1933 Stromungsgesetze in rauhen rohren. *VDI-Forschungsheft* **361**, 1.

Nixon, M., Ronen, E., Friesem, A. A. & Davidson, N. 2013 Observing Geometric Frustration with Thousands of Coupled Lasers. *Physical Review Letters* **110** (18).

Olson, B. J., Shaw, S. W., Shi, C., Pierre, C. & Parker, R. G. 2014 Circulant Matrices and Their Application to Vibration Analysis. *Applied Mechanics Reviews* **66** (4).

Orr, W. F. 1907*a* The stability or instability of the steady motions of a perfect liquid and of a viscous liquid. part ii: A viscous liquid. *Proceedings of the Royal Irish Academy. Section A: Mathematical and Physical Sciences* **27**, 69–138.

Orr, William M'F. 1907*b* The Stability or Instability of the Steady Motions of a Perfect Liquid and of a Viscous Liquid. Part II: A Viscous Liquid. *Proceedings of the Royal Irish Academy. Section A: Mathematical and Physical Sciences* **27**, 69–138, publisher: Royal Irish Academy.

Orszag, S. A. 1971*a* Accurate solution of the Orr–Sommerfeld stability equation. *Journal of Fluid Mechanics* **50** (4), 689–703.

Orszag, S. A. 1971*b* Accurate solution of the orr–sommerfeld stability equation. *Journal of Fluid Mechanics* **50** (4), 689–703.

Orszag, S. A. & Patera, A. T. 1983 Secondary instability of wall-bounded shear flows. *Journal of Fluid Mechanics* **128**, 347–385.

Ou, J., Perot, B. & Rothstein, J. P. 2004 Laminar drag reduction in microchannels using ultrahydrophobic surfaces. *Physics of Fluids* **16** (12), 4635–4643.

Ou, Jia & Rothstein, Jonathan P. 2005 Direct velocity measurements of the flow past drag-reducing ultrahydrophobic surfaces. *Physics of Fluids* **17** (10), 103606.

Paladini, E., Beneddine, S., Dandois, J., Sipp, D. & Robinet, J.-C. 2019 Transonic buffet instability: From two-dimensional airfoils to three-dimensional swept wings. *Physical Review Fluids* **4** (10), 103906.

Parente, E., Robinet, J.-Ch., De Palma, P. & Cherubini, S. 2022 Linear and nonlinear optimal growth mechanisms for generating turbulent bands. *Journal of Fluid Mechanics* **938**, A25.

Park, H., Park, H. & Kim, J. 2013 A numerical study of the effects of superhydrophobic surface on skin-friction drag in turbulent channel flow. *Physics of Fluids* **25** (11), 110815.

Patera, A. T. 1984 A spectral element method for fluid dynamics: Laminar flow in a channel expansion. *Journal of Computational Physics* **54** (3), 468–488.

Philip, J. R. 1972 Flows satisfying mixed no-slip and no-shear conditions. *Zeitschrift für angewandte Mathematik und Physik ZAMP* **23** (3), 353–372.

Picella, F. 2019 Retarder la transition vers la turbulence en imitant les feuilles de lotus. PhD thesis, ENSAM.

Picella, F., Robinet, J.-Ch & Cherubini, S. 2019 Laminar–turbulent transition in channel flow with superhydrophobic surfaces modelled as a partial slip wall. *Journal of Fluid Mechanics* **881**, 462–497.

Picella, F., Robinet, J.-Ch & Cherubini, S. 2020 On the influence of the modelling of superhydrophobic surfaces on laminar–turbulent transition. *Journal of Fluid Mechanics* **901**.

Pralits, J. O., Alinovi, E. & Bottaro, A. 2017 Stability of the flow in a plane microchannel with one or two superhydrophobic walls. *Physical Review Fluids* **2** (1), 013901.

Pralits, J. O., Bottaro, A. & Cherubini, S. 2015 Weakly nonlinear optimal perturbations. *Journal of Fluid Mechanics* **785**, 135–151.

Prigogine, I. & Nicolis, G. 1985 Self-Organisation in Nonequilibrium Systems: Towards A Dynamics of Complexity. In *Bifurcation Analysis: Principles, Applications and Synthesis* (ed. M. Hazewinkel, R. Jurkovich & J. H. P. Paelinck), pp. 3–12. Springer Netherlands.

Pringle, C. C. T. & Kerswell, R.R. 2010 Using nonlinear transient growth to construct the minimal seed for shear flow turbulence. *Physical Review Letters* **105**, 154502.

Rayleigh, L. 1879 On the Stability, or Instability, of certain Fluid Motions. *Proceedings of the London Mathematical Society* **s1-11** (1), 57–72.

Reddy, S. C. & Henningson, D. S. 1993 Energy growth in viscous channel flows. *Journal of Fluid Mechanics* **252**, 209–238.

Reynolds, O. 1883 III. An experimental investigation of the circumstances which determine whether the motion of water shall be direct or sinuous, and of the law of resistance in parallel channels. *Proceedings of the Royal Society of London* **35** (224-226), 84–99.

Robinson, S. K. 1991 Coherent motions in the turbulent boundary layer. *Annual Review of Fluid Mechanics* **23** (1), 601–639.

Rolandi, L. V. 2021 Stability of low reynolds number compressible flows. These de doctorat, Toulouse, ISAE.

Rucklidge, A. M., Silber, M. & Skeldon, A. C. 2012 Three-Wave Interactions and Spatiotemporal Chaos. *Physical Review Letters* **108** (7), 074504, publisher: American Physical Society.

Ruelle, D. & Takens, F. 1971 On the nature of turbulence. *Communications in Mathematical Physics* **20** (3), 167–192.

Saric, W. S., Reed, H. L. & Kerschen, E. J. 2002 Boundary-layer receptivity to freestream disturbances. *Annual Review of Fluid Mechanics* **34** (1), 291–319.

Saric, W. S., Reed, H. L. & White, E. B. 2003 Stability and Transition of Three-Dimensional Boundary Layers. *Annual Review of Fluid Mechanics* **35** (1), 413–440.

Sayadi, T., Hamman, C. W. & Moin, P. 2013 Direct numerical simulation of complete h-type and k-type transitions with implications for the dynamics of turbulent boundary layers. *Journal of Fluid Mechanics* **724**, 480–509.

Schlatter, P., Brandt, L., de Lange, H. C. & Henningson, D. S. 2008 On streak breakdown in bypass transition. *Physics of Fluids* **20** (10), 101505.

Schlichting, H. 1933 Zur enstehung der turbulenz bei der plattenströmung. *Nachrichten von der Gesellschaft der Wissenschaften zu Göttingen, Mathematisch-Physikalische Klasse* **1933**, 181–208.

Schmid, P. 2001 *Stability and Transition in Shear Flows*.

Schmid, P. J. 2007 Nonmodal Stability Theory. *Annual Review of Fluid Mechanics* **39** (1), 129–162.

Schmid, P. J. & Brandt, L. 2014 Analysis of Fluid Systems: Stability, Receptivity, Sensitivity: Lecture notes from the FLOW-NORDITA Summer School on Advanced Instability Methods for Complex Flows, Stockholm, Sweden, 2013. *Applied Mechanics Reviews* **66** (2).

Schmid, P. J. & Henningson, D. S. 1992 A new mechanism for rapid transition involving a pair of oblique waves. *Physics of Fluids A: Fluid Dynamics* **4** (9), 1986–1989.

Schmid, P. J., de Pando, M. Fosas & Peake, N. 2017 Stability analysis for n-periodic arrays of fluid systems. *Physical Review Fluids* **2** (11), 113902.

Schmitz, R. & Zimmermann, W. 1996 Spatially periodic modulated Rayleigh-Bénard convection. *Phys. Rev. E* **53**, 5993–6011.

Schäffel, D., Koynov, K., Vollmer, D., Butt, H.-J. & Schönecker, C. 2016 Local Flow Field and Slip Length of Superhydrophobic Surfaces. *Physical Review Letters* **116** (13), 134501.

Gómez-de Segura, G. & García-Mayoral, R. 2020 Imposing virtual origins on the velocity components in direct numerical simulations. *International Journal of Heat and Fluid Flow* **86**, 108675.

Seo, J., García-Mayoral, R. & Mani, A. 2015 Pressure fluctuations and interfacial robustness in turbulent flows over superhydrophobic surfaces. *Journal of Fluid Mechanics* **783**, 448–473.

Seo, J., García-Mayoral, R. & Mani, A. 2018 Turbulent flows over superhydrophobic surfaces: flow-induced capillary waves, and robustness of air–water interfaces. *Journal of Fluid Mechanics* **835**, 45–85.

Seo, J. & Mani, A. 2016 On the scaling of the slip velocity in turbulent flows over superhydrophobic surfaces. *Physics of Fluids* **28** (2), 025110.

Seo, J. & Mani, A. 2018 Effect of texture randomization on the slip and interfacial robustness in turbulent flows over superhydrophobic surfaces. *Physical Review Fluids* **3** (4), 044601.

Serpieri, J. 2018 Cross-Flow Instability. PhD thesis, Delft University of Technology.

Serpieri, J. & Kotsonis, M. 2016 Three-dimensional organisation of primary and secondary cross-flow instability. *Journal of Fluid Mechanics* **799**, 200–245.

Shikhmurzaev, Y. D. 1996 Dynamic contact angles and flow in vicinity of moving contact line. *AIChE Journal* **42** (3), 601–612.

Sipp, D., Marquet, O., Meliga, P. & Barbagallo, A. 2010 Dynamics and Control of Global Instabilities in Open-Flows: A Linearized Approach. *Applied Mechanics Reviews* **63** (3).

Smyth, W. D. 2003 Secondary kelvin–helmholtz instability in weakly stratified shear flow. *Journal of Fluid Mechanics* **497**, 67–98.

Stroock, A. D., Dertinger, S. K., Whitesides, G. M. & Ajdari, A. 2002 Patterning Flows Using Grooved Surfaces. *Analytical Chemistry* **74** (20), 5306–5312.

Sundin, J., Zaleski, S. & Bagheri, S. 2021 Roughness on liquid-infused surfaces induced by capillary waves. *Journal of Fluid Mechanics* **915**, R6.

Szumbarski, J. & Floryan, J. M. 2006 Transient disturbance growth in a corrugated channel. *Journal of Fluid Mechanics* **568**, 243–272.

Tani, I. & Komoda, H. 1962 Boundary-layer transition in the presence of streamwise vortices. *Journal of the Aerospace Sciences* **29** (4), 440–444.

Tatsumi, T. & Yoshimura, T. 1990 Stability of the laminar flow in a rectangular duct. *Journal of Fluid Mechanics* **212**, 437–449.

Teo, C. J. & Khoo, B. C. 2008 Analysis of Stokes flow in microchannels with superhydrophobic surfaces containing a periodic array of micro-grooves. *Microfluidics and Nanofluidics* **7** (3), 353.

Theofilis, V. 2003 Advances in global linear instability analysis of nonparallel and three-dimensional flows. *Progress in Aerospace Sciences* **39** (4), 249–315.

Tollmien, W. 1930 Über die entstehung der turbulenz pp. 18–21.

Tomlinson, S. 2021 Superhydrophobic surfaces: their hydrodynamic stability, thermal resistance and boundary layers. PhD thesis, Imperial College.

Tomlinson, Samuel D. & Papageorgiou, Demetrios T. 2022 Linear instability of lid- and pressure-driven flows in channels textured with longitudinal superhydrophobic grooves. *Journal of Fluid Mechanics* **932**, publisher: Cambridge University Press.

Trefethen, L.N., Trefethen, A. E., Reddy, S. C. & Driscoll, T. A. 1993 Hydrodynamic stability without eigenvalues. *Science* **261** (5121), 578–584.

Trefethen, Lloyd N. 2000 *Spectral Methods in MATLAB*. Society for Industrial and Applied Mathematics.

Tuckerman, L. S., Chantry, M. & Barkley, D. 2020 Patterns in wall-bounded shear flows. *Annual Review of Fluid Mechanics* **52** (1), 343–367.

Turing, A. M. 1952 The chemical basis of morphogenesis. *Philosophical Transactions of the Royal Society of London. Series B, Biological Sciences* **237** (641), 37–72.

Ustinov, M. V. 2002 Stability of the Flow in a Streaky Structure and the Development of Perturbations Generated by a Point Source Inside It. *Fluid Dynamics* **37** (1), 9–20.

Van Buren, T. & Smits, A. J. 2017 Substantial drag reduction in turbulent flow using liquid-infused surfaces. *Journal of Fluid Mechanics* **827**, 448–456.

Vaughan, N. J. & Zaki, T. A. 2011 Stability of zero-pressure-gradient boundary layer distorted by unsteady klebanoff streaks. *Journal of Fluid Mechanics* **681**, 116–153.

Villegas, M., Zhang, Y., Abu Jarad, N., Soleymani, L. & Didar, T. F. 2019 Liquid-infused surfaces: A review of theory, design, and applications. *ACS Nano* **13** (8), 8517–8536.

Waleffe, F. 1995 Transition in shear flows. Nonlinear normality versus non-normal linearity. *Physics of Fluids* **7** (12), 3060–3066.

Wannier, G. H. 1937 The structure of electronic excitation levels in insulating crystals. *Phys. Rev.* **52**, 191–197.

Wannier, G. H. 1962 Dynamics of band electrons in electric and magnetic fields. *Rev. Mod. Phys.* **34**, 645–655.

Wassermann, P. & Kloker, M. 2002 Mechanisms and passive control of crossflow-vortex-induced transition in a three-dimensional boundary layer. *Journal of Fluid Mechanics* **456**, 49–84.

Wassermann, P. & Kloker, M. 2003 Transition mechanisms induced by travelling crossflow vortices in a three-dimensional boundary layer. *Journal of Fluid Mechanics* **483**, 67–89.

Weiss, S., Seiden, G. & Bodenschatz, E. 2014 Resonance patterns in spatially forced Rayleigh–Bénard convection. *Journal of Fluid Mechanics* **756**, 293–308.

Weiss, S., Seiden, G. & E Bodenschatz, E. 2012 Pattern formation in spatially forced thermal convection. *New Journal of Physics* **14** (5), 053010.

Wexler, J. S., Jacobi, I. & Stone, H. A. 2015 Shear-driven failure of liquid-infused surfaces. *Phys. Rev. Lett.* **114**, 168301.

White, E. B. & Saric, W. S. 2005 Secondary instability of crossflow vortices. *Journal of Fluid Mechanics* **525**, 275–308.

Wintergerste, T. & Kleiser, L. 2000 Secondary stability analysis of nonlinear crossflow vortices. In *Laminar-Turbulent Transition* (ed. H. F. Fasel & W. S. Saric), pp. 583–586. Berlin, Heidelberg: Springer Berlin Heidelberg.

Wong, T.-S., Kang, S. H., Tang, Sindy K. Y., Smythe, E. J., Hatton, B. D., Grinthal, A. & Aizenberg, J. 2011 Bioinspired self-repairing slippery surfaces with pressure-stable omniphobicity. *Nature* **477** (7365), 443–447.

Woolford, B., Prince, J., Maynes, D. & Webb, B. W. 2009 Particle image velocimetry characterization of turbulent channel flow with rib patterned superhydrophobic walls. *Physics of Fluids* **21** (8), 085106.

Wu, X., Moin, P., Wallace, J. M., Skarda, J., Lozano-Durán, A. & Hickey, J.-P. 2017 Transitional–turbulent spots and turbulent–turbulent spots in boundary layers. *Proceedings of the National Academy of Sciences* **114** (27), E5292–E5299.

Xiong, X. & Tao, J. 2020 Linear stability and energy stability of plane Poiseuille flow with isotropic and anisotropic slip boundary conditions. *Physics of Fluids* **32** (9), 094104.

Yu, K. H., Teo, C. J. & Khoo, B. C. 2016 Linear stability of pressure-driven flow over longitudinal superhydrophobic grooves. *Physics of Fluids* **28** (2), 022001.

Zaki, T. A. 2013 From Streaks to Spots and on to Turbulence: Exploring the Dynamics of Boundary Layer Transition. *Flow, Turbulence and Combustion* **91** (3), 451–473.

Zaki, T. A. & Durbin, P. A. 2005 Mode interaction and the bypass route to transition. *Journal of Fluid Mechanics* **531**, 85–111.

Zaki, T. A. & Durbin, P. A. 2006 Continuous mode transition and the effects of pressure gradient. *Journal of Fluid Mechanics* **563**, 357–388.

Zampogna, G. A., Magnaudet, J. & Bottaro, A. 2019 Generalized slip condition over rough surfaces. *Journal of Fluid Mechanics* **858**, 407–436.

Zang, T. A. & Krist, S. E. 1989 Numerical experiments on stability and transition in plane channel flow. *Theoretical and Computational Fluid Dynamics* **1** (1), 41–64.

Zhang, A., Dong, M. & Zhang, Y. 2018 Receptivity of secondary instability modes in streaky boundary layers. *Physics of Fluids* **30** (11), 114102, arXiv: https://doi.org/10.1063/1.5046136.

Zhang, J., Tian, H., Yao, Z., Hao, P. & Jiang, N. 2015 Mechanisms of drag reduction of superhydrophobic surfaces in a turbulent boundary layer flow. *Experiments in Fluids* **56** (9), 179.

Zhang, J., Yao, Z. & Hao, P. 2016 Drag reductions and the air-water interface stability of superhydrophobic surfaces in rectangular channel flow. *Physical Review E* **94** (5), 053117.

Zimmermann, W., Ogawa, A., Kai, S., Kawasaki, K. & Kawakatsu, T. 1993 Wavelength Competition in Convective Systems. *Europhysics Letters* **24** (3), 217.

Antoine JOUIN

Instabilities in spatially periodic systems: application to secondary instabilities and complex surfaces

Résumé : Le présent manuscrit de thèse propose une étude des instabilités dans des écoulements spatialement périodiques. Deux types de périodicité, correspondant à des systèmes physiques sensiblement différents, peuvent être distinguées. Le premier type de périodicité, le plus simple, est géométrique et résulte de la répétition d'un motif ou d'un obstacle qui forcerait spatialement et périodiquement l'écoulement. Un exemple serait l'écoulement au-dessus d'une surface rugueuse ou superhydrophobe. La périodicité pourrait également être générée par une modulation de l'écoulement causée par l'émergence d'une structure cohérente via une instabilité primaire comme c'est le cas pour des stries dans une couche limite. Un cadre permettant la réalisation des analyses de stabilité modale et non-modale d'un système spatialement périodique est proposé. Il est basé sur la théorie de Bloch et des matrices circulantes, couplée à un problème de stabilité bidimensionnel. Un premier cas, qui sert également de validation de la méthode, porte sur la stabilité secondaire d'une couche limite tridimensionnelle. La stabilité secondaire de stries dans une couche limite laminaire est également examinée. Dans ce cas, les analyses non-modales mettent en exergue l'apparition d'un nouveau mécanisme potentiellement responsable de la transition vers la turbulence. Une compétition entre le mécanisme d'Orr et celui de génération des stries conduit également à l'apparition d'un régime de verrouillage de phase. La seconde partie de la thèse porte sur la stabilité d'un écoulement dans un canal dont une des parois est une surface complexe, soit rugueuse ou superhydrophobe. Dans un premier temps, les rugosités sont prises en compte via une technique d'homogénéisation, qui vient approximer l'effet des rugosités par une condition aux limites équivalentes. Une simulation est réalisée et met en évidence la présence de structures similaires à celles trouvées lors de l'analyse de la couche limite tridimensionnelle. La stabilité de ces structures est alors analysée sous cette nouvelle lumière. Les surfaces complexes sont étudiées sans technique d'homogénéisation: pour une surface rugueuse, la forme de la rugosité est prise en compte tandis que ce sont les movements de l'interface pour une surfaace superhydrophobe.

Mots clés : instabilités, système n-périodique, ondes de Bloch, couche limite 3D, stries, surfaces rugueuses et SH

Abstract : This thesis manuscript proposes a study of instabilities in spatially periodic flows. Two types of periodicity, corresponding to significantly different physical systems, can be distinguished. The first type of periodicity, the simplest, is geometric and results from the spatial repetition of a pattern or an obstacle that periodically deforms the flow. An example is the flow above a rough or superhydrophobic surface. The periodicity could also be generated by a modulation of the flow caused by the emergence of a coherent structure via a primary instability as in the case of streaks in a boundary layer. A framework allowing modal and non-modal stability analyses of spatially periodic systems is proposed. It is based on the Bloch theory and circulating matrices, and it is coupled with a two-dimensional stability problem. The secondary instabilities of cross-flow vortices and streaks in a boundary layer are also examined. In this case, the non-modal analyses highlight the appearance of a new mechanism potentially responsible for the transition to turbulence. A competition between the Orr mechanism and that allowing the generation of streaks also leads to the appearance of a phase-locking regime. The second part of the thesis deals with the stability of a flow in a channel where one of the walls is a complex surface, either rough or superhydrophobic. First, the roughnesses are taken into account via a homogenization technique, which approximates the effect of the roughnesses by an equivalent boundary condition. A direct numerical simulation is carried out and highlights the presence of structures similar to those found during the analysis of the three-dimensional boundary layer. The stability of these structures is then analysed under this new light. Then, the case of the flow over a rough wall is considered, taking into account the geometrical complexity of the roughness. The last part of the thesis extends the previous analysis to superhydrophobic surfaces, taking into account the gas-liquid interface dynamics.

Keywords : instabilities, Bloch waves, boundary layer, streaks, rough and superhydrophobic surfaces